Technische Universität München

Dynamics of water mass variations in lake/reservoir dominated regions from multi-sensor Earth observation data and hydrological model outputs

Dissertation

von

Alka Singh

Deutsches Geodätisches Forschungsinstitut

und Lehrstuhl für Geodätische Geodynamik (DGFI-TUM)

Ingenieurfakultät Bau Geo Umwelt

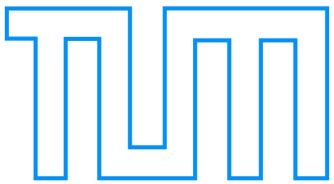

Ingenieurfakultät Bau Geo Umwelt

Deutsches Geodätisches Forschungsinstitut
und Lehrstuhl für Geodätische Geodynamik (DGFI-TUM)

Dynamics of water mass variations in lake/reservoir dominated regions from multi-sensor Earth observation data and hydrological model outputs

Alka Singh

Vollständiger Abdruck der von der Ingenieurfakultät Bau Geo Umwelt der Technischen Universität München zur Erlangung des akademischen Grades eines

Doktor – Ingenieurs (Dr.-Ing.)

genehmigten Dissertation.

Vorsitzender:	Prof. Dr.-Ing. Uwe Stilla
Prüfer der Dissertation:	1. Prof. Dr.-Ing. Florian Seitz
	2. Prof. Dr. Andreas Güntner,
	3. Prof. Dr.-Ing. Markus Disse

Die Dissertation wurde am 10.11.2016 bei der Technischen Universität München eingereicht und durch die Ingenieurfakultät Bau Geo Umwelt am 06.03.2017 angenommen.

Abstract

Lakes and reservoirs store 87% of the earth's total fresh open water. Many of these inland water bodies have been gradually receding over the years. Often they are ungauged or poorly gauged in developing countries. The present study tries to fill this gap by deriving remote sensing based methods for lake/reservoir volume estimation. Heterogeneous and multi-dimensional Earth-observation data and global hydrological models have been used for the purpose. The two test sites analyzed in this study are the Aral Sea in Central Asia and Lake Mead in the United States of America. These waterbodies are undergoing a long-term storage decline, primarily due to significant upstream water abstraction and prolonged drought respectively. The focus of this study is on estimates of gravimetrical and geometrical variations present in these lakes and their environs.

The Gravity Recovery and Climate Experiment (GRACE) satellite mission measures the gravimetrical variations due to hydrological changes within a region. However, the size of study area and the magnitude of mass changes are limitations in GRACE due to its resolution. In order to evaluate geometrical variations of the lakes/reservoirs, multiple altimetry and Landsat missions are combined. The intersection of a lake or a reservoir's bathymetry with the derived water heights from Landsat and altimetry, respectively, generates two independent absolute-water-volumes, referred to as Landsat-bathymetry volume (LBV) and altimetry-bathymetry volume (ABV). A Kalman-based State Space Model (SSM) produces a combined absolute volume time series referred to as CSSME (combined state space model estimate) from LBV and ABV. Another entirely remote-sensing-based approach for the determination of the lake/reservoir volume variations (ALVV) is the truncated pyramid volume method. It combines the water height variations from altimetry with the respective changes of the water surface-area from Landsat. As uncertainties of the lake/reservoir geometry and estimated water heights/area are not available, it is not possible to determine reliable error estimates of different results. The acquired volumes from the three methods (LBV, ABV and ALVV) agree very well with each other for both water bodies. For Lake Mead, all the estimated volumes showed correlation of above 0.98, with in-situ observations. The monthly derivative of the Lake Mead volume (from CSSME) showed a correlation of 0.81 with the Colorado River runoff deficit. It has also been demonstrated that the vertical hydrological fluxes acting over Lake Mead have a negligible contribution to the reservoir volume change because of its small water surface area and steep topography. Due to limited ground observations, only GRACE could validate the Aral Sea volume variations.

However, GRACE observes an integrated mass change not only from the different hydrological compartments but also from the area outside the lake/reservoir because of its limited spatial resolution. Therefore, to incorporate storage contributions of other hydrological compartments from the surroundings of the lake/reservoir, outputs of two global hydrological models, namely the Global Land Data Assimilation System (GLDAS) and Water Gap hydrological model (WGHM), are applied. The results demonstrate a good correspondence between the geometrical estimates of the Aral Sea volume and the gravimetrical variations in the region (correlation coefficients of 0.82). Even though the size of Lake Mead is far below the spatial resolution of GRACE, a correlation of 0.6 is exhibited between the geometrical and gravimetrical observations. It can be stated that the GLDAS-based hybrid storage, which combines the estimated lake/reservoir volume (from CSSME) with soil moisture (SM) and snow water equivalent (SWE) obtained from GLDAS, produces a better estimate of the net water storage variations for the two study areas (~0.87 correlation with the GRACE-derived mass variations). This shows that GRACE is sufficiently sensitive to observe mass variations of a small water body like Lake Mead if the effects from a larger region around the lake/reservoir are modeled properly.

The study demonstrates that lakes/reservoirs can be effectively monitored using remote sensing data, even if the information of the bathymetry is poor. Depending on the availability of data, any of the given (ABV, LBV, and ALVV) lake/reservoir volume estimation methods can be applied. This study also demonstrates that for small regions, regional GRACE analysis approaches (like mascons) for the estimation of water storage changes are much more reliable than global approaches based on spherical harmonics. Therefore, in order to analyze the hydrological state of a region, a careful application and interpretation of the GRACE observations are recommended. The importance of the suggested methods for lake/reservoir volume estimation and its gravimetrical analysis is particularly high in poorly gauged and remotely located regions, where they can act as a good alternative to ground-based observations.

Zusammenfassung

In Seen und Wasserreservoirs sind 87% des Süßwasservorkommens der Erde gespeichert. Viele dieser Inlandgewässer schrumpfen, und besonders in Entwicklungsländern werden Wasserstände gar nicht oder nur eingeschränkt gemessen. Diese Studie beschäftigt sich mit der Entwicklung von Methoden zur Abschätzung des Wasservolumens in Seen und Wasserreservoirs mithilfe mehrdimensionaler Erdbeobachtungsdaten und globaler hydrologischer Modelle. Zwei Gebiete, die in dieser Studie analysiert werden, sind der Aralsee in Zentralasien und der Lake Mead in den USA. Die Wasservorkommen dieser zwei Gewässer nehmen seit langer Zeit kontinuierlich ab, hauptsächlich verursacht durch vermehrte Wasserentnahme flussaufwärts (Aralsee) oder durch anhaltende Dürren (Lake Mead). Diese Studie basiert auf Schätzungen von gravimetrischen und geometrischen Veränderungen in den Beobachtungsgebieten.

Die Satellitenmission „Gravity Recovery and Climate Experiment“ (GRACE) ermöglicht erstmals die regionale Messung von gravimetrischen Variationen, die durch hydrologische Veränderungen hervorgerufen werden. Die räumliche Auflösung der GRACE-Messungen stellt allerdings Anforderungen an die Größe des Studiengebietes und an die Größenordnung der zu beobachtenden Massenveränderungen. Um die geometrischen Veränderungen des Sees/Wasserreservoirs auszuwerten, werden Daten von zahlreichen Altimetrie- und Landsat-Missionen kombiniert. Die Verschneidung der Bathymetrie mit den aus Landsat und Altimetrie abgeleiteten Wasserständen ergibt zwei unabhängig ermittelte Wasservolumen, die im folgenden Landsat-Bathymetrie Volumen (LBV) und Altimetrie-Bathymetrie Volumen (ABV) genannt werden. Außerdem wird eine kombinierte Zeitreihe des Absolutvolumens (bezeichnet als CSSME, „combined state space model estimate“) aus LBV und ABV mithilfe eines „Kalman-based State Space Model“ (SSM) generiert. Eine weitere, allein auf Fernerkundung basierende Methode, die für die Bestimmung der Wasservolumenveränderung (ALVV) angewandt wird, ist die „truncated pyramid volume method“. Sie kombiniert die Veränderung des Wasserstandes basierend auf Altimetrie mit den jeweiligen von Landsat aufgenommenen Veränderungen der Wasseroberfläche. Aufgrund von unbekannten Unsicherheiten in der Geometrie der Gewässeroberflächen und Unsicherheiten in den geschätzten Wasserständen, ist eine zuverlässige Fehlerabschätzung für die verschiedenen Ergebnisse nicht möglich. Die berechneten Wasservolumina der drei Methoden (LBV, ABV und ALVV) stimmen bei beiden Gewässern gut miteinander überein. Für Lake Mead ergaben alle ermittelten Wasservolumen einen Korrelationswert von 0.98 mit In-situ Messungen. Die monatliche Ableitung des

Reservoirvolumens des Lake Mead (von CSSME) zeigte mit dem Defizit des Oberflächenabflusses des Colorado River eine Korrelation von 0.81. Dies verdeutlicht, dass die vertikalen hydrologischen Strömungen, die auf den Lake Mead einwirken, aufgrund seiner geringen Wasseroberfläche und der steilen Topografie einen geringen Einfluss auf die Veränderung des Reservoirvolumens haben. Aufgrund der wenigen Bodenbeobachtungen, konnten Wasservolumenveränderungen des Aralsees nur mit GRACE validiert werden.

Allerdings bildet GRACE aufgrund seiner geringen räumlichen Auflösung nicht nur die Massenveränderung des zu untersuchenden Gewässers, sondern auch die von umliegenden Gebieten in integraler Form ab. Um die Einflüsse von hydrologischen Veränderungen in benachbarten Gebieten zu berücksichtigen, werden die Simulationswerte von zwei globalen hydrologischen Modellen, nämlich dem „Global Land Data Assimilation System“ (GLDAS) und dem „Water Gap hydrological model“ (WGHM), in die Analyse mit einbezogen. Die Studie zeigt, dass geometrische Schätzwerte des Wasservolumens vom Aralsee mit den gravimetrischen Veränderungen in der Region übereinstimmen (Korrelationskoeffizient: 0.82). Obwohl der Lake Mead ein kleineres Gebiet umfasst, als die räumliche Auflösung von GRACE abdeckt, beträgt der Korrelationswert zwischen den geometrischen und gravimetrischen Beobachtungen 0.6. Die Studie zeigt, dass die GLDAS-basierte hybride Wasserspeicherung, die das geschätzte See-/Wasserreservoir-Volumen (von CSSME) mit der von GLDAS berechneten Bodenfeuchtigkeit (SM) und dem sogenannten Schnee/Wasser-Äquivalent (SWE) kombiniert, präziser die Veränderungen des gesamten Wasserhaushaltes in den beiden Studiengebieten widerspiegelt (~0.87 Korrelation mit der GRACE-basierten Massenvariation). Dies zeigt, dass GRACE Massenveränderungen in kleinenWasserkörpern wie dem Lake Mead abbilden kann, wenn Einflüsse von umliegenden Gebieten ausreichend modelliert und berücksichtigt werden.

Diese Studie verdeutlicht, dass Seen und Wasserreservoirs effektiv mithilfe von Fernerkundungsdaten überwacht werden können, selbst wenn kaum Informationen über die Bathymetrie vorhanden sind. Je nach Verfügbarkeit der Daten können alle der hier vorgestellten Methoden (LBV, ABV und ALVV) zur Bestimmung des See-/Reservoir Wasservolumens angewandt werden. Die Studie zeigt auch, dass für kleine Regionen regionale GRACE-Auswertungen (wie z.B. Mascons) für die Abschätzung von Wasserspeicherveränderungen genauere Ergebnisse liefern als globale Ansätze, die auf sphärisch-harmonischen Basisfunktionen basieren. Für die hydrologische Analyse einer Region ist deshalb eine sorgfältige Anwendung und Interpretation der GRACE-Beobachtungen nötig. Besonders in Gebieten, in denen die Wasserstände kaum überwacht werden, sind die vorgestellten Methoden

zur Bestimmung von Veränderungen im Wasservolumen von Seen und Wasserreservoirs von großer Bedeutung, weil sie eine Alternative zu Bodenbeobachtungen darstellen.

Preface

This dissertation integrates the results of following four international peer-reviewed journal articles:

- Singh, A.; Seitz, F.; Schwatke, C.: **Inter-annual water storage changes in the Aral Sea from multi-mission satellite altimetry, optical remote sensing, and GRACE satellite gravimetry**; Remote Sensing of Environment, Vol. 123, pp 187-195, Elsevier, 2012. DOI: 10.1016/j.rse.2012.01.001.

- Singh, A.; Seitz, F.; Schwatke, C.: **Application of Multi-Sensor Satellite Data to observe Water Storage Variations**; Journal of Selected Topics in Applied Earth Observations and Remote Sensing (JSTARS), vol. 6, issue 3, pp 1502–1508, IEEE Geo-science and Remote Sensing Society, 2013. DOI: 10.1109/JSTARS.2013.2258326.

- Singh, A.; Kumar, U.; Seitz, F.: **Remote sensing of storage fluctuations of poorly gauged reservoirs and its state space model (SSM) based estimation;** Remote Sensing, Vol. 7, issue 12, pp 17113–17134, 2015. DOI: 10.3390/rs71215872 (Open source).

- Singh, A.; Seitz, F.; Eicker A.; Güntner A. **Water budget analysis within the surrounding of prominent lakes and reservoirs from multi-sensor Earth observation data and hydrological models: case studies of the Aral Sea and Lake Mead;** Remote Sensing, Vol. 8, pp 953, 2016. DOI: 10.3390/rs8110953 (Open source).

Contents

Abbreviations

ABV	Altimetry-bathymetry-volume
ALVV	Altimetry-Landsat-volume-variation
AVHRR	Advanced Very High-Resolution Radiometer
CSR	Center for Space Research at University of Texas at Austin
CSSME	Combined State Space Model estimate
DEM	Digital Elevation Model
DAHITI	Database for Hydrological Time Series of Inland Waters
ET	Evapotranspiration
EWH	Equivalent Water Height
GFZ	German Research Centre for Geosciences
GLDAS	Global Land Data Assimilation System
GPCC	Global Precipitation Climatology Centre
GPS	Global Positioning System
GRACE	Gravity Recovery and Climate Experiment
GW	Groundwater
IPCC	Intergovernmental Panel on Climate Change
ISODATA	Iterative self-organizing data analysis technique
JPL	Jet Propulsion Laboratory
LBV	Landsat-bathymetry-volume
Mascon	Mass Concentration blocks
MODIS	Moderate-resolution Imaging Spectroradiometer
MSL	Mean Sea Level
NRMSE	Normalized Root Mean Square Error
OpenADB	Open Altimetry DataBase
RMSE	Root Mean Square Error
R	Correlation coefficient
r^2	Coefficient of determination
SH	Spherical Harmonics
SM	Soil moisture
SRB	Selected region boundary
SSM	State Space Model

SW	Surface water bodies (e.g., lakes, reservoirs, rivers, etc.)
SWE	Snow water equivalent
TRMM	Tropical Rainfall Measuring Mission
TWS	Total water storage
USBR	United States Bureau of Reclamation
USGS	United States Geological Survey
WGHM	Water Gap (Global Assessment and Prognosis) hydrological model

1 Introduction

1.1 Background

Changes in the pattern of land use and economic activities (like big hydro power and irrigation projects) have led to excessive-exploitation of water in many regions. The IPCC 2014 Report stresses that the severity and frequency of weather extremities will keep on increasing due to changing climate (Pachauri et al., 2015). This issue has made contemporary societies seriously evaluate current hydrological resources in order to manage them more effectively in different time horizons.

Lakes and reservoirs hold 87% of the fresh surface water body (SW) of the planet (Gleick, 1993). Except for few endorheic lakes, which have evolved into a saline water bodies, most lakes are fresh water. Many inland water bodies have declined dramatically in last few decades (Awange et al., 2008; Feng et al., 2012; Nicholson, 1998; Tourian et al., 2015). Unfortunately, most of the lakes/reservoirs in developing countries are ungauged/ poorly gauged. Widespread loss of ground-based hydrological monitoring networks and the bleak prospects for improvement have now became serious concerns to the scientific community (Shiklomanov et al., 2002; Zhang et al., 2006). Furthermore, the ability of hydrological models to quantify water are also limited by spatial and temporal data gaps, data inconsistencies, instrumental and human errors, etc. (Rodell et al., 2006). Such conditions trigger the exploration of alternative water resource mapping and monitoring tools. In the last few decades, multi-sensor satellite data has provided unprecedented capability to capture the spatial and temporal changes from different dimensions, on a regional and global scale. It has helped us to recognize, for the first time, the dramatic changes that have emerged in water landscape, due to rising sea level, declining snow cover, depleting ground water (GW), and increasing number of floods and droughts (Famiglietti et al., 2015). Many studies (Chao et al., 2008; Dieng et al., 2015; Lettenmaier and Milly, 2009) demonstrate that water impoundment by reservoirs has canceled some land contributions to global sea level rise. This huge fresh water mass, stored in several tens of thousands of dams and lakes, needs to be properly estimated. The study of this complex state-time interaction and observation of distinct hydrological features and properties can be facilitated by different remote sensing based datasets. The availability of observations for mass change from the time variable Gravity Recovery and Climate Experiment (GRACE) mission has revolutionized hydrological estimations by adding another important dimension to their dataset.

1.2 Problem Statement

Given the importance of lakes/reservoir monitoring in a hydrological system and the capabilities of space missions, the following research questions are being addressed in this study:

1. How to monitor geometric and gravimetric changes of a lake/reservoir from space missions.
2. How to compute lake/reservoir water volume from multiple geometrical space missions.
3. How to combine different volume estimates, to derive the most reliable and continuous time-series of lake/reservoir water volume.
4. Assessment of the hydrological state of lake/reservoir dominated regions from a joint analysis of geometrical and gravimetrical information.

1.3 State of the art

Remote sensing provides significant capabilities in mapping surface water and its dynamics from different dimensions.

1.3.1 Satellite imagery for lake surface monitoring

Many studies have used radar and optical imageries for water extent monitoring of lakes/reservoirs and wetlands (Alsdorf et al., 2007; Frappart et al., 2006; Klein et al., 2014; Töyrä et al., 2001). The spatial resolution of the passive microwave radar is very poor because of the weak radiations received by the sensors. Therefore, Synthetic Aperture Radar (SAR) has been increasingly used in inland water monitoring (Baup et al., 2014; Frappart et al., 2005) because of its higher spatial resolution and capability to penetrate tree canopies, cloud cover, etc. However, SAR has problems in delineating water mask when wind-induced waves and emergent vegetation roughen the water surface (Alsdorf et al., 2007). Furthermore, its complex processing and the limited availability of free SAR imageries are additional constraints. Therefore, passive visible/infrared sensors like Landsat, Advanced Very High-Resolution Radiometer (AVHRR), Advanced Spaceborne Thermal Emission and Reflection Radiometer (ASTER) and Moderate-resolution Imaging Spectroradiometer (MODIS) are commonly used for the time-series generation of land-water mask. Landsat is an invaluable resource of global monitoring because of its rich archive, relatively high spatial resolution, and freely available database. It is the most frequently used remote sensing imagery (Fuller et al., 1994; Goward and Williams, 1997; Woodcock et al., 2008; Wulder et al., 2011). To depict inland surface water

body (SW), many global water mask databases have been created (e.g., the Shuttle Radar Topography Mission (SRTM) Water Body Data (SWBD), and A Global Self-consistent, Hierarchical, High-resolution Geography Database (GSHHG)). However, they are primarily of a coarser resolution and most inland water bodies are too small for them. For example, Carroll et al. (2009) generated a 250 m global raster water mask based on MODIS and SWBD. Landsat has enabled relatively high-resolution (30 m) global mapping (Feng et al., 2015; Liao et al., 2014; Verpoorter et al., 2014) but it requires heavy human input. These static water masks represent only one specific temporal snapshot. However, we need dynamic water mask at high spatial resolution, because the outdated water surface-area extent of water bodies introduces significant errors in hydrological state estimation.

To map dynamic water surface from Landsat, different methods have been applied, like thematic classification (Hung and Wu, 2005), single band thresholding (Rundquist et al., 1987; Sethre et al., 2005) and spectral water index, i.e., band ratio approach (Gao, 1996; McFEETERS, 1996; Xu, 2006). Many researchers have also used NIR spectra from optical images to extract water mask (Karimov et al., 2014; Klein et al., 2014; Pietroniro et al., 1999; Verdin, 1996).

1.3.2 Satellite altimetry for lake level monitoring

Satellite altimetry was originally developed for oceanography and ice sheet studies. However, it has been used successfully to monitor the water heights of large rivers (Boergens et al., 2016; Frappart et al., 2006; Khan et al., 2013), lakes (Birkett, 1995; Buma et al., 2016; Cazenave et al., 1997; Cretaux et al., 2005; Crétaux et al., 2016), and wetlands (Dettmering et al., 2016; Papa et al., 2006; Schlaffer et al., 2016). The accuracy of water height observed from altimetry largely depends on the type of the sensor (TOPEX/Poseidon, ERS, Jason, Envisat, ICESat, etc.), size of the water bodies, and the configuration of the terrain (Baup et al., 2014; Crétaux et al., 2011; Ramillien et al., 2005). For a big lake, altimetry can provide accurate water height data, mostly less than 10 cm error (Crétaux et al., 2011). Error recorded in small lakes, in contrast, varies from tens of centimeters to over a meter (Birkett et al., 2011).

To compute water storage, many researchers intersected the digital elevation model (DEM) of the lake/reservoir with the water height time series, derived from the satellite altimetry (Cretaux et al., 2005; Medina et al., 2008). In order to obtain volumetric variations, many researchers also combined the time series of water surface-area from multiple satellites with in-situ observations (Baup et al., 2014; Medina et al., 2010; Smith and Pavelsky, 2009), or with the water height from satellite altimetry (Baup et al., 2014; Duan and Bastiaanssen, 2013; Gao et

al., 2012; Gao, 2015). In this work, the surface water body dynamics is estimated by combinations of altimetry, water extent maps generated from Landsat and bathymetry of the water body.

1.3.3 Satellite gravimetry for terrestrial water storage

Since March 2002, the GRACE mission routinely observes satellite-based estimates of changes in the total water storage (ΔTWS) within the Earth's system (Famiglietti and Rodell, 2013; Kusche et al., 2012; Wahr et al., 2004). To achieve ΔTWS from GRACE, the gravity variations need to be reduced by the redistribution of mass within the atmosphere, solid earth and ocean tides (Forootan and Kusche, 2012; Schmeer et al., 2012; R. Schmidt et al., 2008). The remaining signal is assumed to be the summation of water masses on the surface (in the form of snow, ice, and water) and subsurface (soil moisture (SM) and in the groundwater (GW)) hydrological compartments of the Earth (Güntner, 2008). To compartmentalize this ΔTWS signal, satellite altimetry (Becker et al., 2010; Swenson and Wahr, 2007) and hydrological models (Grippa et al., 2011; Rodell et al., 2006; Van Dijk et al., 2011) are being applied. The closure of the terrestrial water budget by GRACE provides a possibility to estimate hydrological fluxes like precipitation (Rieser et al., 2010; Swenson, 2009), evaporation (Ramillien et al., 2006), and runoff (Ferreira et al., 2013; Lorenz et al., 2014; Sproles et al., 2015).

Several works have evaluated the GRACE signal, to estimate hydrological stocks, particularly for the GW variations (Famiglietti et al., 2011; Jin and Feng, 2013; Joodaki et al., 2014; Richey et al., 2015a, 2015b; Xiao et al., 2015). Many studies have shown the decline in GW storage between 2003 and 2013. The GRACE data helped in identifying eight overstressed aquifers like those of the Middle East (Voss et al., 2013), and the Indus basin aquifer (Tiwari et al., 2009), and the Murzuk-Djado basin (northern Africa) (Richey et al., 2015a, 2015b). GRACE has contributed significantly to the assessment of mass changes in glaciers and ice sheets, and the rise in global mean sea level (MSL) (Gardner et al., 2013; Shepherd et al., 2012; Velicogna et al., 2014; Wouters et al., 2013). Llovel et al. (2010) found that at least part of inter-annual global MSL variability could be attributed to terrestrial water storage variations, as observed from GRACE. The connections between SM variations and GRACE signals have been explored by Abelen et al. (2015) and Abelen and Seitz (2013). As GRACE measures integrated mass changes, it can be used to monitor and characterize the potential for floods (Abelen et al., 2015; Reager et al., 2014; Reager and Famiglietti, 2009), droughts (Houborg et al., 2012; Thomas et al., 2014) and climate change scenarios (J. L. Awange et al., 2013; Blunden and Arndt, 2013; Famiglietti and Rodell, 2013). GRACE-based estimation of drought is evaluated at many

places, for example in California (Chen et al., 2015; Famiglietti et al., 2011; Scanlon et al., 2012), in the Colorado River basin (Castle et al., 2014; Scanlon et al., 2015) and across other locations in the United States (Yi and Wen, 2016). GRACE has also helped in exploring the interaction between the sum of mass fluxes (in/out) in sea level rise and its thermosteric components (i.e., rise due to ocean temperature change) (Ivins et al., 2013; Leuliette and Willis, 2011; Leuliette and Miller, 2009; Willis et al., 2010)

Mass changes observed by GRACE may assess the water budget of lake basins (J.L. Awange et al., 2013; Song et al., 2014; Swenson and Wahr, 2009), river basins (Awange et al., 2014; Castle et al., 2014; Long et al., 2015; Tangdamrongsub et al., 2015), countries (Ehsan Forootan et al., 2014; Wang et al., 2014) and continents (Ramillien et al., 2014). Few studies have compared lake volume variation with GRACE mass variation and hydrological model outputs (Buma et al., 2016; Mulder et al., 2015; Tourian et al., 2015) primarily on a larger scale (e.g., basin level). This work proposes a hybrid approach that combines remote sensing-based lake/reservoir volume estimates with model outputs at a smaller scale to analyze the hydrological behavior observed by GRACE in a lake/reservoir dominated region.

1.3.4 Hydrological modeling of lakes and reservoirs

Global hydrological models help analyzing possible hydrological scenarios and provide a valuable estimation of global water availability during different periods. In this study, we have applied two global hydrological models viz. Noah Global Land Data Assimilation System (GLDAS) and Water Gap hydrological model (WGHM).

To analyse water mass variations observed by GRACE, many studies have applied global hydrological models like Noah GLDAS (Long et al., 2013; Mulder et al., 2015; Proulx et al., 2013; Rodell et al., 2009; Tiwari et al., 2009) and WGHM (Döll et al., 2012, 2014; Landerer et al., 2010). GLDAS estimates land surface states (SM, snow water equivalent (SWE) and canopy interactions) and fluxes like evapotranspiration (ET), heat fluxes, surface and subsurface runoff (Ek et al., 2003; Rodell et al., 2004). WGHM simulates ET and runoff, along with storage in SM, SWE, SW, GW and canopy.

1.4 Outline of the thesis

This cumulative dissertation is based on four articles. Before the discussion on papers, Chapter 2 provides the background of the study area (i.e., the Aral Sea and Lake Mead), and Chapter 3 elaborates on the data description and its preprocessing. Thereafter, each chapter, from four to seven, gives an overview of results in the four peer-reviewed journal publications. Chapter 4

deals with the estimation of the geometrical and gravimetrical parameters of the Aral Sea, using satellite altimetry, Landsat, and GRACE. Chapter 5 compares the volumetric variations estimated by the geometrical and gravimetrical observations from space missions over the Aral Sea. Chapter 6 discusses three algorithms applied for the estimation of lake/reservoir water volume by multiple space missions and an application of a Kalman-based data assimilation method. Chapter 7 deals with the comparison of estimated total water storage variations in the lake/reservoir dominated region by net storage and net fluxes and with the GRACE observations. Chapter 8 deals with the discussion of different methods applied in the estimation of water heights, water masks and gravity fields and the results from the two study sites. Finally, Chapter 9 encapsulates the work with conclusions, a summary and a prospective outlook for the future.

2 Study area

This study is focused in arid/semi-arid regions, where water is the most crucial factor for survival. The water bodies of the two selected regions are mainly fed by glaciers and snowmelts. Therefore, maximum discharge is observed in spring and minimum in autumn. The historical evolution of the two water bodies (Figure 2.1) indicates that they were relatively stable. However, in the recent past they are receding quickly.

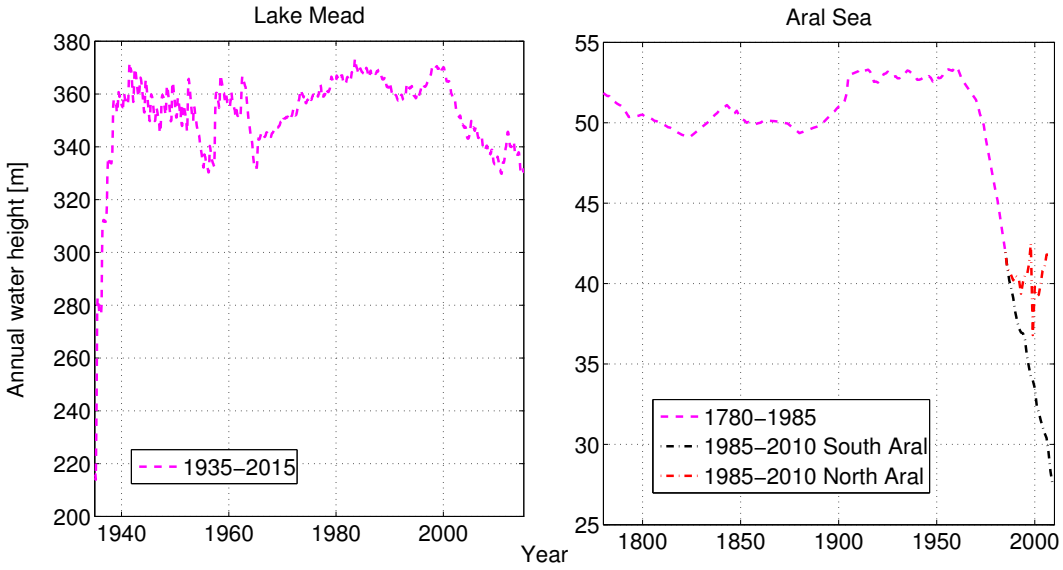

Figure 2.1. Historical evolution of the water height in Lake Mead (left) and the Aral Sea (right).

2.1 Lake Mead

Lake Mead, located in the USA on the Colorado River, has declined drastically in the last decade and a half, due largely to recurring drought since 2000 (Barnett and Pierce, 2008; Rosenberg et al., 2013). It is the largest and one of the most valuable reservoirs in the United States formed after the creation of the Hoover Dam over Colorado River in 1936. This reservoir has a high socioeconomic significance for the region. Since its existence, it has experienced two short droughts (for two years in 1955-57 and less than a year in 1964-65). However, the present prolonged decline in the water height is unprecedented in the reservoir's history (Figure 2.1, left). The reservoir is located in the foothills of the Rocky Mountains and has a very steep topography (Figure 3.4, left). Locally, it also serves recreational purposes, electric power generation, fishing, and most importantly, it is a vital source of water for Las Vegas. The reservoir has annual evaporation loss between 1 and 0.7 km^3, while annual precipitation in the region is less than 10 cm. Therefore, the lake entirely depends on river discharge for its

existence. Low winter snowfall in the Rocky Mountains, reduced precipitation in the basin and high temperatures are the main causes of the decline in water level of Lake Mead. Seager and Vecchi (2010) anticipate that the western United States would be dry in the 21st century and speculates that the transition to a more arid climate may be already under way. Studies suggest that the Colorado River basin will experience the largest reduction in discharge among all the major western U.S. river basins (Das et al., 2011; Gao et al., 2011).

In order to analyze the hydrological state of the ~450 km^2 reservoir and its surroundings we selected the Lake Mead region of approximately 90,000 km^2 between [34.5° to 37.5°N] and [116° to 113°W] (Figure 2.2, left). Lake Mead has dense and comprehensive ground observations to validate different proposed methods and estimations.

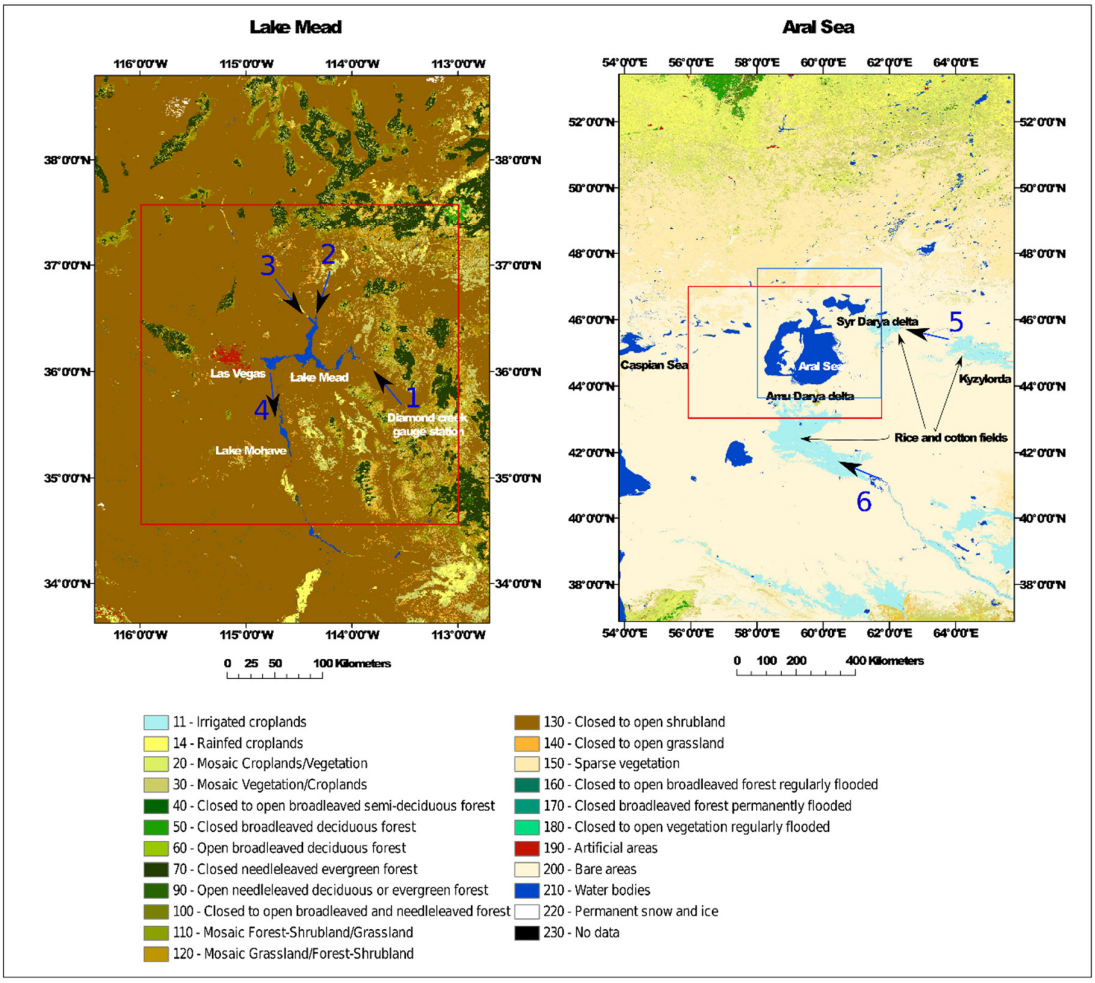

Figure 2.2. Study boxes for the Lake Mead region and the Aral Sea region. River discharge: 1 = Colorado River inflow, 2 = Virgin River, 3 = Muddy River, 4 = Colorado River outflow, 5 = Syr Darya and 6 = Amu Darya. The blue study box is used in Paper-1 and Paper-2, and the red study box in Paper-4. The figure is obtained from Paper-4.

2.2 Aral Sea

The Aral Sea is among the most ancient centers of civilization fed by two main rivers, the Amu Darya and the Syr Darya (Figure 2.2, right) and passing through five countries Kazakhstan, Uzbekistan, Turkmenistan, Tajikistan and Kyrgyzstan). The progressive shallowing of the fourth largest lake in the world started in 1961 (Figure 2.1, right) because of the diversion of river water through the Karakum canal across the Karakum desert (Zavialov, 2005). The second largest irrigation canal in the world is slowly extending the size of the Aral Karakum desert. More than 40% of the river water is lost to evaporation and infiltration from the canal (Forkutsa et al., 2009). Water escapes the route to form lakes and ponds along the way. Consequently, the

rise in GW level has brought soil salt to the surface, leading to widespread salinization and transformed the Amu Darya from a perennial to an intermittent river as it runs through the desert and Khorezm oasis to merge into the Aral Sea (Dodson et al., 2015). Until the 1960s, average annual combined runoff of the Amu Darya and the Syr Darya into the Aral Sea was 56 km^3 (Bortnik and Chistyaeva, 1990), which was reduced to less than 10 km^3 by 2002 (Zavialov, 2005). The climatic conditions of the Aral Sea region are characterized by cold and dry continental patterns, with a 5-11 °C mean annual temperature and 80-200 mm total annual precipitation (Issanova et al., 2015). The lake had annual evaporation of nearly 66 km^3 (Bortnik and Chistyaeva, 1990) but now it is speculated that the figure might have decreased in the last 2-3 decades due to its reduced size and higher salinity.

The western bank of the Sea is formed by the steep cliff of the Ustyurt Plateau, having more than 60 meter trench with a blunt bottom. The western basin has the deepest topography, and the eastern basin has the largest shallow flat-bottomed topography, in the Aral Sea. The lake experiences strong wind controlled surges and winds are most common on the western shore which range from 3 to 30 m/s. The surroundings of the Aral Sea have a predominantly aeolian landform, covered by fine sands and soils with sparse vegetation. The area is highly prone to dust and sand storms. The Aralkum (man-induced desert) and Kyzylkum deserts are the main sources for aeolian dust, sand and salt storms, occurring mainly in a southwestern and at southern direction (Issanova et al., 2015). The Aral Sea was one of the best studied and well sampled inland water bodies on the planet until the 1980s. However, following the collapse of the USSR, field research into its advanced stages of desiccation has reduced significantly (Zavialov, 2005).

To analyze the water mass variation of the ~20,000 km^2 (in 2002) lake by GRACE, we extended the study area to its surroundings. In Paper-1 and Paper-2, the area under study is (~140,000 km^2) between [43.5° to 47.5°N] and [58° to 62°E] (Figure 2.2, right: blue box), while in Paper-4, it is extended to ~210,000 km^2 between [43° to 47°N] and [56° to 62°E] (Figure 2.2, right: red box), in order to address leakage problems in the GRACE solution.

3 Data description and preprocessing

3.1 Landsat

The time series of lake/reservoir shorelines for the Aral Sea and Lake Mead were generated from L1T Landsat scenes (with less than 10% cloud cover and shadows) between January 2002 and December 2014. The Landsat sensors applied in the study are Thematic Mapper (TM), Enhanced Thematic Mapper (ETM+) and Operational Land Imager (OLI), (Table 1), which have been downloaded from www.earthexplorer.usgs.gov. The Landsat images have 16-day repeat cycles, covering the surface area of 185x185 km at a 30 m spatial resolution, except Panchromatic (15 m) and Thermal Infrared Band (60-120 m depending on the sensor).

Table 1. Landsat datasets

	Landsat 5	Landsat 7	Landsat 8
Scanning system	TM	ETM+	OLI
Number of spectral bands	7	8	11
Radiometric resolution	8 bit	8 bit	16 bit
Near infra-red (NIR) band	Band 4 (0.76 - 0.9 micro m)	Band 4 (0.76 - 0.9 micro m)	Band 5 (0.85 - 0.88 micro m)
Operation duration	March 1984 – January 2013	Since April 1999	Since April 2013

3.1.1 Band selection

Water absorbs most of the radiation it receives in the Near-Infrared (NIR) and Shortwave-Infrared (SWIR) electromagnetic regions. For Landsat TM/ETM+ the electromagntic spectrum range for NIR is 0.77 - 0.90 µm (band-4), SWIR-1 is 1.55 - 1.75 µm (band-5), and SWIR-2, also referred to as middle infrared (MIR) is 2.09 - 2.35 µm (band-7). For Landsat OLI the electromagntic spectrum range for NIR is 0.85-0.88 µm (band-5), SWIR-1 is 1.57 - 1.65 µm (band-6) and SWIR-2 is 2.11 - 2.29 µm (band-7). In these bands, water appears very dark and distinguishable from soil and vegetation. Figure 3.1 shows the spectral signature of the seven bands of Landsat-TM from the Aral Sea (captured in October 2006). However, in the Figure 3.1 Landsat-TM band-6 (thermal band) is replaced by its band-7, because the thermal band is not used in the study due to its coarse resolution (120 m). Figure 3.1 indicates that only the NIR band (band-4 of Landsat TM/ETM+) has the potential to differentiate between moist surfaces and shallow water. In other words, deep (West Aral Sea) and relatively shallow (East Aral Sea) water can be clustered in one class (as water) only by the NIR band. Very shallow water or

moist soil (in the given highly saline setting) and moist salt are distingushable as non-water class only in NIR band. In comparison, SWIR-1 and SWIR-2 (band-5 and band-7 of the Landsat-TM) cluster all moist surfaces, including deep and shallow water, in one group and only dry soil and receding marks can be distinguished as non-water (Figure 3.1). Therefore, in Paper-2 and Paper-3, only NIR band is selected to generate land-water mask, while in Paper-1 three water absorption bands, i.e., NIR, SWIR-1, and SWIR-2, are used. Paper-1 multi-spectral approach could have overestimated the area of the East Aral Sea, as seen in Figure 8.2 and discussed in Section 8.1.1. Roach et al. (2012) also emphasized that for separating water from non-water pixels, only shortwave infrared (Landsat-TM band-5) is better than its combination with other spectral bands. However, for our study area, band-4 of Landsat TM/ETM+ is better than band-5, as shown in Figure 3.1.

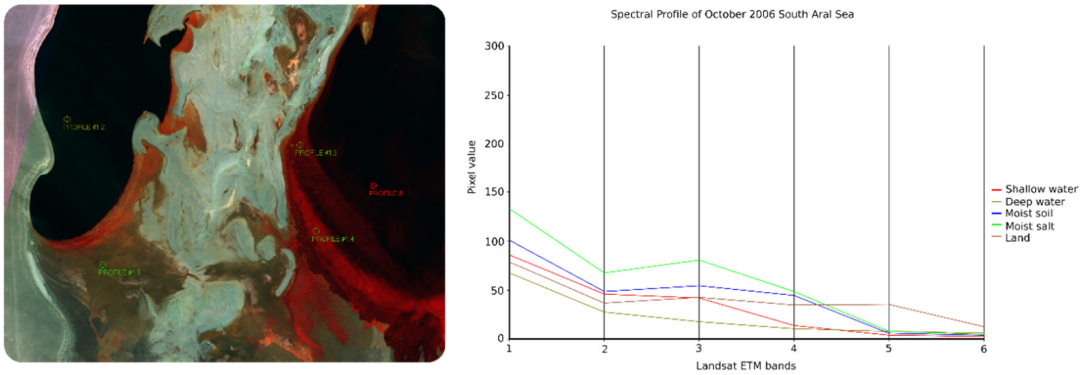

Figure 3.1. Spectral profile of Landsat-ETM shows that only band 4 (NIR) can separate shallow and deep water from other moist surfaces in the Aral Sea lake

3.1.2 Corrections

When more than one scene from different sensors are required to cover a study area (e.g., in the Aral Sea), a radiometric correction of each image is necessary. For each spectral band, the intensity of electromagnetic radiation is recorded in the form of a digital number (DN). The DN values are image specific; i.e., they are dependent on the sensor (TM/ETM+/OLI), specific weather conditions, viewing geometry of the satellite at the moment the image was captured and the location of the sun. The range of DN values depends on its radiometric resolution. For example, Landsat TM measures it on a 0-255 scale, while OLI has radiations on a 0 - 55,000 scale. All images, which are mosaicked, should have similar radiometry. When an OLI image is mosaicked with another Landsat sensor, they need to be corrected to obtain the same radiometric resolution. The images are first connected, and then their gain and bias are calculated, using the header information (a lower limit and an upper limit of the spectral

radiance range). For non-OLI mosaics, only the overlapping areas are color-matched by histogram matching to obtain a seamless mosaic.

3.1.3 Classification

Supervised classification is labor intensive because every time point needs an independent training signature for each cluster. This study required monthly continuous land-water mask. Therefore, unlike Paper-1 and Paper-2, which used supervised classification because a limited number of images were analyzed, Paper-3 applied ISODATA (Iterative Self-Organizing Data Analysis Technique) unsupervised classification (Beigt et al., 2011; Gan et al., 2012), in order to explore possible long-term correspondence with other datasets (altimetry and GRACE). Other unsupervised classification methods, such as two-band water indices (McFEETERS, 1996; Xu, 2006) or single-band thresholding (Jain et al., 2005; Klein et al., 2014), are not suitable for this study. This is because the threshold value will vary at every time point with the changing salinity of the lake. The accuracy of these classification methods largely depends on the determination of threshold to discriminate the reflectance of water and non-water pixel, which is the most critical part of this classification method (Klein et al., 2014). However, in the present study, multiple images of different times and salinity have been analyzed. Therefore, a thematic ISODATA unsupervised classification of a single band (NIR) can be stated as suitable to get continuous time series of water mask. The ISODATA unsupervised classifier assumes the existence of different clusters of pixels with similar spectral characteristics. The interpreter gives the number of cluster centers, which are randomly initiated. The pixels are assigned to the cluster with the shortest distance. The class centers are recalculated based on standard deviation and distance between the clusters in every iteration and it can split classes with too much variance and merge classes that are similar, in each iteration. It forms a matrix of euclidian distance between cluster centers. The process continues until either the percentage of pixels that change categories are below the threshold indicated by the interpreter, or a maximum number of iterations given by the interpreter has been performed. The classification results are ideally validated on the ground. However, field visits to the study area are outside the scope of this study. Nevertheless, many studies have applied ISODATA classification on Landsat images to determine water class. Beigt et al. (2011) identified different turbidity levels in a water channel, Ucuncuoglu et al. (2006) diagnosed the turbidity pattern of a bay, while Jung et al., (2011) delineated flooded areas. Few studies also validated an ISODATA classified land-cover maps in the field. To illustrate, Ahmad and Sufahani, (2012) obtained 93% agreement with the reference map and Odindi et al., (2012) derived 82-86% accuracy in urban classification of

land-use and land-cover. Though, there are many better land-use classification methods like neural network, fuzzy classification, etc., in this study ISODATA classification has been selected because of its simplicity and robustness.

3.1.4 Uncertainties

Water with different depths and turbidity has a different spectral signature. The reflectance increases with sediment content and their diameters. Besides, shallow waters have stronger contribution from the bottom layer, which enhances the reflectance of the water body. The spectral signature of soil depends on superficial biochemical constituents, moisture and optical-geometrical scattering of the ground surface (Chuvieco and Huete, 2010). Therefore, wet soil/salt deposited along the shores of saline receding lakes produces a similar reflectance to that of a very shallow saline water body. Furthermore, water roughness promotes greater reflectance and soil roughness decreases reflectance. All these factors are very pronounced in the East Aral Sea, making it difficult to separate the water body from its moist shore. Additionally, the applied lake bathymetry must have lost depth of unknown measure in the past half a century, because of depositions from river and wind erosion. In order to avoid overestimation of lake volume moist soil and very shallow water signatures in Figure 3.1 are not considered as water. All other contrasting spectral properties are also fused together into non-water class after the classification.

Water classification accuracy problems are further pronounced in areas where the background land also includes low albedo features, such as shadows from clouds and mountains. Ideally, spectral bands should be narrow enough to identify specific absorption features that may be blurred otherwise. Sometimes two or more features share the same spectral band. For example, deep water and mountain shadow (like in Lake Mead) have a similar reflectance. A relief map from the DEM of the region is then applied to separate the two classes. Images, which had clouds or their shadows on the shorelines, are rejected. Further, post classification manipulation to fill the SLC-off data gap in the ETM+ sensor scenes introduces additional uncertainty in the extracted water mask (discussed in Section 8.1.1). Extra shorelines generated due to misclassifications or tiny water bodies around the lakes/reservoirs are removed by defining the minimum size of polygons to be extracted from the classified images. The classification accuracy of the OLI Landsat sensor is better than previous sensors, even though it has a similar spatial resolution, due to its higher spectral and radiometric (number of bits used for storing the image in binary format) resolutions. Figure 3.2 shows the Landsat-derived land-water mask and the evolution of the lake during the study period. The Landsat image from November 2014

(yellow area) shows the complete disappearance of the East sub-basin of the Aral Sea, while Lake Mead observed less loss in the area.

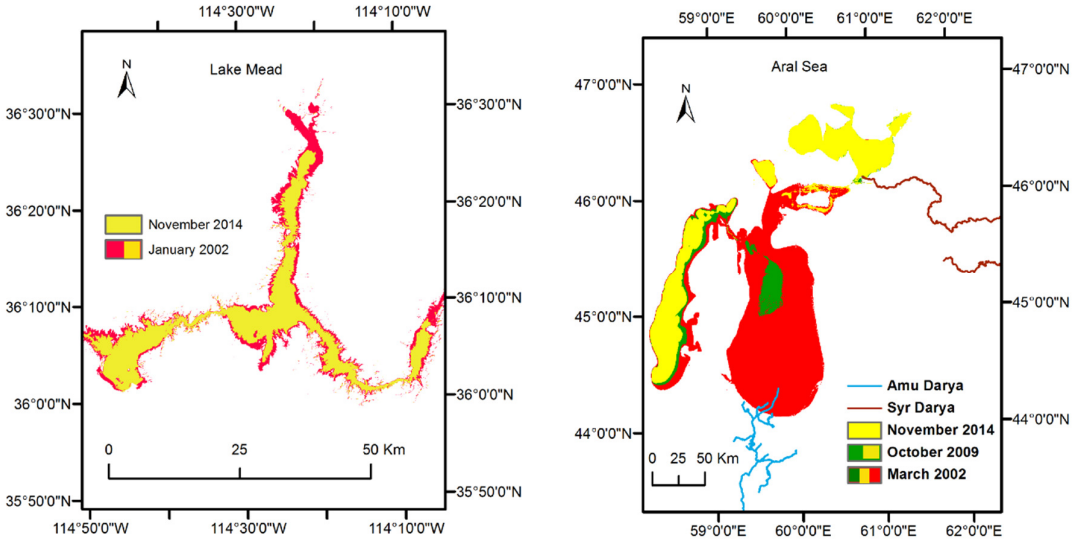

Figure 3.2. Surface area variation observed by Landsat: Lake Mead (left) and the Aral Sea (right), obtained from Paper-3.

3.2 Altimetry

Satellite altimetry provides nadir pointing height observations by recording the travel time, the magnitude and the shape of each sent electromagnetic waveform after reflection from the water surface. The altimetry range ('h' in Figure 3.3) is obtained by a waveform re-tracking of the returned power records from the nadir. A waveform consists of three parts: first a thermal noise, which is a constant power before the first return of a signal to the altimeter; second, a leading edge, which is the main part of the signal, containing maximum information about the surface with an ascending power slope; and finally, a trailing edge, which shows decaying power (Fu and Cazenave, 2000). The waveform re-tracking is performed to identify a mid-power point in the leading edge, which is required for the calculation of the travel time between the satellite altimeter and the water surface. Measurements by radar echoes perform better over spatially homogeneous big regions like the open ocean, because of the better fitting of the shape of the echo waveform to a model functions. However, over inland water bodies, the waveforms often show a noisy leading and trailing edge, which leads to an erroneous range. The main cause of the noise in the inland waveform is the complexity of the surrounding terrain of the water body, water surface roughness, and size and location of the footprint (off-nadir effect). Further, the number of radar echoes collected along the track is based on the extent of water, which also determines the ability to reduce the error in the range estimate. Dedicated waveform re-tracker

algorithms designed for smaller and narrow lakes/reservoirs may improve range estimates (Ričko et al., 2012).

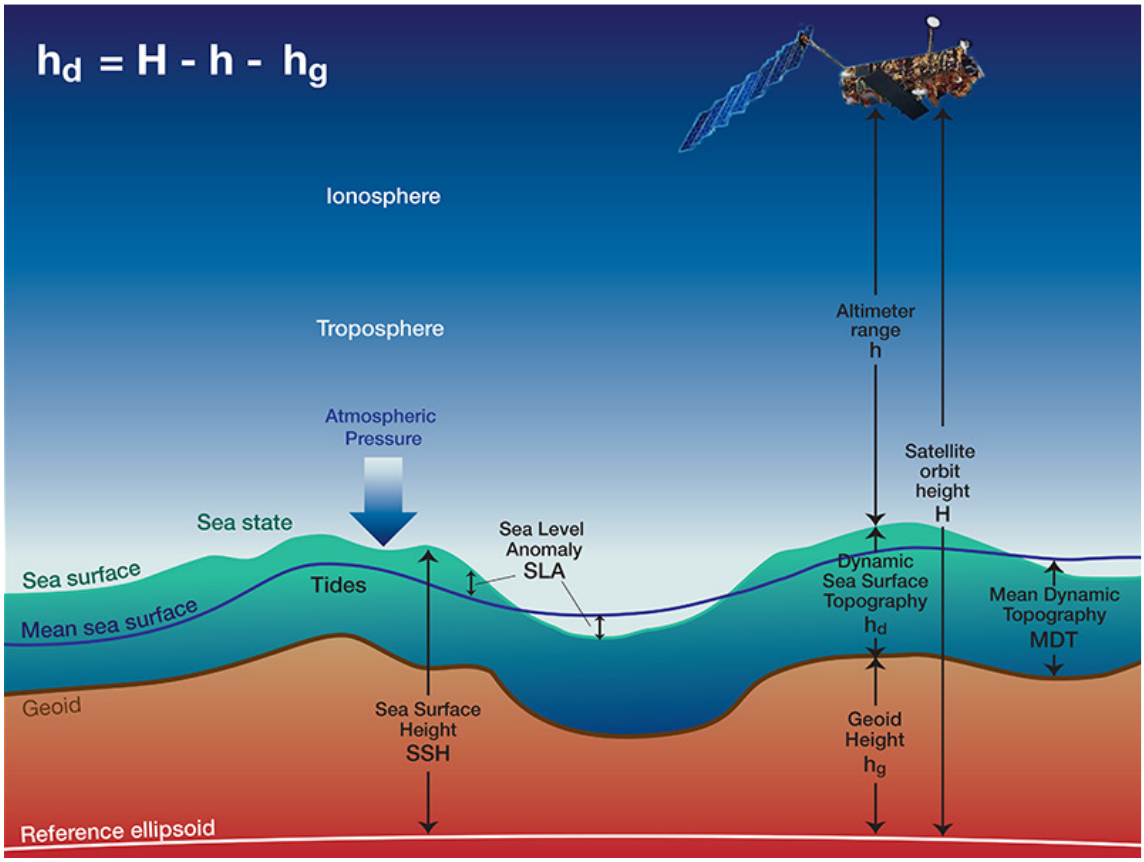

Figure 3.3. Dynamic Sea Surface Height (h_d) estimation from satellite altimetry, on a local geoid, obtained from (ESA: LearnEO, 2016).

Figure 3.3 shows that the dynamic water surface height (h_d) above a local geoid (h_g) can be obtained by reducing the altimetry Range (h) from the satellite orbit height (H) (Equation 1). DORIS, GPS, and Laser tracking systems accurately track the satellite orbit (H). The range measurements (h) are already corrected for all instrumental errors e.g., errors in internal clock due to drift of on-board oscillators, the center of gravity variance due to fuel conception, Doppler Shift (due to the relative velocity between the satellite and the sea surface), etc.).

$$h_d = H - h - h_g - \Delta R \quad (1)$$

The precision of dynamic water surface height (h_d) mainly depends on the improvement in range estimates through waveform retracking and on a broad range of atmospheric and geophysical corrections (ΔR) (Equation 2). The atmosphere slows down the radar pulse, bending its trajectory and causing a path delay of the altimetry signal. This atmospheric refraction effect can be divided into three parts: the delay due to the free electrons in the ionosphere based on the frequency of radar pulse, the delay due to the water vapor in the

troposphere and the delay due to other dry gases (mainly nitrogen and oxygen) of the troposphere (Fernandes et al., 2014). Their respective corrections i.e. ionospheric correction (Δh_{iono}), wet tropospheric correction (Δh_{wet}) and the dry tropospheric correction (Δh_{dry}) vary with the satellites and are widely dependent on the model outputs. The water height variations due to geophysical phenomenon are treated by solid Earth tide correction (Δh_{etide}) and pole tide correction (Δh_{ptide}), but these effects are negligible on small inland water bodies. In order to combine multiple missions, an additional range bias correction (Δh_{rad}) as a constant offset is applied for each mission, to calculate water height with respect to a common reference orbit of Topex/Posidon (Bosch et al., 2014). All the applied correction models have their inherent errors, which introduce additional uncertainties in the range estimation. Further, the estimated water height is projected on a geoid (h_g), which has its own uncertainty. The study shows that the Eigen-6C3stat geoid is 2-3 cm lower than EGM 2008 predominantly in the East Aral Sea (Figure 8.4). Therefore, the final estimated dynamic water surface height (h_d) cannot be computed with some estimated error bar, because of the unknown uncertainties from different sources.

$$\Delta R = \Delta h_{wet} + \Delta h_{dry} + \Delta h_{iono} + \Delta h_{etide} + \Delta h_{ptide} + \Delta h_{rad} \quad (2)$$

3.3 Bathymetry

In this study, the estimated water height, from the Landsat and altimetry intersects the bathymetry of the water bodies to calculate two absolute water volumes. The Aral Sea bathymetry is obtained by personal contact from Dr. P. Zavialov (the Physical Oceanography Division, Russian Academy of Science) and Prof. Renard (the Stochastic Hydrogeology Group of the University of Neuchâtel). The Aral Sea bathymetry map was originally generated in the 1960s with the poor spatial resolution (~ 900 meters). The bathymetry has changed in the past half a century with the changing drainage pattern and depositions from the increasing deserts that surround it. The maximum modification is noticed in the East part of the Aral Sea due to large-scale shrinking (Figure 3.2, right). Consequently, an unknown error is expected in the volumetric computation for the Aral Sea. In contrast, Lake Mead has a very sharp topography (Figure 3.4, left). The DEM of the region (including bathymetry) is obtained from the United States Bureau of Reclamation (USBR) and regularly maintained by that Agency. The obtained data are transformed into UTM projection and interpolated to a higher resolution by universal kriging.

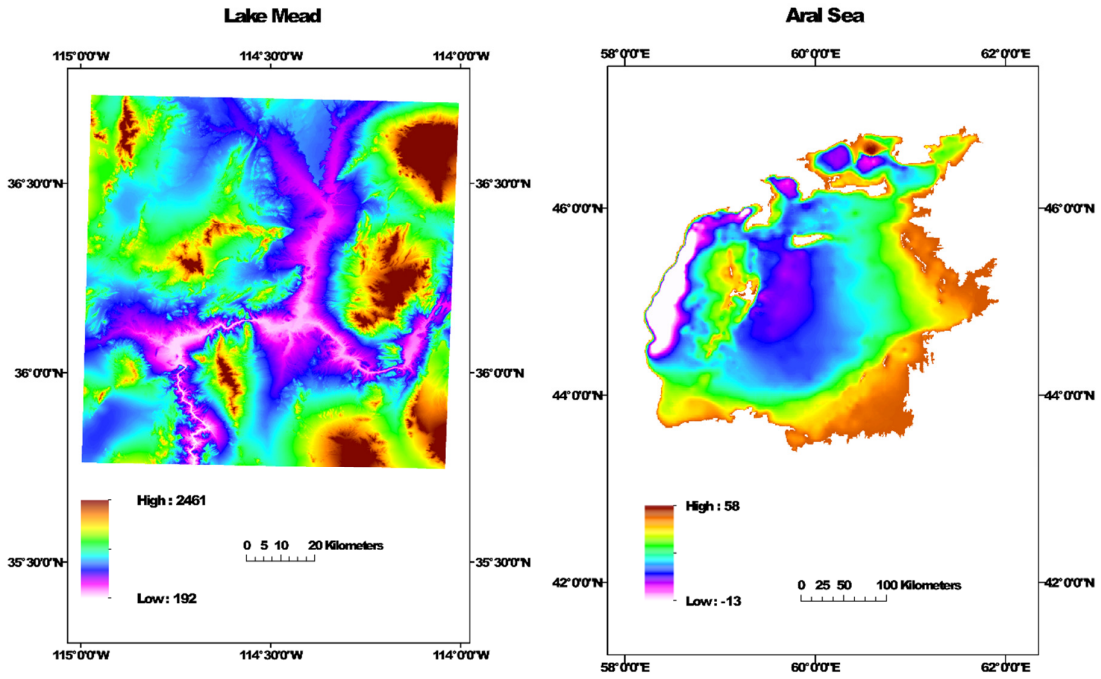

Figure 3.4. DEM of Lake Mead (left) and the Aral Sea (right)

3.4 GRACE

3.4.1 Introduction

The data from the GRACE mission has been widely used to detect mass variations within the Earth's system since its launch in March 2002. It is a constellation of two identical satellites, flying in tandem in a polar orbit at an altitude of approx. 500 km (currently decayed to ~390 km). The twin satellites are separated by ~220 km, which is constantly perturbed by the continuous mass redistribution in the earth system (i.e. mass variations in the atmosphere, Ocean, the Earth's surface, and its interior) and non-gravitational forces like air-drag and solar radiation pressure. A microwave-ranging instrument (K-band and Ka-band) at an accuracy of micrometer precisely tracks the distance between the two satellites. In addition, the satellites are also tracked by a Global Positioning System (GPS) for precise orbit determination. A pair of star cameras provides the necessary orientation of the satellites in space, and an accelerometer measures the non-gravitational forces acting on them. The acquired measurements (Level-0 data) are processed and distributed by Jet Propulsion Laboratory (JPL) Physical Oceanography Distributed Active Archive Center (PO.DAAC), the University of Texas Center for Space Research (CSR) and GeoForschungsZentrum Potsdam (GFZ). The sensor calibrated Level-1 data convert the binary encoded raw measurements to engineering

units and includes quality control flags. Level-2 SH solutions include estimates coefficients for the Earth's gravitational potential, conventionally corrected by Atmospheric and Ocean De-aliasing (AOD) models for the high-frequency variations mainly caused by mass variations in the ocean and the atmosphere. Level-2 mascon solutions include regional gravity field coefficients. Level-3 data are value-added products.

The GRACE measurements are obtained in downward continuation. The measured gravitational potential at satellite's altitudinal height, determines the values of mass change at a lower surface. This technique leads to an additional noise, to the integrated geophysical signal. Further, high-frequency gravity variations on the surface of the Earth get dampened at the satellite's altitudinal height. From the GRACE-derived gravity field changes, monthly equivalent water heights (EWHs) grids are generated. EWHs mean an idealized representation of the thickness of a water surface which changes with the variations of water storage observed by the gravity signal. The accuracy of the EWH estimates from GRACE is assumed to be 1–2 cm, depending on the region and size of the study area (Swenson et al., 2003). Major challenges in deriving EWHs from the gravity variations observed by GRACE are the following:

- The orbit configuration and the constellation of GRACE cause oversampling along track directions and an inadequate space-time sampling of short-term gravity field variations between the neighboring arcs, which add an aliasing effect. The gravity field changes continuously due to tides, atmospheric variations, ocean currents, etc. These short term gravity variations within a month (for a monthly solution) are removed by applying different models and every model has its uncertainties and limitations. Consequently, very high measurement accuracy along the track and un-modeled short periodic changes (due to limitations of the applied models) in an east-west direction create north-south (N-S) stripes in the GRACE data. To reduce correlated errors and high-frequency noise (N-S stripes), decorrelation filters like low pass filtering are conventionally applied which in turn lead to leakage problems (Klees et al., 2008; Kusche, 2007; Wouters and Schrama, 2007). The widely used approach to reconstruct the full signal from the damped signal is by rescaling it with a forward modeling (i.e. applying the same filter) on a Land surface model (LSM).
- A further challenge in retrieving water mass change from GRACE is compartmentalization of the integrated signal. Models or statistical approach like Principal Component Analysis (PCA), Independent Component Analysis (ICA) etc conventionally perform signal separation. Therefore, in the interpretation of the GRACE-derived water mass variations, the limitations of leakage/ de-aliasing and

signal separation as mentioned above have to be considered.

3.4.2 GRACE spherical harmonics (SH) solution

A most common solution for the global gravity field signal is SH basis functions. The SH representation of any scalar function (e.g., gravity field) at a point on the sphere $f(\lambda, \theta)$ at λ longitude and θ co-latitude can be given as Equation 3.

$$f(\lambda, \theta) = \sum_{n=0}^{\infty} \sum_{m=-n}^{n} a_{nm} Y_{nm}(\lambda, \theta) \tag{3}$$

Where,

n and m are degree and order respectively. The spatial resolution of the signal increases with the increasing degree.

a_{nm} is a scaling coefficient in SH at degree n and order m.

$Y_{nm}(\lambda, \theta)$ is a basis function, which can be expressed as Equation 4.

$$Y_{n,m}(\lambda, \theta) = cos(m\lambda) P_{nm}(cos\theta) \tag{4}$$
$$Y_{n,-m}(\lambda, \theta) = sin(m\lambda) P_{nm}(cos\theta)$$

Where,

$P_{nm}(cos\theta)$ depends on latitude and is derived from Legendre function along a meridian. $cos(m\lambda)$ and $sin(m\lambda)$ depends on longitude and is derived from Fourier series along a parallel of latitude.

Static gravity fields in GRACE are expressed in $C_{nm}$and S_{nm} for respectively cos and sin functions. Potential of the gravity field in the outer space at altitude r can be expressed as Equation 5 (Heiskanen and Moritz, 1967).

$$T(r, \lambda, \theta) = \frac{GM}{R} \sum_{n=2}^{n} \left(\frac{R}{r}\right)^{n+1} \sum_{m=0}^{n} (C_{nm} cosm\lambda + S_{nm} sinm\lambda) P_{nm}(sin\theta) \tag{5}$$

Where,

G, M, and R = respectively gravitational constant, Earth's mass and mean radius

$\left(\frac{R}{r}\right)^{n+1}$ = it is an upward continuation term of the gravity field and has an attenuation effect with respect to the altitude r.

The Level-2 SH coefficients used in Paper-1 is release RL04 from GFZ and CSR, and Figure 8.5 uses the latest release RL05 from GFZ. The obtained gravity field approximations contain meridional (N-S) stripe due to correlated errors and aliasing. Correlated errors are treated by a least square polynomial and the isotropic Gaussian filter (Swenson and Wahr, 2006; Wahr et al., 1998) smooths noisy short wavelength components. In spectral domain, the filter (e.g.,

$b(\psi)$) gives less weight to high frequencies, assuming that noise corrupts them. The spherical distance ψ between the data point $(\acute{\lambda}, \acute{\theta})$ and the calculation point (λ, θ) and width (e.g., half width) and the shape (e.g., Gaussian filter) of the operator, controls the smoothing in the spectral domain (Devaraju, 2015). Wahr et al. (1998) modified the Jekeli (1981) Gaussian filter for the GRACE signal smoothing (Equation 6). In Gaussian filter $b(\psi)$ the parameter a in Equation 6 is defined by a smoothing radius ψ_0 (e.g., 300 km) which is the distance at which the weight of the function reduces to a desired fraction (1/n) of the weight at the calculation point. This was defined as one-half by Wahr et al. (1998).

$$b(\psi) = b(\lambda, \theta, \acute{\lambda}, \acute{\theta}) = \frac{a}{\sinh a} e^{a\, cos\psi}, a = \frac{In(n)}{1 - cos\psi_0}, n \in \mathbb{R}_1 \tag{6}$$

The Equation 7 gives the filtered data

$$\bar{T}(r, \lambda, \theta) = \frac{1}{4\pi} \int_0^{2\pi} \int_0^{\pi} T(r, \acute{\lambda}, \acute{\theta}) b(\psi) sin\theta d\theta d\lambda \tag{7}$$

One of the objectives of this study is to relate geometric changes of lakes/reservoirs with the gravimetric variations observed by GRACE. However, we have to select a bigger study area than the lake/reservoir size, because of the limitations in the spatial resolution of GRACE. Further, in the SH post processing for meridional stripes, Gaussian filtering smears out/in the signals from the surroundings, which further decreases the spatial resolution of GRACE. The consequent leakage from the surroundings into the study area is treated by reducing the GRACE signal by results from forward modeling i.e. applying the same filtering on the TWS from a LSM like WGHM. In order to apply the same filtering procedures, the WGHM TWS grids are first converted to SH coefficients, to evaluate a similar attenuation caused by the least square and Gaussian filtering in the spectral domain and the consequence of SH truncation at degree and order 60 (equivalent to a surface spatial resolution of ~300 km). The resulting leakage signal is then reduced from the filtered GRACE signal.

Finally, to reconstruct the water height in the study region, the GRACE signal amplitude is rescaled by applying the same filter procedures on a simulated water height grid of 1 cm within the study region. The simulated grid is also treated like LSM. It is also first developed to SH coefficients and then reduced by least square and Gaussian filter (Swenson and Wahr, 2007) in order to obtain the rescaling coefficient. Lastly, the time series of TWS anomalies is calculated by intersecting the area under study with the mean EWH and reducing it by the entire time-mean baseline.

3.4.3 GRACE mascon solution

In Paper-3, instead of global SH solutions of the GRACE signal, a regional gravity field basis function in the form of Mass Concentration blocks (mascon) is examined. The monthly mascon solution from JPL RL05.1M uses 3° surface spherical cap to directly estimate mass change from the inter-satellite range-rate measurements from Level-1 data (Watkins et al., 2015). It takes a priori conditioning from geophysical models to prevent striping in the GRACE solutions and consequently it has fewer leakage errors (Watkins et al., 2015). The mascon coefficients are then converted to SH coefficients to replace degree 1 and order 'm' (C_{1m}) coefficients (which represent the Earth geocentric motion) by combining numerical ocean models with GRACE (Swenson et al., 2008), and degree 2 and order 0 (C_{20}) coefficients (which represent the Earth's dynamic oblateness) by the solutions from Satellite Laser Ranging (SLR) (Cheng et al., 2011). The SH coefficients are then transformed to gridded EWH on the 0.5° grid, which can be downloaded from the Tellus website (http://grace.jpl.nasa.gov) with 2004-2009 time-mean baseline. However, in this study, the modified SH coefficients are transformed to 0.1° gravity field grid and reduced by its mean over the entire time span (01.2003-12.2014). The rescaling factor for leakage in the mascon solution is derived by the equal area 3°x3° spatial averaging of Noah GLDAS time series and performing a least square fit between a filtered and unfiltered time series (Landerer and Swenson, 2012). These gain coefficients are provided by GRACE Tellus in 0.5° grid as a multiplicative factor (Wiese, 2015).

3.5 Global hydrological models

The TWS observed by GRACE is an integral sum of the different hydrological processes working within a region (Figure 3.5). In order to close the water budget of a region, outputs from two global hydrological models are used to estimate hydrological fluxes and storages in the two lake/reservoir dominated regions in Paper-4.

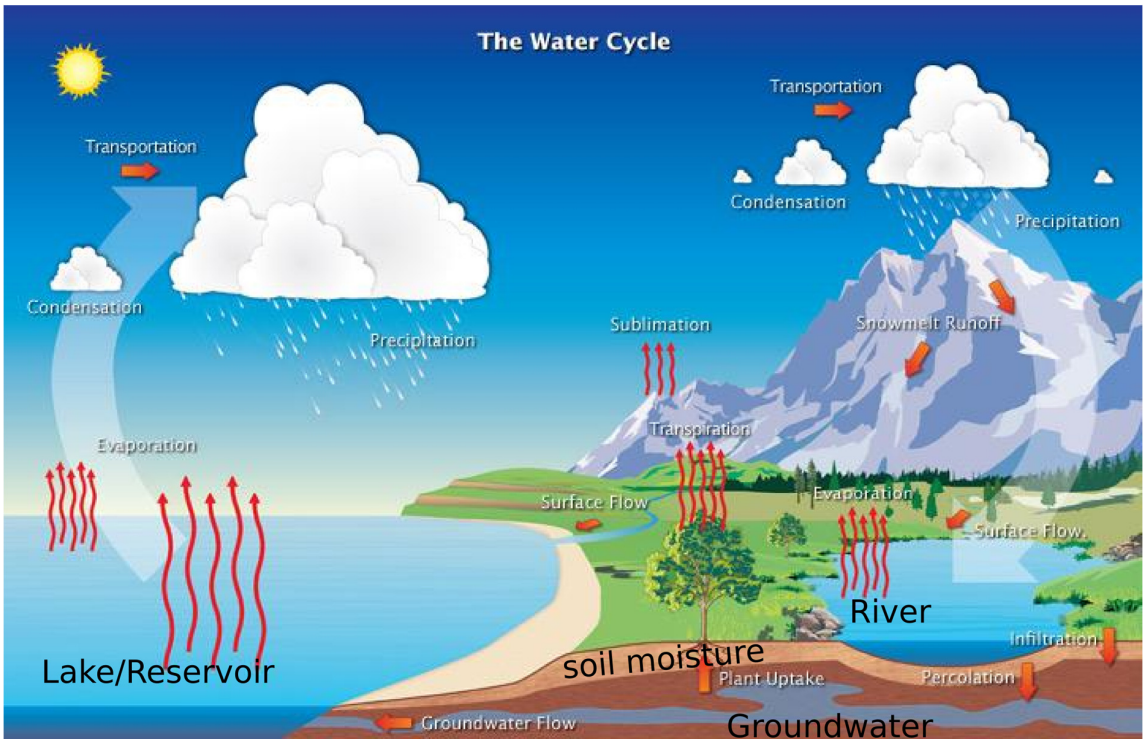

Figure 3.5. Hydrological processes around lakes/reservoirs (NASA, 2016.).

3.5.1 WGHM

The Water GAP (Global Analysis and Prognosis) Hydrological Model (WGHM) calculates daily water storage and water flow at 0.5°x0.5° spatial resolution for all large river basins over the continents, except glaciers (Döll et al., 2003). In the model, the location of lakes/reservoirs and wetlands are obtained by Global Lakes and Wetlands Database (GLWD) (Lehner and Döll, 2004) along with soil map of the world by FAO, precipitation data from the Global Precipitation Climatology Center (GPCC), and global drainage topography from DDM30 (Döll et al., 2003). For another climate forcing data, the European Centre for Medium-Range Weather Forecasts (ECMWF) operational forecast or analysis data is used (e.g. for, temperature, cloudiness, and the number of rainy days per month). The TWS simulated by WGHM is provided into following compartments: SW (which includes lakes, rivers, and reservoirs), SM, GW, SWE and canopy storage. WGHM considers soil as a single layer and its thickness varies with the root-zone of the land cover. It also computes fluxes working in a region i.e., ET, GW recharge, total runoff, base flow and river discharge. In the past few decades, most of the large rivers have been highly altered (Döll et al. 2009; Aus der Beek et al. 2011) and it is imperative for hydrological models to incorporate changing water withdrawal patterns. Therefore, WGHM version 2.2 includes water use models for irrigation, livestock, household, thermal power and manufacturing to

combine the water availability based on structural and technological changes at the global scale (Müller Schmied et al., 2014). It also includes climate forcing and land cover change with model structure refinement. WGHM is controlled by 23 driving parameters and calibrated against mean annual river discharge of total 1,319 gauging stations. Eicker et al. (2014) proposed to calibrate another 22 parameters of WGHM from GRACE data.

3.5.2 GLDAS

The Noah GLDAS covers Earth from 60° S to 90° N. Its 0.25-degree version-1 monthly grid is downloaded from http://mirador.gsfc.nasa.gov (Mirador - Goddard Earth Sciences (GES) Data and Information Center (DISC), 2016). The static parameter fields integrated into GLDAS are the following: vegetation type and its properties derived from AVHRR and MODIS, soil properties obtained from the United States Department of Agriculture (USDA), and elevation data obtained from Global 30 arc-Second Elevation (GTOPO30) (Rodell et al., 2004; Rodell, n.d.). Meteorological forcing datasets included in GLDAS are downscaled Air Force Weather Agency solar radiation, NOAA Climate Prediction Center (CPC) Merged Analysis of Precipitation (CMAP) and NOAA Global Data Assimilation System (GDAS) air temperature, surface pressure, wind speed and land specific humidity (Rodell, n.d.). GLDAS accounts for such land surface states as canopy storage, SWE, and SM stock but it does not simulate GW and SW stocks (Rodell et al., 2004). Therefore, the TWS from GRACE cannot be compared with the sum of stocks from GLDAS due to incomplete storage estimation (missing GW and SW stocks). Nevertheless, it has been extensively used to estimate GW by reducing other stocks from GRACE (Mulder et al., 2015; Rodell et al., 2009; Tiwari et al., 2009). GLDAS also estimates ET, snowmelt, surface temperature and ground heat fluxes, which are provided at an hourly rate per square meter, which needs to be multiplied by the number of hours in the corresponding month. SM estimates by Noah GLDAS are provided in four layers (at 0 – 10cm, 10 – 40cm, 40 – 100 cm and 100 – 200 cm depth) in kg/m^2. GLDAS integrates MODIS snow cover for SWE estimations and provides it in kg/m^2.

3.6 Statistical model evaluations methods

3.6.1 Root mean square error (RMSE)

RMSE is also known as the root mean square deviation, which measures the difference between observed values and model predicted values. Their individual differences are known as residuals and RMSE is defined as the square root of the mean squared residuals (Equation 8).

$$RMSE = \sqrt{\frac{\sum_{i=1}^{n}\left(X_{obs,i} - X_{model,i}\right)^2}{n}} \quad (8)$$

Where X_{obs} are observed values and X_{model} are modelled values at time *i* from *n* observations. It is the most frequently used to distinguish model performance and have the same unit as the input data.

3.6.2 Normalized root mean square error (NRMSE)

NRMSE is a non-dimensional form of RMSE. NRMSE can be expressed in % error, as a normalized RMSE by the mean of the observed data (Equation 9) and is sometimes referred to as the scatter index (SI) (Zambresky, 1989). In the study, NRMSE is not applied for the error estimation of derivative and differential plots because when observations have both negative and positive values then normalization by mean gives erroneous value.

$$NRMSE = \frac{RMSE}{\overline{X_{obs}}} \quad (9)$$

3.6.3 Pearson product-moment correlation coefficient (*r*)

Correlation coefficient indicates the strength and direction of a linear relationship between two variables (Goodwin and Leech, 2006; Rodgers and Nicewander, 1988). The Pearson product-moment correlation coefficient is also known as Pearson correlation coefficient, which is obtained by dividing the covariance of the two variables by the product of their standard deviations (Equation 10).

$$r = \frac{\sum_{i=1}^{n}(x_i - \bar{x}).(y_i - \bar{y})}{\sqrt{(\sum_{i=1}^{n}(x_i - \bar{x})^2 . \sum_{i=1}^{n}(y_i - \bar{y})^2)}} \quad (10)$$

The correlation $r = +1$ in the case of a perfect increasing linear relationship, and vice versa. The values between $+1$ and -1 indicates the degree of linear relationship between the two variables and coefficients close to 0 shows no relationship between the two variables.

3.6.4 Coefficient of determination (r^2)

The square of the Pearson correlation coefficient (r^2) is known as the coefficient of determination. It describes how much of the variance between the two variables is described by the linear fit. In other words, it estimates the fraction of the variance (fluctuation) in *y* that is explained/ predictable by *x* in a simple linear regression. The r^2 value is between $+1$ and 0 and indicates the strength of the linear association between *x* and *y*.

The study preferred to use r^2 when the model represents some underlying construct, for

example, to compare the estimated volumes from different methods in Paper-3. When the relative strength of association is estimated among the variables not equally representative of a single underlying construct then r is preferred (Paper-4). In this thesis (except for the Paper-3), in order to keep homogeneous expression for a statistical relationship between two variables, only r is used. However, the difference between r and r^2 is superficial and there is no inherent reason to prefer one over the other (Johnson, 2011).

4 Paper-1

Inter-annual Water Storage Changes in the Aral Sea from Multi-mission Satellite Altimetry, Remote Sensing, and GRACE Satellite Gravimetry

Singh, A.; Seitz, F.; Schwatke, C.; Remote Sensing of Environment, Vol. 123, pp 187-195, Elsevier, ISSN 0034-4257, 2012. DOI: 10.1016/j.rse.2012.01.001.

4.1 Highlights

- This study for the first time analyzed the variations in remote sensing based geometrical and gravimetrical changes in a relatively small area focusing on a lake. Most of the previous studies observed big lakes along with their basins while comparing altimetry and GRACE.
- Until this study, GRACE observed water storage in and around lakes/reservoirs had been often analyzed by a global hydrological model. To elaborate, Huang and Halpenny (2007) inspected the Great Lakes basin by using GLDAS and Wang et al. (2011) analyzed the Three Gorges Reservoir (TGR) of China by applying WGHM.
- For the first time, Landsat 30 m spatial resolution data is combined with multi-mission altimetry data to obtain a comprehensive geometric picture of the Aral Sea storage variations. Previous studies used coarse resolution sensors, for example, Kravtsova and Tarasenko (2010) applied 250 m spatial resolution MODIS data for the monitoring of the Aral Sea.
- The study gives an overview of the possibility of applying geometrical and gravimetrical approaches in the Aral Sea region. However, the applied methods are improved in follow-up publications.

4.2 Extended abstract

In this study, the Aral Sea mass variations are computed for the period 2002-2011 by multi-mission altimetry, Landsat, and GRACE gravity field mission. Multiple satellite altimetry missions provided a dense ground coverage and continuous long-term time-series of the lake. Figure 4.1 shows that Jason-1, Jason-2, and Envisat have good inter-mission correspondence. Therefore, only these missions are used in Paper-2. The Figure 4.1 indicates that the Aral Sea suffered a continuous decline in water height during this period. An exception was the North Aral Sea, which increased by approximately 1 meter because of the construction of the Dike Kokaral Dam in 2005; consequently, this part of the lake got stabilized (Figure 4.1, bottom panel).

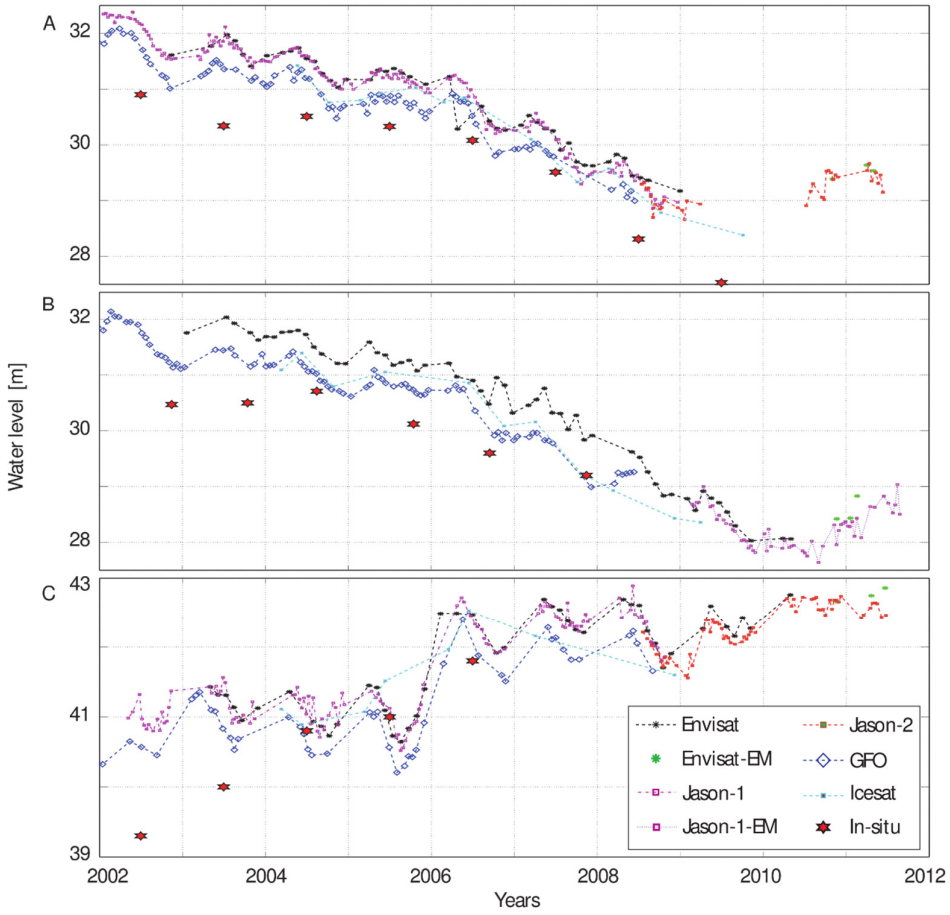

Figure 4.1. Altimetry water height: (A) East Aral Sea, (B) West Aral Sea and (C) North Aral Sea.

Figure 4.2 shows the Landsat-derived coastlines of the Aral Sea, at three-time points, with the passes of all the applied altimetry missions. The Figure indicates that the East Aral Sea was very well observed by Envisat, GFO, ICESat and Jason1 until 2009. Later, due to its reduced extent and ending of many altimetry missions, limited observations are recorded. Similarly, the West Aral Sea was mainly observed by Envisat until July 2010. Thereafter, only Jason1–EM (extended mission) observed the lake. This illustrates that a harmonized multi-mission approach is the only solution to obtain a continuous observation of the water height, mainly due to the retirement of missions (e.g., Envisat, Jason-1 and their extended missions) and reducing size of the lake.

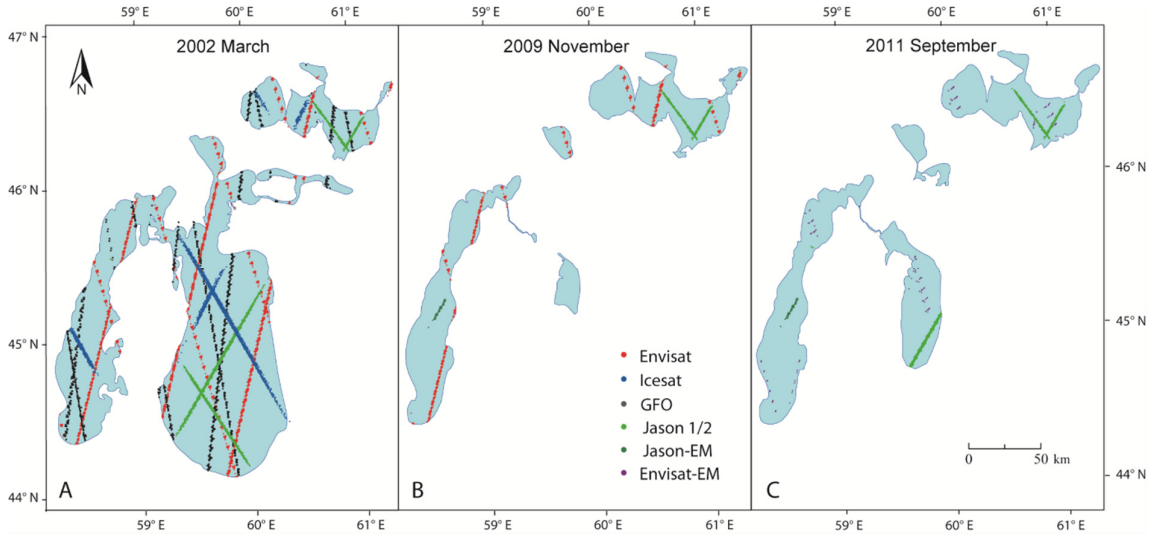

Figure 4.2. Multi-mission altimetry passes over the Aral Sea on the Landsat-derived coastline: (A) March 2002, (B) November 2009 and (C) September 2011.

In addition to the geometrical evolution observed by Landsat and altimetry, gravimetrical variations of the lake and its surroundings have been estimated by GRACE. All missions observed the continuous desiccation until the beginning of 2009 and a subsequent abrupt gain, mainly due to unusual discharge from the Amu Darya in 2009-2010 (Figure 4.3, bottom panel). The Landsat-derived extent of the lake increased a little later (Figure 4.3, upper panel: red line) than the Amu Darya inflow (Figure 4.3, lower panel: blue line) because the discharge got abstracted in the big Amu Darya delta and many surrounding small lakes. GRACE observed the mass gain even earlier (Figure 4.3, upper panel: black line) because of its integral signals from other different hydrological compartments and its larger extent of observation (discussed in Paper-4).

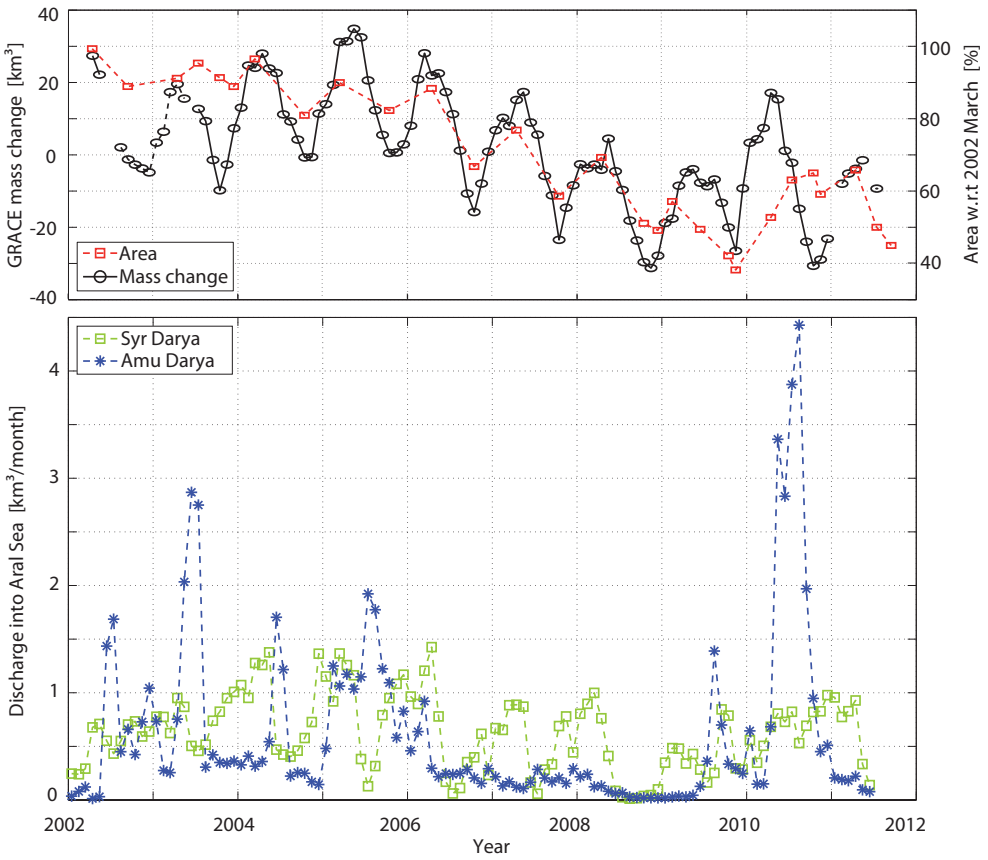

Figure 4.3. Upper panel: The mass change observed by GRACE (left axis) and change in surface area of the Aral Sea (right axis). Lower panel: The Amu Darya and Syr Darya's monthly discharge into the Aral Sea.

This study demonstrates that for ungauged or poorly gauged water bodies like the Aral Sea, remote sensing can be used as a powerful tool to measure temporal variations in the water storage by comparing water height via satellite altimetry, surface area via coastlines derived from optical images and TWS via GRACE. This motivated the exploration of methods for the precise volumetric variation estimation of the lake in Paper-2 and Paper-3.

Declaration of own contribution

The conception of this paper was developed jointly by F. Seitz and A. Singh. A. Singh has worked on the computation of biannual surface area from Landsat and water height from multiple altimetry data. C. Schwatke provided the necessary program to read the altimetry data and apply required corrections. F. Seitz has worked on the GRACE time series processing and its description in the manuscript. A. Singh wrote the manuscript, excluding the GRACE section. F. Seitz modified the text through comments on the content and linguistic issues. The overall own contribution is estimated at **65 %.**

5 Paper-2

Application of Multi-Sensor Satellite Data to observe water storage variations

Singh, A.; Seitz, F.; Schwatke, C.; Selected Topics in Applied Earth Observations and Remote Sensing (JSTARS), vol. 6, issue 3, pp 1502–1508, IEEE Geo-science and Remote Sensing Society, 2013. DOI: 10.1109/JSTARS.2013.2258326.

5.1 Highlights

- Paper-1 illustrates that Jason-1, Jason-2 and Envisat observations are most suitable to obtain continuous water height estimation. Therefore, in Paper-2, the Aral Sea water volume is derived by intersecting water height from these missions with the digital bathymetry model of the Aral Sea (Figure 5.1).
- The study compares the geometric and gravimetric volumes of the Aral Sea.

5.2 Extended abstract

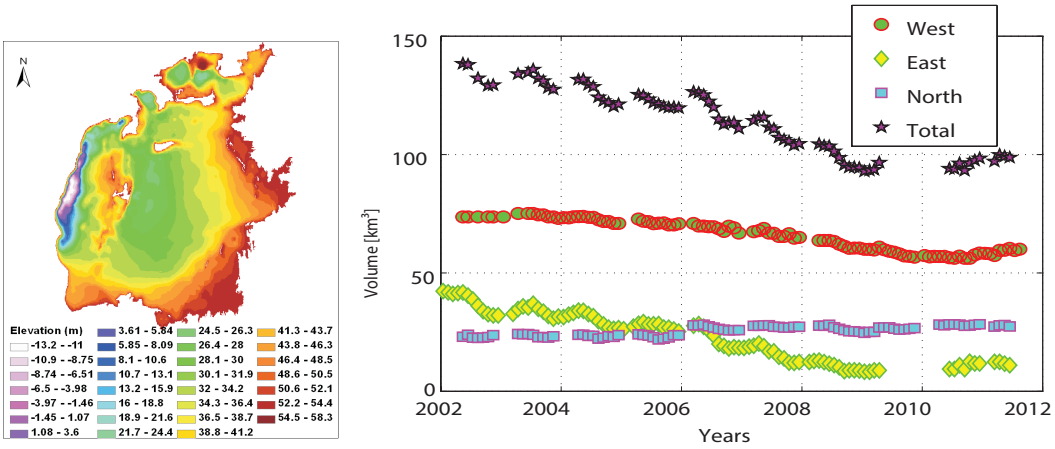

Figure 5.1. Left: bathymetry of the Aral Sea; Right: water volumes computed for each basin and their sum.

The sum of the water volume variations of each of the sub-basins of the Aral Sea, derived from altimetry water height and the bathymetry intersection (Figure 5.1), is subsequently analyzed with the mass variations observed by GRACE. The results showed a long-term receding trend in the gravimetric signal (4 km^3/year) as well as in the geometric signal (5 km^3/year) of the Aral Sea (Figure 5.2). However, due to the complicated nature of GRACE signal they cannot be compared one-on-one.

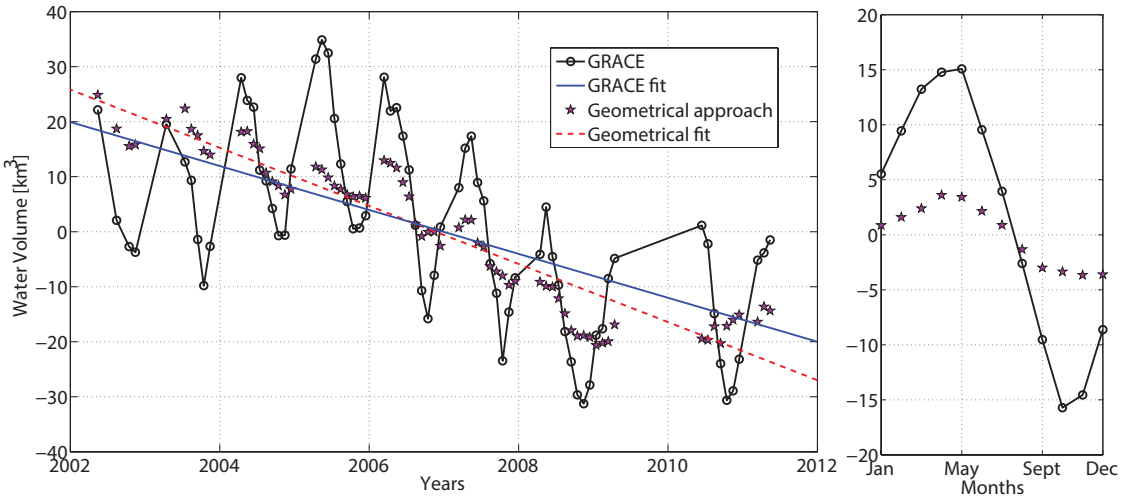

Figure 5.2. Left: Volume of the Aral Sea resulting from GRACE and the geometrical approach; Right: Respective composite seasonal cycles of Lake water storage.

The paper shows that gravimetric variations in the region agreed well with the geometrical changes of the Aral Sea. This fact motivated the authors to extend the study to another test site with a smaller water body and accurately estimate lake/reservoir volume in Paper-3.

Declaration of own contribution

The idea of generating a lake volume by bathymetry and water height intersection has its source in Paper-1. A. Singh, based on the programs provided by C. Schwatke in the previous work, has reprocessed the water height and recomputed the surface area of the Aral Sea. The GRACE gravity field time series has been obtained from the previous paper. The manuscript has been first written and designed by A. Singh and F. Seitz added GRACE description and constructively modified it through comments on the content and linguistic issues. The overall own contribution is estimated as **85 %**

6 Paper-3

Remote Sensing of Storage Fluctuations of Poorly Gauged Reservoirs and State Space Model (SSM)-Based Estimation

Singh, A.; Kumar, U.; Seitz, F.**;** Remote Sensing, Vol. 7, issue 12, pp 17113–17134, 2015. DOI: 10.3390/rs71215872 (Open source).

6.1 Highlights

- The paper proposes a new water-height estimation method by selected-region boundary (SRB) approach, using Landsat-derived shorelines and bathymetry of the water body.
- Two absolute water volume estimation methods Landsat-bathymetry volume (LBV) and Altimetry-bathymetry volume (ABV) are demonstrated. They intersected bathymetry of the waterbody with the calculated heights from Landsat shorelines (through SRB) for LBV and satellite radar altimetry for ABV.
- The study also discusses an entirely remote sensing based altimetry-Landsat volumetric variation method (ALVV). It applies the truncated pyramid model to integrate the change in area (observed by Landsat) with the change in water height (observed by altimetry).
- Further, an assimilation of the estimated absolute volumes (LBV and ABV) is demonstrated by applying the Kalman filter-based state space model.
- The study also updated the bathymetry of the East Aral Sea, which is more than half a century old.

6.2 Extended abstract

The paper demonstrated water-volume estimation methods of lakes/reservoirs by three independent approaches, using multiple satellite missions (Figure 6.1). The methods are applied in a well-measured reservoir (Lake Mead) and a poorly gauged lake with an inaccurate bathymetry (the Aral Sea).

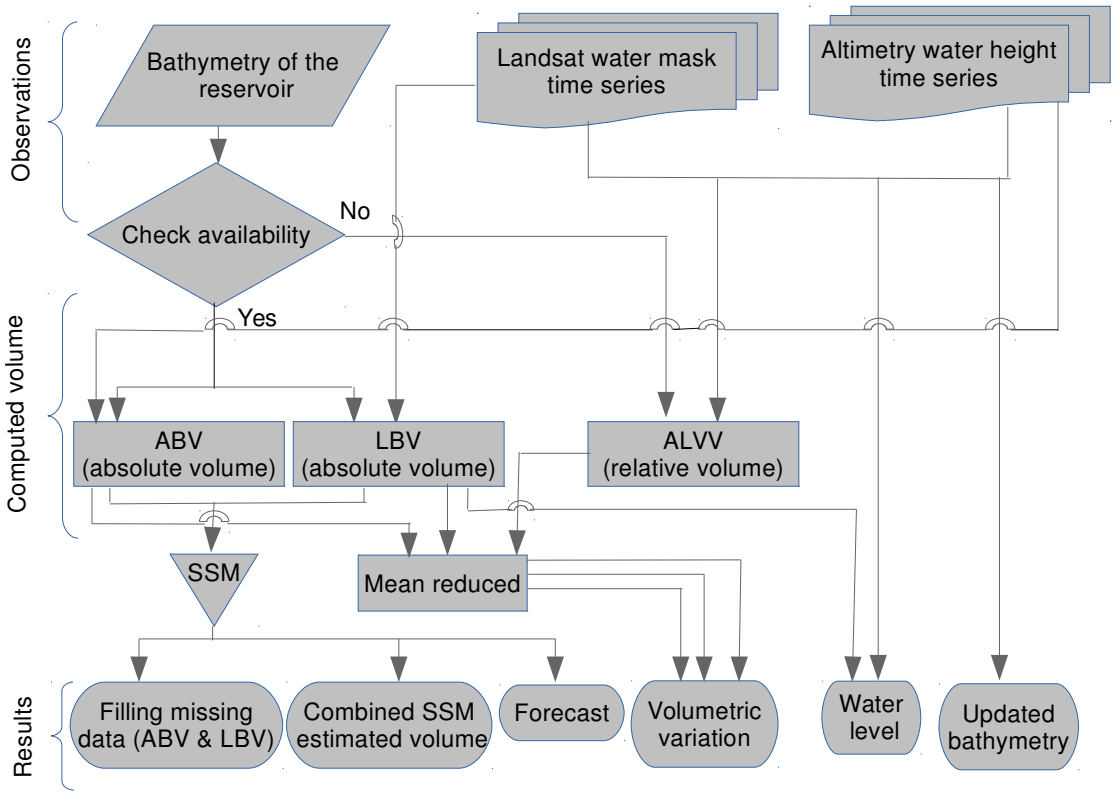

Figure 6.1. The methodology implemented in the Paper-3 for the lake/reservoir volume estimation.

To obtain two independent absolute lake/reservoir volumes, the bathymetry of the water bodies are intersected with the water heights estimated from altimetry and Landsat. The water height from satellite altimetry is obtained from DAHITI. However, to retrieve water height from Landsat shorelines is not trivial, because the border pixels of land-water mask intersected with the bathymetry have significant variance in the height. The derived range of heights can be due to uncertainties in the water mask (discussed in 3.1.4), coarse bathymetry and high gradients. The study proposes to select a subsection of the water boundary (referred as SRB, selected region boundary), based on knowledge of the study site. The criteria for the selection of region are the following: (1) lower gradient of subsection, to obtain less height variations within a 30 meter pixel (spatial resolution of the mask); (2) comparatively stable region, which is not under direct flow of water (river mouth) to uphold the concept of an equipotential surface. Figure 6.2 shows the estimated water height from Landsat and altimetry missions with the uncertainty in the SRB water height estimation. Uncertainties in the altimetry observations from all the analyzed water bodies provided by DAHITI are less than 30 cm. It only accounts for the error resulting from Kalman filtering applied by DAHITI (which is below 15cm for Lake Mead, 27cm for the East Aral, 12 cm for the West Aral and 10 cm for the North Aral). The water

height obtained from the developed Landsat SRB method and altimetry showed over 0.99 correlation with ground observations for Lake Mead. For the Aral Sea, due to lack of ground observations, we cross-validated the altimetry and Landsat observations, and they also have a good agreement. The East Aral Sea has some disagreement between 2008 and 2012 water height estimations. The observations from altimetry for this period are relatively less reliable because the radar echoes have a similar waveform from highly saline shallow water and smooth and from the flat surface of the shrinking East Aral Sea. Further, the observations at the river mouth are not representative of the equipotential lake surface. Figure 6.2 also shows dispersion between the two missions for the North Aral Sea; however, its NRMSE is 1.2%.

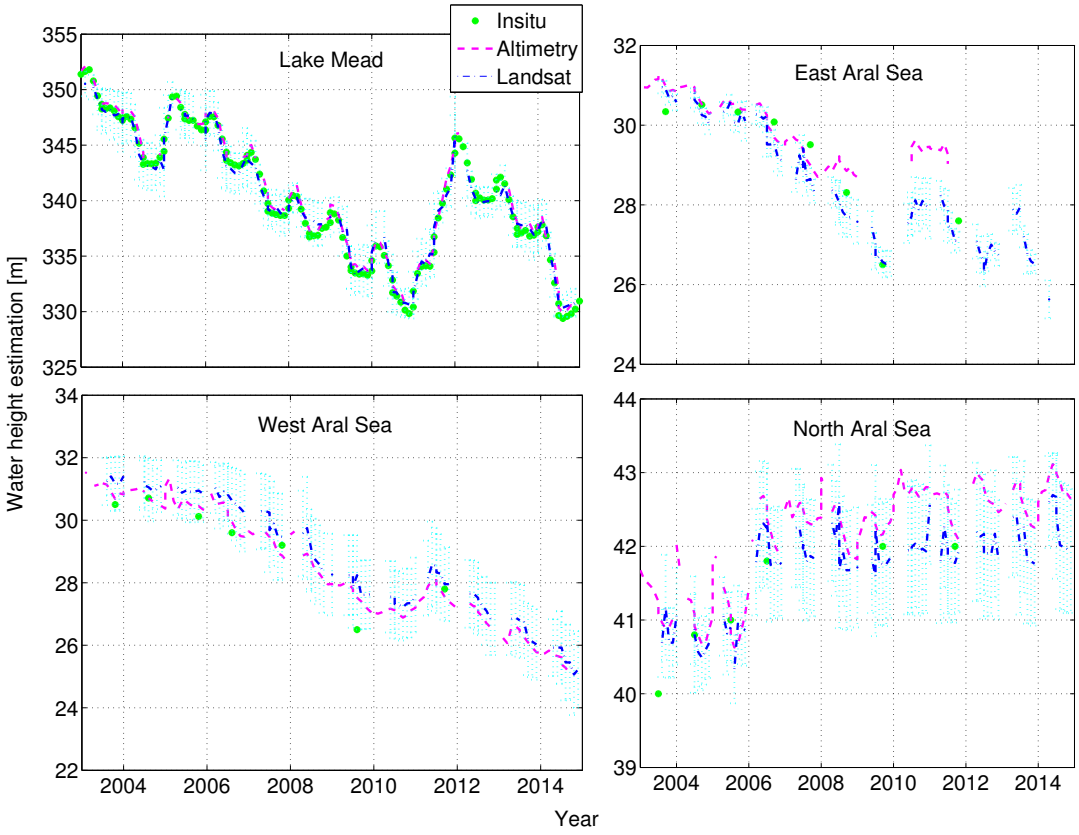

Figure 6.2. Water height variations estimated by altimetry and Landsat (selected region boundary method), for Lake Mead and the three sub-basins of the Aral Sea.

Apart from the absolute volume estimations (ABV and LBV), Paper-3 discusses a completely remote sensing approach (ALVV) to obtain lake/reservoir volume variation (Figure 6.3). Some of the previous studies also estimated the water volume variations by combining changes in the surface area with the corresponding water height. The applied inverted pyramid method (Abileah et al., 2011; Crétaux et al., 2016) is a better approach compared to the rectangular formation (Frappart et al., 2011), because natural surfaces are never in a regular box shape, and

their nearest approximation can be assumed like a pyramid (Equation 11).

$$ALVV = \sum_{t=1}^{n} \frac{1}{3} \times (H_t - H_{t-1}) \times \left(A_t + A_{t-1} + \sqrt{(A_t \times A_{t-1})}\right) \quad (11)$$

where,

$ALVV$ = Total volume change with respect to the initial state (t_0) at the n^{th} month

A_t = Area of the water extent at month t and A_{t-1} = Area of the water extent at the previous month

H_t = Elevation of the water body at month t and H_{t-1} = Elevation of the water body at the previous month. n = Number of months.

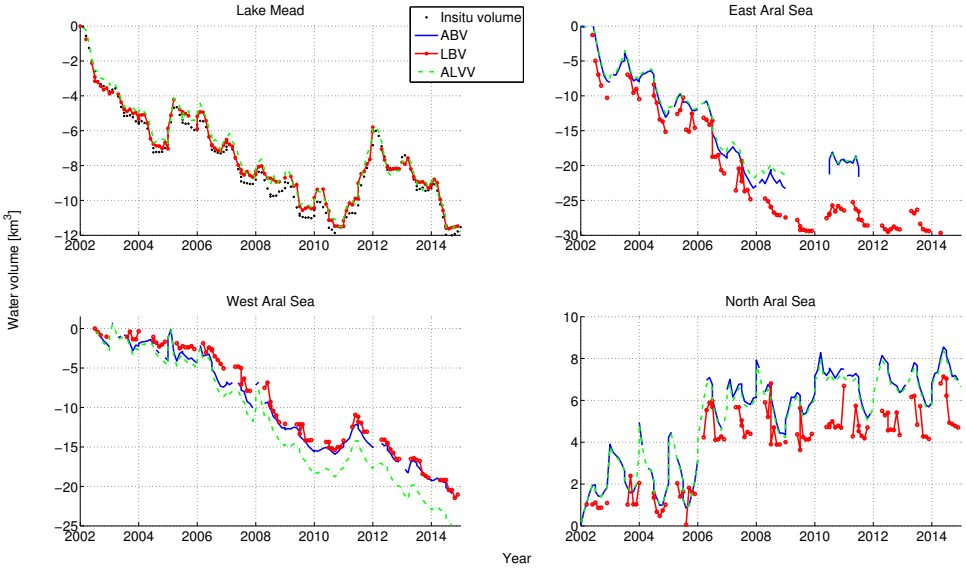

Figure 6.3. Volumetric variations computed by the three independent methods (ABV= altimetry bathymetry volume, LBV=Landsat bathymetry volume and ALVV=altimetry Landsat volumetric variations) for Lake Mead and the three sub-basins of the Aral Sea.

To obtain a combined state space model estimate (CSSME) from the two absolute volumes (ABV and LBV), a Kalman-filter-based state space model (SSM) has been applied (Figure 6.4). The Lake Mead CSSME has high coherence with the ground observations (a correlation of 0.98 or r^2 of 0.97 and 1.8% NRMSE or 0.35 km^3 RMSE), and its forecast performed well (a correlation of 0.86 or r^2 of 0.75 and 3% NRMSE or 0.35 km^3 RMSE). All estimated volumes of Lake Mead demonstrated above 0.98 correlation with in-situ observations, while for the Aral Sea due to lack of ground observations, the CSSME is compared with the input volumes (ABV and LBV). The West Aral Sea showed good agreement having correlations of more than 0.98 (r^2>0.97) and NRMSE 2.7% (1 km^3 RMSE) with LBV and 1.6% (0.5 km^3 RMSE) with ABV. The East Aral Sea (until December 2007) showed correlations of above 0.94 (r^2>0.89) and

NRMSE 12% (1.9 km^3 RMSE) with LBV and 2.7% (0.49 km^3 RMSE) with ABV, and the North Aral Sea has a correlation of 0.91 (r^2=0.83) and 3.2% NRMSE (0.82 km^3 RMSE).

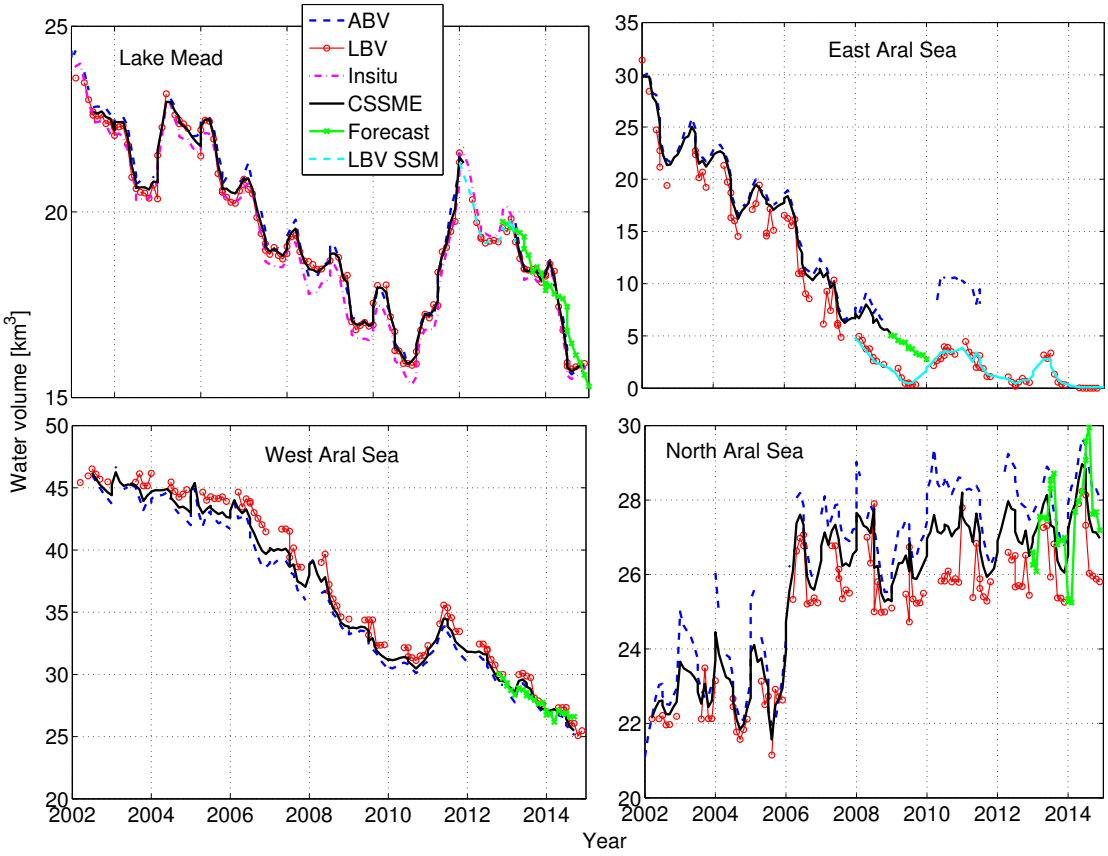

Figure 6.4. Combined state space model estimates (CSSME) from the two absolute volumes (ABV= altimetry bathymetry volume, LBV=Landsat bathymetry volume) of Lake Mead and the three sub-basins of the Aral Sea.

The receding water left the lakebed open and more prone to erosion. The time-series of shorelines (from Landsat) and the corresponding water heights (from altimetry) processed in the study provided an opportunity to formulate a detailed bathymetry of the East Aral Sea (Figure 6.5) that has been lost. The developed bathymetry is made freely available through the PANGAEA data archive (Singh, A. and Seitz, F.; 2015), which can be useful when the lake regains its lost area in future.

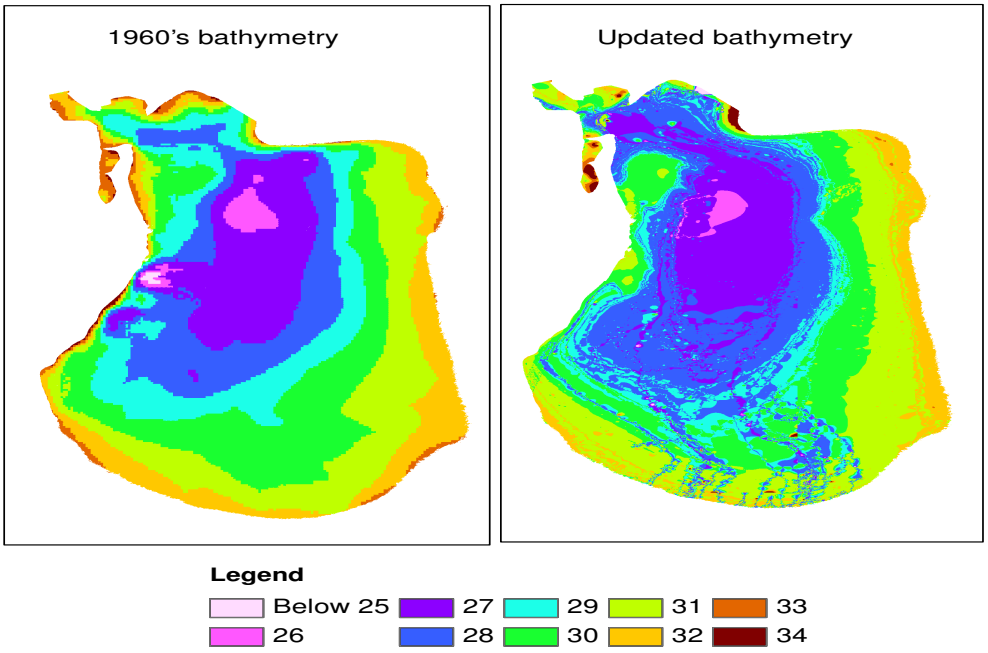

Figure 6.5. Updated bathymetry of the East Aral Sea, above mean sea level [meters]. (publically available through PANGEA archive)

Declaration of own contribution

A. Singh conceptualized the manuscript and produced the three water volume time series. U. Kumar computed the assimilated volume by Kalman based state space model. A. Singh has written the manuscript, and U. Kumar helped in formulating the SSM theory in the manuscript. F. Seitz contributed to the paper through discussions and comments. Analysis of the results and compilation of the figures has been done by A. Singh. The overall own contribution is estimated at 75-**80 %.**

7 Paper-4

Water budget analysis within the surrounding of prominent reservoirs from multi-sensor Earth observation data and hydrological models: case studies of the Aral Sea and Lake Mead

Singh, A.; Seitz, F.; Eicker A.; Güntner A.**;** Remote Sensing, Vol. 8, pp 953, 2016. DOI: 10.3390/rs8110953 (Open source).

7.1 Highlights

- The study validates the estimated volume from Paper-3 by net runoff deficit and mass variations from the GRACE signal.
- It analyses the hydrological state and water budget of the regions dominated by lake/reservoir, using multi-sensor data and hydrological model outputs.
- It evaluates contributors in the regional gravimetric variations.
- It demonstrates that the TWS from GRACE can be better analyzed by the net hybrid-storages (i.e. sum of the CSSME based lake/reservoir volume estimates and hydrological model-based SM, and SWE estimates), than the net hydrological fluxes (precipitation data products reduced by hydrological model-based evapotranspiration and net in-situ runoff deficit).
- For the analyzed regions, the GLDAS-based hybrid storage exhibits better agreement with the mass variation observed by GRACE than the WGHM-based estimates.

7.2 Extended abstract

The hydrological budget of a region is determined by the horizontal and vertical water fluxes acting in both inward and outward directions. These integrated water fluxes alter the total water storage and consequently the gravitational force of the region. This study evaluates the TWS in lake/reservoir dominated regions through three approaches viz. fluxes, storages, and gravity. The flux ($\frac{\Delta S}{dt}$) in a region is the sum of ET, precipitation (P) and net in-situ surface runoff (ΔR) (Equation 12). Based on the applied datasets, two net fluxes are derived: Flux-1 is obtained by combining the GPCC precipitation with the WGHM ET and in-situ runoff and Flux-2 is

obtained by combining the TRMM-3B43 precipitation product with the GLDAS ET and in-situ runoff.

$$\frac{\Delta S}{dt} = P - ET + \Delta R \tag{12}$$

The estimation of the water storage change (ΔS) in a region is the sum of storages in ΔSM, ΔSWE, ΔGW and ΔSW (Equation 1312). The study neglected the role of GW interaction both in storage and fluxes due to lack of direct observations. The hybrid storages combine the remote sensing-based lake/reservoir volume estimates (derived in Paper-3) with the ΔSWE and ΔSM from hydrological model outputs. The WGHM based hybrid storage is referred to as Storage-1 and the GLDAS-based hybrid storage is known as Storage-2.

$$\Delta S = \Delta SM + \Delta SWE + \Delta SW + \Delta GW \tag{13}$$

To determine the TWS from GRACE in the study area, JPL 3° spherical cap mascon solutions are analyzed. The size of the study boxes is chosen in such a way that it can be resolved by GRACE and at the same time, the hydrological mass variations in the vicinity of the reservoirs influence the GRACE measurements as little as possible. The Lake Mead study box is based on the size of the mascon (3°x3°). The Aral Sea surface area was approx. 20,000 km^2 in spring 2003 (with 92.5 km^3 volume). Hence it required data from more than two mascons to cover the entire Aral Sea. The study area was extended towards the west of the Aral Sea in order to include the entire signal of the Aral Sea mass change from which we assumed that it is smoothed over the complete western mascon (Figure 7.1, right).

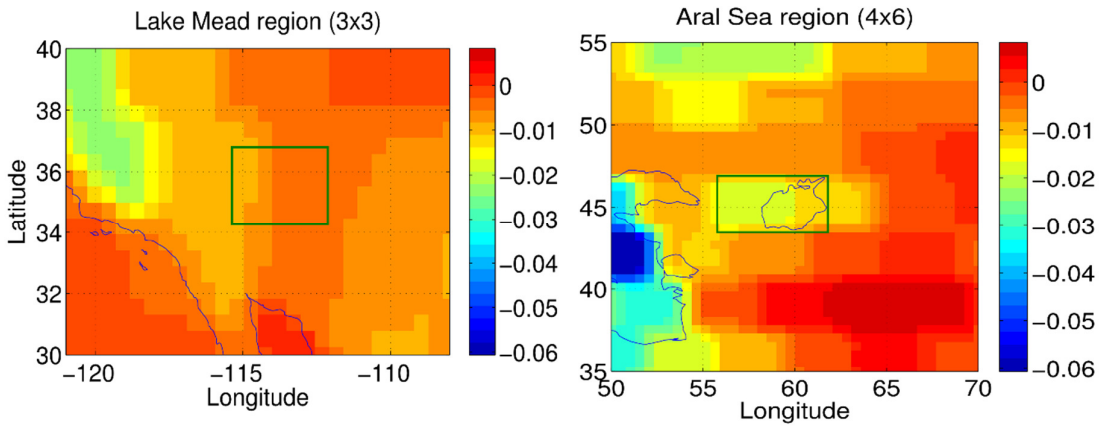

Figure 7.1. GRACE-derived trend of the equivalent water height (meter/year) between 2003 and 2014. The size of the study area was chosen according to the mascon grid. The Lake Mead region is 3°x3° where Lake Mead is located at the center (left). The Aral Sea region is 4°x6°covering the entire lake and two mascon grid cells.

The paper observed a good inter-annual agreement between all datasets and in the different

phases of mass variations estimated by GRACE. The periods of more than average rainfall and an increase in net runoff coincided with an increase in the GRACE signal. The results show that the dynamics revealed by the GRACE signal can be better explored by the hybrid method (which combines CSSME based lake/reservoir volume estimates with hydrological model outputs), than the sum of vertical and horizontal fluxes. Correlation of the GRACE signal with the GLDAS based Storage-2 estimate is 0.87 in the Lake Mead region and 0.88 in the Aral Sea region, while the WGHM based storage has 0.58 and 0.87 for the respective regions. The Aral Sea volume variation is the major contributor in the Aral Sea region GRACE signal with 0.82 correlation while in the Lake Mead region the contribution of the different hydrological compartments varied over time. Hence, Lake Mead showed only 0.60 correlation.

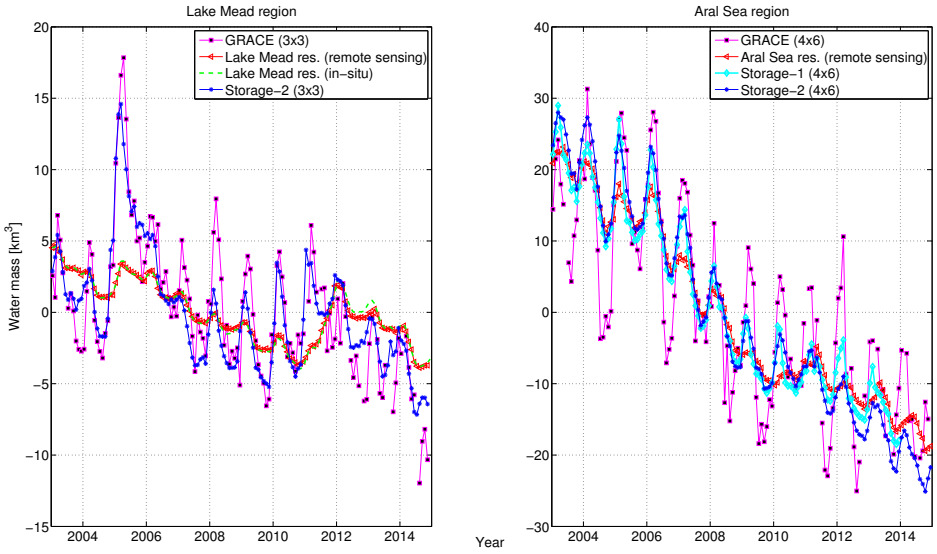

Figure 7.2. TWS observed by GRACE compared with the best estimates and the lake/reservoir volume: (left) the Lake Mead region and (right) the Aral Sea region.

Apart from looking at a bigger study box, the study demonstrates the closing of the water budget of the Lake Mead water body because of the availability of extensive in-situ data. Net hydrological fluxes acting on Lake Mead are estimated by obtaining evaporation (only from the water body) from the Boulder Canyon Operations Office, runoff data from the 'Water Accounting Reports' of the USBR and precipitation over the reservoir is calculated from the TRMM (3B43) data. Figure 7.3 shows that the net reservoir flux agrees very well with the reservoir storage variation (Figure 6.4, top left panel) having a correlation of 0.90 with the in-situ and 0.81 with the remote sensing-based estimates. The negative vertical flux (blue line in Figure 7.3) shows that evaporation loss from the reservoir is greater than precipitation, and it has a tiny contribution to the net flux. The reservoir variation is mainly driven by a change in

net runoff from the Colorado River, which indicates that accurate estimation of reservoir water volume can improve our knowledge of runoff dynamics.

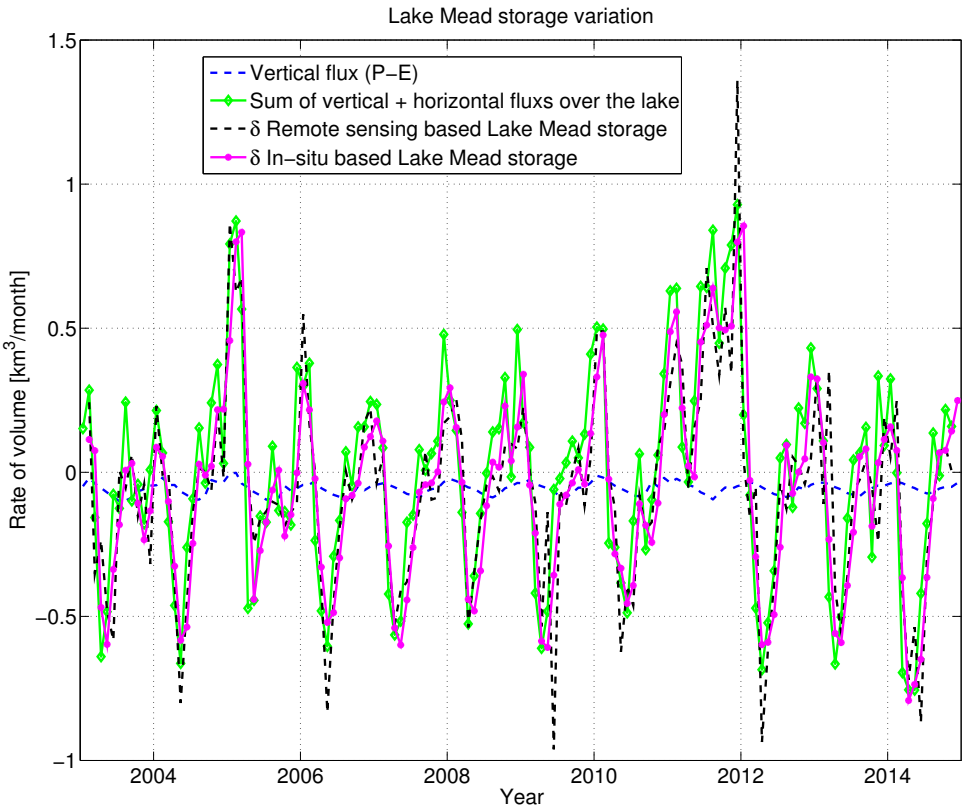

Figure 7.3. Lake Mead reservoir volume variation compared with the hydrological fluxes.

Declaration of own contribution

A. Singh conceptualized the idea of the computation of an overall water budget of the lake dominated regions through different approaches. A. Eicker provided the EWH from mascon GRACE solution matrices and wrote a paragraph on mascon theory. A. Güntner provided the WGHM output matrices and discussed the results. F. Seitz being P.I. of the project provided the necessary guidelines. The creation of figures and the writing of the first manuscript has been done by A. Singh. All the co-authors helped in the improvement of the manuscript through constructive comments. The overall own contribution is estimated at **85 %.**

8 Discussion

Arid regions, in general, face tremendous difficulty in quantifying the ΔTWS due to huge infiltration and ET loss. The loss is considerably greater than the total precipitation return, which is at the expense of runoff, groundwater recharge and shrinking of the lakes/reservoirs. The study generated time series of water height and water-surface-area from altimetry and Landsat respectively, using different approaches. Further, GRACE gravity field observations are evaluated using regional and global basis functions. The Section 8.1 will discuss the difference between the applied methods and the reasoning for the change in approach during different publications. In order to evaluate the discussed methods, for the estimation of volumetric change in lake/reservoir dominated regions, using remote sensing data and hydrological model outputs, the given two study sites are selected. The Section 8.2 will discuss the obtained results from the study sites.

8.1 Difference between the applied methods/approaches in different publications

8.1.1 Landsat-derived surfaces-water-areas in Paper-1, Paper-2, and Paper-3

Paper-1 applies a spectral combination of NIR, SWIR-1, and SWIR-2 bands while Paper-2 and Paper-3 utilize only NIR band of the Landsat images. The three Landsat bands fall in the water absorption region of the electromagnetic spectrum ("Introduction to Remote Sensing," 2010; Lillesand et al., 2015). However, Section 3.1.1 and Figure 3.1 show that NIR band is a most suitable band for this region, considering the spectral reflectance of the saline and shallow East Aral Sea. In order to classify the NIR band, Paper-2 applies the Maximum likelihood supervised classifier while Paper-3 applied the ISODATA unsupervised classifier. For deep water bodies both methods have an excellent agreement in land-water delineation. The area estimated by both methods have a correlation coefficient of 0.97 and 3% NRMSE for the West Aral Sea and a correlation coefficient of 0.95 and 1.7% NRMSE for the North Aral Sea. However, for the shallow region with mixed pixels (discussed in Section 3.1.4), the two classification methods differ in their estimates at a few time points (Figure 8.1, top panel). Overall, however, their agreement is good (0.96 correlation coefficient), although the error in area estimation is high (18% NRMSE).

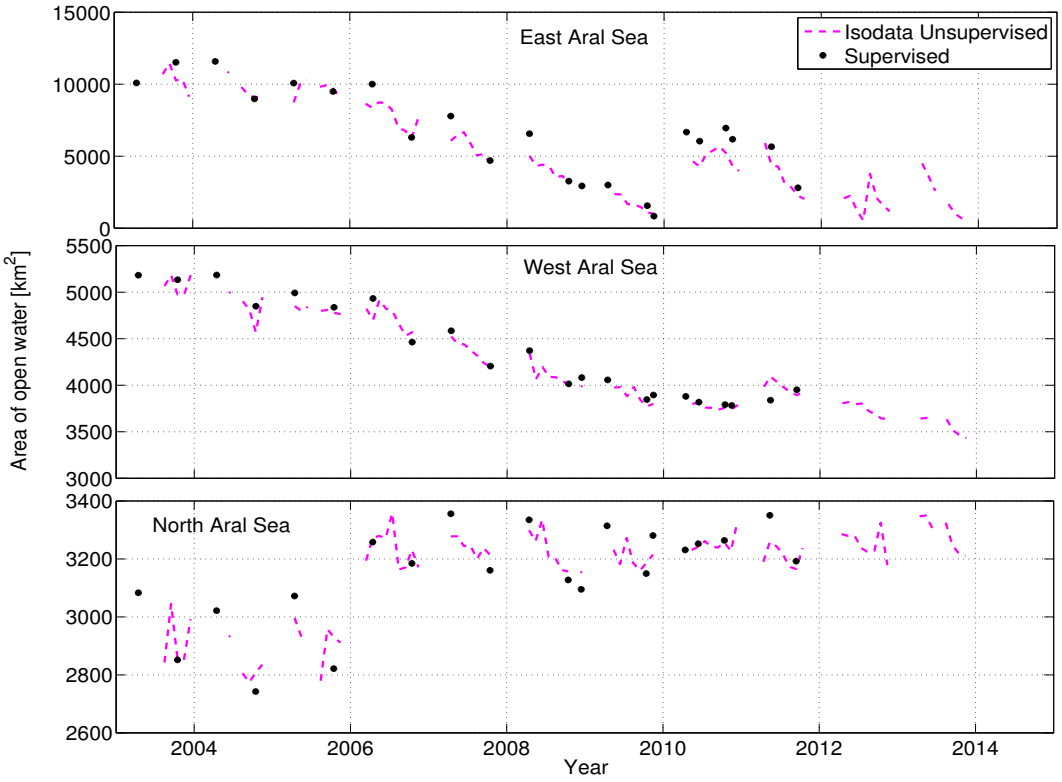

Figure 8.1. Area estimation of the Aral Sea by supervised and unsupervised classifications from Landsat images.

The East Aral Sea has undergone huge water-surface-area variations. Considering the complicated spectral profile of the region (discussed in Section 3.1.4), the land water delineation is not trivial in this region. An example of the impact of classification and band combinations is demonstrated in Figure 8.2, on Landsat ETM+ image of the South Aral Sea from May 2010. The multispectral image (NIR, SWIR-1, and SWIR-2 as used in Paper-1) is classified by supervised classification into four clusters (Figure 8.2, panel-1). In Figure 8.2 blue represents water-body, cyan represents shallow water, red is considered as either moist soil/very-shallow water or reflection from a very coarse surface and light lemon is land. The Landsat NIR band (Figure 8.2, panel-2) is classified by supervised classification (Figure 8.2, panel-3) and unsupervised classification (Figure 8.2, panel-4). As discussed in Section 3.1.1, the SWIR bands cluster all moist surfaces, including the water-body, in one group. Therefore, in the multispectral image (Figure 8.2, panel-1) classification of indistinguishable clusters is hard to separate. Consequently, water-body cluster (blue areas) has high commission error in the multispectral image (Figure 8.2, panel-1). The water class of the supervised classified image (only blue area in Figure 8.2, panel-3) has relatively similar water surface area, the water-body and shallow water clusters (blue and cyan, respectively) are merged into a water class in the

unsupervised NIR band classified image (Figure 8.2, panel-4). Figure 8.2 shows that the supervised classified single NIR band (Panel-3) produces better water mask than the other two (Panel-1 and Panel-4), but it is a labor intensive process. Therefore, unsupervised classified and post classification merging of clusters (panel-4, blue + cyan) is considered as a more suitable approach for producing water mask time series, in this study. However, incorrect labeling of the clusters after unsupervised classification can introduce significant error. For example, it can lead to significant omission error if blue and cyan clusters in Figure 8.2 (panel-4) are not merged. Therefore, in Paper-3, the Aral Sea images are classified into 10 clusters, out of which, in most cases, the first two clusters are merged to form a water class and remaining clusters are merged into a non-water class. However, the decision is taken based on visual interpretation and no ground verification is executed.

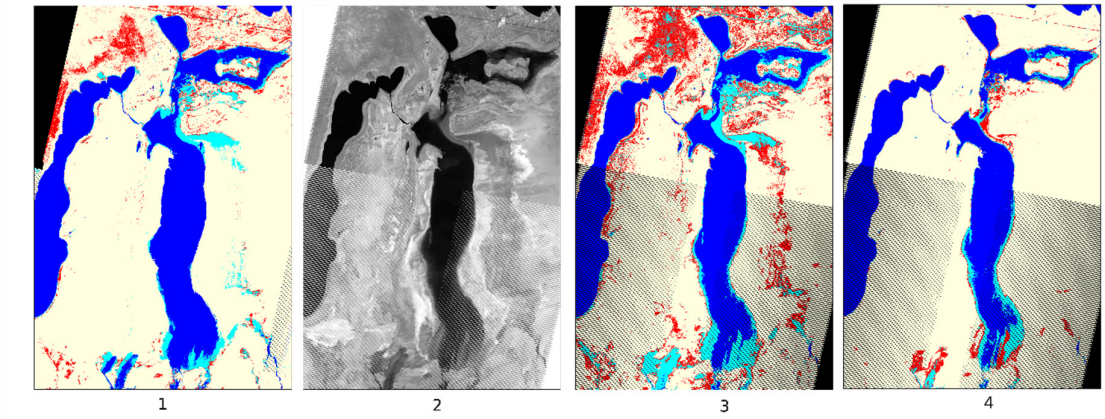

Figure 8.2. Landsat images of the Aral Sea from May 2010. Supervised classification of a multispectral image, as used in Paper-1 (panel-1), and the NIR band (panel-2); the supervised classified NIR band as used in Paper-2 (panel-3); and the unsupervised classified NIR band as used in Paper-3 (panel-4). The water-body is shown in blue, cyan represent shallow water, red is either moist soil/very shallow water or reflection from a very coarse surface and light lemon is the land. The black stripes are data gaps due to SLC-off in ETM+ images.

Most of the Landsat images obtained during the study period are from ETM+ sensor, which has data gaps due to Scan Line Corrector (SLC) failure since May 2003. ETM+ scene has an estimated 22 percent data loss because of the SLC failure ("SLC-off Products: Background," 2010). Figure 8.2 shows that lower part of the mosaic of the Aral Sea has an SLC-off ETM+ image, which is corrected in panel-1 by lateral filling from the adjoining passes before classification. To compare the improvement in the data gap filling, the right panels show the classified images without extra mosaic from lateral sides. However, 4-5 pixels data gap still exists after lateral filling, which is usually corrected after classification by recursive focal filling. The post-classification manipulations lead to an increase in uncertainty in the extracted

shorelines. The Landsat TM and OLI sensors have no artifacts due to SLC-off gap fillings, but their availability is limited during this period.

8.1.2 Altimetry-derived water heights in Paper-1/Paper-2 and Paper-3

The estimated water heights by satellite altimetry in Paper-1 /Paper-2 (obtained from OpenADB) are more than 50-70 cm higher than the estimated heights in Paper-3 (obtained from DAHITI) for the East and West Aral Sea (Figure 8.3). Indeed, they have used the same altimetry missions with an addition Saral-Altika mission added in DAHITI (launched in 2013). The difference between the estimated heights can mainly be assigned to the difference in the waveform retracking algorithms. DAHITI version 4.3 applied an improved threshold waveform retracking (Schwatke et al., 2015) while Paper-1/Paper-2 measurements are based on an ocean retracker. The North Aral Sea water heights are similar (Figure 8.3, lowermost panel) from both databases because, in this case, both used an ocean waveform retracker.

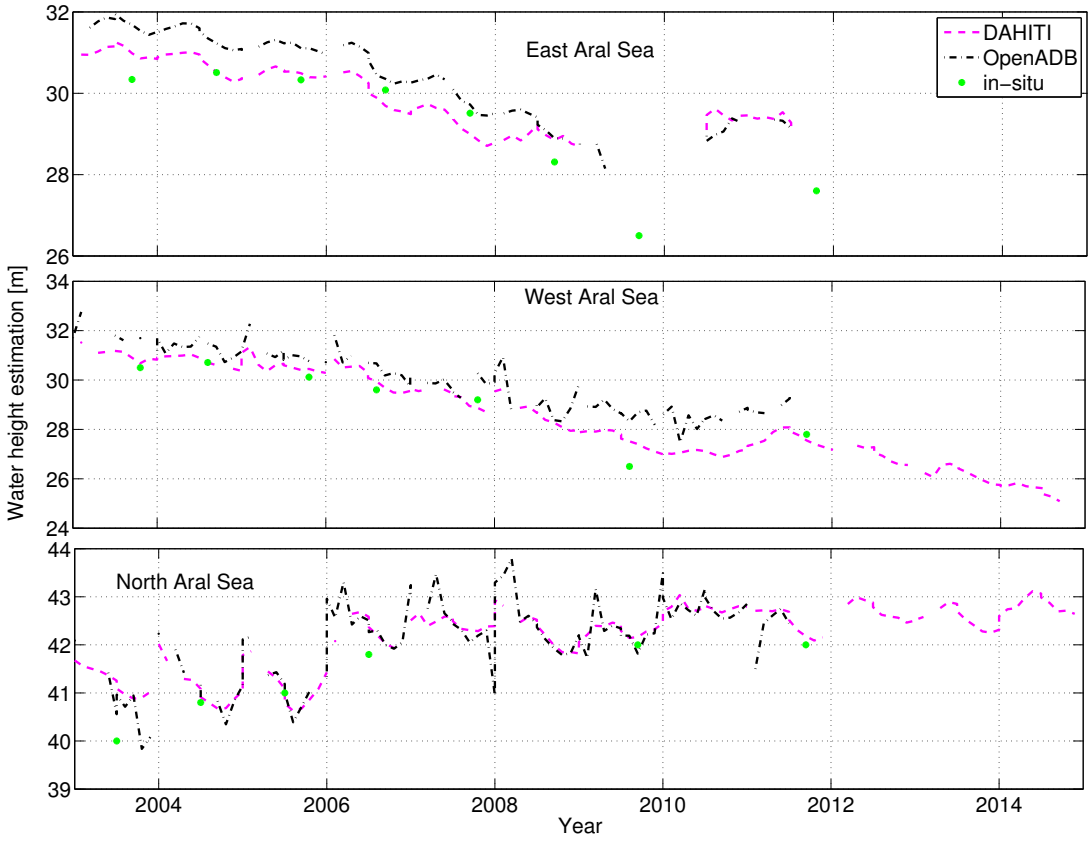

Figure 8.3. Altimetry water height estimations

For all remote sensing observations, a ground segment to calibrate and validate the data is imperative. Given the poorly gauged situation of the Aral Sea, improvement in the estimations

by changing the waveform-retracking algorithm cannot be quantified. The limited in-situ water heights (obtained from cawater-info.net website) are without metadata, and therefore are less reliable. However, they have better proximity to the DAHITI observations than OpenADB (Figure 8.3). Nevertheless, the combined multi-mission altimetry time-series from DAHITI have less temporal jumps because of the application of Kalman filtering and support vector regression outlier rejection methods, on the calculated water heights by Equation-1 (Schwatke et al., 2015).

The water heights in Paper-2 are estimated on the EGM2008 geoid, while DAHITI uses the Eigen-6C3stat geoid. Figure 8.4 shows the difference between these two geoids; Eigen-6C3stat is 2-3 cm lower than EGM2008, predominantly in the East Aral Sea. Eigen-6C3stat is computed from a combination of Laser Geodynamics Satellite (LAGEOS), GRACE and Gravity field and steady-state ocean circulation explorer (GOCE) data, augmented with DTU10 surface gravity data and EGM2008 geoid grid, corresponding to approximately 10 km spatial resolution (Förste et al., 2014). Therefore, geoid approximation by Eigen-6C3stat can be considered as an improvement over EGM 2008.

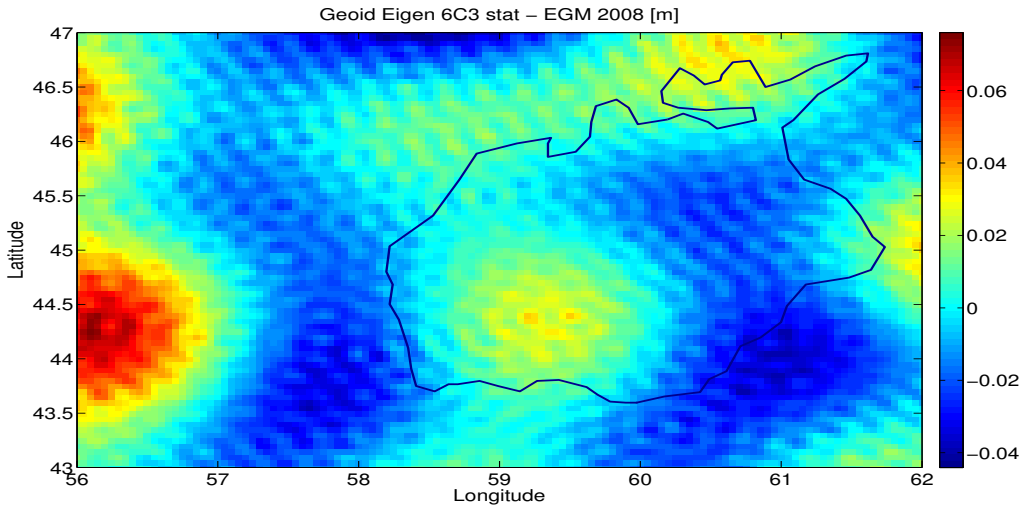

Figure 8.4. Difference in geoid between Eigen-6C3stat and EGM2008.

8.1.3 The SH (Paper-1) and mascon (Paper-4) GRACE Solutions in the Aral Sea region

The Aral Sea study area (~200,000 km^2) is big enough for a reliable GRACE analysis while the

Lake Mead study region (~90,000 km^2) is at the margin of the spatial resolution of GRACE, which is determined by the wavelength of the mass variations. Because of the marginal size of the Lake Mead region, comparisons of SH and mascon GRACE solutions are conducted only in the Aral Sea region. The SH GRACE solution is based on global basis functions. It needs dedicated processing to remove noise and aliasing due to poor sensitivity in the east-west direction. The N-S strips in the SH solution are removed by Gaussian filtering, which causes signal dampening (discussed in Section 3.4.2). In order to rescale the attenuated signal, due to SH truncation and Gaussian smoothing, the same filtering procedures are applied to a simulated water layer of 1cm within the study area (Swenson and Wahr, 2007). In contrast, the mascon GRACE solution recovers a localized signal within a 3° mascon cell, and apriori geophysical constraints are applied for its individual basis function to filter out the noise present within the within a 3° cell. Therefore, it requires no additional empirical de-striping filter like the SH solution. Additionally, the gridded rescaling coefficients of the mascon GRACE solution (Wiese, 2015), provided by the GRACE Tellus website, are significantly smaller. Therefore, the inter-annual signal of the rescaled SH solutions has a higher amplitude than the mascon inter-annual signal (Figure 8.5). Watkins et al. (2015) also emphasized the difference between SH and mascon GRACE solutions and the possibility of substantial uncertainties that exist with the SH rescale factor derivations. The effect of rescaling is lower in large basin due to less leakage. They found a good agreement between the two GRACE solutions for 50 large hydrological basins because the effect of rescaling is lower in large basins, due to less leakage. Apart from the differences in amplitude, the two solutions have different inter-annual progression. The SH sinusoidal curve shows the mass variations of the Aral Sea region, which is contaminated by the strong adjacent signals of the Caspian Sea. E. Forootan et al. (2014) demonstrated that Caspian Sea gained significant mass in 2005-2006 and have similar progression (as the light blue curve in Figure 8.5) for period 2003-2011. The mascon GRACE solution captures the local mass variations much better. It shows a continuously declining water mass signal as detected by the geometrical analysis of the lake and the hybrid mass storage estimated in Paper-4.

Figure 8.5. Inter-annual mass variations observed by the mascon and SH GRACE solutions and the TWS simulated by WGHM.

Figure 8.5 compares the impact of rescaling on the ΔTWS, resulting from SH and mascon GRACE solutions. The sum of all hydrological storage compartments simulated by WGHM for the Aral Sea region is also converted into SH coefficients, filtered and rescaled in a similar way. The rescaled WGHM ΔTWS and SH GRACE solution have comparable inter-annual signals (magenta and light blue curves respectively in Figure 8.5). However, the ΔTWS simulated by WGHM is almost entirely made up of SW storage. Figure 8.6 shows that the total discharge estimated by the WGHM from the Amu Darya and the Syr Darya is much higher than the in-situ discharge (obtained from cawater-info.net website). Further, Paper-4 also demonstrated that the SM and SWE are highly underestimated by the model, indicating that WGHM has a deficient model structure or parameterization for this region. Therefore, ΔTWS estimated from WGHM and SH cannot be cross-validated in this region.

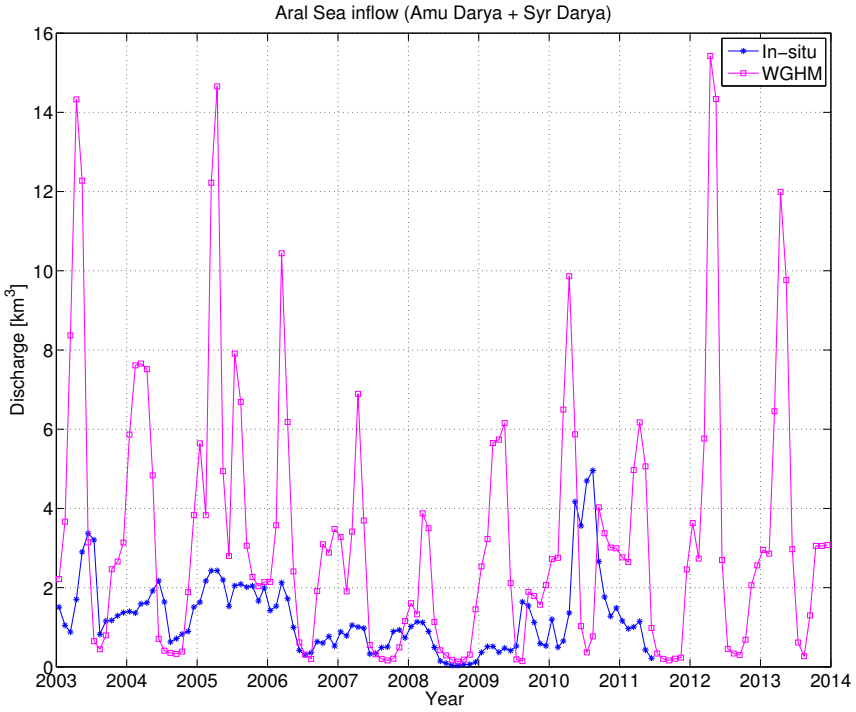

Figure 8.6 Total discharge from the Amu Darya and the Syr Darya, from in-situ observations and WGHM simulations.

The rescaling factor for the mascon GRACE solution is derived from Noah GLDAS (Watkins et al., 2015). However, GLDAS has no SW and GW stocks, and Paper-4 shows that the Aral Sea (1960's water surface area) has been masked out for all simulations in the GLDAS model. The absence of Aral Sea mass dynamics might have some effect in the GLDAS based rescaling factor estimation for the mascon solution. Therefore, SH leakage correction based on WGHM might have led to an overestimation of the mass change, and GLDAS based rescaling of the mascon GRACE signal might have led to an underestimation of the same. The comparison suggests that there is a need for a cautious analysis of different GRACE solutions, their signal characteristics and the overall applicability of GRACE.

8.2 Results

During the study period (2002-2014) the Aral Sea and Lake Mead shrunk approximately 46 and 11.5 km³ respectively. Given the impact of these hydrological variations, it is imperative to formulate robust monitoring system for the estimations and forecasts of the water budget of the regions.

8.2.1 Lake Mead

The Colorado basin has been facing enormous difficulties since a decade and a half due to severe prolonged drought and low snowmelt runoff. Therefore, precise storage estimation in all the hydrological compartments is key to appropriate water management. The situation gets worse as reliance on aquifers grows due to increasing demand from a growing population. The population of 3°x3° area of the Lake Mead region increased by more than 1 million (as derived from the Gridded Population of the World Version 3 (GPWv3) data) between 2000 and 2015 (Center for International Earth Science Information Network - CIESIN - Columbia University, 2015). Recurring drought in the Colorado basin, in the last 15 years is taxing the system, not only on the surface but in the subsurface storage (Lindsey, 2015). This has led to a sharp fall in the water mass since 2012, as observed by GRACE (Figure 8.7, left).

Lake Mead volume is mainly driven by net runoff from the Colorado River (Figure 7.3). Monthly derivative of Lake Mead volume estimated by the CSSME method (Figure 7.3), demonstrated a very good correspondence with the monthly derivative of in-situ reservoir volume measurements (0.86 correlation and 0.18 km^3 RMSE) and with the net flux (0.8 correlation and 0.2 km^3 RMSE). Each of the three independent reservoir volume estimation methods discussed in this study (ABV, LBV, and ALVV) demonstrated above 0.98 correlation, having maximum RMSE (0.53 km^3) for ALVV (Figure 6.4) with the in-situ observations. The study area of the Lake Mead region (90,000 km^2) is relatively small for the GRACE analysis, leading to signal dampening. Longuevergne et al. (2013) emphasized that the GRACE signal is underestimated for point masses when the basin area is smaller than 300,000 km^2. Nevertheless, the mascon solutions showed an excellent correspondence with the Storage-2 (0.87 correlation and 2.3 km^3 RMSE) discussed in Paper-4 and shown in Figure 8.7 (left), but it needs to be cautiously interpreted, considering the uncertainties in the estimates.

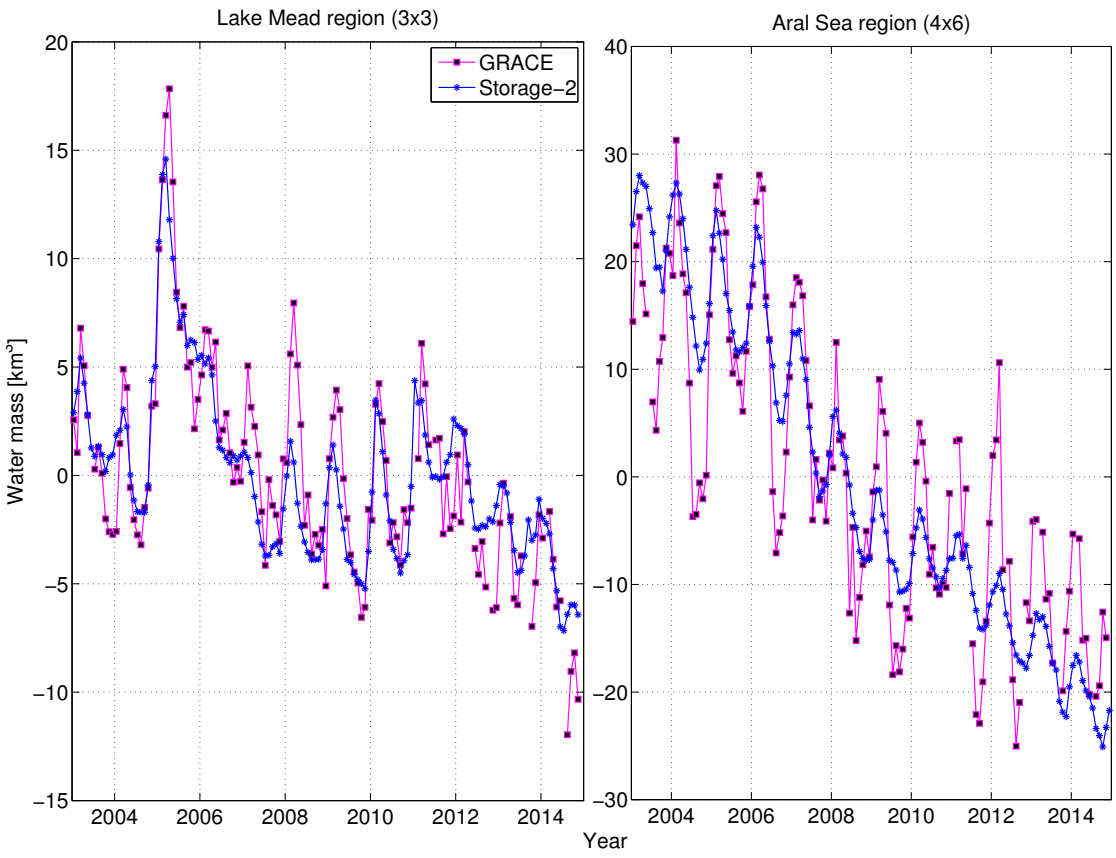

Figure 8.7 Mascon GRACE TWS compared to the estimated hybrid storage (Storage-2)

8.2.2 Aral Sea

The Aral Sea lost two-thirds of its water-surface-area within the study period, with the complete disappearance of its large shallow eastern lobe. In 2002 (at the beginning of the study period), the Aral Sea was divided into two parts, the small North Aral Sea and the big South Aral Sea (Figure 3.2, right). The big South Aral Sea within a year split into a deep and elongated West Aral Sea and the shallow East Aral Sea. The East Aral Sea changes its size frequently; it reached a minimum size in 2009, but heavy runoff in 2010 from the Amu Darya and the Syr Darya delayed its inevitable complete desiccation until 2014.

Unlike Lake Mead, the Aral Sea volume estimations cannot be validated because of the lack of ground observations. Furthermore, the volume estimation methods have higher uncertainties due to inaccurate bathymetry (more than half a century old) and complicated spectral reflectance, affecting the remote sensing based observations (discussed in Section 3.1.4 and Section 0). Nevertheless, the estimated volumes (LBV and ABV) have good correspondence with each other, for each of the sub-basin of the Aral Sea (discussed in Section 6.2). The East Aral Sea observed maximum difference between the two estimates (13% NRMSE (2.4 km^3

RMSE) and a correlation coefficient of 0.92), because of maximum uncertainties in the remote sensing based observations for this region, while the deep West Aral Sea estimations have a correlation coefficients of 0.97 and 4.5% NRMSE (1.6 km^3 RMSE) between LBV and ABV. Further, the 1960s bathymetry of the Aral Sea has been updated for its Eastern lobe by integrating the continuously shrinking contour lines up to the bottom of the East Aral Sea (Figure 6.5).

In order to validate the huge mass variations occurring in the Aral Sea, the SH (Paper-1) and mascon (Paper-4) GRACE solutions are explored. Section 8.1.3 discussed the contamination of the SH GRACE solution from the Caspian Sea. The mascon GRACE solution showed an excellent correspondence with the hybrid storages (Storage-1 and Storage-2 discussed in Paper-4) (~0.88 correlation and ~7 km^3 RMSE) because the lake is the major contributor (0.82 correlation and 7.8 km^3 RMSE) of the inter-annual signal in the Aral Sea region (Figure 8.7, right). High RMSE in hybrid storage (~7 km^3) corresponds to the underestimation of volume from SM by the hydrological models and the role of surface water storage in the delta regions and several small lakes. Nevertheless, the seasonal amplitude of mascon GRACE solution is also uncertain because of the unknown constraints applied in the mascon estimations and the selection of the size and location of the study box. Furthermore, errors and uncertainties are larger for small regions compared to larger-scale spatial averages.

9 Conclusion

The study is aimed towards the investigation of lake/reservoir monitoring methods using multiple sensors and models. It analyzed the water state of the two water bodies at two different locations by using global data. Thus the proposed method can be extended to other lakes/reservoirs.

9.1 Research questions

How to monitor geometric and gravimetric changes of a lake/reservoir from space missions.

In order to explore a lake's geometry, this study has demonstrated remote sensing based water height and water surface area determination methods. To derive continuous water-height time series, multi-mission satellite altimetry has been explored. The study demonstrated a good agreement between Jason-1, Jason-2, and Envisat for the Aral Sea water height measurements (Figure 4.1). The topography of the surroundings, the location of the altimetry track, and the size of the lake/reservoir defines the reliability of the altimetry measurements. Furthermore, for an inland water bodies the applied corrections and waveform retracking algorithms also play a significant role (discussed in Section 3.2). For example, for the Aral Sea, a difference of 50-70 cm water height is noticed by changing the ocean waveform retracker to an improved threshold waveform retracker (Hwang et al., 2006) (Figure 8.3). Nevertheless, observations from multiple altimetry missions with dedicated inland-water waveform-retracking algorithms tremendously improved the ability to investigate hydrological processes within a region.

In order to obtain a time series of lake/reservoir water surface area, multi-mission Landsat images are combined. The study demonstrates that compared to other Landsat bands, the NIR spectral band has a better ability to cluster water (deep and shallow) and non-water (moist surface/very shallow water/land) pixels in a fuzzy saline region like the Aral Sea (discussed in Section 3.1.1). Classification of the land-water pixels in a highly saline and shallow region like the East Aral Sea is not trivial (discussed in Section 3.1.4). Further, correction of the diagonal stripings in the Landsat ETM+ SLC-off images due to data gaps, introduces additional uncertainties in the retrieved land-water mask. The derived land-water mask at a 30-meter spatial resolution provides a coastline and water surface area of the lake/reservoir for each epoch. This coastline time series, together with the satellite altimetry water-heights, provided the possibility to generate a three-dimensional geometrical structure (bathymetry) of the East Aral Sea (Figure 6.5).

GRACE can add another dimension to our understanding of the hydrology in a lake/reservoir region, if the variations in the lake/reservoir volume are significant enough for the sensitivity of GRACE. In order to derive ΔTWS based on the variations in the distance between the twin GRACE satellites caused by the underlying hydrological perturbations, many dedicated mathematical solutions have been evaluated by different scientists (e.g., Kusche, 2007; M. Schmidt et al., 2008; Watkins et al., 2015). In this study, we have applied two GRACE solutions: one based on global spherical harmonic basis functions (see Section 3.4.2) and another based on localizing basis functions (mascon, see Section 3.4.3). For small areas (like this study), localizing basis functions are significantly more reliable than the global SH solutions (Section 8.1.3). Nevertheless, the GRACE observed mass variations and the lake/reservoir geometry can be compared in terms of their inter-annual development to evaluate the role of the lake/reservoir in the mass change of the region. In this study, correlation between the lake/reservoir geometrical volume and the gravimetrical mass variations observed by the mascon GRACE solutions for the Aral Sea region is 0.82 and for the Lake Mead region is 0.60 (Figure 7.2).

How to compute lake/reservoir water volume from multiple geometrical space missions.

In order to determine the volume of a lake/reservoir, either of the two parameters from the given three dimensions (i.e., water height, water surface area and bathymetry) needs to be combined. For regions with no ground observations, an entirely remote sensing based approach of estimating volumetric variations from an inverted pyramid model (ALVV) can be applied (Equation 11). In Paper-3, a new method of water height estimation from the water mask-bathymetry intersection by a selection of a subsection of the water boundary (SRB) has been proposed. The selection criteria are based on the geography of the region: First, a lower gradient section of the border should be selected to obtain less height variation within each 30 meter pixel. Second, a relatively stable section should be chosen, one that is not under a direct flow of water, to uphold the concept of an equipotential surface. The extracted water height from the SRB undergo box plot outlier rejection, and the mean of the remaining pixels is considered as the water height of that epoch.

The uncertainties in the determination of the lake/reservoir volume are highly depended on the water height estimations in all the three methods. It is difficult to conduct uncertainty quantification of the derived height/volume because different sources may introduce significantly different error characteristics. Possible sources of uncertainties in Landsat-derived height starts from the instrumental error in acquiring DN of the captured scene, its

preprocessing, classification (Section 3.1.4), post classification manipulations (Section 8.1.1), and the estimation of water height by SRB (Section 6.2). Similarly, altimetry-derived height has possible uncertainties from instrumental errors, captured waveform, applied geophysical corrections (Equation 2), and errors from the respective models (Section 3.2) and waveform retracking algorithms (Section 0). The two absolute water volume time series have an additional uncertainty from the integrated bathymetry.

As an example, for the given regions, the methodological uncertainty in the DAHITI altimetry-derived water height is less than 30 cm and Landsat-derived water height by SRB method provided a big range of uncertainty (0.5-3 m), depending upon the topography of the lake/reservoirs. Nevertheless, for Lake Mead, both methods showed excellent agreement (99% correlation and 0.2% NRMSE) with the in-situ observations, with the RMSE of 59 cm for the Landsat-SRB water height and 67 cm in the altimetry water height. However, similar validation is not possible for the Aral Sea because of the lack of in-situ data. Therefore, they are cross-validated and an excellent correlation is obtained between water heights observed by the two methods (altimetry and Landsat-SRB) (Figure 6.2) for all sub-basins. The West Aral Sea has a correlation coefficient of 0.97 (r^2 of 0.94), the East Aral Sea has 0.90 (r^2 of 0.82) and the North Aral Sea showed 0.56 correlation (r^2 of 0.32), with NRMSE less than 1.5% (less than 50 cm RMSE) for all the sub-basins. The estimated water heights are intersected by the digital bathymetry of the lake/reservoir to produce two absolute volume estimates as altimetry-bathymetry volume (ABV) and Landsat-bathymetry volume (LBV). The estimated volumetric variations from the three methods, i.e., ABV, LBV, and ALVV, agreed well for both study areas (Figure 6.3).

How to combine different volume estimates to derive the most reliable and continuous surface-water-volume time-series.

Three independent lake/reservoir volume estimation methods are suggested in the previous section. According to the availability of the datasets, the combination of these methods can be used to generate a continuous long-term lake/reservoir water volume time-series. During the study period, there were a few months when no altimetry observations were available for Lake Mead due to inter-mission gap between the Envisat and Saral/Altika missions. Similarly, for the Aral Sea, due to the shrinking of the lake, no altimetry track passes were available through the remnant water body of the East Aral Sea. Likewise, Landsat also has had no reliable images for few months, possibly due to storms, clouds or acquisition error. In such cases, a combination of the two estimation volumes (ABV and LBV) can provide uninterrupted reliable lake/reservoir volume estimate. The study demonstrated an application of the Kalman filter

based state space model (SSM) (Figure 6.3) for combining the two volumes. It can be used not only for data assimilation and missing data modifications but also for the near-future forecast. Due to the unavailability of observation errors, a random error is initialized, which is recursively minimized by SSM based on posterior error covariance and assuming Gaussian error distribution (Durbin and Koopman, 2012). Despite all the given uncertainties, for Lake Mead, the estimated CSSME volume has an excellent correlation of 0.98 (r^2 of 0.97) and 1.8% NRMSE (0.35 km^3 RMSE) with in-situ observations. The results show that the lake/reservoir can be effectively monitored using remote sensing data, even with inaccurate bathymetry.

Assessment of the hydrological state of lake/reservoir-dominated regions from a joint analysis of geometrical and gravimetrical information.

In order to interpret the integrated gravimetrical signals observed by GRACE in the lake/reservoir dominated regions, multi-sensor Earth observation data, and hydrological model outputs are applied. The GRACE signal includes mass variations from the lake/reservoir, other hydrological compartments, and leakage from the adjoining area. The study compares net storages (SM, SWE, and SW), net fluxes (P, ET, and R), and the ΔTWS by GRACE to assess the hydrological state of the lake/reservoir dominated regions. The results demonstrate that due to higher uncertainties in the vertical hydrological fluxes, the hybrid storage approach of combining remote sensing-based reservoir volume estimates with the hydrological model outputs, provides a better possibility for the estimation of total storage, and showed a better agreement with the GRACE ΔTWS (Figure 7.2). The study shows that even though Lake Mead is a very small reservoir for the GRACE resolution when the magnitude of mass change is significant (either in the reservoir or in its surroundings), GRACE is sufficiently sensitive to observe it. In contrast, the Aral Sea is a big lake and acts as a main driving force for the inter-annual mass signal of GRACE in the region. However, the lake is located close to the Caspian Sea, and hydrological variations in this adjoining bigger water mass have a significant impact on the global SH GRACE solutions. Therefore, a local mascon GRACE solution is examined for this region, which demonstrated better agreement with the estimated hybrid storage (0.88 correlation, Figure 8.7).

The study shows that the difference between mass variations estimated by the SH and the mascon GRACE solutions are larger for a smaller region due to signal leakage, in the case of the SH solutions (Figure 8.5). The Section 3.4.2 and 8.1.3 discussed the impact of de-striping algorithms of SH solutions, which can not only remove some real geophysical signals but also alter the shape, size, and orientation of the signal based on the surrounding mass variations. Therefore, GRACE-derived water mass variations need to be cautiously applied and evaluated,

especially for a small study box. Nevertheless, the study shows that regional GRACE solutions (like mascon) can resolve finer mass changes (even as small as Lake Mead) and can help to better interpret local hydrological variations (especially for the cases like the Aral Sea which has stong surrounding signals). Furthermore, for poorly monitored regions such as the Aral Sea, where reliable data availability is limited, accurate estimation of lake/reservoir storage and combined analysis with the GRACE-based mass change can significantly improve our understanding of the hydrological state of the region.

9.2 Summary and outlook

The aforementioned multi-sensor methods for lake/reservoir volume and hybrid-storage estimations can be seen as a promising approach for the analysis of hydrological processes in a lake/reservoir dominated region. Depending on the availability of data, any of the given methods (ABV, LBV, ALVV and CSSME) can be selected to produce dynamic estimates of lake/reservoir volume, which is particularly advantageous for remotely located and/or ungauged/poorly-gauged lakes/reservoirs. However, the size of the study area in both test sites is small for the GRACE resolution. Further, the hybrid-storage approach of combining hydrological model outputs with the estimated lake/reservoir volume can be used to interpret the hydrological dynamics of the lake/reservoir dominated region. Nevertheless, accurately closing the water budget is still an open problem. Further, critical evaluation and interpretation of the GRACE signal and the estimated volumes are mandatory, considering the uncertainties in the estimation of different parameters.

In the past few decades, observational heritage of terrestrial hydrology has evolved with unprecedented data availability, and expertise in modeling and data assimilation. This study explored the possibility of remote sensing-based monitoring of the hydrological state of lake/reservoir dominated regions, at a smaller scale. However, there are many open questions and possibilities for the improvement of the current methodology. Some of the remaining challenges and perspectives for future work are highlighted below:

- Smaller water bodies that are not traceable by altimetry can be estimated by the intersection of extrapolated DEM and Landsat water mask, in order to obtain total SW storage in a region. For example, in this study, many small lakes and delta water storage are not estimated, which added to the underestimation of the seasonal signal in the Aral Sea region (discussed in 4.3 of Paper-4)
- During winter months, because of the ice-sheet and snow, the land-water boundaries are hard to distinguish by optical sensors. Thermal-data has poor resolution, but a fused

dataset with a high-resolution optical data can be a solution. Many researchers have demonstrated the potential of fused images (Ghassemian, 2016; Ha et al., 2012; Jong-Hyun Park et al., 1999)

- Other regional GRACE solutions or improved filter design like DDK, wavelet, etc., can be tested in the Aral Sea region. The contamination of the Aral Sea SH-GRACE solutions by the signals from the big Caspian Sea water mass, needs a critical leakage correction.
- Most of the hydrological models consider a lake/reservoir area as stationary. The variations in the water surface area not only affect the availability of water for evaporation but also the estimation of SM. Variability of SM is more in the region immediately adjacent to the lake/reservoir than in areas further away. Combining remote sensing based products with the accurate lakes/reservoirs estimate and GRACE ΔTWS at a basin scale can significantly improve hydrological model storage approximation.
- The study can be extended to a basin scale by using additional remote sensing based data for SM (like SMAP, SMOS, etc.), SWE (like AMSRE, etc.) and ET (like MODIS, Meteosat, etc.). The increase in the extent of a study region to a basin scale will increase the possibilities of adding many satellite missions and reduce the uncertainties of the GRACE signal. However, it will also introduce new problems/uncertainties through additional data. Nevertheless, advancements in sensor capabilities with the emerging missions/datasets will tremendously increase the application and performance of the hydrological estimations. For example, the Surface Water and Ocean Topography (SWOT) mission is expected to launch in 2020. It will improve our capability for water volume estimation from lakes/reservoirs and wetlands, making it possible to estimate runoff more accurately. The GRACE Follow-on mission is scheduled to launch by August 2017 (Flechtner et al., 2014), and future improved GRACE missions are under design (Famiglietti and Rodell, 2013). The GRACE-FO will have laser interferometer with more accurate inter-satellite distance estimation.

Recommendations for the water management in the study areas.

- The Aral Sea has lost its big eastern lobe within the study period. However, subsequent seasonal refilling from the Amu Darya may bring the East Aral Sea back for few months, but it is not sustainable considering the vast shallow open water evaporation loss. Micklin (2010) also emphasized that it would be better to channelize the Amu Darya runoff directly into the West Aral Sea. Further, an increase in river discharge is possible

by addressing technical flaws of infiltration and evaporation loss from the drainage system.

- In both study regions, switching to less water-intensive crops can help in reducing the water crises. For example, de Beurs et al. (2015) observed some increase in vegetation index and decline in ET in the south of the Aral Sea with a change in crop type, from cotton to wheat.
- A water source fails at one end but has effects thousands of kilometers away (Subramanian et al., 2014; Vörösmarty et al., 2010). Therefore, long-term transboundary cooperation within the entire drainage network is needed to re-evaluate the changing climatic and geophysical conditions.
- Developing a dedicated remote sensing data-based terrestrial hydrological measurement framework to map and monitor water resources can be especially useful in poorly gauged and/or remotely located regions. However, the uncertainties of different datasets and models/approaches must be taken into consideration.

"As far as the laws of mathematics refer to reality, they are not certain; and as far as they are certain, they do not refer to reality."

— Albert Einstein

References

Abelen, S., Seitz, F., 2013. Relating satellite gravimetry data to global soil moisture products via data harmonization and correlation analysis. Remote Sens. Environ. 136, 89–98. doi:10.1016/j.rse.2013.04.012

Abelen, S., Seitz, F., Abarca-del-Rio, R., Güntner, A., 2015. Droughts and Floods in the La Plata Basin in Soil Moisture Data and GRACE. Remote Sens. 7, 7324–7349. doi:10.3390/rs70607324

Abileah, R., Vignudelli, S., Scozzari, A., 2011. A completely remote sensing approach to monitoring reservoirs water volume. Int. Water Technol. J. 1, 59–72.

Ahmad, A., Sufahani, S.F., 2012. Analysis of Landsat 5 TM data of Malaysian land covers using ISODATA clustering technique, in: 2012 IEEE Asia-Pacific Conference on Applied Electromagnetics (APACE). Presented at the 2012 IEEE Asia-Pacific Conference on Applied Electromagnetics (APACE), pp. 92–97. doi:10.1109/APACE.2012.6457639

Alsdorf, D.E., Rodríguez, E., Lettenmaier, D.P., 2007. Measuring surface water from space. Rev. Geophys. 45, RG2002. doi:10.1029/2006RG000197

Awange, J.L., Anyah, R., Agola, N., Forootan, E., Omondi, P., 2013. Potential impacts of climate and environmental change on the stored water of Lake Victoria Basin and economic implications. Water Resour. Res. 49, 8160–8173. doi:10.1002/2013WR014350

Awange, J.L., Forootan, E., Fleming, K., Odhiambo, G., 2014. Dominant Patterns of Water Storage Changes in the Nile Basin During 2003–2013, in: Lakshmi, V., Alsdorf, D., Anderson, rtha, Biancamaria, S., Cosh, M., Entin, J., Huffman, G., Kustas, W., Oevelen, P. van, Painter, T., Parajka, J., Rodell, tthew, Rüdiger, C. (Eds.), Remote Sensing of the Terrestrial Water Cycle. John Wiley & Sons, Inc, pp. 367–381. ISBN: 978-1-118-87208-6

Awange, J.L., Forootan, E., Kusche, J., Kiema, J.B.K., Omondi, P.A., Heck, B., Fleming, K., Ohanya, S.O., Gonçalves, R.M., 2013. Understanding the decline of water storage across the Ramser-Lake Naivasha using satellite-based methods. Adv. Water Resour. 60, 7–23. doi:10.1016/j.advwatres.2013.07.002

Awange, J.L., Sharifi, M.A., Ogonda, G., Wickert, J., Grafarend, E.W., Omulo, M.A., 2008. The Falling Lake Victoria Water Level: GRACE, TRIMM and CHAMP Satellite Analysis of the Lake Basin. Water Resour. Manag. 22, 775–796. doi:10.1007/s11269-007-9191-y

Barnett, T.P., Pierce, D.W., 2008. When will Lake Mead go dry? Water Resour. Res. 44, W03201. doi:10.1029/2007WR006704

Baup, F., Frappart, F., Maubant, J., 2014. Combining high-resolution satellite images and altimetry to estimate the volume of small lakes. Hydrol. Earth Syst. Sci. 18, 2007–2020. doi:10.5194/hess-18-2007-2014

Becker, M., LLovel, W., Cazenave, A., Güntner, A., Crétaux, J.-F., 2010. Recent hydrological behavior of the East African great lakes region inferred from GRACE, satellite altimetry and rainfall observations. Comptes Rendus Geosci. 342, 223–233. doi:10.1016/j.crte.2009.12.010

Beigt, D., Cuadrado, D.G., Piccolo, M.C., 2011. Study of the surface water circulation in San Blas channel (Argentina) using landsat imagery. Braz. J. Oceanogr. 59, 241–252. doi:10.1590/S1679-87592011000300004

Birkett, C., Reynolds, C., Beckley, B., Doorn, B., 2011. From Research to Operations: The USDA Global Reservoir and Lake Monitor, in: Vignudelli, S., Kostianoy, A.G., Cipollini, P., Benveniste, J. (Eds.), Coastal Altimetry. Springer Berlin Heidelberg,

Berlin, Heidelberg, pp. 19–50.
Birkett, C.M., 1995. The contribution of TOPEX/POSEIDON to the global monitoring of climatically sensitive lakes. J. Geophys. Res. Oceans 100, 25179–25204. doi:10.1029/95JC02125
Blunden, J., Arndt, D.S., 2013. State of the Climate in 2012. Bull. Am. Meteorol. Soc. 94, S1–S258. doi:10.1175/2013BAMSStateoftheClimate.1
Boergens, E., Dettmering, D., Schwatke, C., Seitz, F., 2016. Treating the Hooking Effect in Satellite Altimetry Data: A Case Study along the Mekong River and Its Tributaries. Remote Sens. 8, 91. doi:10.3390/rs8020091
Bortnik, V.N., Chistyaeva, S.P., 1990. Hydrometeorology and Hydrochemistry of the USSR Seas. Aral Sea Leningr. Gidrometeoizdat VII, 196.
Bosch, W., Dettmering, D., Schwatke, C., 2014. Multi-Mission Cross-Calibration of Satellite Altimeters: Constructing a Long-Term Data Record for Global and Regional Sea Level Change Studies. Remote Sens. 6, 2255–2281. doi:10.3390/rs6032255
Buma, W.G., Lee, S.-I., Seo, J.Y., 2016. Hydrological Evaluation of Lake Chad Basin Using Space Borne and Hydrological Model Observations. Water 8, 205. doi:10.3390/w8050205
Carroll, M.L., Townshend, J.R., DiMiceli, C.M., Noojipady, P., Sohlberg, R.A., 2009. A new global raster water mask at 250 m resolution. Int. J. Digit. Earth 2, 291–308. doi:10.1080/17538940902951401
Castle, S.L., Thomas, B.F., Reager, J.T., Rodell, M., Swenson, S.C., Famiglietti, J.S., 2014. Groundwater depletion during drought threatens future water security of the Colorado River Basin. Geophys. Res. Lett. 41, 2014GL061055. doi:10.1002/2014GL061055
Cazenave, A., Bonnefond, P., Dominh, K., Schaeffer, P., 1997. Caspian sea level from Topex-Poseidon altimetry: Level now falling. Geophys. Res. Lett. 24, 881–884. doi:10.1029/97GL00809
Center for International Earth Science Information Network - CIESIN - Columbia University, 2015. Gridded Population of the World, Version 4 (GPWv4): Population Count.
Chao, B.F., Wu, Y.H., Li, Y.S., 2008. Impact of artificial reservoir water impoundment on global sea level. Science 320, 212–214. doi:10.1126/science.1154580
Chen, H., Tong, S.T.Y., Yang, H., Yang, Y.J., 2015. Simulating the hydrologic impacts of land-cover and climate changes in a semi-arid watershed. Hydrol. Sci. J. 60, 1739–1758. doi:10.1080/02626667.2014.948445
Cheng, M., Ries, J.C., Tapley, B.D., 2011. Variations of the Earth's figure axis from satellite laser ranging and GRACE. J. Geophys. Res. Solid Earth 116, B01409. doi:10.1029/2010JB000850
Chuvieco, E., Huete, A., 2010. Fundamentals of satellite remote sensing. Taylor & Francis, Boca Raton, FL.
Crétaux, J.-F., Abarca-del-Río, R., Bergé-Nguyen, M., Arsen, A., Drolon, V., Clos, G., Maisongrande, P., 2016. Lake Volume Monitoring from Space. Surv. Geophys. 1–37. doi:10.1007/s10712-016-9362-6
Crétaux, J.-F., Jelinski, W., Calmant, S., Kouraev, A., Vuglinski, V., Bergé-Nguyen, M., Gennero, M.-C., Nino, F., Abarca Del Rio, R., Cazenave, A., Maisongrande, P., 2011. SOLS: A lake database to monitor in the Near Real Time water level and storage variations from remote sensing data. Adv. Space Res. 47, 1497–1507. doi:10.1016/j.asr.2011.01.004
Cretaux, J.-F., Kouraev, A., Berge-Nguyen, M., Cazenave, A., Papa, F., 2005. Satellite Altimetry for Monitoring Lake Level Changes, in: Vogtmann, H., Dobretsov, N. (Eds.), Transboundary Water Resources: Strategies for Regional Security and Ecological Stability, NATO Science Series. Springer Netherlands, pp. 141–146.
Das, T., Pierce, D.W., Cayan, D.R., Vano, J.A., Lettenmaier, D.P., 2011. The importance of

warm season warming to western U.S. streamflow changes. Geophys. Res. Lett. 38, L23403. doi:10.1029/2011GL049660

de Beurs, K.M., Henebry, G.M., Owsley, B.C., Sokolik, I., 2015. Using multiple remote sensing perspectives to identify and attribute land surface dynamics in Central Asia 2001–2013. Remote Sens. Environ. 170, 48–61. doi:10.1016/j.rse.2015.08.018

Dettmering, D., Schwatke, C., Boergens, E., Seitz, F., 2016. Potential of ENVISAT Radar Altimetry for Water Level Monitoring in the Pantanal Wetland. Remote Sens. 8, 596. doi:10.3390/rs8070596

Devaraju, B., 2015. Understanding filtering on the sphere: experiences from filtering GRACE data. Verlag der Bayerischen Akademie der Wissenschaften, München.

Dieng, H.B., Champollion, N., Cazenave, A., Wada, Y., Schrama, E., Meyssignac, B., 2015. Total land water storage change over 2003–2013 estimated from a global mass budget approach. Environ. Res. Lett. 10, 124010. doi:10.1088/1748-9326/10/12/124010

Dodson, J., Betts, A.V.G., Amirov, S.S., Yagodin, V.N., 2015. The nature of fluctuating lakes in the southern Amu-dar'ya delta. Palaeogeogr. Palaeoclimatol. Palaeoecol. 437, 63–73. doi:10.1016/j.palaeo.2015.06.026

Döll, P., Hoffmann-Dobrev, H., Portmann, F.T., Siebert, S., Eicker, A., Rodell, M., Strassberg, G., Scanlon, B.R., 2012. Impact of water withdrawals from groundwater and surface water on continental water storage variations. J. Geodyn. 59–60, 143–156. doi:10.1016/j.jog.2011.05.001

Döll, P., Kaspar, F., Lehner, B., 2003. A global hydrological model for deriving water availability indicators: model tuning and validation. J. Hydrol. 270, 105–134. doi:10.1016/S0022-1694(02)00283-4

Döll, P., Müller Schmied, H., Schuh, C., Portmann, F.T., Eicker, A., 2014. Global-scale assessment of groundwater depletion and related groundwater abstractions: Combining hydrological modeling with information from well observations and GRACE satellites. Water Resour. Res. 50, 5698–5720. doi:10.1002/2014WR015595

Duan, Z., Bastiaanssen, W.G.M., 2013. Estimating water volume variations in lakes and reservoirs from four operational satellite altimetry databases and satellite imagery data. Remote Sens. Environ. 134, 403–416. doi:10.1016/j.rse.2013.03.010

Durbin, J., Koopman, S.J., 2012. Time Series Analysis by State Space Methods: Second Edition. Oxford University Press.

Eicker, A., Schumacher, M., Kusche, J., Döll, P., Schmied, H.M., 2014. Calibration/Data Assimilation Approach for Integrating GRACE Data into the WaterGAP Global Hydrology Model (WGHM) Using an Ensemble Kalman Filter: First Results. Surv. Geophys. 35, 1285–1309. doi:10.1007/s10712-014-9309-8

Ek, M.B., Mitchell, K.E., Lin, Y., Rogers, E., Grunmann, P., Koren, V., Gayno, G., Tarpley, J.D., 2003. Implementation of Noah land surface model advances in the National Centers for Environmental Prediction operational mesoscale Eta model. J. Geophys. Res. Atmospheres 108, 8851. doi:10.1029/2002JD003296

ESA: LearnEO, 2016. URL http://www.learn-eo.org/rlib/img/altimetry_ssh_dt_780x585.png (accessed 9.19.16).

Famiglietti, J.S., Cazenave, A., Eicker, A., Reager, J.T., Rodell, M., Velicogna, I., 2015. Satellites provide the big picture. Science 349, 684–685. doi:10.1126/science.aac9238

Famiglietti, J.S., Lo, M., Ho, S.L., Bethune, J., Anderson, K.J., Syed, T.H., Swenson, S.C., de Linage, C.R., Rodell, M., 2011. Satellites measure recent rates of groundwater depletion in California's Central Valley. Geophys. Res. Lett. 38, L03403. doi:10.1029/2010GL046442

Famiglietti, J.S., Rodell, M., 2013. Water in the Balance. Science 340, 1300–1301. doi:10.1126/science.1236460

Feng, L., Hu, C., Chen, X., Cai, X., Tian, L., Gan, W., 2012. Assessment of inundation

changes of Poyang Lake using MODIS observations between 2000 and 2010. Remote Sens. Environ. 121, 80–92. doi:10.1016/j.rse.2012.01.014

Feng, M., Sexton, J.O., Channan, S., Townshend, J.R., 2015. A global, high-resolution (30-m) inland water body dataset for 2000: first results of a topographic–spectral classification algorithm. Int. J. Digit. Earth 1–21. doi:10.1080/17538947.2015.1026420

Fernandes, M.J., Lázaro, C., Nunes, A.L., Scharroo, R., 2014. Atmospheric Corrections for Altimetry Studies over Inland Water. Remote Sens. 6, 4952–4997. doi:10.3390/rs6064952

Ferreira, V.G., Gong, Z., He, X., Zhang, Y., Andam‐Akorful, S.A., 2013. Estimating Total Discharge in the Yangtze River Basin Using Satellite-Based Observations. Remote Sens. 5, 3415–3430. doi:10.3390/rs5073415

Flechtner, F., Sneeuw, N., Schuh, W.-D. (Eds.), 2014. Observation of the System Earth from Space - CHAMP, GRACE, GOCE and future missions, Advanced Technologies in Earth Sciences. Springer Berlin Heidelberg, Berlin, Heidelberg.

Forkutsa, I., Sommer, R., Shirokova, Y.I., Lamers, J.P.A., Kienzler, K., Tischbein, B., Martius, C., Vlek, P.L.G., 2009. Modeling irrigated cotton with shallow groundwater in the Aral Sea Basin of Uzbekistan: I. Water dynamics. Irrig. Sci. 27, 331–346. doi:10.1007/s00271-009-0148-1

Forootan, E., Kusche, J., 2012. Separation of global time-variable gravity signals into maximally independent components. J. Geod. 86, 477–497. doi:10.1007/s00190-011-0532-5

Forootan, E., Kusche, J., Loth, I., Schuh, W.-D., Eicker, A., Awange, J., Longuevergne, L., Diekkrüger, B., Schmidt, M., Shum, C.K., 2014. Multivariate Prediction of Total Water Storage Changes Over West Africa from Multi-Satellite Data. Surv. Geophys. 35, 913–940. doi:10.1007/s10712-014-9292-0

Forootan, E., Rietbroek, R., Kusche, J., Sharifi, M.A., Awange, J.L., Schmidt, M., Omondi, P., Famiglietti, J., 2014. Separation of large scale water storage patterns over Iran using GRACE, altimetry and hydrological data. Remote Sens. Environ. 140, 580–595. doi:10.1016/j.rse.2013.09.025

Förste, C., Bruinsma, S., Abrikosov, O., Flechtner, F., Marty, J.-C., Lemoine, J.-M., Dahle, C., Neumayer, H., Barthelmes, F., König, R., Biancale, R., 2014. EIGEN-6C4 - The latest combined global gravity field model including GOCE data up to degree and order 1949 of GFZ Potsdam and GRGS Toulouse. Presented at the EGU General Assembly Conference Abstracts, p. 3707.

Frappart, F., Minh, K.D., L'Hermitte, J., Cazenave, A., Ramillien, G., Le Toan, T., Mognard-Campbell, N., 2006. Water volume change in the lower Mekong from satellite altimetry and imagery data. Geophys. J. Int. 167, 570–584. doi:10.1111/j.1365-246X.2006.03184.x

Frappart, F., Papa, F., Güntner, A., Werth, S., Santos da Silva, J., Tomasella, J., Seyler, F., Prigent, C., Rossow, W.B., Calmant, S., Bonnet, M.-P., 2011. Satellite-based estimates of groundwater storage variations in large drainage basins with extensive floodplains. Remote Sens. Environ. 115, 1588–1594. doi:10.1016/j.rse.2011.02.003

Frappart, F., Seyler, F., Martinez, J.-M., León, J.G., Cazenave, A., 2005. Floodplain water storage in the Negro River basin estimated from microwave remote sensing of inundation area and water levels. Remote Sens. Environ. 99, 387–399. doi:10.1016/j.rse.2005.08.016

Fu, L.-L., Cazenave, A., 2000. Satellite Altimetry and Earth Sciences: A Handbook of Techniques and Applications. Academic Press.

Fuller, R.M., Hall, J.R.B., Groom, G.B., Parr, T.W., 1994. The Land Cover Map of Great

Britain and its applications. Annu. Rep. Inst. Terr. Ecol. 1993, 89–95.
Gan, T.Y., Zunic, F., Kuo, C.-C., Strobl, T., 2012. Flood mapping of Danube River at Romania using single and multi-date ERS2-SAR images. Int. J. Appl. Earth Obs. Geoinformation 18, 69–81. doi:10.1016/j.jag.2012.01.012
Gao, B., 1996. NDWI—A normalized difference water index for remote sensing of vegetation liquid water from space. Remote Sens. Environ. 58, 257–266. doi:10.1016/S0034-4257(96)00067-3
Gao, H., 2015. Satellite remote sensing of large lakes and reservoirs: from elevation and area to storage. Wiley Interdiscip. Rev. Water 2, 147–157. doi:10.1002/wat2.1065
Gao, H., Birkett, C., Lettenmaier, D.P., 2012. Global monitoring of large reservoir storage from satellite remote sensing. Water Resour. Res. 48, W09504. doi:10.1029/2012WR012063
Gao, Y., Vano, J.A., Zhu, C., Lettenmaier, D.P., 2011. Evaluating climate change over the Colorado River basin using regional climate models. J. Geophys. Res. Atmospheres 116, D13104. doi:10.1029/2010JD015278
Gardner, A.S., Moholdt, G., Cogley, J.G., Wouters, B., Arendt, A.A., Wahr, J., Berthier, E., Hock, R., Pfeffer, W.T., Kaser, G., Ligtenberg, S.R.M., Bolch, T., Sharp, M.J., Hagen, J.O., Broeke, M.R. van den, Paul, F., 2013. A Reconciled Estimate of Glacier Contributions to Sea Level Rise: 2003 to 2009. Science 340, 852–857. doi:10.1126/science.1234532
Ghassemian, H., 2016. A review of remote sensing image fusion methods. Inf. Fusion 32, Part A, 75–89. doi:10.1016/j.inffus.2016.03.003
Gleick, P.H., 1993. Water in Crisis: Chapter 2 (Oxford University Press) 1993. Oxford UniversityPress, New York.
Goodwin, L.D., Leech, N.L., 2006. Understanding Correlation: Factors That Affect the Size of r. J. Exp. Educ. 74, 249–266. doi:10.3200/JEXE.74.3.249-266
Goward, S.N., Williams, D.L., 1997. Landsat and earth systems science: development of terrestrial monitoring. Photogramm. Eng. Remote Sens. 63, 887–900.
Grippa, M., Kergoat, L., Frappart, F., Araud, Q., Boone, A., de Rosnay, P., Lemoine, J.-M., Gascoin, S., Balsamo, G., Ottlé, C., Decharme, B., Saux-Picart, S., Ramillien, G., 2011. Land water storage variability over West Africa estimated by Gravity Recovery and Climate Experiment (GRACE) and land surface models. Water Resour. Res. 47, W05549. doi:10.1029/2009WR008856
Güntner, A., 2008. Improvement of Global Hydrological Models Using GRACE Data. Surv. Geophys. 29, 375–397. doi:10.1007/s10712-008-9038-y
Ha, W., Gowda, P.H., Howell, T.A., 2012. A review of potential image fusion methods for remote sensing-based irrigation management: part II. Irrig. Sci. 31, 851–869. doi:10.1007/s00271-012-0340-6
Heiskanen, W.A., Moritz, H., 1967. Physical Geodesy. W H Freeman Co San Franc. doi:10.1017/S0016756800048834
Houborg, R., Rodell, M., Li, B., Reichle, R., Zaitchik, B.F., 2012. Drought indicators based on model-assimilated Gravity Recovery and Climate Experiment (GRACE) terrestrial water storage observations. Water Resour. Res. 48, W07525. doi:10.1029/2011WR011291
Huang, J., Halpenny, J., 2007. Estimating variation of groundwater storage within the Great Lakes Water Basin from GRACE, soil moisture and lake levels. Presented at the Joint International GSTM and DFG SPP Symposium, GFZ Postdam, Germany. URL http://mt.dgfi.tum.de/typo3_mt/fileadmin/20071015-17-Potsdam/di_0830_08_huang.pdf (accessed 09.01.2016).
Hung, M. -C., Wu, Y. -H., 2005. Mapping and visualizing the Great Salt Lake landscape

dynamics using multi-temporal satellite images, 1972–1996. Int. J. Remote Sens. 26, 1815–1834. doi:10.1080/0143116042000298324

Hwang, C., Guo, J., Deng, X., Hsu, H.-Y., Liu, Y., 2006. Coastal Gravity Anomalies from Retracked Geosat/GM Altimetry: Improvement, Limitation and the Role of Airborne Gravity Data. J. Geod. 80, 204–216. doi:10.1007/s00190-006-0052-x

Introduction to Remote Sensing, 2010. URL http://www.seos-project.eu/modules/remotesensing/remotesensing-c01-p05.html (accessed 11.6.10).

Issanova, G., Abuduwaili, J., Galayeva, O., Semenov, O., Bazarbayeva, T., 2015. Aeolian transportation of sand and dust in the Aral Sea region. Int. J. Environ. Sci. Technol. 12, 3213–3224. doi:10.1007/s13762-015-0753-x

Ivins, E.R., James, T.S., Wahr, J., O. Schrama, E.J., Landerer, F.W., Simon, K.M., 2013. Antarctic contribution to sea level rise observed by GRACE with improved GIA correction. J. Geophys. Res. Solid Earth 118, 3126–3141. doi:10.1002/jgrb.50208

Jain, S.K., Singh, R.D., Jain, M.K., Lohani, A.K., 2005. Delineation of Flood-Prone Areas Using Remote Sensing Techniques. Water Resour. Manag. 19, 333–347. doi:10.1007/s11269-005-3281-5

Jekeli, C., 1981. Alternative methods to smooth the Earth's gravity field.

Jin, S., Feng, G., 2013. Large-scale variations of global groundwater from satellite gravimetry and hydrological models, 2002–2012. Glob. Planet. Change 106, 20–30. doi:10.1016/j.gloplacha.2013.02.008

Johnson, W., 2011. Correlation and explaining variance: To square or not to square? Intelligence 39, 249–254. doi:10.1016/j.intell.2011.07.001

Jong-Hyun Park, Wikantika, K., Tateishi, R., 1999. Comparison of four different methods to fuse multi-sensor and multi-resolution remotely sensed data for urban topographic mapping. IEEE, pp. 1203–1205. doi:10.1109/IGARSS.1999.774578

Joodaki, G., Wahr, J., Swenson, S., 2014. Estimating the human contribution to groundwater depletion in the Middle East, from GRACE data, land surface models, and well observations. Water Resour. Res. 50, 2679–2692. doi:10.1002/2013WR014633

Jung, H.C., Alsdorf, D., Moritz, M., Lee, H., Vassolo, S., 2011. Analysis of the relationship between flooding area and water height in the Logone floodplain. Phys. Chem. Earth Parts ABC, Recent Advances in Mapping and Modelling Flood Processes in Lowland Areas 36, 232–240. doi:10.1016/j.pce.2011.01.010

Karimov, A.K., Šimůnek, J., Hanjra, M.A., Avliyakulov, M., Forkutsa, I., 2014. Effects of the shallow water table on water use of winter wheat and ecosystem health: Implications for unlocking the potential of groundwater in the Fergana Valley (Central Asia). Agric. Water Manag. 131, 57–69. doi:10.1016/j.agwat.2013.09.010

Khan, H.H., Khan, A., Ahmed, S., Gennero, M.-C., Minh, K.D., Cazenave, A., 2013. Terrestrial water dynamics in the lower Ganges—estimates from ENVISAT and GRACE. Arab. J. Geosci. 6, 3693–3702. doi:10.1007/s12517-012-0629-z

Klees, R., Revtova, E.A., Gunter, B.C., Ditmar, P., Oudman, E., Winsemius, H.C., Savenije, H.H.G., 2008. The design of an optimal filter for monthly GRACE gravity models. Geophys. J. Int. 175, 417–432. doi:10.1111/j.1365-246X.2008.03922.x

Klein, I., Dietz, A.J., Gessner, U., Galayeva, A., Myrzakhmetov, A., Kuenzer, C., 2014. Evaluation of seasonal water body extents in Central Asia over the past 27 years derived from medium-resolution remote sensing data. Int. J. Appl. Earth Obs. Geoinformation 26, 335–349. doi:10.1016/j.jag.2013.08.004

Kravtsova, V.I., Tarasenko, T.V., 2010. Space monitoring of Aral Sea degradation. Water Resour. 37, 285–296. doi:10.1134/S0097807810030036

Kusche, J., 2007. Approximate decorrelation and non-isotropic smoothing of time-variable GRACE-type gravity field models. J. Geod. 81, 733–749. doi:10.1007/s00190-007-0143-3

Kusche, J., Klemann, V., Bosch, W., 2012. Mass distribution and mass transport in the Earth system. J. Geodyn., Mass Transport and Mass Distribution in the System Earth 59–60, 1–8. doi:10.1016/j.jog.2012.03.003

Landerer, F.W., Dickey, J.O., Guntner, A., 2010. Terrestrial water budget of the Eurasian pan-Arctic from GRACE satellite measurements during 2003–2009. J. Geophys. Res. Atmospheres 115, D23115. doi:10.1029/2010JD014584

Landerer, F.W., Swenson, S.C., 2012. Accuracy of scaled GRACE terrestrial water storage estimates. Water Resour. Res. 48, W04531. doi:10.1029/2011WR011453

Lehner, B., Döll, P., 2004. Development and validation of a global database of lakes, reservoirs and wetlands. J. Hydrol. 296, 1–22. doi:10.1016/j.jhydrol.2004.03.028

Lettenmaier, D.P., Milly, P.C.D., 2009. Land waters and sea level. Nat. Geosci. 2, 452–454. doi:10.1038/ngeo567

Leuliette, E., Willis, J., 2011. Balancing the Sea Level Budget. Oceanography 24, 122–129. doi:10.5670/oceanog.2011.32

Leuliette, E.W., Miller, L., 2009. Closing the sea level rise budget with altimetry, Argo, and GRACE. Geophys. Res. Lett. 36, L04608. doi:10.1029/2008GL036010

Liao, A., Chen, L., Chen, J., He, C., Cao, X., Chen, J., Peng, S., Sun, F., Gong, P., 2014. High-resolution remote sensing mapping of global land water. Sci. China Earth Sci. 57, 2305–2316. doi:10.1007/s11430-014-4918-0

Lillesand, T.M., Kiefer, R.W., Chipman, J.W., 2015. Remote sensing and image interpretation, Seventh edition. ed. John Wiley & Sons, Inc, Hoboken, N.J.

Lindsey, R., 2016. World of Change: Water Level in Lake Powell : Feature Articles.URL http://earthobservatory.nasa.gov/Features/WorldOfChange/lake_powell.php (accessed 7.19.16).

Llovel, W., Becker, M., Cazenave, A., Crétaux, J.-F., Ramillien, G., 2010. Global land water storage change from GRACE over 2002–2009; Inference on sea level. Comptes Rendus Geosci. 342, 179–188. doi:10.1016/j.crte.2009.12.004

Long, D., Scanlon, B.R., Longuevergne, L., Sun, A.Y., Fernando, D.N., Save, H., 2013. GRACE satellite monitoring of large depletion in water storage in response to the 2011 drought in Texas. Geophys. Res. Lett. 40, 3395–3401. doi:10.1002/grl.50655

Long, D., Yang, Y., Wada, Y., Hong, Y., Liang, W., Chen, Y., Yong, B., Hou, A., Wei, J., Chen, L., 2015. Deriving scaling factors using a global hydrological model to restore GRACE total water storage changes for China's Yangtze River Basin. Remote Sens. Environ. 168, 177–193. doi:10.1016/j.rse.2015.07.003

Longuevergne, L., Wilson, C.R., Scanlon, B.R., Crétaux, J.F., 2013. GRACE water storage estimates for the Middle East and other regions with significant reservoir and lake storage. Hydrol Earth Syst Sci 17, 4817–4830. doi:10.5194/hess-17-4817-2013

Lorenz, C., Kunstmann, H., Devaraju, B., Tourian, M.J., Sneeuw, N., Riegger, J., 2014. Large-Scale Runoff from Landmasses: A Global Assessment of the Closure of the Hydrological and Atmospheric Water Balances*. J. Hydrometeorol. 15, 2111–2139.

McFEETERS, S.K., 1996. The use of the Normalized Difference Water Index (NDWI) in the delineation of open water features. Int. J. Remote Sens. 17, 1425–1432. doi:10.1080/01431169608948714

Medina, C., Gomez-Enri, J., Alonso, J.J., Villares, P., 2010. Water volume variations in Lake Izabal (Guatemala) from in situ measurements and ENVISAT Radar Altimeter (RA-2) and Advanced Synthetic Aperture Radar (ASAR) data products. J. Hydrol. 382, 34–48. doi:10.1016/j.jhydrol.2009.12.016

Medina, C.E., Gomez-Enri, J., Alonso, J.J., Villares, P., 2008. Water level fluctuations derived from ENVISAT Radar Altimeter (RA-2) and in-situ measurements in a subtropical waterbody: Lake Izabal (Guatemala). Remote Sens. Environ. 112, 3604–3617. doi:10.1016/j.rse.2008.05.001

Micklin, P., 2010. The past, present, and future Aral Sea. Lakes Reserv. Res. Manag. 15, 193–213. doi:10.1111/j.1440-1770.2010.00437.x

Mirador - Goddard Earth Sciences (GES) Data and Information Center (DISC), 2016. URL http://mirador.gsfc.nasa.gov./ (accessed 4.28.16).

Mulder, G., Olsthoorn, T.N., Al-Manmi, D.A.M.A., Schrama, E.J.O., Smidt, E.H., 2015. Identifying water mass depletion in northern Iraq observed by GRACE. Hydrol Earth Syst Sci 19, 1487–1500. doi:10.5194/hess-19-1487-2015

Müller Schmied, H., Eisner, S., Franz, D., Wattenbach, M., Portmann, F.T., Flörke, M., Döll, P., 2014. Sensitivity of simulated global-scale freshwater fluxes and storages to input data, hydrological model structure, human water use and calibration. Hydrol Earth Syst Sci 18, 3511–3538. doi:10.5194/hess-18-3511-2014

NASA, 2016. URL http://earthobservatory.nasa.gov/Features/Water/images/water_cycle.jpg (accessed 9.19.16).

Nicholson, S.E., 1998. Historical Fluctuations of Lake Victoria and Other Lakes in the Northern Rift Valley of East Africa, in: Lehman, J.T. (Ed.), Environmental Change and Response in East African Lakes, Monographiae Biologicae. Springer Netherlands, pp. 7–35. doi:10.1007/978-94-017-1437-2_2

Odindi, J., Mhangara, P., Kakembo, V., 2012. Remote sensing land-cover change in Port Elizabeth during South Africa's democratic transition. South Afr. J. Sci. 108. doi:10.4102/sajs.v108i5/6.886

Pachauri, R.K., Mayer, L., Intergovernmental Panel on Climate Change (Eds.), 2015. Climate change 2014: synthesis report. Intergovernmental Panel on Climate Change IPCC, Geneva, Switzerland.

Papa, F., Prigent, C., Durand, F., Rossow, W.B., 2006. Wetland dynamics using a suite of satellite observations: A case study of application and evaluation for the Indian Subcontinent. Geophys. Res. Lett. 33. doi:10.1029/2006GL025767

Pietroniro, A., Prowse, T., Peters, D.L., 1999. Hydrologic assessment of an inland freshwater delta using multi-temporal satellite remote sensing. Hydrol. Process. 13, 2483–2498. doi:10.1002/(SICI)1099-1085(199911)13:16<2483::AID-HYP934>3.0.CO;2-9

Proulx, R.A., Knudson, M.D., Kirilenko, A., VanLooy, J.A., Zhang, X., 2013. Significance of surface water in the terrestrial water budget: A case study in the Prairie Coteau using GRACE, GLDAS, Landsat, and groundwater well data. Water Resour. Res. 49, 5756–5764. doi:10.1002/wrcr.20455

Ramillien, G., Frappart, F., Cazenave, A., Guntner, A., 2005. Time variations of land water storage from an inversion of 2 years of GRACE geoids. Earth Planet. Sci. Lett. 235, 283–301. doi:10.1016/j.epsl.2005.04.005

Ramillien, G., Frappart, F., Güntner, A., Ngo-Duc, T., Cazenave, A., Laval, K., 2006. Time variations of the regional evapotranspiration rate from Gravity Recovery and Climate Experiment (GRACE) satellite gravimetry. Water Resour. Res. 42, W10403. doi:10.1029/2005WR004331

Ramillien, G., Frappart, F., Seoane, L., 2014. Application of the Regional Water Mass Variations from GRACE Satellite Gravimetry to Large-Scale Water Management in Africa. Remote Sens. 6, 7379–7405. doi:10.3390/rs6087379

Reager, J.T., Famiglietti, J.S., 2009. Global terrestrial water storage capacity and flood potential using GRACE. Geophys. Res. Lett. 36, L23402. doi:10.1029/2009GL040826

Reager, J.T., Thomas, B.F., Famiglietti, J.S., 2014. River basin flood potential inferred using GRACE gravity observations at several months lead time. Nat. Geosci. doi:10.1038/ngeo2203

Richey, A.S., Thomas, B.F., Lo, M.-H., Famiglietti, J.S., Swenson, S., Rodell, M., 2015a. Uncertainty in global groundwater storage estimates in a Total Groundwater Stress framework. Water Resour. Res. 51, 5198–5216. doi:10.1002/2015WR017351

Richey, A.S., Thomas, B.F., Lo, M.-H., Reager, J.T., Famiglietti, J.S., Voss, K., Swenson, S., Rodell, M., 2015b. Quantifying renewable groundwater stress with GRACE. Water Resour. Res. 51, 5217–5238. doi:10.1002/2015WR017349

Ričko, M., Birkett, C.M., Carton, J.A., Crétaux, J.-F., 2012. Intercomparison and validation of continental water level products derived from satellite radar altimetry. J. Appl. Remote Sens. 6, 061710–061710. doi:10.1117/1.JRS.6.061710

Rieser, D., Kuhn, M., Pail, R., Anjasmara, I.M., Awange, J., 2010. Relation between GRACE-derived surface mass variations and precipitation over Australia. Aust. J. Earth Sci. 57, 887–900. doi:10.1080/08120099.2010.512645

Roach, J.K., Griffith, B., Verbyla, D., 2012. Comparison of three methods for long-term monitoring of boreal lake area using Landsat TM and ETM+ imagery. Can. J. Remote Sens. 38, 427–440. doi:10.5589/m12-035

Rodell, M., 2016. LDAS | Land Data Assimilation Systems. URL http://ldas.gsfc.nasa.gov/gldas/GLDASforcing.php (accessed 8.29.16).

Rodell, M., Chen, J., Kato, H., Famiglietti, J.S., Nigro, J., Wilson, C.R., 2006. Estimating groundwater storage changes in the Mississippi River basin (USA) using GRACE. Hydrogeol. J. 15, 159–166. doi:10.1007/s10040-006-0103-7

Rodell, M., Houser, P.R., Jambor, U., Gottschalck, J., Mitchell, K., Meng, C.-J., Arsenault, K., Cosgrove, B., Radakovich, J., Bosilovich, M., Entin*, J.K., Walker, J.P., Lohmann, D., Toll, D., 2004. The Global Land Data Assimilation System. Bull. Am. Meteorol. Soc. 85, 381–394. doi:10.1175/BAMS-85-3-381

Rodell, M., Velicogna, I., Famiglietti, J.S., 2009. Satellite-based estimates of groundwater depletion in India. Nature 460, 999–1002. doi:10.1038/nature08238

Rodgers, J.L., Nicewander, W.A., 1988. Thirteen Ways to Look at the Correlation Coefficient. Am. Stat. 42, 59. doi:10.2307/2685263

Rosenberg, E.A., Clark, E.A., Steinemann, A.C., Lettenmaier, D.P., 2013. On the contribution of groundwater storage to interannual streamflow anomalies in the Colorado River basin. Hydrol Earth Syst Sci 17, 1475–1491. doi:10.5194/hess-17-1475-2013

Rundquist, D.C., Lawson, M.P., Queen, L.P., Cerveny, R.S., 1987. The Relationship Between Summer-Season Rainfall Events and Lake-Surface Area1. JAWRA J. Am. Water Resour. Assoc. 23, 493–508. doi:10.1111/j.1752-1688.1987.tb00828.x

Scanlon, B.R., Longuevergne, L., Long, D., 2012. Ground referencing GRACE satellite estimates of groundwater storage changes in the California Central Valley, USA. Water Resour. Res. 48, W04520. doi:10.1029/2011WR011312

Scanlon, B.R., Zhang, Z., Reedy, R.C., Pool, D.R., Save, H., Long, D., Chen, J., Wolock, D.M., Conway, B.D., Winester, D., 2015. Hydrologic implications of GRACE satellite data in the Colorado River Basin. Water Resour. Res. n/a-n/a. doi:10.1002/2015WR018090

Schlaffer, S., Chini, M., Dettmering, D., Wagner, W., 2016. Mapping Wetlands in Zambia Using Seasonal Backscatter Signatures Derived from ENVISAT ASAR Time Series. Remote Sens. 8, 402. doi:10.3390/rs8050402

Schmeer, M., Schmidt, M., Bosch, W., Seitz, F., 2012. Separation of mass signals within GRACE monthly gravity field models by means of empirical orthogonal functions. J. Geodyn., Mass Transport and Mass Distribution in the System Earth 59–60, 124–132. doi:10.1016/j.jog.2012.03.001

Schmidt, M., Seitz, F., Shum, C.K., 2008. Regional four-dimensional hydrological mass variations from GRACE, atmospheric flux convergence, and river gauge data. J. Geophys. Res. Solid Earth 113, B10402. doi:10.1029/2008JB005575

Schmidt, R., Petrovic, S., Güntner, A., Barthelmes, F., Wünsch, J., Kusche, J., 2008. Periodic components of water storage changes from GRACE and global hydrology models. J. Geophys. Res. Solid Earth 113, B08419. doi:10.1029/2007JB005363

Schwatke, C., Dettmering, D., Bosch, W., Seitz, F., 2015. DAHITI – an innovative approach for estimating water level time series over inland waters using multi-mission satellite altimetry. Hydrol Earth Syst Sci 19, 4345–4364. doi:10.5194/hess-19-4345-2015

Seager, R., Vecchi, G.A., 2010. Greenhouse warming and the 21st century hydroclimate of southwestern North America. Proc. Natl. Acad. Sci. 107, 21277–21282. doi:10.1073/pnas.0910856107

Sethre, P.R., Rundquist, B.C., Todhunter, P.E., 2005. Remote Detection of Prairie Pothole Ponds in the Devils Lake Basin, North Dakota. GIScience Remote Sens. 42, 277–296. doi:10.2747/1548-1603.42.4.277

Shepherd, A., Ivins, E.R., A, G., Barletta, V.R., Bentley, M.J., Bettadpur, S., Briggs, K.H., Bromwich, D.H., Forsberg, R., Galin, N., Horwath, M., Jacobs, S., Joughin, I., King, M.A., Lenaerts, J.T.M., Li, J., Ligtenberg, S.R.M., Luckman, A., Luthcke, S.B., McMillan, M., Meister, R., Milne, G., Mouginot, J., Muir, A., Nicolas, J.P., Paden, J., Payne, A.J., Pritchard, H., Rignot, E., Rott, H., Sørensen, L.S., Scambos, T.A., Scheuchl, B., Schrama, E.J.O., Smith, B., Sundal, A.V., Angelen, J.H. van, Berg, W.J. van de, Broeke, M.R. van den, Vaughan, D.G., Velicogna, I., Wahr, J., Whitehouse, P.L., Wingham, D.J., Yi, D., Young, D., Zwally, H.J., 2012. A Reconciled Estimate of Ice-Sheet Mass Balance. Science 338, 1183–1189. doi:10.1126/science.1228102

Shiklomanov, A.I., Lammers, R.B., Vörösmarty, C.J., 2002. Widespread decline in hydrological monitoring threatens Pan-Arctic Research. Eos Trans. Am. Geophys. Union 83, 13. doi:10.1029/2002EO000007

Singh, A., Seitz, F., 2015. Updated bathymetric chart of the East Aral Sea. URL http://doi.pangaea.de/10.1594/PANGAEA.855779 (accessed 12.21.15).

SLC-off Products: Background, 2010. URL http://landsat.usgs.gov/products_slcoffbackground.php (accessed 11.1.10).

Smith, L.C., Pavelsky, T.M., 2009. Remote sensing of volumetric storage changes in lakes. Earth Surf. Process. Landf. 34, 1353–1358. doi:10.1002/esp.1822

Song, C., Huang, B., Ke, L., Richards, K.S., 2014. Seasonal and abrupt changes in the water level of closed lakes on the Tibetan Plateau and implications for climate impacts. J. Hydrol. 514, 131–144. doi:10.1016/j.jhydrol.2014.04.018

Sproles, E.A., Leibowitz, S.G., Reager, J.T., Wigington, P.J., Famiglietti, J.S., Patil, S.D., 2015. GRACE storage-runoff hystereses reveal the dynamics of regional watersheds. Hydrol. Earth Syst. Sci. 19, 3253–3272. doi:10.5194/hess-19-3253-2015

Subramanian, A., Brown, B., Wolf, A.T., 2014. Understanding and overcoming risks to cooperation along transboundary rivers. Water Policy 16, 824. doi:10.2166/wp.2014.010

Swenson, S., 2009. Assessing High-Latitude Winter Precipitation from Global Precipitation Analyses Using GRACE. J. Hydrometeorol. 11, 405–420. doi:10.1175/2009JHM1194.1

Swenson, S., Chambers, D., Wahr, J., 2008. Estimating geocenter variations from a combination of GRACE and ocean model output. J. Geophys. Res. Solid Earth 113, B08410. doi:10.1029/2007JB005338

Swenson, S., Wahr, J., 2009. Monitoring the water balance of Lake Victoria, East Africa, from space. J. Hydrol. 370, 163–176. doi:10.1016/j.jhydrol.2009.03.008

Swenson, S., Wahr, J., 2007. Multi-sensor analysis of water storage variations of the Caspian Sea. Geophys. Res. Lett. 34, L16401. doi:10.1029/2007GL030733

Swenson, S., Wahr, J., Milly, P.C.D., 2003. Estimated accuracies of regional water storage variations inferred from the Gravity Recovery and Climate Experiment (GRACE). Water Resour. Res. 39, 1223. doi:10.1029/2002WR001808

Tangdamrongsub, N., Steele-Dunne, S.C., Gunter, B.C., Ditmar, P.G., Weerts, A.H., 2015. Data assimilation of GRACE terrestrial water storage estimates into a regional

hydrological model of the Rhine River basin. Hydrol Earth Syst Sci 19, 2079–2100. doi:10.5194/hess-19-2079-2015

Thomas, A.C., Reager, J.T., Famiglietti, J.S., Rodell, M., 2014. A GRACE-based water storage deficit approach for hydrological drought characterization. Geophys. Res. Lett. 41, 2014GL059323. doi:10.1002/2014GL059323

Tiwari, V.M., Wahr, J., Swenson, S., 2009. Dwindling groundwater resources in northern India, from satellite gravity observations. Geophys. Res. Lett. 36. doi:10.1029/2009GL039401

Tourian, M.J., Elmi, O., Chen, Q., Devaraju, B., Roohi, S., Sneeuw, N., 2015. A spaceborne multisensor approach to monitor the desiccation of Lake Urmia in Iran. Remote Sens. Environ. 156, 349–360. doi:10.1016/j.rse.2014.10.006

Töyrä, J., Pietroniro, A., Martz, L.W., 2001. Multisensor Hydrologic Assessment of a Freshwater Wetland. Remote Sens. Environ. 75, 162–173. doi:10.1016/S0034-4257(00)00164-4

Ucuncuoglu, E., Arli, O., Eronat, A.H., 2006. Evaluating the impact of coastal land uses on water-clarity conditions from Landsat TM/ETM+ imagery: Candarli Bay, Aegean Sea. Int. J. Remote Sens. 27, 3627–3643. doi:10.1080/01431160500500326

Van Dijk, A., Renzullo, L.J., Rodell, M., 2011. Use of Gravity Recovery and Climate Experiment terrestrial water storage retrievals to evaluate model estimates by the Australian water resources assessment system. Water Resour. Res. 47.

Velicogna, I., Sutterley, T.C., van den Broeke, M.R., 2014. Regional acceleration in ice mass loss from Greenland and Antarctica using GRACE time-variable gravity data. Geophys. Res. Lett. 41, 8130–8137. doi:10.1002/2014GL061052

Verdin, J.P., 1996. Remote sensing of ephemeral water bodies in western Niger. Int. J. Remote Sens. 17, 733–748. doi:10.1080/01431169608949041

Verpoorter, C., Kutser, T., Seekell, D.A., Tranvik, L.J., 2014. A global inventory of lakes based on high-resolution satellite imagery. Geophys. Res. Lett. 41, 2014GL060641. doi:10.1002/2014GL060641

Vörösmarty, C.J., McIntyre, P.B., Gessner, M.O., Dudgeon, D., Prusevich, A., Green, P., Glidden, S., Bunn, S.E., Sullivan, C.A., Liermann, C.R., Davies, P.M., 2010. Global threats to human water security and river biodiversity. Nature 467, 555–561. doi:10.1038/nature09440

Voss, K.A., Famiglietti, J.S., Lo, M., de Linage, C., Rodell, M., Swenson, S.C., 2013. Groundwater depletion in the Middle East from GRACE with implications for transboundary water management in the Tigris-Euphrates-Western Iran region. Water Resour. Res. 49, 904–914. doi:10.1002/wrcr.20078

Wahr, J., Molenaar, M., Bryan, F., 1998. Time variability of the Earth's gravity field: Hydrological and oceanic effects and their possible detection using GRACE. J. Geophys. Res. Solid Earth 103, 30205–30229. doi:10.1029/98JB02844

Wahr, J., Swenson, S., Zlotnicki, V., Velicogna, I., 2004. Time-variable gravity from GRACE: First results. Geophys. Res. Lett. 31, L11501. doi:10.1029/2004GL019779

Wang, S., Huang, J., Li, J., Rivera, A., McKenney, D.W., Sheffield, J., 2014. Assessment of water budget for sixteen large drainage basins in Canada. J. Hydrol. 512, 1–15. doi:10.1016/j.jhydrol.2014.02.058

Wang, X., de Linage, C., Famiglietti, J., Zender, C.S., 2011. Gravity Recovery and Climate Experiment (GRACE) detection of water storage changes in the Three Gorges Reservoir of China and comparison with in situ measurements. Water Resour. Res. 47, W12502. doi:10.1029/2011WR010534

Watkins, M.M., Wiese, D.N., Yuan, D.-N., Boening, C., Landerer, F.W., 2015. Improved methods for observing Earth's time variable mass distribution with GRACE using spherical cap mascons. J. Geophys. Res. Solid Earth 120, 2014JB011547.

doi:10.1002/2014JB011547
Wiese, D.N., 2015. GRACE monthly land water mass grids netcdf release 5.0 | PO.DAAC. URL https://podaac.jpl.nasa.gov/dataset/TELLUS_LAND_NC_RL05 (accessed 3.31.16).
Willis, J.K., Chambers, D.P., Kuo, C.Y., Chum, C.K., 2010. Global sea level rise. Oceanography 23, 26–35.
Woodcock, C.E., Allen, R., Anderson, M., Belward, A., Bindschadler, R., Cohen, W., Gao, F., Goward, S.N., Helder, D., Helmer, E., Nemani, R., Oreopoulos, L., Schott, J., Thenkabail, P.S., Vermote, E.F., Vogelmann, J., Wulder, M.A., Wynne, R., 2008. Free Access to Landsat Imagery. Science 320, 1011a–1011a. doi:10.1126/science.320.5879.1011a
Wouters, B., Bamber, J.L., van den Broeke, M.R., Lenaerts, J.T.M., Sasgen, I., 2013. Limits in detecting acceleration of ice sheet mass loss due to climate variability. Nat. Geosci 6, 613–616.
Wouters, B., Schrama, E.J.O., 2007. Improved accuracy of GRACE gravity solutions through empirical orthogonal function filtering of spherical harmonics. Geophys. Res. Lett. 34, L23711. doi:10.1029/2007GL032098
Wulder, M.A., White, J.C., Masek, J.G., Dwyer, J., Roy, D.P., 2011. Continuity of Landsat observations: Short term considerations. Remote Sens. Environ. 115, 747–751. doi:10.1016/j.rse.2010.11.002
Xiao, R., He, X., Zhang, Y., Ferreira, V., Chang, L., 2015. Monitoring Groundwater Variations from Satellite Gravimetry and Hydrological Models: A Comparison with in-situ Measurements in the Mid-Atlantic Region of the United States. Remote Sens. 7, 686–703. doi:10.3390/rs70100686
Xu, H., 2006. Modification of normalised difference water index (NDWI) to enhance open water features in remotely sensed imagery. Int. J. Remote Sens. 27, 3025–3033. doi:10.1080/01431160600589179
Yi, H., Wen, L., 2016. Satellite gravity measurement monitoring terrestrial water storage change and drought in the continental United States. Sci. Rep. 6, 19909.
Zambresky, L., 1989. A verification study of the global WAM model December 1987 - November 1988. ECMWF, Shinfield Park, Reading.
Zavialov, P.O., 2005. Physical Oceanography of the Dying Aral Sea. Springer Science & Business Media.
Zhang, J., Xu, K., Yang, Y., Qi, L., Hayashi, S., Watanabe, M., 2006. Measuring Water Storage Fluctuations in Lake Dongting, China, by Topex/Poseidon Satellite Altimetry. Environ. Monit. Assess. 115, 23–37. doi:10.1007/s10661-006-5233-9

Acknowledgements

I could not have embarked upon this journey without the help and support of countless people over the years. Foremost, I would like to express my sincere gratitude to my Doktorvater, Prof. Florian Seitz, for his endless patience, guidance and invaluable support in writing of all the publications. Thank you for your continuous help, ignoring my mistakes and always being there, whenever I needed you. My sincere thanks to Prof. Andreas Güntner for his encouragements, insightful comments and fruitful discussions. I extend my thanks to Prof. Markus Disse and Prof. Uwe Stilla for their time and interest in reading and evaluating my dissertation.

I am truly fortunate to have had the opportunity to work with Sarah Abelen and Susanne Schnitzer. Be it professional, cultural or personal, I have wonderful memories of them. Thanks Sarah for your endless support, since my first day in Munich until the end of this journey.. Your thought provoking suggestions in every sphere of life are always inspirational and I cannot imagine Munich without you. Thanks Susanne for your genuinely good nature and being so friendly that I was able to reach out to you for almost everything.

I would like to express my deepest appreciation for the financial support granted through fellowships by Erasmus Mundus WILLPower fellowship, Women's Bureau of the TUM, German Research Foundation DFG and TUM International Center. I thank Prof. Annette Menzel, Prof. Florian Seitz, Dr. Karin Hedman and Mrs. Larissa Danschina from TUMexchange for helping me to obtain fellowships in TUM.

I would also like to express my gratitude to the International Graduate School of Science and Engineering (IGSSE) for providing me an opportunity to work in CLIVARHydro (Signals of Climate Variability in Continental Hydrology from Multi-Sensor Space and In-situ Observations and Hydrological Modeling) project. I thank the German Geodetic Research Institute (DGFI-TUM) and Institute for Astronomical and Physical Geodesy (IAPG) for providing me necessary infrastructure. Gratitude is extended to all my co-authors, who made this dissertation possible, namely, Prof. Florian Seitz, Christian Schwatke, Prof. Ujjwal Kumar, Prof. Annette Eicker, and Prof. Andreas Güntner. I would like to thank Eva, Wenjing, and Francessca for the lunchtime chitchats, Eren and Marcello for our intercultural discussions and all other DGFI colleagues for providing me a very congenial working environment.

I would like to express my appreciation to my Indian friends in Germany Vinaya, Rajaram, Aditya, Balaji, Jayani, Krinamurthy, Thushara, Pradeesh for all the fun time we have had in the last five-six years. Vinaya, the pious and homely ambience provided by you and your family,

always attracted us. Balaji, your spirit of adventure concerning research as well as nature have been always inspiring. Thanks for all your support in improving my understanding of GRACE and the awesome time we had together. Appreciation is also expressed to Catherine Champniers and Grace Frank for the English proofreading of the dissertation.

Finally, I would like to acknowledge the innumerable sacrifices made by my husband Amit, in shouldering a fair share of the parenting and household burdens while I pursued this final degree and taking me through all the difficulties as a highly supportive, deeply loving and supremely caring partner. Very special thanks to my little angel (Bhuvan), who always made my life more meaningful with her cute smile. I am highly grateful to my parents (Manju Devi and Avinash Singh) and Buaji (Prof. Bhuvan Chandel) for their blessings, believing in me and encouraging me at every step. Above all, my gratitude to all those forces, divine and natural that enabled me to complete this challenging task and for providing contacts with some of the most wonderful people ever.

APPENDIX: Publications

Paper-1

Singh, A.; Seitz, F.; Schwatke, C.: **Inter-annual water storage changes in the Aral Sea from multi-mission satellite altimetry, optical remote sensing, and GRACE satellite gravimetry**; Remote Sensing of Environment, Vol. 123, pp 187-195, Elsevier, ISSN 0034-4257, DOI: 10.1016/j.rse.2012.01.001, 2012.

Remote Sensing of Environment 123 (2012) 187–195

Contents lists available at SciVerse ScienceDirect

Remote Sensing of Environment

journal homepage: www.elsevier.com/locate/rse

Inter-annual water storage changes in the Aral Sea from multi-mission satellite altimetry, optical remote sensing, and GRACE satellite gravimetry

Alka Singh [a,*], Florian Seitz [a], Christian Schwatke [b]

[a] Earth Oriented Space Science and Technology (ESPACE), Technische Universität München, Arcisstr. 21, 80333 Munich, Germany
[b] Deutsches Geodätisches Forschungsinstitut, Alfons-Goppel-Str.11, 80539 Munich, Germany

ARTICLE INFO

Article history:
Received 12 August 2011
Received in revised form 6 January 2012
Accepted 8 January 2012
Available online 24 April 2012

Keywords:
Aral Sea
Satellite altimetry
Optical remote sensing
Satellite gravimetry
GRACE
Water mass variation

ABSTRACT

The estimation of water storage variations in lakes is essential for water resource management activities in a region. In areas of ungauged or poorly gauged water bodies, satellite altimetry acts as a powerful tool to measure changes in surface water level. Remote sensing provides images of temporal coastline variations, and a combination of both measurement techniques can indicate a change in water volume. In this study variations of the water level of the Aral Sea were computed for the period 2002–2011 from the combination of radar and laser satellite altimetry data sets over the lake. The estimated water levels were analyzed in combination with coastline changes from Landsat images in order to obtain a comprehensive picture of the lake water changes. In addition to these geometrical observations temporal changes of water storage in the lake and its surrounding were computed from GRACE satellite gravimetry. With respect to its temporal evolution the GRACE results agree very well with the geometrical changes determined from altimetry and Landsat. The advancing desiccation until the beginning of 2009 and a subsequent abrupt gain of water in 2009–2010 due to exceptional discharge from Amu Darya can clearly be identified in all data sets.

1. Introduction

Water stored in surface reservoirs (i.e. lakes and rivers) is the best accessible form for human consumption. But at the same time terrestrial surface water is one of the most uncertain components of continental hydrology with respect to its spatial and temporal distribution (Solomon et al., 2007). In this study we address the Aral Sea, a saline lake located in an arid zone of central Asia at 45° north and 60° east. Until 1960, it was the fourth largest lake worldwide after the Caspian Sea, Lake Superior and Lake Victoria (Zavialov, 2005). From then onwards it experienced a devastating decline, mainly due to diversion of water from its two primary inlet rivers the Amu Darya and the Syr Darya for agricultural purposes (Bortnik, 1999; Crétaux et al., 2005; Micklin, 1988).

Temporal variations of the level and the surface extent of the water body are linked to the changes in water storage and can be traced in observations of satellite altimetry and in optical or radar remote sensing images. Unfortunately for several years, availability of continuous in-situ water level observations has been limited in this region. A few gauge stations are located upstream, but due to evaporation and infiltration from canals, which were built on sand without sufficient sealing, an unknown fraction of water runoff may be lost in-between the observation point and the lake (Froebrich & Kayumov, 2004). Satellite altimetry was designed to measure oceanic surface water height but has demonstrated its potential for estimating changes in the level of terrestrial water bodies as well (Birkett, 1995; Cazenave et al., 1997; Getirana et al., 2009; Morris & Gill, 1994; Prigent et al., 2007) and has already been used on the Aral Sea (Calmant et al., 2009; Crétaux et al., 2005; Crétaux et al., 2008; Kouraev et al., 2008). MODIS Terra images (250 m spatial resolution) were used by Kravtsova (2005) to observe seasonal variations in the Aral Sea surface in spring and autumn for the period 2000–2004. Since the spatial extent of the affected region is large related changes of water mass can be identified in observations of temporal variations of the Earth's gravity field from space. The dedicated satellite mission GRACE has been continuously monitoring gravity field variations since almost a decade at a spatial resolution of about 300 km and a temporal resolution of better than one month. GRACE satellite gravity data was used in many studies to estimate terrestrial water storage changes (Güntner, 2008; Ramillien et al., 2005; Seitz et al., 2008; Werth et al., 2009). Large parts of the gravity signal (tides, atmosphere, and oceans) are already removed during pre-processing; consequently the remaining signals mainly reflect changes in water storage in the region.

In our study we compare the results of geometrical and gravimetrical space and in-situ observation techniques for the time frame between 2002 and 2011. The usefulness of the combination of heterogeneous data sets has previously been demonstrated for other surface water bodies, e.g. for the East African lakes (Becker et al., 2010), the Amazon (Frappart et al., 2008) or the Ganges (Papa et

* Corresponding author. Tel.: +49 8928923190.
E-mail address: alka.singh@bv.tum.de (A. Singh).

0034-4257/$ – see front matter © 2012 Elsevier Inc. All rights reserved.
doi:10.1016/j.rse.2012.01.001

al., 2008). In Section 2 variations of the water level in the Aral Sea and its sub basins from satellite altimetry will be presented and discussed. Section 3 outlines the geometrical variations of the lake surface from optical remote sensing images from Landsat. In Section 4 we present time series of water storage changes from GRACE satellite gravimetry. The temporal evolution of the mass changes with respect to the development of the lake geometry is discussed in Section 5, and conclusions from the work are provided in Section 6.

2. Changes in water level

The present appearance of the Aral Sea is not unique in its entire history. The paleo-variability of the Aral Sea was characterized by similar fluctuations in the past forced by natural climate changes. But in contrast, the continuous severe decline of the lake level that started in the 1960s is primarily caused by strong anthropogenic consumption (Boroffka et al., 2005; Zavialov, 2005). Fig. 1 shows a time series of the mean lake level in yearly intervals since 1780. Data between 1780 and 1960 (pre-desiccation time) has been collected by Rogov (1957), data between 1911 and 2006 has been published in the frame of the INTAS-0511 REBASOWS project (Nachtnebel et al., 2006).

The curve shows a decline of a few meters twice in the 19th century. During the first half of the 20th century the lake surface remained on a stable height. But since the beginning of the 1960s an immense decrease of the lake level due to the expansion of an irrigation project that drained out its two major tributaries can be observed (Micklin, 1988). In 1986 the lake was split into two parts: the smaller North Aral Sea and the larger South Aral Sea. The South Aral Sea continued its shallowing while the level of the North Aral Sea fluctuated with the construction, demolition and reconstruction of a dam between the two parts of the Aral Sea. In the 180 years between 1780 and 1960 the lake had experienced only fluctuations of smaller than 5 m. On the contrary it faced a decline of more than 25 m over the past 50 years.

In this study we focus on the quantitative changes of the Aral Sea from spring 2002 until autumn 2011. Water level changes were determined from radar altimetry measurements from Jason-1, Jason-1 extended mission (EM), Jason-2, Envisat, Envisat extended mission (EM) and GFO, complemented by laser altimetry measurements from Icesat (for details see Table 1). The radar altimeter satellites provide a significantly higher temporal resolution (10–35 days) than Icesat (91 days). On the other hand the laser altimeter Icesat provides more precise observations because of its smaller footprint (70–90 m) and higher frequency. Data were obtained from the Open Altimetry Data Base (OpenADB) of the German Geodetic Research Institute (DGFI) at http://openadb.dgfi.badw.de/.

Heights are provided with respect to the geoid EGM2008 (Pavlis et al., 2008). All observations were corrected for atmospheric delay and geophysical effects using calibration models and/or onboard measurements for ionosphere, dry troposphere, wet troposphere, and solid Earth tides (see Fu & Cazenave, 2001 for details). Model based ionospheric corrections were applied since corrections based on onboard radiometer data are not applicable over inland water bodies. All above mentioned missions except GFO are equipped with a dual frequency system (Ku and C band) from which respective corrections can be modeled. GFO observations were corrected by data from Global Ionosphere Maps (GIM; Schaer et al., 1996). Wet tropospheric corrections are based on ECMWF (European Centre for Medium-Range Weather Forecasts) data except for Jason 1 which was corrected by data from the JMR (Jason-1 Microwave Radiometer) following Brown (2010). An ultra stable oscillator range correction was applied to Envisat observations. Altimetry observations between December and March could be affected by errors due to ice cover, since the reflection of the signal on ice differs significantly from reflections on open water (Kouraev et al., 2008). To prevent a contamination of the measurements by reflections from land, only observation points with a distance of more than 5 km from the coast were considered. For this purpose twice a year in spring and autumn water masks generated from Landsat data were applied in order to account for the continuous changes of the coastline. As a consequence less reliable altimetry observations are available (Fig. 2) during periods when the horizontal extent of the lake is small.

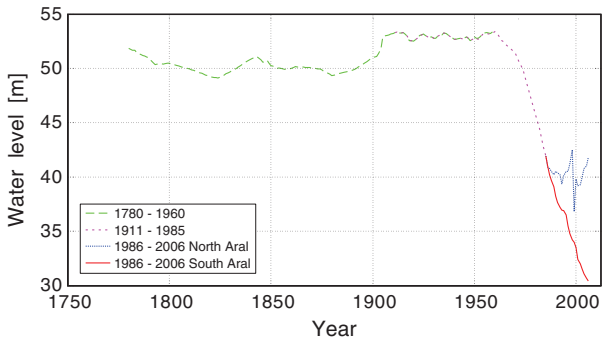

Fig. 1. Water level changes in the Aral Sea (1780–2006).

The east basin of the Aral Sea, for example, was observed in October 2009 by Icesat for the last time before the mission was retired in the same month. For almost half a year (November 2009–June 2010) no observations from the east basin are available, while it has been observed very well in earlier years by Envisat, GFO, Icesat and Jason1 (Figs. 2 and 3). After October 2010 Envisat–EM was capable of providing some measurements over that part of lake (Fig. 2, right), however due to problems of Envisat over ice-covered regions only few of these observations are reliable. The west basin is inadequately observed especially in its northern part mainly because fewer passes are available in this region (Envisat/Envisat EM and few Icesat observations) and furthermore the lake is so narrow that most of the data points are rejected due to the 5 km criteria. The southern part of the west basin was well observed by GFO, Envisat and Icesat until 2010, but afterwards only observations from Jason1–EM and very few reliable data points from Envisat–EM are available. In general all basins have been sparsely observed by altimetry for the last three years, firstly because fewer missions are available (i.e. only Jason2, Jason1–EM and few Envisat–EM observations) and secondly because of the smaller extent of the lake.

With these limitations, a multi-mission altimetry data combination provides maximum information on the development of the lake level. A best possible harmonization was reached between the different missions by selecting similar calibration models as far as feasible. An additional cross calibration of the range bias was applied by estimating a constant offset of each mission relative to the orbit of Topex/Posidon (Bosch & Savcenko, 2007). Inter and intra mission crossover analysis was done over the east and north basin where the passes of GFO, Icesat, Envisat and Jason1 are close enough to compare the calibrated data with respect to each other. A nominal ground track on geographically fixed segments was maintained by aggregating all observations within a 10 km radius to a mean value per cycle.

Fig. 3, shows the results of our multi-mission altimetry analysis for the different basins of the Aral Sea. Here we approximate the lake level of each basin as a flat surface, i.e. we do not distinguish between the various locations of the footprints within an individual basin. The observations show the picture of one of the worst environmental catastrophes by illustrating the drastic drop of the water level in the west and east basins. The observations of all missions agree very well to each other. Besides the trends all curves feature clear seasonal signals. Data from altimetry agree quite closely to annual in-situ observations from the previously mentioned INTAS-0511 REBASOWS project (Nachtnebel et al., 2006) and from observations collected during expeditions on the west basin (Zavialov, 2010). In-situ

Table 1
Altimetry data used in this study.

Satellite	Agency	R.r.a. (*) diameter	Revisit	Pass numbers	From	Until	Source
JASON-1	CNES, NASA	16 cm	10 days	142, 107, 218	January 2004	January 2009	http://sealevel.jpl.nasa.gov/missions/jason1/
JASON-2	CNES, NASA	16 cm	10 days	142, 107, 218	July 2008	August 2011	http://sealevel.jpl.nasa.gov/missions/ostmjason2/
JASON-1 extended mission	CNES, NASA	16 cm	10 days	107	February 2009	August 2011	http://sealevel.jpl.nasa.gov/newsroom/spotlights/index.cfm?FuseAction=ShowNews&NewsID=338
Envisat, RA2	ESA	20 cm	35 days	0126, 0211, 0797, 0253, 0711, 0167, 0670, 0625, 0584	January 2004	July 2010	http://envisat.esa.int/earth/www/object/index.cfm?fobjectid=3774
Envisat extended mission	ESA	20 cm	30 days	0139, 0369, 455, 0685, 0730, 0771	October 2010	July 2011	http://www.esa.int/esaCP/SEM08O1OWUF_index_0.html
GFO	US Navy	16 cm	17 days	253, 156, 339, 425	January 2004	September 2008	http://ibis.grdl.noaa.gov/SAT/gfo/bmpcoe/default.htm/
IceSAT	NASA	18 cm	91 days	2660, 0799, 0561, 0458, 0293, 0696, 0055, 0531, 0190	January 2004	October 2009	http://icesat.gsfc.nasa.gov/icesat/

(*) R.r.a. = retro reflector array.

observations are available until 2006 (North Aral Sea), 2007 (west basin) and 2009 (east basin) with one data point per year. Although an offset of about 50–70 cm exists between the altimetry missions and in-situ observations, they follow the same trend. The reason for the offset could be a difference in the reference systems since all altimetry measurements refer to EGM2008 while the in-situ observations refer to the mean seal level of the Baltic Sea. Furthermore, the in-situ water levels are given as one data point per year with (except for the west basin) no information about the time of acquisition.

The most drastic changes in water level were observed in the South Aral Sea, i.e. the east and west basin. The east basin suffered nearly 3.5 m decline in eight years (2002–2009) while the level of the west basin fell by about 4 m. The curve of the North Aral is significantly different due to the construction of the Dike Kokaral dam in October 2005. After its completion the water level increased by about two meters within only half a year. The inflow from the Syr Darya revived the North Aral and led to a rather stable water level since 2006 with fluctuations of less than 1 m. On the other hand the construction of the dam accelerated the desiccation in the other two basins from 2006 as the dam cut off the South Aral Sea from the tributary Syr Darya. Only in the case of overflow of the North Aral Sea water from this river is diverted into the southern basins. The east basin reached the stage of drying up of most of its area in 2009 (which led to the previously mentioned non-availability of reasonable altimetry data until the lake level started to rise again in 2010). Jason-2 observations indicate that the lake had regained more than 0.5 m by the last seven months of 2010 as a consequence of exceptionally strong inflow from the Amu Darya (see Section 5). This increase of the lake level was followed by the normal seasonal decline in summer 2011. A clear seasonal variability of the lake level due to season-dependent inflow and evaporation is obvious for all basins.

3. Changes in the lake surface area

Changes in the coastline of the Aral Sea and therewith of the horizontal lake extent were derived from Landsat multi-spectral remote sensing data (30 m spatial resolution) for a month in spring and autumn every year from 2002 to 2011. Due to the high computational effort of the data analysis we restricted ourselves to two snapshots per year. However, during periods of special interest (see Fig. 5 and Section 5) the coastline was also computed for some additional months in order to get a better insight into the temporal development of the lake extent. Precision and terrain corrected Landsat images were obtained from USGS Earth Explorer website (http://earthexplorer.usgs.gov). Three Landsat images were combined in order to cover the entire area of the Aral Sea. Due to the presence of clouds and data problems in the course of the image acquisition it was not always possible to obtain an image combination with all images acquired within one month. In such cases images of two subsequent months were taken into account (e.g. for the spring season images from April and March, or for the autumn season images from October and September) in order to produce a complete picture of the horizontal lake geometry.

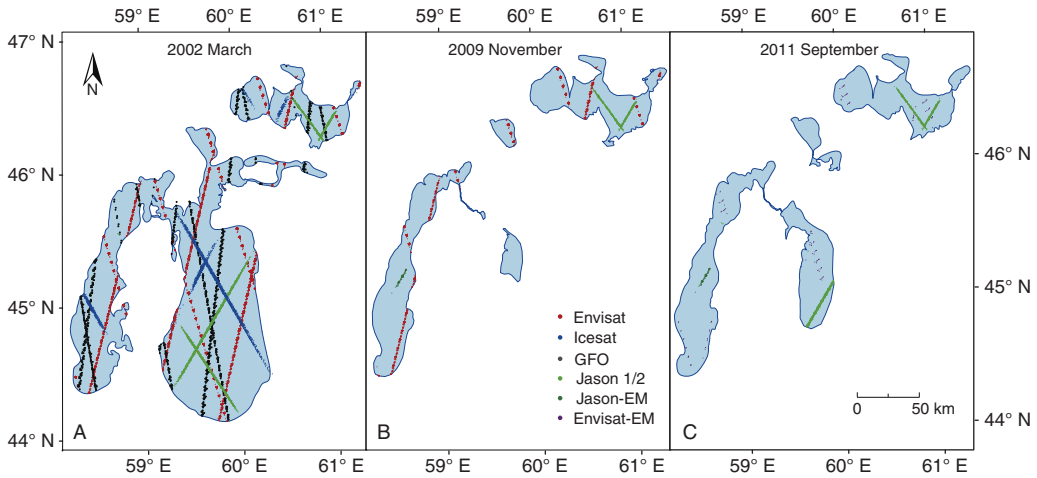

Fig. 2. Passes of different satellite altimetry missions over the Aral Sea in (A) March 2002, (B) November 2009 and (C) September 2011.

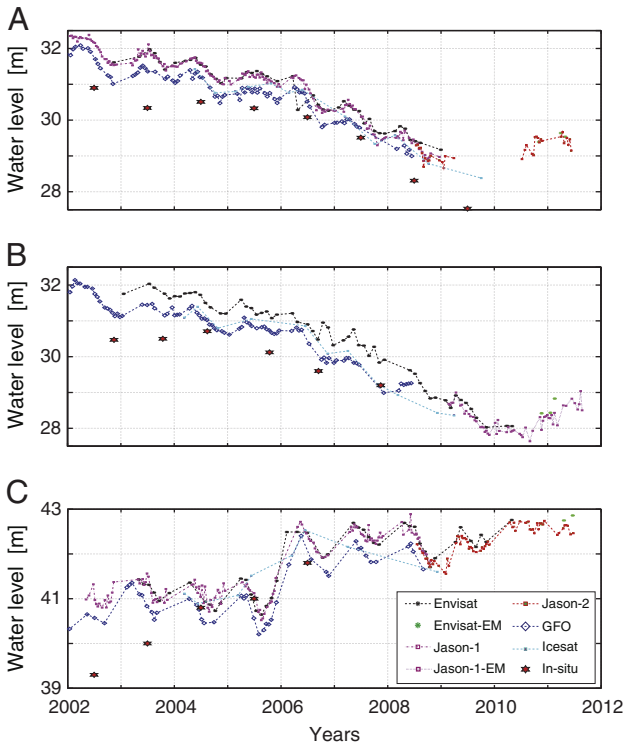

Fig. 3. Water level changes in the (A) east basin, (B) west basin and (C) North Aral Sea from multi-mission altimetry and in-situ observations.

Water absorption bands, i.e. short wave infra-red (SWIR), near infra-red (NIR) and middle infra-red (MIR) bands of Landsat images were stacked. The three Landsat images per date were mosaicked to a complete map of the Aral area. The mosaicked images were then classified with a maximum likelihood supervised classifier (MLC) to generate a water mask. The MLC was trained by the a priori knowledge of the spectral signature of water and non water classes. In the course of this training step the variance/covariance matrix of the training site classes is calculated. Based on Bayesian statistics the probability of a pixel belonging to the class is estimated. A pixel is assigned to the class which has the highest probability. Accuracy assessments of the classified images were done by a confusion/error matrix formed by reference data in columns and classified data in rows. In this study an original image was used in place of reference data, and pixels from stratified random sampling were verified visually. The producer accuracy for all classified images was found to be between 85 and 90%. This value indicates how well a certain area is classified. It is computed by dividing the number of pixels of the reference class that were correctly classified with the total number of pixels of that reference class. The classified image was then transformed into a boolean image in order to obtain the water mask.

A few Landsat images feature striping errors due to a failure of the scan line corrector (SLC) that led to a permanent data loss (http://landsat.usgs.gov/products_slc_off_data_information.php). In the used spectral bands (bands 3, 5 and 7) a SLC gap has a maximum width of 14 pixels. In order to avoid negative effects on the extracted water boundary by applying a destriping algorithm (e.g., a low pass convolution filter) we preferred to fill the scan gaps with data for the same location from the closest cycle. In most of the cases this substitution of data decreased the scan line gap to 2–3 pixels, which can be filled by simple low pass filter without a strong effect on the boundary lines. In few severe cases, when a close cycle was not available (e.g. due to clouds), the classified images have been digitized and edited manually to generate a polygon vector layer. The area under water was subsequently calculated from each of the generated seasonal masks. Fig. 4 shows the drastic changes in the extent of the Aral Sea during the analyzed period. Between spring 2002 and autumn 2009 a clear signal of desiccation is visible. This decline is followed by a significant increase of the lake extent reaching its maximum revived stage between autumn 2010 and spring 2011. This period is followed by substantial decline until the end of our data set.

During spring the area under water is generally larger due to substantial inflow of melt water from the tributaries of the lake (Kravtsova, 2005) and relatively low evaporation during the winter months. On the contrary, strong evaporation during the summer months and a cooling of the lake towards autumn lead to lower water levels in the second half of the year. Fig. 5 shows the temporal evolution of the lake surface area with respect to spring 2002 for the entire lake and separately for its sub-basins. The seasonal changes of the lake surface area are obvious in all curves.

In 2002 the Aral Sea consisted of two completely separated sub-basins, the North Aral Sea and the larger South Aral Sea. The latter was later divided into two parts (west and east basin), connected by a narrow channel. The shrinking rate of the Aral Sea is largest in the east basin, while a negative trend can also be seen for the west basin. The curve for the surface area of the North Aral Sea shows a stable geometry with normal seasonal variations after an increase due to the construction of the dam in 2005/2006. Thus it matches the characteristics of the corresponding curve of the lake level (Fig. 3). The west basin suffered comparatively little loss in area over the first eight years of our analysis (2002–2009), but it also does not show any significant increase in size in 2010 where the signal of re-flooding can clearly be observed in the east basin. This relative stability of the area of the west basin can be explained by its steeper coastline (Zavialov, 2005). Some inflow from ground water (Jarsjo, 2004) also compensates the water loss by evaporation to a certain extent. Overall, the east basin, being quite shallow (Roget et al., 2009), experienced the largest changes of coastline and surface area over the analyzed period. After the erection of the Dike Kokaral dam it was cut-off from its former tributary Syr Darya (see above). An especially rapid decrease of the surface area of the east basin was observed in 2006. This strong reduction of the lake size can be attributed to increased evaporation due to high temperature anomalies between 1 and 3 °C and very dry conditions in the region during this year

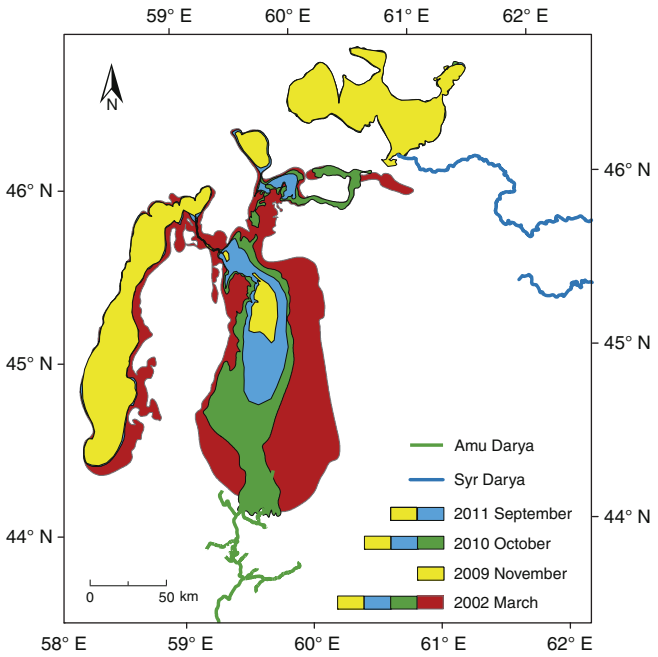

Fig. 4. Change of the Aral Sea surface area during the study period from Landsat images.

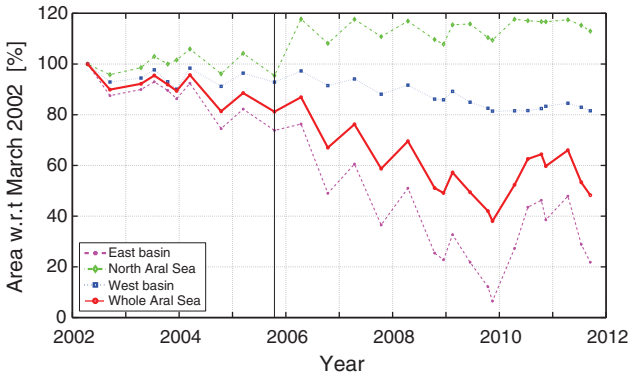

Fig. 5. Percentage change of the surface area of the Aral Sea and its basins with respect to March 2002. At this reference, the respective absolute values of the surface extent amounted to 20,370 km^2 (whole Aral Sea), 2850 km^2 (North Aral Sea), 4660 km^2 (west basin), and 12,860 km^2 (east basin). The vertical black line indicates the construction of the Dike Kokaral dam.

(Arguez, 2007) in combination with almost no water inflow from the Amu Darya in 2006 (see Fig. 8).

The Aral Sea as a whole suffered 62% area loss within eight years (spring 2002–autumn 2009), out of which the east basin contributes the largest fraction: With respect to its extent in spring 2002 only 6% were left in autumn 2009. With the shrinking of the lake salt crusts of up to 2–10 km width formed along the coast (Kravtsova & Tarasenko, 2010). The boundary of this moist salty surface changes its shape frequently, especially in the shallow east basin. Once the crust dries up it is eroded by strong winds that are prevalent in the region. As a consequence the topography of the land that has fallen dry changes quickly due to the salty dust storms. This explains why during the refilling in April 2010 the lake did not regain a similar same shape as it had before although it nearly reached the same surface area (52% of the area of spring 2002) as it had in autumn 2008 (Fig. 5).

4. Mass changes in the region of the Aral Sea observed from by GRACE

Ongoing changes of sea surface area and height are associated with strong variations of water mass being stored in the individual basins. These storage changes map into satellite-based observations of temporal variations of the Earth's gravity field as they are provided from the dedicated satellite gravity field mission GRACE (Gravity Recovery And Climate Experiment) (Tapley et al., 2004; Wahr et al., 2004). Several previous studies have shown the potential of GRACE observations for the estimation of hydrological storage variations in continental regions (e.g., Ramillien et al., 2008; Schmidt et al., 2008; Seitz et al., 2008). Due to the characteristics and height of the GRACE orbit, meaningful results are restricted to regions not smaller than 200,000 km^2 (Swenson & Wahr, 2007). At this scale the maximum temporal resolution amounts to approximately one month. The coarse resolution of GRACE prevents the assessment of water storage for each individual sub basin of the Aral Sea from satellite gravimetry. Instead we provide quasi-monthly estimates of water mass variability within the region confined by the minimum and maximum latitudes of 43.5°N and 47.5°N and by the minimum and maximum longitudes of 58°E and 62°E respectively. This quadrangle comprises the area of the Aral Sea in its historic dimensions and thus the entire region affected by desiccation over the past decades. Its surface area amounts to 220,000 km^2. Even though this study region is much larger than the present surface of the Aral Sea it can be assumed that the prominent part of mass variations on long (i.e. inter-annual) time scales originates from the long-term storage change of water in the Aral Sea. Other sources of water storage variations in its surrounding area (e.g. variations in groundwater, soil moisture or snow cover) are expected to predominantly result in seasonal variations. Therefore we interpret the GRACE signal reduced by seasonal components as an approximation of the long-term water storage in the Aral Sea.

Our GRACE analyses are based on quasi-monthly sets of spherical harmonic coefficients of the Earth's gravity field (GRACE Level-2 data) as provided by the GFZ German Research Centre for Geosciences and the Center for Space Research (CSR), USA, in its well-established latest releases RL04 (Bettadpur, 2007; Flechtner et al., 2010). Mass redistributions on sub-monthly time scales (e.g. due to Earth and ocean tides, atmospheric pressure variations and ocean circulation) would lead to alias effects of the gravity estimates from GRACE in the course of the inversion of the GRACE monthly gravity field solutions. Therefore, those effects are reduced from the GRACE observations already during pre-processing using respective background models; see Flechtner (2007) for details. For continental non-polar regions the largest part of the remaining gravity field changes provided in the monthly Level-2 GRACE products is assumed to reflect mass redistributions within the continental hydrology.

We analyze monthly GRACE gravity field solutions covering the time span from April 2002 (CSR)/August 2002 (GFZ) until July 2011. Due to orbit maneuvers and data problems, few individual months are unavailable. Variations of the gravity field are computed with respect to a long-term mean, i.e. the mean GRACE gravity field over the entire time span. In a spherical harmonic synthesis the coefficients of the residual monthly solutions complete up to degree and order 60 are converted into geographical grids of so-called equivalent water height (EWH) variations (Wahr et al., 1998). EWHs mean an idealized representation of surface mass densities in terms of a thin water layer that needs to be added to (or removed from) the Earth's surface. By expressing GRACE-derived gravity field changes in changes of the thickness of a water layer, it is implicitly assumed that the total observed gravity signal is caused by variations of water storage. The accuracy of the EWH estimates from GRACE is assumed to be 1–2 cm, depending on region and size of the study area (Swenson et al., 2003; Wahr et al., 2006).

Mission-specific errors in the GRACE Level-2 data that show up as meridional stripes in maps of gravity field variations have to be treated in the course of the conversion of the gravity field coefficients into EWH variations. Those errors emerge from satellite orbit characteristics and measurement limitations which result in an in-ability to separate spherical coefficients at all degrees and orders, in particular near orders of resonant coefficients. In addition un-modeled mass fluctuations on sub-monthly timescales (see above) cause high-frequency aliasing. In order to minimize the effects of these errors on the solutions of monthly EWH variations algorithms for smoothing and destriping are applied. In our study we follow the widely used procedures described by Swenson and Wahr (2006) and Wahr et al. (1998), in which correlated errors in the gravity field coefficients are reduced by a least squares polynomial filter and noisy short wavelength components are smoothed using an isotopic Gaussian filter with a half-width of 300 km. As a consequence of Gaussian smoothing, leakage effects from strong mass signals outside of our region of interest emerge (Baur et al., 2009; Swenson & Wahr, 2007). In order to eliminate this contamination of the mass signal within the Aral region, leakage effects from the surrounding area are forward modeled using the WaterGAP Global Hydrology Model (WGHM; Döll et al., 2003) on which the same Gaussian filter is applied. The resulting leakage signal is subsequently reduced from the GRACE signal in the study area. A final correction step accounts for the attenuation of the mass signal as a consequence the spherical harmonic truncation at degree and order 60 and the Gaussian smoothing. In order to derive meaningful values, the GRACE signal amplitude needs to be rescaled. Following the procedure outlined by Swenson and Wahr (2007) a simulated water layer of 1 cm within the study region was developed into spherical harmonic coefficients up to degree and order 60. Taking into account the filter procedure described above, these coefficients

were applied in a spherical harmonic synthesis in order to reconstruct the water height in the study region. The relation of the simulated and the mean of the reconstructed water height (i.e. 1 cm vs. 0.38 cm) let us conclude that the GRACE signal is attenuated by a factor of 2.6. Therefore each value of the grid is multiplied by this factor. We compare the result of our own GRACE Level-2 data analysis from GFZ and CSR with a result based on publicly available spherical harmonic coefficients based on GFZ RL04 data that have been decorrelated using the filter DDK1 after Kusche et al. (2009). These coefficients are provided by the International Centre for Global Earth Models (ICGEM) at http://icgem.gfz-potsdam.de/ICGEM.

Fig. 6 displays the rescaled results of the GRACE analysis in the study area. Water mass variations (provided in units of km^3) are derived by multiplying the surface area of the region with monthly averages of the gridded EWH residuals. The dashed curves show the complete GRACE signal in quasi-monthly time steps from the GFZ, CSR and DDK1 solutions respectively. The bold solid curve represents the mean of the three solutions and the thin solid curve is the long-term component of this mean curve, i.e. a composite seasonal cycle is removed. The results of the two approaches based on the GFZ data agree very well whereas the curve computed from CSR data shows larger discrepancies especially during the second half of the study period. This lets us conclude that the spread of the results is dominated by the different processing strategies at GFZ and CSR rather than on the different approaches for the conversion of the Level-2 data into EWH variations.

Besides a pronounced annual cycle the GRACE signal indicates a clear long-term mass loss between 2005 and 2008. The effect of the previously mentioned anomalous warm and dry conditions of the year 2006 (cf. Section 3) can also be identified in the observations of GRACE that indicate a strong decrease of water storage during summer 2006. From the end of 2009 until mid-2010 the GRACE observations indicate a strong increase of mass in the Aral region which is followed by a rapid decline to the previous level.

Between mid-2005 and the end of 2008 approximately 60 km^3 of water mass were lost in the study area. In a rough calculation we relate this mass loss to a change of the water level given the mean surface areas of the lake in 2005 (around 18,000 km^2) and in 2009 (about 10,000 km^2) (cf. Fig. 5). For simplicity we take 14,000 km^2 as a mean value of the lake's surface area during this period. For this horizontal extent the observed mass loss of 60 km^3 of water corresponds to a sea level change of about 4.3 m which coincides well with the observations from satellite altimetry (Figs. 5 and 6). Since the actual lake geometry is much more complex this estimate can of course only be viewed as a rough plausibility check. Due to its integrative nature the GRACE signal also contains contributions from other mass changes (e.g. due to surface or groundwater variations) in the proximity of the lake whose magnitude and origin are widely unknown. Especially during periods, when the spatial extent of the lake is small (i.e. when the largest part of our GRACE study area is not covered by water), the relative contribution of mass changes from other sources is increased. Due to the limited spatial resolution of GRACE this problem cannot be solved by a stepwise adaptation of the size of the study area to the respective extent of the lake. For a more precise estimation of the contribution of the lake water change to the GRACE signal volume variations of the lake can be computed considering its actual bathymetry (Crétaux et al., 2005). But since the bathymetry of the lake has been shown to be subject to considerable changes resulting from the previously mentioned dust storms such computations are a challenging task for future research (see Section 6) and beyond the scope of the present paper.

5. Discussion

Fig. 7 shows the mean curve of the GRACE solutions with the temporal change of the surface area of the entire Aral Sea (bold solid line from Fig. 5). In this figure only values for those GRACE months are displayed for which the surface area has been computed. Both curves clearly resemble each other in terms of inter-annual and seasonal variations and the correlation coefficient between the curves amounts to 0.74. The characteristics of both curves match well between 2004 and 2008, but the agreement is less good during the first two and the last two years of our analysis. While the minima of the GRACE curve in the autumn of 2008, 2009 and 2010 reach very similar values, the curve of the surface area as well as the time series of the water level (see Fig. 3) feature a clear minimum in autumn 2009. However it has to be kept in mind that GRACE is sensitive not only for variations of water mass within the lake but also for the integral effect of all mass changes in the surrounding of the Aral Sea.

In the Priaralie region, i.e. the region compassing the mouths of the two rivers Amu Darya and Syr Darya, a significant fraction of the incoming water is diverted before it reaches the lake. This holds especially for the region of the very large Amu Darya delta. A part of the diverted water subsequently evaporates or is accumulated as groundwater around the Aral Sea (Nezlin et al., 2004). In either case its positive or negative mass effect affects the GRACE signal in our study region but it is not reflected in the observations of the lake geometry.

In order to study the effect of the surrounding area, data on the water delivery from both rivers into the Aral Sea and its delta were analyzed that is provided by the INTAS-0511 REBASOWS project (Nachtnebel et al., 2006) on the website http://www.cawater-info.net. In Fig. 8 variations of the lake surface area and the mass changes from GRACE are compared with in-situ water discharge observations from Amu Darya and Syr Darya. Discrepancies between the curves of

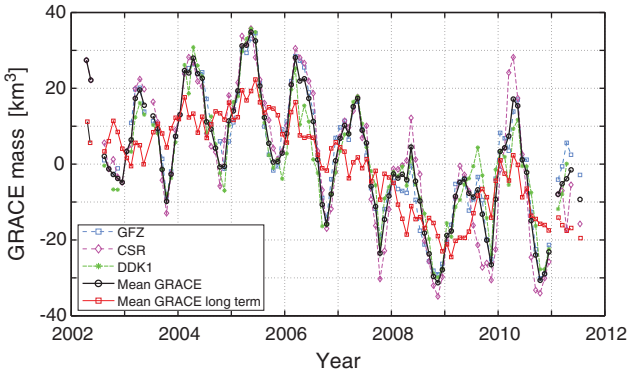

Fig. 6. Variations of equivalent water mass in the Aral region from GRACE satellite gravimetry. Dashed curves: three different GRACE solutions; solid bold curve: mean of the three solutions; thin solid curve: mean long-term signal (solid bold curve reduced by seasonal variations).

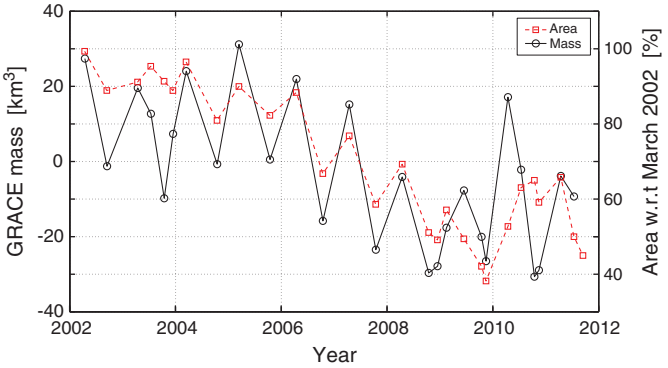

Fig. 7. Mass change in the Aral region from GRACE (solid; left axis) in comparison with the total Aral Sea surface area from Landsat (dashed; right axis) for corresponding epochs.

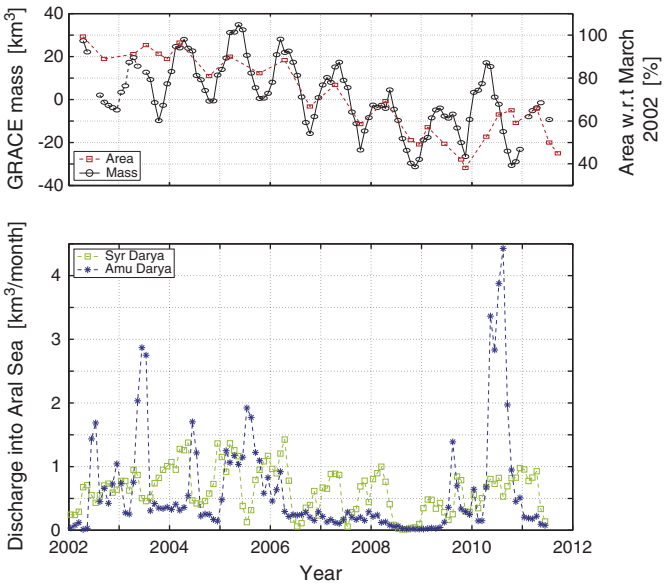

Fig. 8. Monthly discharge from Amu Darya and Syr Darya into the Aral Sea (lower panel) in comparison with the mass change observed by GRACE (upper panel; left axis) and the total Aral Sea surface area (upper panel; right axis).

the surface area and the mass signal occur mainly during periods of strong inflow from the Amu Darya into the Aral Sea.

GRACE shows a minimum of water mass by the end of 2008. During this time almost no discharge was observed at both rivers. Some discharge of Syr Darya in the beginning of 2009 increased the water level of the North Aral Sea that had reached its minimum stage by the end of 2008 (Fig. 3). In summer 2010 an abnormally increased discharge into the Aral Sea was observed at Amu Darya. This flood led to the strongest increase of the lake level and extent during our study period. A time lag of few months is obvious between the GRACE curve and the lake water extent. Again this can be explained by the sensitivity of GRACE for signals from the adjoining region. The usual strong intra-annual shrinking of the lake (i.e. lower water levels in autumn than in spring) cannot be observed in 2010 because of the exceptional water inflow from Amu Darya during summer 2010. The lake has experienced a similar anomaly of the annual cycle in 2003 where relatively strong inflow (the second largest amount in our study period) also attenuated the usual minimum in autumn. Also here a comparable phase difference between GRACE and the lake extent is visible.

In general there is a very good agreement between the curve of the discharge measured at the Syr Darya gauge station and the GRACE signal. Since the GRACE study area covers a large part of the region east of the Aral Sea through which the Syr Darya is passing, GRACE is sensitive to the water transport of the river and hydrological processes (evaporation, infiltration, water management) in this region. In particular during the first seven years the inter-annual signal component of both time series (i.e. the increase from 2002 to 2005 and the decrease between 2005 and 2008) matches in both curves. For the last years of our analysis the GRACE time series has mainly been influenced by the exceptional water transport from Amu Darya.

In 2010 GRACE observed a decrease in mass between April and September. On the other side a significant refilling of lake was ongoing during this period due to the strongest inflow from the Amu Darya during the whole study period. Between August and November 2010 the discharge curve dropped back to its previous low level. The GRACE curve precedes the discharge curve of Amu Darya by two to three months. This can also be seen in other years with strong discharge from Amu Darya (e.g. 2003). Since the Amu Darya is passing through the Kara-Kum desert a large amount of surface water is lost due to seepage which is accompanied by the accumulation of groundwater along the river bed and around the Aral Sea (Nezlin et al., 2004). It is assumed that in the case of strong runoff from Amu Darya aquifers around the Aral Sea are filled before the water reaches the lake and thus influence the observations of GRACE.

Fig. 9 relates the lake area to mass changes from GRACE. Data points are taken from Fig. 7. The line shows a best fit estimate that has been computed in a least squares adjustment procedure. A statistically significant linear relationship indicates the link between the GRACE mass estimates and the Aral Sea water surface at the inter-annual scale.

6. Conclusions

The combination of multi-satellite data of the Aral region allows for a comprehensive study of the hydrological conditions in this area. Satellite altimetry, remote sensing, and satellite gravimetry provide information on various aspects of the ongoing storage changes in the Aral Sea and its basins that are largely related to anthropogenic activities. While satellite altimetry and remote sensing data allow for an accurate assessment of a three dimensional geometrical change of the lake surface, satellite gravimetry is capable of observing the related variations of water mass. Even though the spatial resolution of geometrical and gravimetrical observations is very different, both types of observations provide valuable and unique information on different aspects of the hydrological situation.

The observations revealed that the impact of desiccation on the lake geometry is most severe in the comparatively shallow east basin. The completion of the Dike Kokaral dam resulted in a splitting of the smaller North Aral Sea from the larger South Aral Sea. While the dam led to a stabilization of the water level of the north basin, the south basin suffered an increased desiccation since it was cut off from the tributary Syr Darya, and the water discharge from the Amu Darya was too low (especially during 2006–2009; see Fig. 8) to compensate for the high rate of evaporation due to its very large size. Since the deeper west basin is characterized by a steeper coastline, the horizontal shrinkage of the west basin is comparatively low while the water level varies significantly. The patterns of desiccation and subsequent refilling observed by the geometrical observation techniques are also clearly visible in the GRACE satellite gravimetry data. However due to the small size of the lake a direct comparison of observed mass variations and the lake geometry is very difficult since the GRACE signal is strongly affected by the variability of the water mass in the adjoining area.

Therefore we aim at an independent computation of mass variations from water volume changes in a next step of our project. In a

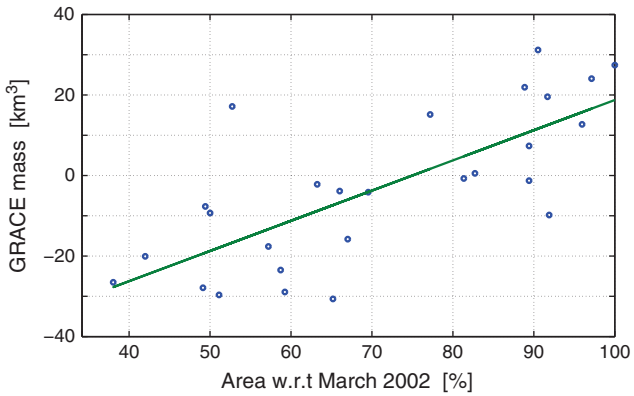

Fig. 9. Quantitative comparison between the total Aral Sea surface area and GRACE mass change (data taken from Fig. 7).

geometrical approach time-variable masks of water surface extent from Landsat shall be intersected with a high-resolution DEM, using satellite altimetry as vertical constraint. This way volume changes from geometrical observation techniques and mass change from gravity field observations can be compared qualitatively which will also allow for an improved assessment of the influence of hydrological mass variations in the proximity of the lake. The study has shown that all applied data sets correspond well with respect to their temporal development. Therefore multi-satellite approaches can be seen as a very promising method for the analysis of hydrological processes also in regions that are poorly monitored by in-situ observations.

Acknowledgments

The authors acknowledge the financial support by the WILLPower Erasmus Mundus Cooperation Window and by the International Graduate School of Science and Engineering (IGSSE) of the Technische Universität München, Germany. Further we thank Dr. Andreas Güntner from GFZ Potsdam for his constructive remarks on the manuscript that led to a substantial improvement of the paper.

References

Arguez, A. (2007). State of the climate in 2006. *Bull. Am. Meteorol. Soc.*, *88*, (135 pp, Washington, USA).

Baur, O., Kuhn, M., & Featherstone, W. (2009). GRACE-derived ice-mass variations over Greenland by accounting for leakage effects. *Journal of Geophysical Research*, *114*, B06407, doi:10.1029/2008JB006239.

Becker, M., Llovel, W., Cazenave, A., Güntner, A., & Crétaux, J. -F. (2010). Recent hydrological behavior of the East African great lakes region inferred from GRACE, satellite altimetry and rainfall observations. *Comptes Rendus Geoscience*, *342*(3), 223–233, doi:10.1016/j.crte.2009.12.010.

Bettadpur, S. (2007). Gravity recovery and climate experiment level-2 gravity field product user handbook. *GRACE 327–734, CSR Publ. GR-03-01, Rev 2.3*. Austin, USA: University of Texas (19 pp.).

Birkett, C. M. (1995). The contribution of TOPEX/POSEIDON to the global monitoring of climatically sensitive lakes. *Journal of Geophysical Research*, *100*(12), 25179–25204.

Boroffka, N. G. O., Obernhänsli, H., Achatov, G. A., Aladin, N. V., Baipakov, K. M., Erzhanova, A., et al. (2005). Human settlements on the northern shores of Lake Aral and water level changes. *Mitigation and Adaptation Strategies for Global Change*, *10*(1), 71–85, doi:10.1007/s11027-005-7831-1.

Bortnik, V. N. (1999). Alteration of water level and salinity of the Aral sea. In M. Glantz (Ed.), *Creeping environmental problems and sustainable development in the Aral Sea Basin* (pp. 47–65). Cambridge, UK: Cambridge University Press.

Bosch, W., & Savcenko, R. (2007). Satellite altimetry: multi-mission cross calibration. In P. Tregoning, & R. Rizos (Eds.), *Dynamic Planet IAG Symposia*, *130*. (pp. 51–56), doi:10.1007/978-3-540-49350-1_8.

Brown, S. (2010). A novel near-land radiometer wet path-delay retrieval algorithm: application to the Jason-2/OSTM advanced microwave radiometer. *IEEE Transactions Geoscience and Remote Sensing*, *48*, 4.

Calmant, S., Seyler, F., & Cretaux, J. F. (2009). Monitoring continental surface waters by satellite altimetry. *Surveys in Geophysics*, *29*(4–5), 247–269, doi:10.1007/s10712-008-9051-1.

Cazenave, A., Bonnefond, P., Dominh, K., & Schaeffer, P. (1997). Caspian Sea level from Topex-Poseidon altimetry: level now falling. *Geophysical Research Letters*, *24*(8), 881–884, doi:10.1029/97GL00809.

Crétaux, J. F., Calmant, S., Romanovski, V., Shabunin, A., Lyard, F., Bergé-Nguyen, M., et al. (2008). An absolute calibration site for radar altimeters in the continental domain: Lake Issykkul in Central Asia. *Journal of Geodesy*, *83*(8), 723–735, doi:10.1007/s00190-008-0289-7.

Crétaux, J. F., Kouraev, A. V., Papa, F., Bergé-Nguyen, M., Cazenave, A., Aladin, N., et al. (2005). Evolution of sea level of the Big Aral Sea from satellite altimetry and its implications for water balance. *Journal of Great Lakes Research*, *31*(4), 520–534, doi:10.1016/S0380-1330(05)70281-1.

Döll, P., Kaspar, F., & Lehner, B. (2003). A global hydrological model for deriving water availability indicators: model tuning and validation. *Journal of Hydrology*, *270*(1–2), 105–134, doi:10.1016/S0022-1694(02)00283-4.

Flechtner, F. (2007). Gravity recovery and climate experiment AOD1B product description document for product releases 01 to 04. *Tech. Rep. GRACE327-750, Rev. 3.1*. Germany: GFZ Potsdam.

Flechtner, F., Dahle, C., Neumayer, K. H., König, R., & Förste, C. (2010). The release 04 CHAMP and GRACE EIGEN gravity field models. In F. Flechtner, M. Mandea, & T. Gruber (Eds.), *System earth via geodetic–geophysical space techniques* (pp. 41–58). Berlin: Springer 978-3-642-10228-8.

Frappart, F., Papa, F., Famiglietti, J. S., Prigent, C., Rossow, W., & Seyler, F. (2008). Interannual variations of river water storage from a multiple satellite approach: a case study for the Rio Negro River basin. *Journal of Geophysical Research*, *113*, D21104, doi:10.1029/2007JD009438.

Froebrich, J., & Kayumov, O. (2004). Water management aspects of Amu Darya, in dying and dead seas climatic versus anthropic causes. In Nihoul (Ed.), *NATO science series IV: earth and environmental sciences*, *36*. (pp. 49–76)Dordrecht, The Netherlands: Kluwer Academic Publishers.

Fu, L., & Cazenave, A. (2001). *Satellite altimetry and Earth sciences: a handbook of techniques and applications*. London, UK: Academic Press 464 pp.

Getirana, A. C. V., Bonnet, M. P., Calmant, S., Roux, E., Rotunno-Filho, O. C., & Mansur, W. J. (2009). Hydrological monitoring of poorly gauged basins based on rainfall–runoff modeling and spatial altimetry. *Journal of Hydrology*, *379*(3–4), 205–219, doi:10.1016/j.jhydrol.2009.09.049.

Güntner, A. (2008). Improvement of global hydrological models using GRACE data. *Surveys in Geophysics*, *29*(4–5), 375–397, doi:10.1007/s10712-008-9038-y.

Jarsjo, J. (2004). Groundwater discharge into the Aral Sea after 1960. *Journal of Marine Systems*, *47*(1–4), 109–120, doi:10.1016/j.jmarsys.2003.12.013.

Kouraev, A. V., Shmaraev, M. N., Buharizin, P. I., Naumenko, M. A., Crétaux, J. F., Mognard, N., et al. (2008). Ice and snow cover of continental water bodies from simultaneous radar altimetry and radiometry observations. *Surveys in Geophysics*, *29*(4–5), 271–295, doi:10.1016/j.jmarsys.2008.03.016.

Kravtsova, V. I. (2005). The Aral Sea and coastal zone degradation: monitoring by space images. *Proceedings of 31st International Symposium on Remote Sensing of Environment*. Russia: Saint Petersburg.

Kravtsova, V. I., & Tarasenko, T. V. (2010). Space monitoring of Aral Sea degradation. *Water Research*, *37*(3), 285–296, doi:10.1134/S0097807810030036.

Kusche, J., Schmidt, R., Petrovic, S., & Rietbroek, R. (2009). Decorrelated GRACE time-variable gravity solutions by GFZ, and their validation using a hydrological model. *Journal of Geodesy*, *83*(10), 903–913, doi:10.1007/s00190-009-0308-3.

Micklin, P. P. (1988). Desiccation of the Aral Sea, a water management disaster in the Soviet Union. *Science*, *241*, 1170–1176.

Morris, C. S., & Gill, S. K. (1994). Evaluation of the TOPEX/POSEIDON altimeter system over the Great Lakes. *Journal of Geophysical Research*, *99*(C12), 24527–24539, doi:10.1029/94JC01642.

Nachtnebel, H. P., Holzmann, H., Dukhovny, V., Sorokin, A., Roschenko, Y., et al. (2006). The rehabilitation of the ecosystem and bioproductivity of the Aral Sea under conditions of water scarcity. *Final report of the INTAS project 0511 REBASOWS*. Austria: Vienna 75 pp.

Nezlin, N., Kostianovy, A., & Lebedev, A. (2004). Interannual variations of the discharge of Amu Darya and Syr Darya estimated from global atmospheric precipitation. *Journal of Marine Systems*, *47*, 67–75.

Papa, F., Güntner, A., Frappart, F., Prigent, C., & Rossow, W. (2008). Variations of surface water extent and water storage in large river basins: a comparison of different global data sources. *Geophysical Research Letters*, *35*, L11401, doi:10.1029/2008GL033857.

Pavlis, N. K., Holmes, S. A., Kenyon, S. C., & Factor, J. K. (2008). An earth gravitational model to degree 2160: EGM2008. *Geophysical Research Abstracts*, *10* EGU2008-A-01891.

Prigent, C., Papa, F., Aires, F., Rossow, W. B., & Matthews, E. (2007). Global inundation dynamics inferred from multiple satellite observations, 1993–2000. *Journal of Geophysical Research*, *112*, D12107, doi:10.1029/2006JD007847.

Ramillien, G., Famiglietti, J., & Wahr, J. (2008). Detection of continental hydrology and glaciology signals from GRACE: a review. *Surveys in Geophysics*, *29*(4–5), 361–374, doi:10.1007/s10712-008-9048-9.

Ramillien, G., Frappart, F., Cazenave, A., & Guntner, A. (2005). Time variations of land water storage from an inversion of 2 years of GRACE geoids. *Earth and Planetary Science Letters*, *235*(1–2), 283–301, doi:10.1016/j.epsl.2005.04.005.

Roget, E., Zavialov, P., Khan, V., & Muñiz, M. A. (2009). Geodynamical processes in the channel connecting the two lobes of the Large Aral Sea. *Hydrology and Earth System Sciences*, *13*(11), 2265–2271, doi:10.5194/hess-13-2265-2009.

Rogov, M. M. (1957). *Hydrology of the Amudarya Delta. Gidrometeoizdat.* (255 pp.). Russia: Leningrad (in Russian).

Schaer, S., Beutler, G., Rothacher, M., & Springer, T. (1996). Daily global ionosphere maps based on GPS carrier phase data routinely produced by the CODE analysis center. *Proceedings of the IGS AC Workshop*. MD, USA: Silver Spring.

Schmidt, M., Seitz, F., & Shum, C. K. (2008). Regional four-dimensional hydrological mass variations from GRACE, atmospheric flux convergence, and river gauge data. *Journal of Geophysical Research*, *113*, B10402, doi:10.1029/2008JB005575.

Seitz, F., Schmidt, M., & Shum, C. K. (2008). Signals of extreme weather conditions in Central Europe in GRACE 4-D hydrological mass variations. *Earth and Planetary Science Letters*, *268*(1–2), 165–170, doi:10.1016/j.epsl.2008.01.001.

Solomon, S., Qin, D., Manning, M., Chen, Z., Marquis, M., & Averyt, K., et al. (Eds.). (2007). *Climate Change 2007: The Physical Science Basis, Contribution of Working Group I to the Fourth Assessment Report of the Intergovernmental Panel on Climate Change*. Cambridge, UK: Cambridge University Press.

Swenson, S., & Wahr, J. (2006). Post-processing removal of correlated errors in GRACE data. *Geophysical Research Letters*, *33*, L08402, doi:10.1029/2005GL025285.

Swenson, S., & Wahr, J. (2007). Multi-sensor analysis of water storage variations of the Caspian Sea. *Geophysical Research Letters*, *34*, L16401, doi:10.1029/2007GL030733.

Swenson, S., Wahr, J., & Milly, P. (2003). Estimated accuracies of regional water storage variations inferred from the Gravity Recovery and Climate Experiment (GRACE). *Water Resources Research*, *39*(8), doi:10.1029/2002WR001736.

Tapley, B., Bettadpur, S., Ries, J., Thompson, P., & Watkins, M. (2004). GRACE measurements of mass variability in the Earth system. *Science*, *305*, 503–505, doi:10.1126/science.1099192.

Wahr, J., Molenaar, M., & Bryan, F. (1998). Time variability of the Earth's gravity field: hydrological and oceanic effects and their possible detection using GRACE. *Journal of Geophysical Research*, *103*(B12), 30205–30229, doi:10.1029/98JB02844.

Wahr, J., Swenson, S., & Velicogna, I. (2006). Accuracy of GRACE mass estimates. *Geophysical Research Letters*, *33*, L06401, doi:10.1029/2005GL025305.

Wahr, J., Swenson, S., Zlotnicki, V., & Velicogna, I. (2004). Time-variable gravity from GRACE: first results. *Geophysical Research Letters*, *31*, L11501, doi:10.1029/2004GL019779.

Werth, S., Güntner, A., Petrovic, S., & Schmidt, R. (2009). Integration of GRACE mass variations into a global hydrological model. *Earth and Planetary Science Letters*, *277*(1–2), 166–173, doi:10.1016/j.epsl.2008.10.021.

Zavialov, P. O. (2005). *Physical oceanography of the dying Aral Sea* (pp. 22–56). Chichester, UK: Springer Praxis Book.

Zavialov, P. O. (2010). Physical oceanography of the Large Aral Sea. In A. G. Kostianoy, & A. N. Kosarev (Eds.), *The Aral Sea environment: the handbook of environmental chemistry*, *7*. (pp. 123–145)Berlin Germany: Springer, doi:10.1007/698_2009_4.

Paper-2

Singh, A.; Seitz, F.; Schwatke, C.: **Application of Multi-Sensor Satellite Data to observe Water Storage Variations**; Selected Topics in Applied Earth Observations and Remote Sensing (JSTARS), vol. 6, issue 3, pp 1502–1508, IEEE Geo-science and Remote Sensing Society, ISSN:1939-1404, DOI: 10.1109/JSTARS.2013.2258326.

Application of Multi-Sensor Satellite Data to Observe Water Storage Variations

Alka Singh, *Member, IEEE*, Florian Seitz, and Christian Schwatke

***Abstract*—In this study we apply geometric and gravimetric observations from various Earth observation satellites in order to estimate the variability in a lake with respect to its geometrical extent and water storage. Our test case is the Aral Sea, located in the arid zone of central Asia. Due to the diversion of its primary inlet rivers for irrigation purposes the lake suffered a devastating decline until its south eastern part had almost dried out in 2009. The study is focused on the period of the satellite gravity field mission GRACE from 2002 onwards. We present the change of the lake's surface extent based on optical remote sensing data from Landsat images that were analyzed for spring and autumn each year. Height variations of the lake surface were computed from multi-mission satellite altimetry. Both the surface extent and the water stage of the lake reached an absolute minimum in autumn 2009. However in 2010 a clear reversal of the negative trend of the previous years is visible. A geometrical intersection of the water level with a digital elevation model allows for estimating water volume changes. The resulting volume changes are subsequently analyzed with respect to satellite-based estimates of mass variations observed by GRACE. The results reveal that water storage variations in the Aral Sea are indeed the principal contributor to the GRACE signal of mass variations in this region. The different observations from all missions agree very well with respect to their temporal behavior.**

***Index Terms*—GRACE, Landsat, satellite altimetry, volume changes.**

I. Introduction

WATER stored in surface water bodies plays a key role in the global hydrological cycle. A large number of recent satellite missions with different objectives are available today, allowing us to study the extent and dynamics of many continental water bodies on a wide scale and in remote areas.

Until the 1960s, the Aral Sea was the fourth largest lake in the world. From then onwards a catastrophic drying process has been ongoing due to undersupply of water as a result of the diversion of its tributaries for irrigation [1]. In this paper we analyze geometrical changes of the lake surface and compare deduced variations of the lake volume with gravimetric (i.e. mass-related) variations in the region. Volume changes are geometrically determined from water height variations observed by multi-sensor altimetry in combination with a digital elevation model of the lake floor. Gravity field changes have been observed by the dedicated satellite gravity field mission GRACE (Gravity Recovery and Climate Experiment) since 2002. It has been demonstrated in several studies that GRACE has the potential to observe hydrological storage variations in continental regions [2], [3]. The time-frame of our study is 2002–2011.

Manuscript received September 29, 2012; revised January 28, 2013; accepted March 06, 2013. Date of publication May 15, 2013; date of current version June 17, 2013. This work was supported in part by the Erasmus Mundus WillPower fellowship and the International Graduate School of Science and Engineering (IGSSE).

A. Singh is with the Chair for Geodetic Geodynamics, Institute of Astronomical and Physical Geodesy, Technsche Universität München (TUM), 80333 Munich, Germany (e-mail: alka.singh@bv.tum.de).

F. Seitz is with the Chair for Geodetic Geodynamics, Institute of Astronomical and Physical Geodesy, Technsche Universität München (TUM). He is also with the German Geodetic Research Institute (Deutsches Geodätisches Forschungsinstitut, DGFI), Munich, Germany (e-mail: seitz@bv.tum.de).

C. Schwatke is with the German Geodetic Research Institute (Deutsches Geodätisches Forschungsinstitut, DGFI), Munich, Germany (e-mail: schwatke@dgfi.badw.de).

Color versions of one or more of the figures in this paper are available online at http://ieeexplore.ieee.org.

Digital Object Identifier 10.1109/JSTARS.2013.2258326

II. Geometrical Changes of the Aral Sea

Temporal changes of the storage in a water body are related to changes of its level and surface extent. Such variations can be traced in observations from satellite altimetry and optical remote sensing images [4]. Volumetric variations can be deduced by intersecting these observations with a digital bathymetry model of the water body.

A. Water Extent

Changes in the Aral Sea surface area were derived from Landsat satellite images every year for spring and autumn between 2002 and 2011. Some additional months were also computed for periods of seasonal anomalies. Bulk download of the Landsat images was performed from http://earthexplorer.usgs.gov not only for the area under water, but also for adjoining regions to fill SLC-off (Scan Line Corrector) gaps in the Landsat7 (ETM+) datasets. From May 2003 Landsat7 suffered a failure in the SLC, which resulted in stripe-type data gaps. Six sets of images were mosaicked for each time frame to generate a complete picture of the lake at 30 m spatial resolution and to fill the gaps as good as possible. Remaining data gaps were filled by convolving first 5×5 followed by 3×3 mean focal filters. Because of frequent changes in the lake geometry in one of its sub-basins, preceding and subsequent images were not found to be suitable to fill the gaps as they sometimes create artifacts due to a too long time lag between usable images. Respective land/water masks were generated through image processing techniques using a maximum likelihood supervised classifier in IDL-ENVI through batch processing. Morphological operations were carried out on all masks to remove minor artefacts in the images through erode and dilation. For each of the three sub-basins of the Aral Sea (north, east and west) we obtained a time-series of the area covered by water.

Fig. 1 shows seasonal and long-term variations of the surface area for the three basins between 2002 and 2012 in twice-yearly

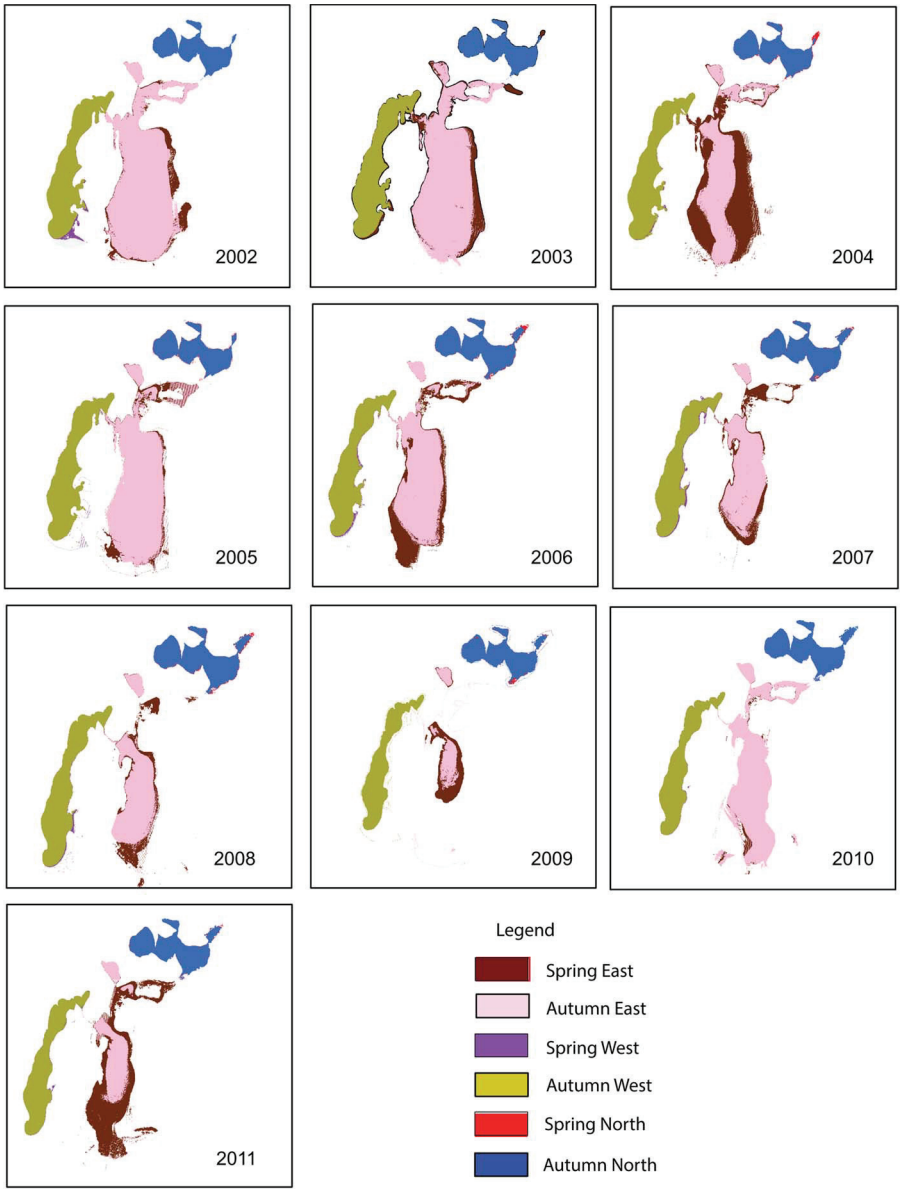

Fig. 1. Seasonal and long-term change of the Aral Sea surface area in spring and autumn during 2002–2011 observed from Landsat images.

snapshots (color coded). A clear process of desiccation is evident between 2002 and 2009. The year 2010 was observed as a reviving year for the lake due to a significant inflow from its primary inlets Amu Darya and Syr Darya [Fig. 7]. After 2010 desiccation continued. The largest changes are observed in the shallow east basin. Within only seven years it shrunk to less than 10% of its area observed in 2002 and lost nearly 10,000 km^2. The west basin suffered consistent changes but with far smaller amplitude [cf. Fig. 3, left]. The North Aral Sea, in contrast, features a different development, as it remained comparatively stable, except for the years 2005–2006, when its size increased by nearly 10%, due to the construction of the Dike Kokaral dam in 2005.

B. Water Level

During the last two decades satellite altimetry has been widely applied to monitor water levels of many continental water bodies [5]–[7]. In our study, water level time series were generated by combining observations from radar altimetry missions, i.e. Jason-1, Jason-2, Jason-1 extended mission (EM), and Envisat. The lake was very well observed by different altimetry missions in the first part of our study period, but unfortunately later not only the lake size shrank, but also several altimetry missions retired. As a result the lake was only observed by Jason-2 and Jason-1-EM by the end of our study period. All observations were corrected for atmospheric delay and geophysical effects, i.e. for ionosphere, dry troposphere, wet troposphere, and solid Earth tides using calibration models.

Altimetry data and correction models were downloaded from DGFI's open altimetry data base (OpenADB) at http://openadb.dgfi.badw.de. Heights refer to the geoid EGM2008. An additional cross calibration of the range bias was applied to harmonize the observations between different missions. Observation points at a distance less than 5 km from the coast were rejected

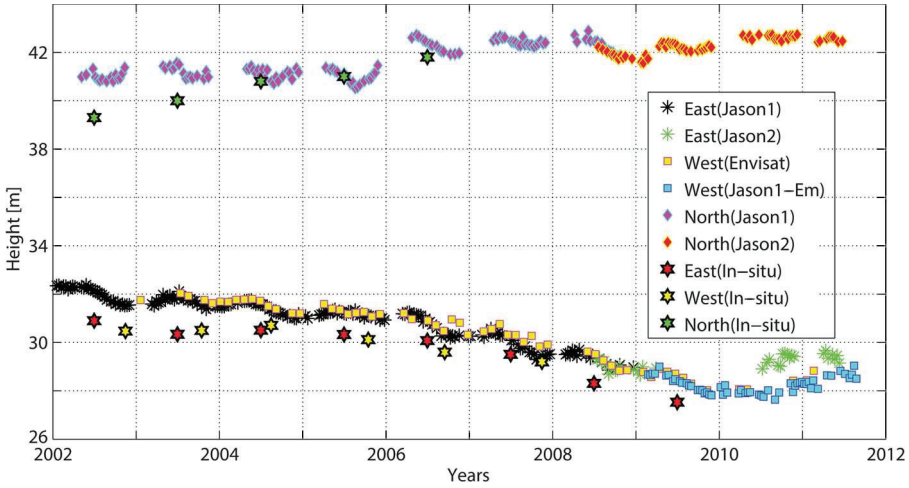

Fig. 2. Water level changes in the east and west basin (upper panel) and North Aral Sea (lower panel) from multi-mission altimetry and in-situ observations.

to avoid any contamination of the measurements by land reflection. For this purpose the water masks generated from Landsat data were applied. Water masks were re-projected from UTM to a geographic coordinate system, resampled from 30 m onto a 0.025° grid, and finally eroded by a 3 × 3 matrix to obtain the masks from which we deduced the 5 km range from the coast.

The altimetry observations from all missions agree very well within a range of few decimetres [Fig. 2]. The temporal development of the lake level as seen by altimetry is in concordance with in-situ data available from the INTAS-0511 REBASOWS project (www.cawater-info.net) [8] and an expedition to the west basin [9]. However, an almost constant offset between the altimetry observations and in-situ data exists due to different height systems used as reference. Fig. 2 upper panel shows a clear seasonal pattern and a drastic drop of the water level until the end of 2009 for the South Aral (east and west basin). As a consequence of the shrinking of the lake there is a lack of observations of the east basin for almost half a year (November 2009 until June 2010). By this time the small channel between the two basins of the South Aral Sea dried out completely, and the west basin was separated. It continued to recede until summer 2010. As it is deep and also fed by ground water, its decline was accompanied by a relatively small change of its volume. After spring 2010 both southern basins revived and expanded both vertically and horizontally [cf. Fig. 3, left] due to exceptionally strong inflow from the Amu Darya (see Discussion). The North Aral Sea remained almost stable with nearly 1 m of annual fluctuation and an additional gain of approximately 1 m in 2005/2006. This rise resulted from the construction of the dam by which the South Aral Sea was cut off from its former tributary Syr Darya. The dam which is usually closed is only released in the rare event of an extraordinary inflow from the Syr Darya. Fig. 3 compares time series of surface area and water height for all basins. Both quantities show a very similar development. In the shallow east basin their correlation is 0.98. The scatter plot between the two quantities shows a distinct linear relationship [Fig. 3, right]. West and north basin feature more pronounced variations in the water level than in the surface area due to larger depth and steeper shorelines. Correlation coefficients between water level and surface area amount to 0.94 (north) and 0.77 (west) respectively.

C. Lake Volume

Volumes of the basins were computed by intersecting a digital elevation model (DEM) of the Aral Sea floor (provided by Dr. P. Zavialov from the Physical Oceanography Division, Russian Academy of Science though personal communication) with the water levels computed from altimetry [10]. We used a mean water level from all altimetry missions for each basin to generate volumetric time-series. We transformed a 1° × 1° bathymetry model onto a 30 m grid using a bilinear algorithm. Depth values are provided w.r.t. the Kronstadt gauge. In order to obtain heights of the sea floor w.r.t. the geoid, a constant offset of 53 m had to be subtracted from the model [5] [Fig. 4, left]. Water stages per 30 m pixel were generated by subtracting the DEM from water levels observed by altimetry. For each basin, water volumes were computed by integrating corresponding water columns with negative values (positive values correspond to areas uncovered by water). The mean of the total volume of the Aral Sea [Fig. 4, right] over the entire study period is 101.76 km^3; this value was subtracted from the monthly observations in order to compute volumetric variations. These variations were later compared with the mass signals derived from the GRACE gravity field mission in the Aral Sea region; see below. As the bathymetry map was generated in the 1960s and the spatial resolution is rather poor, we expect an (unknown) error in the volumetric computation. This error can, however, be viewed as marginal for our comparison since the resolution of the GRACE data is limited to a spatial scale of a few hundred kilometers.

III. Gravimetric Changes in the Aral Sea Region

The Gravity Recovery and Climate Experiment (GRACE) twin satellite mission was launched in 2002 to measure the Earth's gravity field and monitor mass variations over space and time around the planet [17]. The twin spacecraft uses a microwave ranging system to accurately measure changes in the distance between two satellites that are caused by minute

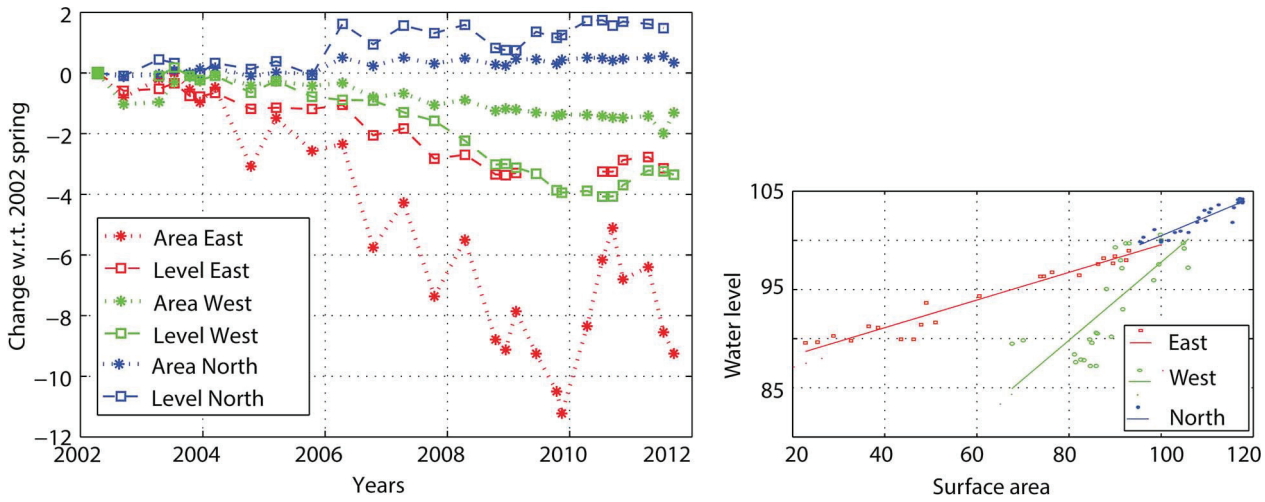

Fig. 3. Left: Changes in the Aral Sea water level in meters and surface area in 1000 km^2 for each basin with respect to its state in spring 2002 (East, West and North Aral had water levels of 32, 32 and 41 m and surface areas of 12.000, 5.200 and 2.800 km^2 respectively). Right: Least squares linear regression between the scatter plot of water level and surface area of each basin, both given in percent (100% corresponds to spring 2002).

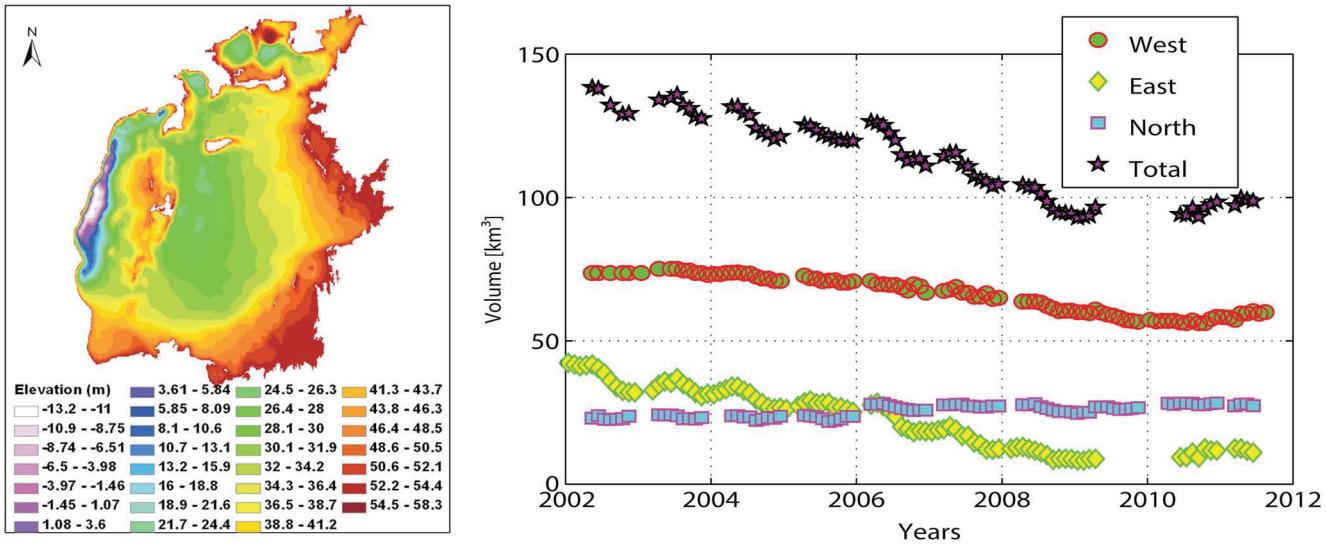

Fig. 4. Left: Digital elevation model of the Aral Sea floor; Right: water volumes computed for each basin and their sum.

variations in Earth's gravitational attraction. The mission is sensitive to large-scale mass variations in the Earth system and many studies in last decade have demonstrated its usability to monitor water storage changes [2], [3], [18]. On spatial scales larger than a few hundred km a temporal resolution of approximately one month can be achieved. Due to the mission's coarse resolution it is not possible to distinguish between individual contributions of water mass changes from the three sub-basins of the Aral Sea to the observed signal of mass variations in the region. For our GRACE analysis we chose a $4^\circ \times 4^\circ$ quadrangle comprising all basins. This area is five times larger than the area of the lake in 2002. Consequently the observations of GRACE are also significantly influenced by other (predominantly hydrological) mass variations in the surrounding area (e.g. groundwater, snow, soil moisture, water in rivers and floodplains, etc.) that are partly characterized by a distinct seasonal variability.

We used quasi-monthly sets of spherical harmonic coefficients of the Earth's gravity field (GRACE Level-2 data) provided by the German Research Centre for Geosciences (GFZ), Germany, and the Centre for Space Research (CSR), USA. Redistributions of mass due to Earth and ocean tides, atmospheric pressure variations and ocean circulation were removed already during pre-processing via respective background models [11]. Therefore the remaining signals in our study area can be assumed to reflect the redistribution of mass within the continental hydrology. Variations of the gravity field w.r.t. a mean field over the entire time span are expressed in so-called equivalent water height (EWH) variations that were computed via spherical harmonic synthesis [12]. In order to minimize aliasing effects, algorithms for smoothing and de-striping were applied [4], [13]. Contaminations by leakage effects from the surroundings of our study area due to the spherical harmonic truncation at degree/order 60 were reduced on the basis of the Water-GAP Global Hydrology Model (WGHM) [14], [15], on which the same Gaussian filter were applied. In Fig. 5 the results for mass variations from GRACE for the study area are displayed in units of km^3 (Equivalent Water Volume; derived from the multiplica-

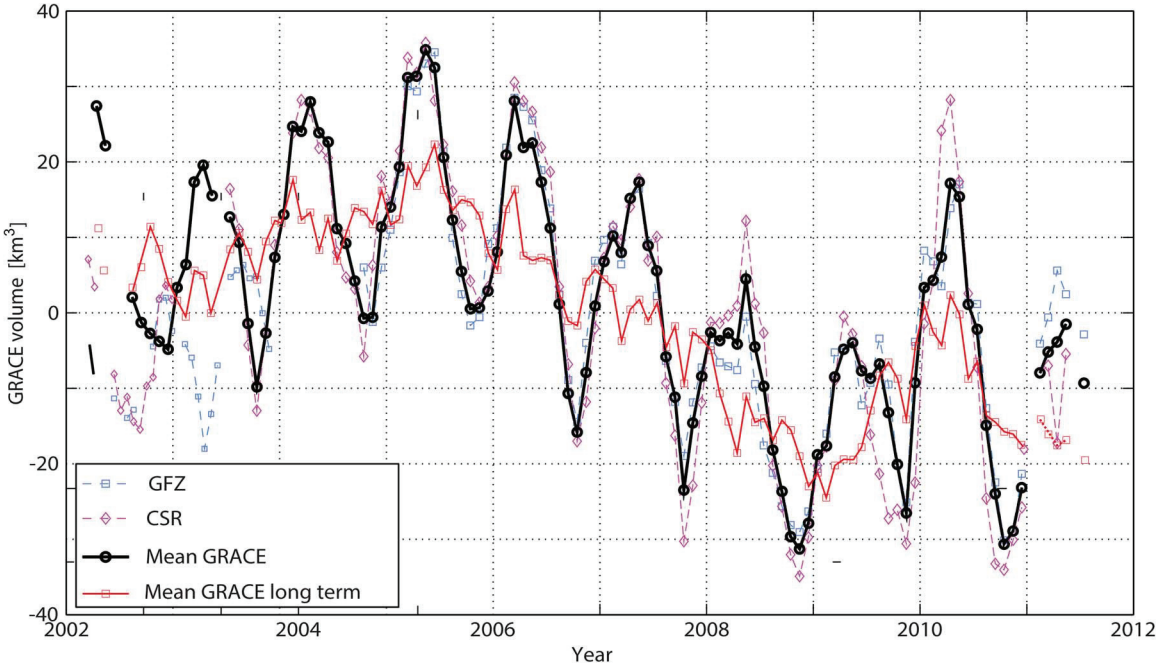

Fig. 5. Variations of equivalent water volume in the Aral region from GRACE satellite gravimetry. Values are anomalies w.r.t. a long term mean over the GRACE era. Dashed curves: two different GRACE solutions; solid bold curve: mean of the two solutions; thin solid curve: mean long-term signal (solid bold curve reduced by seasonal variations).

tion of EWH changes with the area). The CSR solution shows slightly larger amplitudes, especially during the second half of the study period.

Nevertheless, in general the two solutions from GFZ and CSR are very consistent. For further comparisons we use the mean of both solutions [Fig. 5]. A pronounced annual cycle and a clear long term mass loss (in particular between 2005 and 2008) followed by a significant increase is obvious. The temporal development of the signal agrees with the observations from Landsat and the altimetry missions.

IV. Discussion

The comparison of GRACE-derived volume estimates with water volume variations computed from altimetry and the bathymetry model shows a good agreement of both curves in terms of trend and seasonal variability [Fig. 6]. The correlation coefficient between the volumes from GRACE and the geometrical approach is 0.74 over the entire study period. During the period of the strongest desiccation (2004–2009) the correlation amounts to 0.85. Composite seasonal cycles of the curves were computed from the mean values of each month over the entire time frame [Fig. 6, right]. Both cycles show a seasonal variation of volume with consistent phase. The trend observed by GRACE (4 $\mathrm{km}^3/\mathrm{year}$) is somewhat smaller than the trend computed from the geometrical approach (5 $\mathrm{km}^3/\mathrm{year}$) [Fig. 6, left]. GRACE observations indicate that between mid-2005 and the end of 2008 approximately 60 km^3 of water mass were lost, of which the lake contributed only 30 km^3. The total water volume loss of the lake between 2002 and 2009 was nearly 45 km^3, followed by a gain of not more than 10 km^3 in 2010. On the other hand GRACE observed 40 km^3 of fluctuation in the year 2010 [Fig. 5]. This comparison reveals that even though the lake produces a dominant mass signal, GRACE observations are also highly influenced by mass changes in the surrounding of the Aral Sea. As stated above, the integrative GRACE signal contains contributions from other hydrological signals originating in the proximity of the lake. Their magnitude and origin are largely unknown. But as stated above some of the hydrological compartments feature a distinct seasonal variability (e.g. snow, groundwater). Therefore the annual amplitudes of the mean GRACE curve can be expected to be larger than the annual amplitudes of the lake volume change.

Since our study area of GRACE is significantly larger than the lake itself, GRACE also observes the Priaralie delta region, encompassing large parts of the two rivers Amu Darya and Syr Darya delta. A significant fraction of the incoming water gets diverted in this region (e.g. for irrigation purposes) and never reaches the lake. Therefore it cannot be expected that the mass signal seen by GRACE and the volume change of the lake fully resemble each other.

The GRACE minimum in 2008 is related to a dry period with almost no water inflow from both rivers [Fig. 7]. In 2010 the GRACE curve follows the curve of the water discharge from the Amu Darya. The integrated amount of water reaching the lake by the Amu Darya and the Syr Darya was approximately 20 km^3 and 10 km^3 respectively. During this year GRACE observed a fluctuation of 40 km^3. The difference can be explained by corresponding changes in other hydrological compartments. During 2010 the Aral Sea also gained nearly 10 km^3 water volume but it did not suffer such a significant drop as observed from GRACE and the Amu Darya discharge. This can be partly explained by the travel time that the water needs to reach the lake through the dried-out surroundings. During the summer, when GRACE

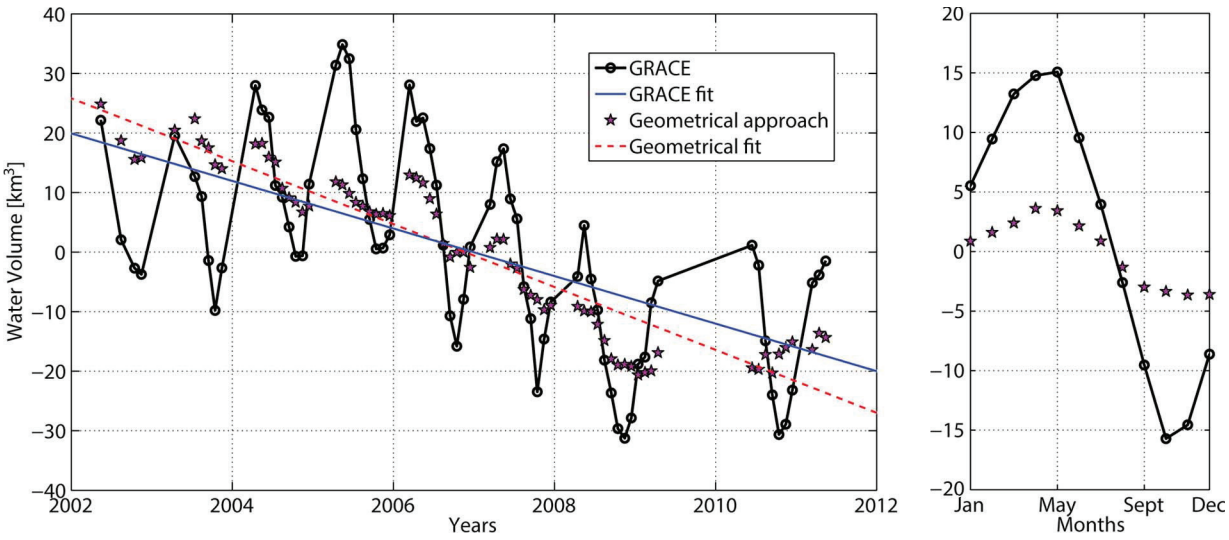

Fig. 6. Left: Volume change in $[\mathrm{km}^3/\mathrm{year}]$ of the Aral Sea resulting from GRACE and the geometrical approach; Right: Respective composite seasonal cycles of lake water storage.

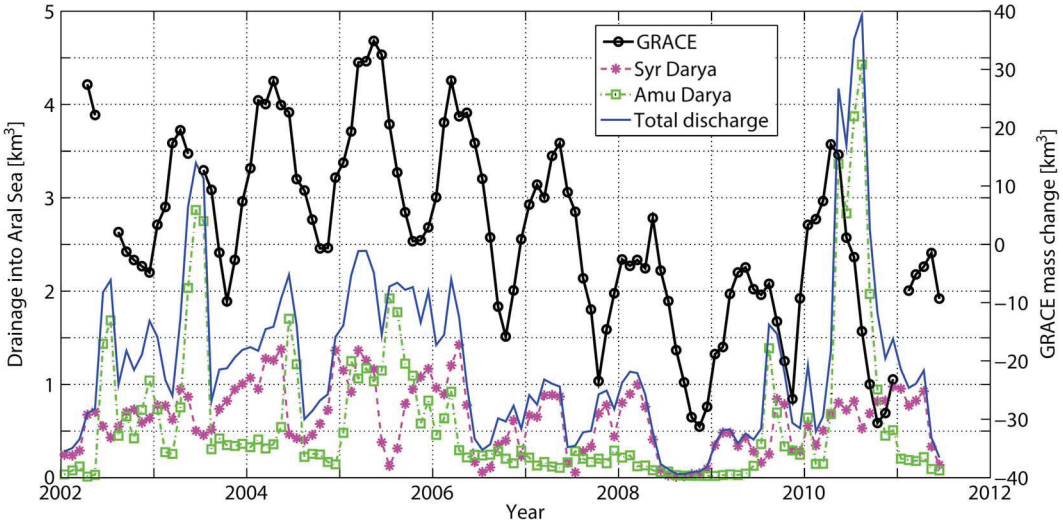

Fig. 7. Monthly discharge from Amu Darya, Syr Darya and their sum into the Aral Sea (axis on the left), compared with GRACE (axis on the right).

already observed a drastic mass loss, presumably due to strong evaporation from the large open surface area of the irrigated region in the surroundings, the lake continued refilling throughout this period followed by an obvious decline in 2011 which is also well observed in GRACE.

V. Conclusions

A generally good agreement between observed mass variations from GRACE and lake water volume variations has been found. GRACE features a much more pronounced inter-annual signal, but the long-term characteristics of gravimetrical and geometrical data are very similar. Hence, water storage in the Aral Sea turned out to be a strong contributor to the long-term mass change observed by GRACE. However there are also significant contributions from other mass signals in the area surrounding the lake. The comparison of geometrically based volume estimates with GRACE mass changes provides a promising means to analyse and separate the GRACE signals and—in turn—to estimate mass change signals in other hydrological compartments such as ground water. The combination of multi-satellite data proved to be effective in a comprehensive analysis of the hydrological condition of a region which otherwise is very poorly monitored by in-situ observations. Future work will comprise the analysis of the residual GRACE signal with respect to its consistency with soil moisture, snow and ground-water changes from observations and hydrological models.

References

[1] V. I. Kravtsova and T. V. Tarasenko, "Space monitoring of Aral Sea degradation," *Water Res.*, vol. 37, no. 3, pp. 285–296, 2010.

[2] G. Ramillien, J. S. Famiglietti, and J. Wahr, "Detection of continental hydrology and glaciology signals from GRACE: A review," *Surveys in Geophysics*, vol. 29, no. 4–5, pp. 361–374, 2008, 10.1007/s10712-008-9048-9.

[3] F. Seitz, M. Schmidt, and C. K. Shum, "Signals of extreme weather conditions in central europe in GRACE 4-D hydrological mass variations," *Earth and Planetary Science Letters*, vol. 268, no. 1–2, pp. 165–170, 2008, 10.1016/j.epsl.2008.01.001M.

[4] A. Singh, F. Seitz, and C. Schwatke, "Inter-annual water storage changes in the Aral Sea from multi-mission satellite altimetry, optical remote sensing, and GRACE satellite gravimetry," *Remote Sens. Environ.*, vol. 123, pp. 187–195, 2012, 10.1016/j.rse.2012.01.001.
[5] J.-F. Crétaux *et al.*, "Evolution of sea level of the big Aral Sea from satellite altimetry and its implications for water balance," *J. Great Lakes Research*, vol. 31, no. 4, pp. 520–534, 2005.
[6] S. Calmant, F. Seyler, and J. F. Crétaux, "Monitoring continental surface waters by satellite altimetry," *Surveys in Geophysics*, vol. 29, no. 4–5, pp. 247–269, Jan. 2009.
[7] Becker, W. LLovel, A. Cazenave, A. Güntner, and J.-F. Crétaux, "Recent hydrological behavior of the east african great lakes region inferred from GRACE, satellite altimetry and rainfall observations," *Comptes Rendus Geosciences*, 2010, 10.1016/j.crte.2009.12.010.
[8] H. P. Nachtnebel, H. Holzmann, and V. Dukhovny *et al.*, "The Rehabilitation of the Ecosystem and Bioproductivity of the Aral Sea Under Conditions of Water Scarcity," Final report of the INTAS project 0511 REBASOWS, Vienna, Austria, 2006, p. 75.
[9] P. O. Zavialov, "Physical oceanography of the large Aral Sea," in *The Aral Sea Environment: The Handbook of Environmental Chemistry*, A. G. Kostianoy and A. N. Kosarev, Eds. Berlin, Germany: Springer, 2010, vol. 7, pp. 123–145.
[10] F. Seitz, K. Hedman, F. Meyer, and H. Lee, "Multi-sensor space observation of heavy flood and drought conditions in the Amazon region," in *Earth on the Edge: Science for a Sustainable Planet, IAG Symposia*, C. Rizos and P. Willis, Eds. Berlin, Germany: Springer, 2013, vol. 139.
[11] F. Flechtner, "Gravity Recovery and Climate Experiment AOD1B Product Description Document for Product Releases 01 to 04," Potsdam, Germany, Tech. Rep. GRACE 327-750, Rev. 3.1, GFZ, 2007.
[12] J. Wahr, M. Molenaar, and F. Bryan, "Time variability of the Earth's gravity field: Hydrological and oceanic effects and their possible detection using GRACE," *J. Geophys. Res.*, vol. 103, no. B12, pp. 30205–30229, 1998.
[13] S. Swenson and J. Wahr, "Multi-sensor analysis of water storage variations of the caspian sea," *Geophys. Res. Lett.*, vol. 34, p. L16401, 2007, 10.1029/2007GL030733.
[14] P. F. Döll, F. Kaspar, and B. Lehner, "A global hydrological model for deriving water availability indicators: Model tuning and validation," *J. Hydrol.*, vol. 270, no. 1–2, pp. 105–134, 2003, 10.1016/S0022-1694(02)00283-4.
[15] J. Kusche, R. Schmidt, S. Petrovic, and R. Rietbroek, "Decorrelated GRACE time-variable gravity solutions by GFZ, and their validation using ahydrological model," *J. Geodesy*, vol. 83, no. 10, pp. 903–913, 2009, 10.1007/s00190-009-0308-3.
[16] J. Wahr, M. Molenaar, and F. Bryan, "Time variability of the Earth's gravity field: Hydrological and oceanic effects and their possible detection using GRACE," *J. Geophys. Res.*, vol. 103, no. B12, pp. 30205–30229, 1998, 10.1029/98JB02844.
[17] B. Tapley, S. Bettadpur, J. Ries, P. Thompson, and M. Watkins, "GRACE measurements of mass variability in the earth system," *Science*, vol. 305, pp. 503–505, 2004, 10.1126/science.1099192.
[18] M. Schmidt, F. Seitz, and C. K. Shum, "Regional four-dimensional hydrological mass variations from GRACE, atmospheric flux convergence, and river gauge data," *J. Geophys. Res.*, vol. 113, no. B10, p. B10402, 2008, 10.1029/2008JB005575.

Alka Singh received the M.A. degree in geography from the Awadesh Pratap Singh University Rewa, in 2005 and Advance Diploma in Remote Sensing and GIS Applications from the Jamia Milia Islamia University, New Delhi, India, in 2007. She obtained the M.Sc. in geoinformatics from the Faculty of Geo-Information Science and Earth Observation (ITC), Enschede, The Netherlands, in 2009. Since July 2010 she has been pursuing the Ph.D. at the Institute for Astronomical and Physical Geodesy, Technical University Munich, Germany.

Florian Seitz received the M.Sc. degree in geodesy from the Technische Universität München (TUM), Germany, in 2000. In 2004 he received the Ph.D. degree from TUM with distinction, and in 2011 he received the post-doctoral lecture qualification (Habilitation) in space geodesy.

After his graduation in 2000, he joined the German Geodetic Research Institute (Deutsches Geodätisches Forschungsinstitut, DGFI) in Munich, Germany, where he collaborated in various projects in the fields of Earth rotation, gravity field and surface geometry. During 2006 he joined NASA's Jet Propulsion Laboratory, Pasadena, CA, USA. In 2007 he returned to the TUM as an Assistant Professor for Earth Oriented Space Science and Technology, and in 2012 he was appointed full Professor for Geodetic Geodynamics at the TUM and Director of the DGFI.

Prof. Seitz was appointed Fellow of the International Association of Geodesy (IAG) in 2011 in recognition of his services rendered as Chair of an international study group in the frame of IAG's Inter-Commission Committee on Theory (ICCT).

Christian Schwatke was born in Munich, Germany, in 1980. He received the diploma and Master degree in computer science from the University of Applied Science, Munich, Germany, in 2008.

Since 2008, he has been an Research Associate at the Deutsches Geodätisches Forschungsinstitut (DGFI). His research interest includes satellite altimetry over lakes, rivers, and wetlands.

Since 2010, he has been Chair of the EUROLAS Data- and Operation-Center within the International Laser Ranging Service (ILRS).

Paper-3

Singh, A.; Kumar, U.; Seitz, F.: **Remote sensing of storage fluctuations of poorly gauged reservoirs and its state space model (SSM) based estimation;** Remote Sensing, Vol. 7, issue 12, pp 17113–17134, 2015. DOI: 10.3390/rs71215872 (Open source).

remote sensing

MDPI

Article

Remote Sensing of Storage Fluctuations of Poorly Gauged Reservoirs and State Space Model (SSM)-Based Estimation

Alka Singh [1,*], Ujjwal Kumar [2] and Florian Seitz [1]

Received: 9 October 2015; Accepted: 7 December 2015; Published: 18 December 2015
Academic Editors: Magaly Koch and Prasad S. Thenkabail

[1] Deutsches Geodätisches Forschungsinstitut, Technische Universität München, Arcisstr. 21, 80333 Munich, Germany; florian.seitz@tum.de
[2] School of Environment & Natural Resources (SENR), Doon University, 248001 Dehradun, India; ujjwalkumarin@yahoo.co.in
* Correspondence: alka.singh@bv.tum.de; Tel.: +49-89-23031-1214; Fax: +49-89-23031-1240

Abstract: To reduce hydrological uncertainties in the regular monitoring of poorly gauged lakes and reservoirs, multi-dimensional remote sensing data have emerged as an excellent alternative. In this paper, we propose three methods to delineate the volume of such equipotential water bodies through a combination of altimetry (1D), Landsat (2D) and bathymetry (2D) data, namely an altimetry-bathymetry-volume method (ABV), a Landsat-bathymetry-volume method (LBV) and an altimetry-Landsat-volume-variation method (ALVV). The first two data products are further merged by a Kalman-filter-based state space model (SSM) to obtain a combined estimate (CSSME) time series and near future prediction. To validate our methods, we tested them on the well-measured Lake Mead and further applied them on the poorly gauged Aral Sea, which has inaccurate bathymetry and very limited ground observation data. We updated the lake bathymetry of the Aral Sea, which was more than half a century old. The resultant remote sensing products have a very good long-term agreement among each other. The Lake Mead volume estimations are very highly coherent with the ground observations for all cases ($R^2 > 0.96$ and NRMSE < 2.1%), except for the forecast ($R^2 = 0.75$ and NRMSE = 3.7%). Due to lack of *in situ* data for the Aral Sea, the estimated volumes are compared, and the entire Aral Sea LBV and ABV have $R^2 = 0.91$ and NRMSE = 5.5%, and the forecast compared to CSSME has $R^2 = 0.60$ and NRMSE = 2.4%.

Keywords: remote sensing product; water storage; Landsat; altimetry; state space model (SSM); lakes and reservoirs; Lake Mead; Aral Sea

1. Introduction

Lakes and reservoirs are vital not only because they are a major source of water for domestic and industrial usage for human beings, but also because of their riparian zones, where some of the most bio-diverse ecosystems exist. Eventually the rapidly changing water volume of lakes and reservoirs disturbs not only human settlements that are dependent on them, but also whole ecosystems. Therefore regular monitoring and dynamic modeling of water volume variations are crucial for the proper management of this limited but highly essential resource. On a global scale, relatively few water bodies are regularly monitored by traditional *in situ* measurements. In the last few decades, satellite remote sensing has evolved as a promising alternative for regular global monitoring of water resources [1–3]. Satellite altimetry is now a well-established tool for inland water level estimation [4–7] and Landsat, with its long archive, free availability and relatively high-resolution database, delivers one of the most frequently used remote sensing data sets [8–11].

In this paper, we explored the potential of multi-dimensional satellite remote-sensing-based reservoir water volume estimation methods. We evaluated the monthly volume dynamics of the Aral Sea and Lake Mead using three independent methods. First, we used the altimetry-bathymetry-volume (ABV) method, which intersects the digital elevation model (DEM) of the reservoir bathymetry with the water level time series generated from satellite altimetry observations [12,13]. Secondly, we used the Landsat-bathymetry-volume (LBV) method, which is relatively less explored. In this method, the water height time series is generated by the intersection of the bathymetry of the reservoir with the temporal evolution of the shorelines generated from the Landsat images. Andreoli *et al.* [14] integrated a 90 m SRTM (Shuttle Radar Topography Mission) DEM with 75 m–1 km ENVISAT images and averaged the water levels at the boundary buffer to derive water height. In other previous studies, *in situ* water levels were combined with satellite-derived areas to obtain the volume [13,15,16]. Thirdly, we used the altimetry Landsat volume variation (ALVV) method by combining the water level from satellite altimetry with the respective surface area of the reservoir to obtain the volumetric variations [16–19]. Other groups [16,20] used a similar approach of estimating volumes by three methods; however, they either combined *in situ* observations or used existing elevation-volume relationships or storage capacities of the reservoirs from different databases. In this paper, we present a new LBV method for reservoir volume estimation and compare it to the results obtained from the ABV and ALVV methods. Furthermore, we design a Kalman-filter-based state space model to combine the estimated absolute volume from LBV and ABV. In our study, we did not use any ground observation information other than the bathymetry of the water body. If bathymetry is not available then one can extrapolate the best available DEM to fill the masked waterbody, considering gradual change in the Earth's geometry. For our methods, even an approximate bathymetry can be sufficient, which is later updated (for the range of observed heights during the study).

These methods have inherent unknown uncertainties because of the inaccuracy of the DEM and errors in the measurement of satellite observations (discussed later). For the ungauged reservoirs where there is no ground information to validate, it is difficult to say which is the more accurate estimation of reservoir volume. Therefore, we propose combining the absolute volumes from ABV and LBV using a Kalman-filter-based state space model (SSM). The state space model or state space time series analysis (as applied in this work) has applications in many different fields [21–24]. Wallerman *et al.* [25] presented a Bayesian state space model of forest attributes using field measurements and remote sensing data. In this study, we present a Kalman-filter-based state space model for remote sensing data assimilation and time series analysis. SSM is robustly capable of dealing with the trends, seasonality, interventions and uncertainties in a time series. In this study, the SSM has also been used to fill the missing values in ABV and LBV and to predict two years' water volume, based on the time series of combined estimates. Besides, as a by-product, we generated the latest bathymetry for the receded reservoirs, which could be used for estimating future refilling and variations. The methodology of this paper is described in Figure 1; within this paper, we use the word "reservoir" for all water bodies including both artificial and natural lakes.

To validate our algorithms, we estimated the absolute volume and volumetric variations of two drastically declining water bodies: the Aral Sea (an ungauged/poorly gauged lake) and Lake Mead (a very well monitored and recorded reservoir). The Aral Sea was the fourth largest lake in the world until the 1960s [26]; however, it has lost 85% of its area and 92% of its water volume in the past half century (1960s–2012) [27]. Moreover, the population dependent on the Aral Sea has increased by four times [28]. Lake Mead is the largest capacity reservoir in the United States and dropped to 39% of its capacity in July 2014 (Bureau of Reclamation). The topography of the two test sites is quite different; the Aral Sea is located in the central Asian plains whereas Lake Mead is in the foothills of the Rocky Mountains, enabling analysis of our methods in different scenarios.

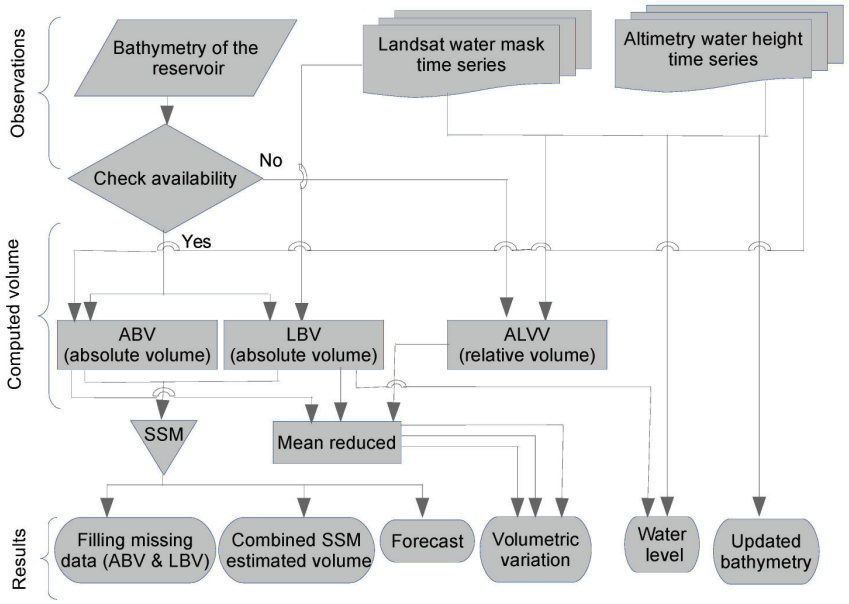

Figure 1. Methodology of the paper.

2. Data and Pre-Processing

2.1. Changes in the Shoreline

The monthly time-series of the Landsat TM/ETM+/OLI images, from January 2002 to December 2014 are downloaded from www.earthexplorer.usgs.gov. To cover the entire Aral Sea, a minimum of four sets of Landsat images are required, while Lake Mead is covered by only one Landsat image for each observation. Furthermore, in the Aral Sea region almost no interpretable images are available for 3–4 months during winter (from December to March) because of ice, snow and storms, while Lake Mead does not have such climatic conditions. For the Aral Sea, only 84 mosaicked sets can be produced from a combination of the all Landsat satellites during the study period, while Lake Mead is over sampled by 250 snap shots for the same duration. To produce a monthly time series, data gaps are filled by a SSM-based missing data modification method (described in Sections 3.2.3 and 4.3.1) and oversampled data within a month are averaged.

Additional pre-processing is required for Landsat ETM+ images from 31 May 2003 because of a scan line corrector (SCL) failure in the sensor, which caused a 22% loss in any given scene. Scaramuzza *et al.* [29] demonstrated that for a single image, local linear histogram matching provides a good result for SLC-off gap filling, which employs a triangulation technique in a moving window of each missing pixel. Therefore, for Lake Mead, the Delaunay triangulation method is used to fill the data gap by calculating triangles from surrounding good pixels. In the case of the Aral Sea, the Delaunay triangulation filling method can introduce classification errors because of the adjoining very bright pixels from the salt deposits of the shrinking lake. Therefore, two extra Landsat scenes are mosaicked to fill the SLC-off stripes from adjacent paths. Hence, a total of six scenes for each timeframe is mosaicked for the Aral Sea, which were acquired on different dates within a month. The overlapping areas are color matched by histogram matching to obtain a seamless mosaic. The images are geo-rectified by the nearest-neighbor resampling method to co-register them during the mosaic operation. The resultant image still had some residual gaps. Therefore, the mosaicked scenes with an SLC-off gap are first classified, then filled by focal filling (3–5 times). Consequently, the mask size increased; therefore, after complete filling, one border pixel is deleted per focal filling instance to reduce the mask to approximately its original size and shape.

The mosaicked near-infrared band of Landsat images are classified by an unsupervised isodata classifier to obtain the water mask at a 30 m spatial resolution. The Aral Sea has a complex spectral signature due to salt deposits and shallow water; therefore it is first classified into 10 spectral clusters, which are later merged into two, as water and non-water. First, two spectral clusters are mostly identified as water bodies by visual interpretation; the remaining classes are set as land. In the shallow East Aral Sea, the water boundary is not very clear, so that even the visual interpretation is uncertain. Unfortunately, we have no ground data from the Aral Sea to verify the classification results. For Lake Mead, direct two-class isodata classification was sufficient because of its deep structure and clear water boundary. The shallow East Aral Sea disappeared completely during the study period, while relatively little change is observed in the size and shape of Lake Mead (Figure 2).

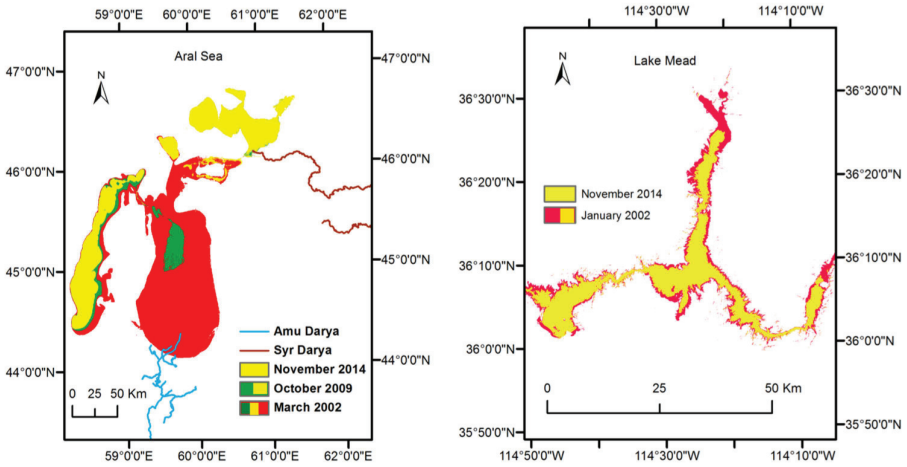

Figure 2. Receding shorelines observed from Landsat. **Left**: the Aral Sea, and **right**: Lake Mead.

2.2. Changes in Water Level

In this study, observations of satellite altimetry are taken from high frequency data of Envisat, Jason1, Jason2, Jason1 extended and Saral/Altika mission, using all passes and missions available at coordinates shown in Table 1. The time series of water levels have been derived from DGFI's data-base for inland waters (DAHITI) at http://dahiti.dgfi.tum.de/en/ [5].

Table 1. Details of used altimetry missions.

Reservoir	Longitude (Degrees)	Latitude (Degrees)	Mission	Pass
Mead	−114.49	36.137	Envisat	0811
			Jason1 extended	180
			Saral/Altika	0811
North Aral	60.7489	46.5211	Envisat	0126, 0167, 0625
			Jason1	218, 107
			Jason2	218, 107
			Saral/Altika	0126, 0167, 0625
East Aral	59.7146	44.9415	Jason1	142, 107
			Jason2	142, 107
			Saral/Altika	0670
West Aral	58.5626	45.1947	Envisat	0797, 0212
			Jason1 extended	107
			Jason2	142
			Saral/Altika	0797, 0212

Lake Mead *in situ* elevation data are taken from a local power-house datum at coordinates of 36.02°N, 114.74°W. The power-house datum is 0.762 m above the North American Vertical Datum of 1988 (NAVD-88). Therefore, we added the difference to bring the altimetry observations to the *in situ* power-house reference system.

2.3. Bathymetry

In this study, we collected DEMs from different sources and modified them to obtain the best possible bathymetry. For the Aral Sea, the digital contour map at 1 m contour spacing, derived from a 1960s 1/500,000 scale map, is provided by Prof. Renard [30] by personal communication. The given map is re-projected to UTM Zone 40 over WGS84 North datum. The poly-lines are converted to a point feature class for interpolation. Universal kriging of the point data, modeled by spherical semi-variogram and re-sampled by bilinear interpolation generates the raster digital bathymetry model at 30 m resolution. The resultant digital bathymetry model showed better agreement with the shoreline time-series generated from Landsat images than the model used in our earlier publication [31].

The 1-m spatial resolution DEM for Lake Mead is generated from the 5 ft. resolution triangulated irregular network (TIN) data provided by the Bureau of Reclamation, projected to UTM Zone 11, NAD83 datum. For security reasons, the Hoover dam storage region was masked out in the data provided. To replace the missing data, another 10 m resolution DEM of Lake Mead was downloaded from USGS database [32] and interpolated to 1 m intervals. The combined 1 m spatial resolution bathymetry is used in the study for Lake Mead.

3. Methodology

3.1. Methods for Reservoir Volume Estimation

3.1.1. Altimetry-Bathymetry-Volume (ABV) Method

Water level observations from satellite altimetry are intersected with the bathymetry of the water body to produce the absolute water volume (ABV) by integrating all water height columns within a reservoir (discussed in Section 4.3.1 for Lake Mead and Section 4.3.2 for the Aral Sea). The resultant absolute volumes are further reduced by the first observation of the time series to obtain volume variation during the study period (discussed in Section 4.2).

3.1.2. Landsat-Bathymetry-Volume (LBV) Method

The Landsat-bathymetry-volume method is based on the assumption that the lake and reservoirs can be considered flat equipotential surfaces. Theoretically, the shorelines of the masked bathymetry image can be considered as one contour line, and all border pixels should have the same height. Extracting the water height from the masked bathymetry is not trivial because in reality, the extracted border pixels have a large range and elevation variance. This can be due to uncertainty in the water mask, coarse bathymetry and high gradients. Taking into account all these issues, we obtain a range of water heights from the shoreline and bathymetry intersection. The algorithm developed to obtain the final height from the Landsat mask is described in Figure 3.

We traced the border of the masked bathymetry clockwise and collected the boundary pixel values to obtain the entire boundary vector (EBV), starting from the first column of the mask from the left (Figure 4, red asterisks). At the same time, we selected a subsection of the water body (Figure 4, red rectangles) based on the knowledge of the study site to obtain selected region boundary (SRB) values. We proposed two criteria for the selection of the subsection of the basin. (1) The subsection should have a comparatively lower gradient, so that there is less height variation within each 30 m pixel; (2) It should be comparatively stable, *i.e.*, not under direct flow of water (Figure 4: red magenta arrow shows the river mouth) to uphold the concept of an equipotential surface.

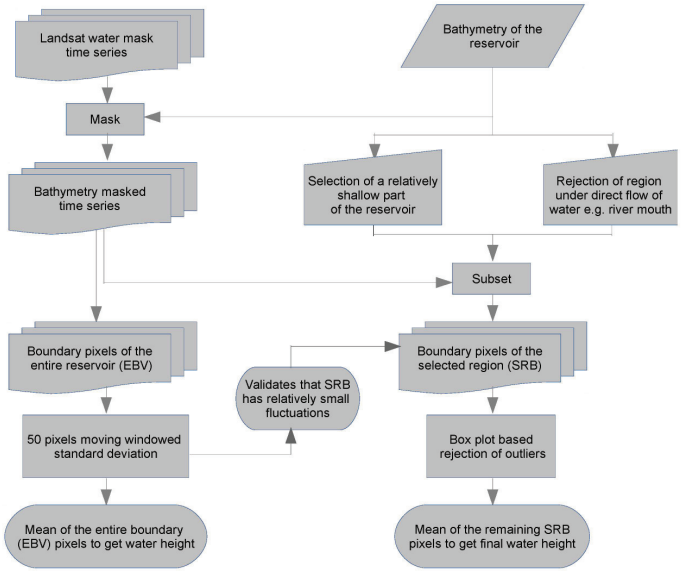

Figure 3. Algorithm of water level estimation in the LBV method: rectangular boxes indicate processes, trapezoids indicate the manual operation and multiple document boxes indicate the time series of the images.

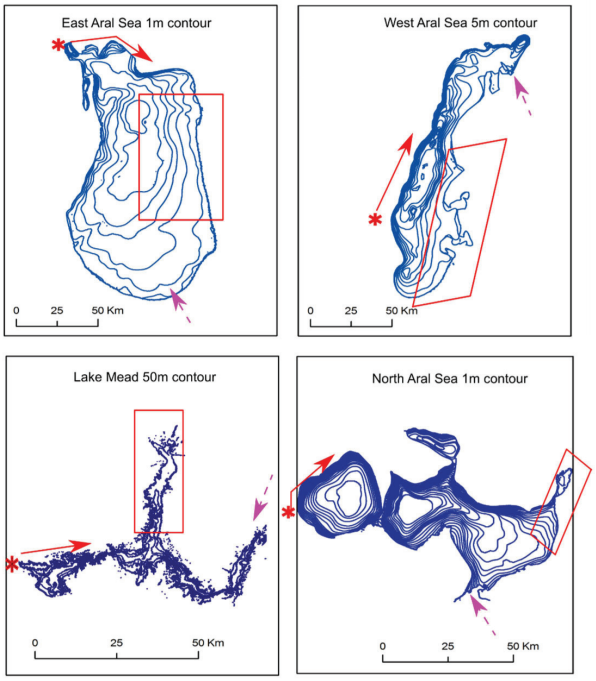

Figure 4. Contour of reservoirs; * starting point of boundary pixel collection; the red rectangle is the subsection of the reservoirs for selected area boundary pixels and the large magenta dashed arrow shows the mouth of the river.

As examples, Landsat image shorelines for every fifth available epoch from the East Aral Sea are plotted in Figure 5. The plot shows the elevation variation along the shoreline; the blue lines on the left axis are EBV, the red lines are the pixels from SRB; and the green plot on the right axis shows the standard deviation of the 50 adjacent pixels of EBV. The 50-pixel moving window standard deviation

indicates that there are regions in the reservoir that always have relatively low elevation variance. For example, in the East Aral Sea, less than 10 cm of dispersion is observed from the eastern and southern ends (Figure 4). The beginning and end of EBV have relatively high standard deviations (Figure 5) because of close contours in the western and northern sides of the East Aral Sea (Figure 4). This demonstrates that the area selected for SRB is relatively stable.

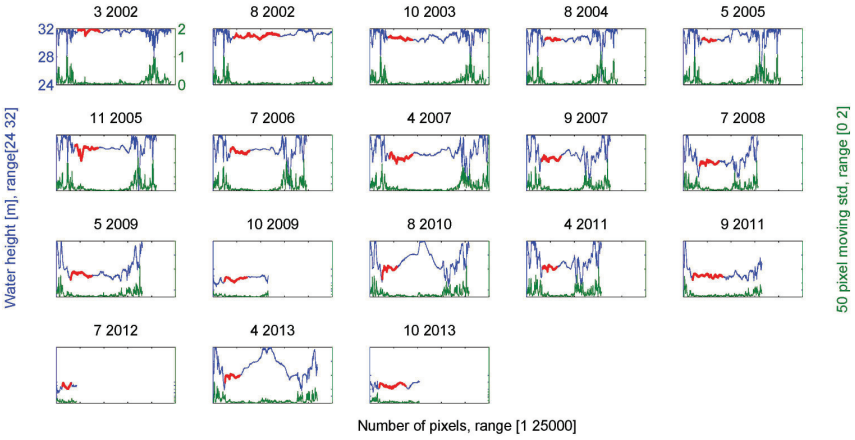

Figure 5. (**Left**) Boundary pixels of the East Aral Sea obtained from Landsat mask at different time points: blue line is the entire boundary vector (EBV), red portions are pixels from the selected region boundary (SRB); (**Right**) 50-pixel moving standard deviation of EBV.

In addition, we rejected pixels from the southern part of the East Aral Sea, because it is at the river mouth, and during flood events, it would not be an equipotential surface. We can observe this phenomenon in the subplots of Figure 5, e.g., floods of August 2010 and April 2013. A wide range of water heights are observed during the flood events from the southern part (Figure 5), although a 50-pixel standard deviation is still low. Therefore, EBV estimates higher water height during the flood events than SRB, because of the violation of equipotential surface assumption (discussed in Section 4.1). The total number of pixels along the shoreline are also significantly reduced during the study period because of the shrinking of the East Aral Sea (Figure 5). A similar phenomenon is observed from all other reservoirs; therefore, pixels from the SRB regions shown as red rectangles in Figure 4 are processed to obtain the water height from all reservoirs.

The outliers from the SRB vectors (Figure 5: red line) are rejected on the box plot distributional assessment basis [33,34]. To find the outliers, a lower quantile (Q1), upper quantile (Q3) and inter-quantile range (H) are calculated for each SRB vector. Values lower than (Q1 − Q3) × H and higher than (Q3 + Q3) × H are considered outliers and hence rejected. The final water height for each shoreline is assigned by taking the mean of the remaining elevation vector.

Finally, the absolute water volume time series (LBV) is generated for each reservoir from the SRB elevations by integrating the entire water height column within the shoreline (discussed in Section 4.3.1 for Lake Mead and Section 4.3.2 for the Aral Sea). Similar to ABV, LBV time series are also reduced by the first observation to obtain volume variations (discussed in Section 4.2).

3.1.3. Altimetry-Landsat Volume Variation (ALVV) Method

In many cases, bathymetry of a water body is not available. Here a completely remote sensing based approach can be the best alternative for volume variation estimation. Unlike the first two methods, instead of using a DEM, we combined the area calculated from Landsat and the elevation calculated from altimetry to produce the volumetric changes in the water body using a pyramid frustum volume estimation method. This method assumes the water body to be an inverted truncated pyramid [18]. It computes the change in volume at each time step with the change in the elevation

and area of the truncated inverted pyramid with respect to the previous time step. The cumulative summation of each time step volume change derived from the trapezoidal volume formula is given in Equation (1).

$$ALVV = \sum_{t=1}^{n} \frac{1}{3} \times (H_t - H_{t-1}) \times \left(A_t + A_{t+1} + \sqrt{(A_t \times A_{t+1})} \right) \quad (1)$$

where

$ALVV$ = Total volume change with respect to the initial state (t_0) at the nth month

A_t = Area of the water extent at month t and A_{t-1} = Area of the water extent at the previous month

H_t = Elevation of the water body at month t and H_{t-1} = Elevation of the water body at the previous month. n = Number of months.

The two observation time series of the water surface area and water level are often difficult to synchronize because the dates of acquisition of data from Landsat and different altimetry missions are often not the same. For Lake Mead, area and elevation data points that fall within the same 10-day period are used. For the Aral Sea, a monthly window is used because the whole lake is covered by combining three Landsat paths; therefore, a single date cannot be assigned per observation. The outliers are rejected on the basis of the quantile quantile plot [35] and then from the extracted area and water level samples, a linear relationship is derived (Figure 6). The coefficient of determination (R^2) between the area and elevation shows a strong linear correlation (>0.92) with NRMSE <2% for all of the reservoirs, except the East Aral Sea (NRMSE = 6%), because of the large area-level ratio due to its almost flat structure. Therefore, the derived relationship can be used to fill the missing values in any of the two sets of data. In the case of unavailability of both datasets, the time series is interpolated based on nearest neighbors. The resultant continuous monthly area level data are used in Equation (1) to estimate storage variations (discussed in Section 4.2).

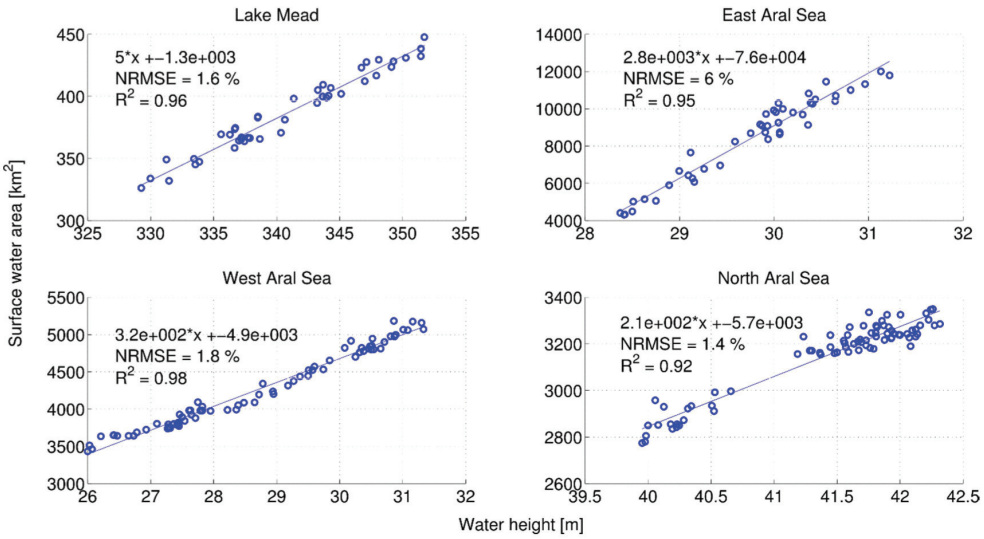

Figure 6. Surface area and water height relation.

3.2. State Space Model for the Estimation and Prediction of Absolute Volume Time Series

3.2.1. Structure of a State Space Model (SSM)

State space modeling provides a unified methodology for treating a wide range of problems in time series analysis such as forecasting, signal extraction and estimation of parameters. It assumes that an unobserved series of vectors, in our case true volume x, is associated with a series of observations (ABV and LBV) y_1 and y_2, which determine the development of the system over time. The relation

between x_t and y_t is specified by the state space model. The state-space model or dynamic linear model (DLM), in its basic form, employs an order one vector auto regression as the state equation (Equation (2)) [36].

$$x_t = \phi x_{t-1} + w_t \tag{2}$$

where the state equation determines the rule for the generation of the $p \times 1$ system state vector x_t from the past $p \times 1$ state x_{t-1} for time points $t = 1, ..., n$. We assume that the, process noise w_t is $p \times 1$ independent and identically distributed, zero-mean normal vectors with covariance matrix Q (i.i.d. N (0, Q)) and ϕ is a state transition matrix. The process noise represents some sudden change in the trend, e.g., a flood in our case. In the DLM, we assume the process starts with a normal vector x_0 that has mean μ_0 and $p \times p$ error covariance matrix σ_0.

Further, the SSM assumes that we observe the state vector x_t indirectly by its linear transformed version with added noise (Equation (3)) *i.e.*, unknown observational error associated with ABV and LBV in this case.

$$y_t = A_t x_t + v_t \tag{3}$$

where A_t is a $q \times p$ measurement matrix and v_t is a measurement noise vector ~i.i.d. N (0, R) with measurement noise covariance matrix R. Equation (4) is called the observation or measurement equation.

The primary aim of any analysis involving the state-space model would be to produce estimators for the underlying unobserved signal x_t given the data $Y_s = \{y_1, y_2\}$, to time s by minimizing error covariance. When $s < t$, the problem is called forecasting or prediction; when $s = t$, the problem is called filtering; and when $s > t$, the problem is called smoothing, which is used for filling the data gap. The solution to these problems is accomplished via the Kalman filter and smoother [36]. Throughout the discussion, we will use the following definitions:

$$\text{Estimation } x_t^s = E\left(x_t | Y_s\right) \tag{4}$$

and

$$\text{Error covariance } P_{t_1,t_2}^s = E\{(x_{t_1} - x_{t_1}^s)(x_{t_2} - x_{t_2}^s)'\} \tag{5}$$

The Kalman filter minimizes the state error covariance matrix P by weighted least squares using Q (Equation (8)) and R (Equation (12)). Therefore, the Kalman filter can be considered as a predictor-corrector system.

3.2.2. The Kalman Filter

For the state space model specified in Equations (2) and (3), state propagation and state error propagation is defined by Equations (6) and (7) for $t = 1, \ldots, n$

$$x_t^{t-1} = \phi x_{t-1}^{t-1} + w_t \tag{6}$$

$$P_t^{t-1} = \phi P_{t-1}^{t-1} \phi' + Q \tag{7}$$

The prior state estimate (Equation (6)) and the prior error covariance (Equation (7)) are updated based on observations y_t to obtain the posterior state estimate (Equation (8)) and the posterior error covariance (Equation (9)). The prediction for $t > n$ is accomplished via Equations (6) and (7) with initial conditions $x_n^n | P_n^n$.

$$x_t^t = x_t^{t-1} + K_t \left(y_t - A_t x_t^{t-1}\right) \tag{8}$$

$$P_t^t = \left[I - K_t A_t\right] P_t^{t-1} \tag{9}$$

where

$$K_t = P_t^{t-1} A_t' \left[A_t P_t^{t-1} A_t' + R\right]^{-1} \tag{10}$$

The Kalman gain K_t is computed by a recursive least squares solution, which trades off state uncertainty and measurement noise. Equations (8) and (10) suggest that when the magnitude of R is small, the measurements are accurate, and then the state estimate depends mostly on the measurements and vice versa. The new measurements add to knowledge of the system; therefore, the estimated error decreases in Equation (9). The posterior uncertainty or covariance is always less than the prior as it is reduced by the multiple of the Kalman gain (Equation (10)). Important byproducts of the filter are the innovations (prediction errors)

$$\epsilon_t = y_t - E\left(y_t \mid Y_{t-1}\right) = y_t - A_t x_t^{t-1} \tag{11}$$

and the corresponding variance-covariance matrices

$$var\left(\epsilon_t\right) = var[A_t\left(x_t - x_t^{t-1}\right) + v_t\Big] = A_t P_t^{t-1} A_t' + R \tag{12}$$

The proof of these Kalman filter equations can be found in Shumway and Stoffer, (2011) [37].

3.2.3. Missing Data Modifications

An attractive feature available within the state-space framework is its ability to treat time series that have been observed irregularly over time. The definition of smoothing described above is used to obtain the estimate for missing data [37].

3.2.4. Estimates of Underlying Signal from Two Observation Time Series

In the present study, the absolute water volume estimates have been obtained from two observation time series LBV and ABV. We suppose that both series observe the same signal of actual water volume of the reservoir x_t with different error in the measurements (v_{t1} and v_{t2}). In our case the state transition model ϕ and measurement model A_t are the identity matrix.

$$y_{t1} = x_t + v_{t1} \text{ and } y_{t2} = x_t + v_{t2} \tag{13}$$

more compactly,

$$\begin{pmatrix} y_{t1} \\ y_{t2} \end{pmatrix} = \begin{pmatrix} 1 \\ 1 \end{pmatrix} x_t + \begin{pmatrix} v_{t1} \\ v_{t2} \end{pmatrix} \tag{14}$$

where

$$R = var\begin{pmatrix} v_{t1} \\ v_{t2} \end{pmatrix} = \begin{pmatrix} r_{11} & 0 \\ 0 & r_{22} \end{pmatrix} \tag{15}$$

Here r_{11} and r_{22} are the variance of the observation error v_{t1} and v_{t2} respectively, which is equal to one at $t = 1$. In our case, we do not know the noise in ABV and LBV. Therefore at $t = 1$ we randomly put some value for v_{t1} and v_{t2}, which is recursively optimized to estimate error by Equations (11) and (12). The Combined SSM estimate (CSSME) takes the mean of LBV and ABV reduced by their respective error (Equation (16)).

$$x_t = 1/2\left\{(y_{t1} - v_{t1}) + (y_{t2} - v_{t2})\right\} \tag{16}$$

It is reasonable to suppose that the unknown common signal x_t, can be modeled as a random walk with drift (Equation (17)) of the form

$$x_t = \delta + x_{t-1} + w_t \tag{17}$$

with δ = stochastic trend component of the signal, computed on every step by maximum likelihood estimator. The estimation of unknown parameters contained in Q and R, which define this model, is carried out using the Kalman recursion as described above.

3.2.5. Signal Extraction and Forecasting

Once the CSSME is obtained from ABV and LBV time series data by applying the aforementioned procedure, the recursive six monthly forecast for the next two years has been carried out based on CSSME time series. Since CSSME exhibits trend as well as seasonality, we consider the series to be the sum of a trend component, a seasonal component, and white noise. The CSSME series can be expressed as the Equation (18) [37]

$$y_t = T_t + S_t + v_t \tag{18}$$

where T_t is trend and S_t is the seasonal component. Suppose we allow the trend to increase exponentially; that is,

$$T_t = \phi T_{t-1} + w_{t1} \tag{19}$$

where the coefficient $\phi > 1$ characterizes the increase and $\phi < 1$ charaterizes the decrease. Let the seasonal component be modeled as

$$S_t + S_{t-1} + S_{t-2} + S_{t-3} = w_{t2} \tag{20}$$

which corresponds to assuming the seasonal component is expected to sum to zero over a complete period or four quarters. w_{t1} and w_{t2} are the trend and seasonal noise respectively.

The model can be expressed in state-space form as below. Let $x_t = (T_t, S_t, S_{t-1}, S_{t-2})\prime$ be the state vector, then the state equation (Equation (2)) can be written as (Equation (21))

$$\begin{bmatrix} T_t \\ S_t \\ S_{t-1} \\ S_{t-2} \end{bmatrix} = \begin{bmatrix} \phi & 0 & 0 & 0 \\ 0 & -1 & -1 & -1 \\ 0 & 1 & 0 & 0 \\ 0 & 0 & 1 & 0 \end{bmatrix} \begin{bmatrix} T_{t-1} \\ S_{t-1} \\ S_{t-2} \\ S_{t-3} \end{bmatrix} + \begin{bmatrix} w_{t1} \\ w_{t2} \\ 0 \\ 0 \end{bmatrix} \tag{21}$$

and the measurement equation (Equation (3)) as

$$y_t = [1\ 1\ 0\ 0] \begin{bmatrix} T_t \\ S_t \\ S_{t-1} \\ S_{t-2} \end{bmatrix} + v_t \tag{22}$$

with $R = r_{11}$ and

$$Q = \begin{bmatrix} q_{11} & 0 & 0 & 0 \\ 0 & q_{22} & 0 & 0 \\ 0 & 0 & 0 & 0 \\ 0 & 0 & 0 & 0 \end{bmatrix} \tag{23}$$

The model reduces to state space form, (Equations (2) and (3)), with $p = 4$ and $q = 1$. The parameters to be estimated by maximum likelihood for the model are the noise variance in the measurement equations (r_{11}), the model variances corresponding to the trend and seasonal components (q_{11} and q_{22}, respectively), and the transition parameter ϕ that models the increasing or decreasing trend. This model is used for forecasting purposes. Most of the equations presented in the SSM section are directly adapted from Shumway and Stoffer (2011) [37].

4. Results

4.1. Water Height

Lake Mead is often observed twice per year by Landsat and therefore the oversample height measurements were averaged per month. On the other hand, the lake has no altimetry observations for one year in 2012 due to an intermission gap. There, the Landsat-SRB height can be a good substitute.

Furthermore, the altimetry measurements obtained from the East Aral Sea for 2008 are contaminated by the reflection from land due to shrinking of the reservoir. Later available observations for 2010 and 2011 from altimetry have overestimated the water height due to flood and land boundary contamination as altimetry tracks cross the East Aral Sea from its southern end. These effects can be noticed in Figure 7 (top right), the Landsat-EBV (green line) and altimetry (blue line) observed false high, because during the flood event, the assumption of an equipotential surface get abandoned. Consequently, water heights observed from the southern part of East Aral Sea are higher than the relatively stable part selected in the Landsat-SRB (red line). Therefore, for the East Aral Sea from 2008, only Landsat-SRB water heights are used, and meaningful comparisons of the models for the reservoir are restricted until December 2007.

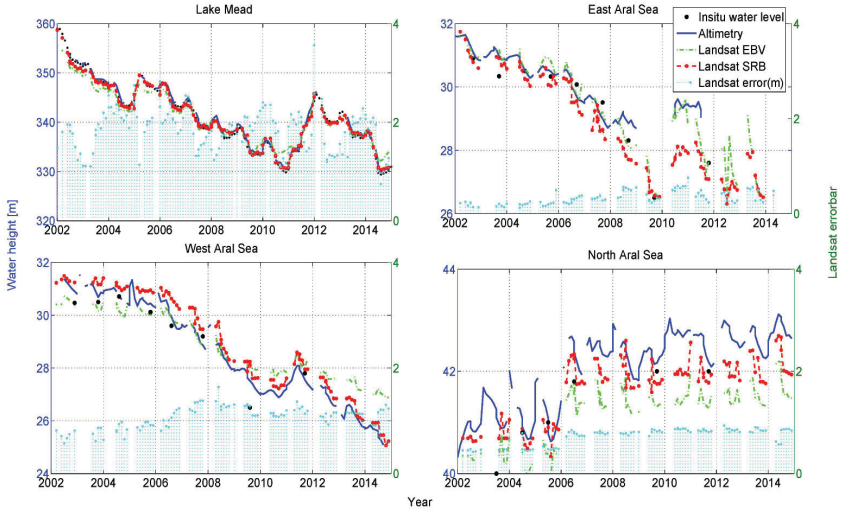

Figure 7. (**Left**) Water height observed by altimetry, Landsat: entire boundary vector (EBV), selected region boundary (SEB) and *in situ*; (**Right**) error bar for Landsat-SRB water height.

The water heights derived by the Landsat-SRB (Figure 7: red dashed line) from 2D Landsat masks are in very good agreement with the observed heights from satellite altimetry for all of the reservoirs. Landsat-EBV (Figure 7: green line) has measured higher elevations particularly during extreme events; for example, during the extreme droughts of the West Aral Sea (2014) and Lake Mead (2010 and 2014), and during floods of the East Aral Sea (2010 and 2013).

The approximate decrease in water height observed in Lake Mead, the East Aral Sea and the West Aral Sea during 2002–2014 are 28 m, 6 m and 6.5 m respectively, while a 2 m gain is observed for the North Aral Sea (Figure 7).

4.2. Volumetric Variation

To compare volumetric variations from ALVV, absolute volumes from ABV and LBV are subtracted by the first observation of each time series (Figure 8), which changes with respect to the January 2002 observation. The ALVV method can be applied to the reservoirs where no ground observations of the structure of the lakebed are available; thus, the volume cannot be calculated from ABV and LBV. These methods are preliminarily tested for Lake Mead, which has daily *in situ* data to validate the results, and the algorithms are then applied to the three sub-parts of the Aral Sea. The reduced ABV and LBV has a very good agreement with the *in situ* observations of Lake Mead and between each other in all of the sub-parts of the Aral Sea (discussed in Section 4.4.2). The North Aral Sea results are statistically poor but qualitatively the results are within the acceptable range (discussed in Section 4.4.1).

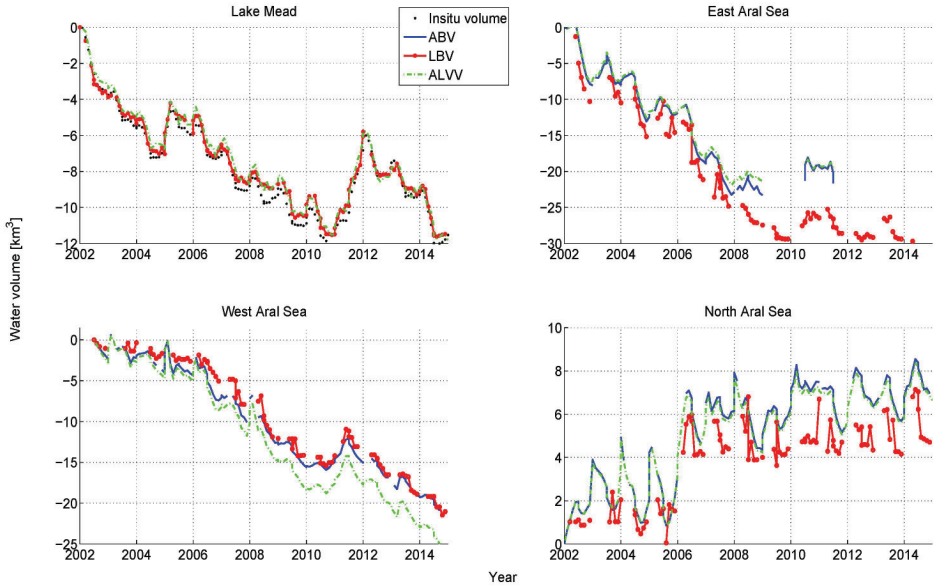

Figure 8. Volumetric variation computed by ABV, LBV and ALVV methods for the three sub-parts of the Aral Sea and for Lake Mead.

4.3. SSM Estimation and Prediction

4.3.1. Standard Case of Lake Mead

Lake Mead has been considered as a standard case to demonstrate the effectiveness of SSM because *in situ* data are available for the reservoir to verify the results. The SSM estimations for Lake Mead are plotted in Figures 9 and 10; a similar process is applied for the other reservoirs of the Aral Sea and their results are shown in Figure 11.

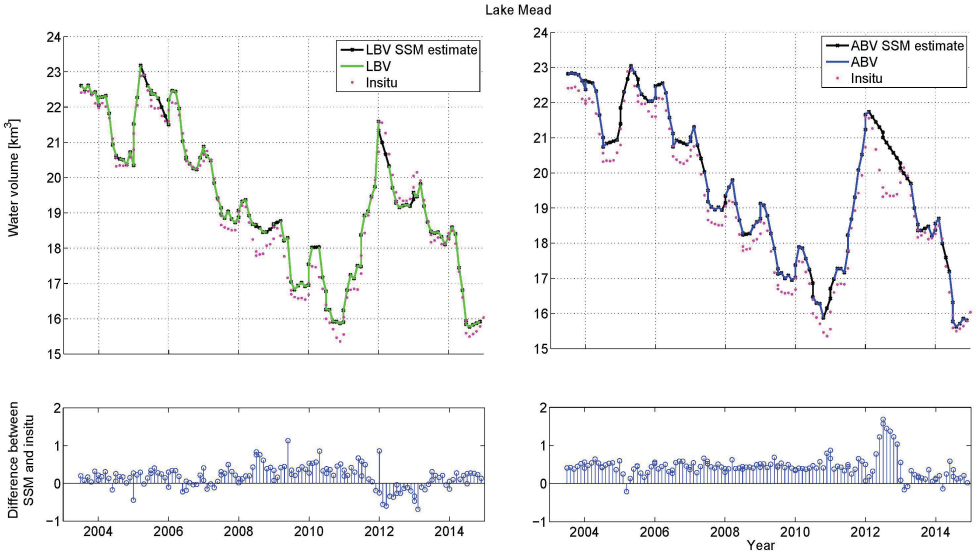

Figure 9. Missing data modification by SSM for the Lake Mead. (**Top left**) Landsat-bathymetry-volume (LBV) estimation and data gap filled by SSM; (**Bottom left**) difference between LBV-SSM estimates and *in situ* observations; (**Top right**) altimetry-bathymetry-volume (ABV) estimation and data gap filled by SSM; (**Bottom right**) difference between ABV-SSM estimates and *in situ* observations.

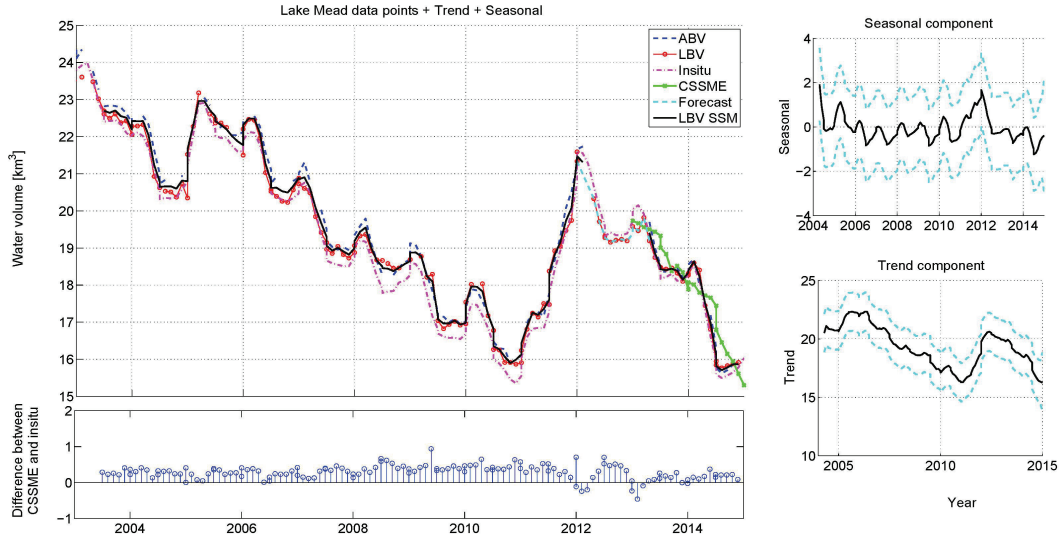

Figure 10. Lake Mead SSM analysis. (**Top left**) The combined SSM estimate (CSSME) (magenta line) and the forecast (green line) for 2013 and 2014; (**Bottom left**) difference between CSSME and *in situ* observations; (**Top right**) estimated seasonal component; (**Bottom right**) estimated trend component. The dashed cyan lines indicate the upper and lower 95% confidence limit.

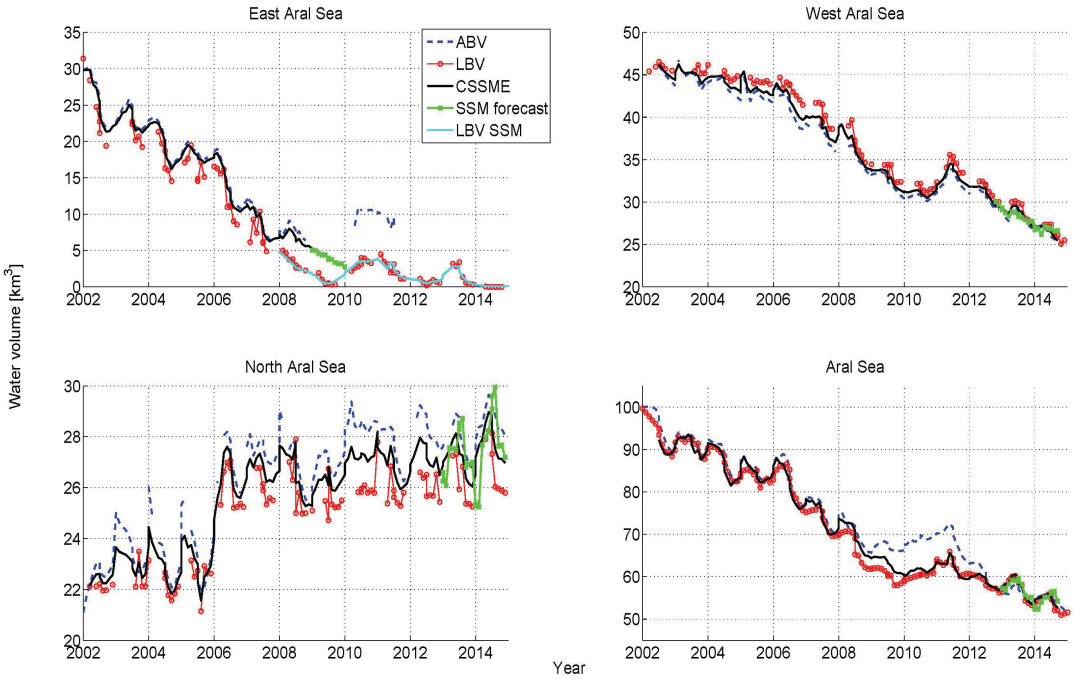

Figure 11. Aral Sea absolute volume (ABV and LBV), Combined SSM estimates, and SSM forecast.

Filling up the Missing Data with SSM

Since our datasets (ABV and LBV) have many missing values from all the reservoirs, these gaps are filled dynamically by respective ABV-SSM and LBV-SSM estimates (Figure 9). Consistent positive offset is observed in ABV and also frequently in LBV (Figure 9: bottom plot), which might be due to overestimation of height by altimetry and Landsat-SRB because of the difference in the geoid of the

sites of measurement. The *in situ* measurements are taken from the western side of Lake Mead near Hoover dam, and altimetry and Landsat-SRB observations are from Overton Arm of Lake Mead at north. However, LBV offset has a slightly lesser magnitude than ABV. Therefore, the ABV-SSM has a relatively high RMSE with respect to *in situ* observations, relative to the LBV-SSM (Table 2).

Table 2. Comparison of results from all the reservoirs by root mean square error (RMSE) and coefficient of determination (R^2).

Reservoir	Compared Results		RMSE (NRMSE)	R^2
Lake Mead	Landsat-SRB water height	*In situ* water height	0.59 m (0.2%)	0.99
	Altimetry water height	*In situ* water height	0.67 m (0.2%)	0.99
	Landsat bathymetry volume (LBV)	*In situ* absolute volume	0.32 km^3 (1.6%)	0.98
	Altimetry bathymetry volume (ABV)	*In situ* absolute volume	0.41 km^3 (2.1%)	0.97
	Altimetry Landsat volume variation (ALVV)	*In situ* reduced by first obs. (volume variation)	0.53 km^3	0.96
	ALVV	LBV reduced by first obs.	0.31 km^3	0.98
	ALVV	ABV reduced by first obs.	0.06 km^3	0.99
	Combined SSM estimate (CSSME)	*In situ* absolute volume	0.35 km^3 (1.8%)	0.97
	CSSME	LBV	0.32 km^3 (1.6%)	0.98
	CSSME	ABV	0.41 km^3 (2.1%)	0.97
	CSSME Forecast	CSSME	0.53 km^3 (3.0%)	0.80
	CSSME Forecast	*In situ* absolute volume	0.66 km^3 (3.7%)	0.75
West Aral Sea	Landsat-SRB water height	Altimetry water height	0.44 m (1.5%)	0.94
	LBV	ABV	1.58 km^3 (4.5%)	0.94
	ALVV	LBV reduced by first obs.	1.73 km^3	0.94
	ALVV	ABV reduced by first obs.	1.09 km^3	0.97
	CSSME	LBV	1.00 km^3 (2.7%)	0.97
	CSSME	ABV	0.50 km^3 (1.6%)	0.99
	CSSME Forecast	CSSME	0.52 km^3 (1.9%)	0.76
North Aral Sea	Landsat-SRB water height	Altimetry water height	0.50 m (1.2%)	0.32
	LBV	ABV	1.59 km^3 (6.0%)	0.23
	ALVV	LBV reduced by first obs.	1.46 km^3	0.56
	ALVV	ABV reduced by first obs.	0.15 km^3	0.99
	CSSME	LBV	0.82 km^3 (3.2%)	0.83
	CSSME	ABV	0.82 km^3 (3.1%)	0.83
	CSSME Forecast	CSSME	1.09 km^3 (3.9%)	0.23
East Aral Sea	Landsat-SRB water height (January 2002–December 2007)	Altimetry water height	0.33 m (1.0%)	0.82
	LBV (01.2002–12.2007)	ABV (January 2002–December 2007)	2.40 km^3 (13%)	0.85
	ALVV	LBV reduced by first obs.	4.26 km^3	0.51
	ALVV	ABV reduced by first obs.	0.67 km^3	0.99
	CSSME (January 2002–December 2007)	LBV (January 2002–December 2007)	1.92 km^3 (12.0%)	0.89
	CSSME (January 2002–December 2007)	ABV (January 2002–December 2007)	0.49 km^3 (2.7%)	0.99
Entire Aral Sea	LBV	ABV	4.10 km^3 (5.5%)	0.91
	CSSME Forecast	CSSME	1.40 km^3 (2.4%)	0.60

Combined SSM Estimate (CSSME) and Forecast

We generated SSM estimates for all the reservoirs to assimilate the calculated remote sensing product from Landsat and altimetry. All the series have a clear seasonal cycle of six months and a trend signal, which gradually decreases over time, except for the North Aral Sea. The trend and seasonal components of the time series are modeled according to Equations (19) and (20), and the results are shown in the right panel of Figure 10. The model CSSME has also been used to make six month recursive forecasts for the next two years. The CSSME is extrapolated first for the 6 months and then again for the next 6 months and so on, to get forecasts from January 2013 until December 2014 for all of the reservoirs, except the East Aral Sea.

The Lake Mead trend shows a drop of approximately 1 km^3 per year with a maximum seasonality of 1 km^3 except during the 2011 flood, when the lake gained almost 8 km^3 water. The CSSME for 2012 is substituted by the LBV-SSM because of the lack of altimetry observations for this year; nevertheless, from March 2013 the CSSME series (Figure 10: black line) is again updated by the combined ABV and LBV observations. The forecast (Figure 10: green line) fits very well with the CSSME estimate (3% NRMSE) and with the *in situ* (3.7% NRMSE).

4.3.2. CSSME and Forecast for Aral Sea

A similar process of filling in missing data, assimilating ABV and LBV to obtain CSSME and model forecast is applied in all the sub-parts of the Aral Sea. The West Aral Sea decreased in volume by approximately 20 km^3, showing a dominant trend component. The CSSME for the West Aral Sea showed good agreement of estimate with its both input ABV and LBV ($R^2 > 0.97$ and NRMSE < 2.7%) and with its forecast (0.76 R^2 and 1.9% NRMSE). On the other hand, the North Aral Sea has many jumps in the data and a relatively strong seasonal signal.

Because of shrinking of the East Aral Sea, the ABV series has many missing observations after December 2008. Therefore, CSSME is estimated until December 2008 and forecast is done only for one year (2009) because there was no CSSME to do recursive forecast. The LBV-SSM estimate is plotted for the January 2008–December 2015 duration in the Figure 11 for the East Aral Sea (the lake ultimately dried up in 2014). The entire Aral Sea plot in Figure 11 is an integration of its three parts. The largest difference between ABV and LBV is observed between 2010 and 2012 because of the East Aral Sea shrinking and overestimation by altimetry due to flooding (discussed in Section 4.1).

4.4. Validation

To validate our results *R*-squared values (which indicate a relative measure of fit) and root mean square error (RMSE) (which gives the absolute fit of one time series with respect to other time series) are estimated (Table 2). Additionally, NRMSE is computed by normalizing the RMSE against the mean of the measurements. However, NRMSE can be misleading if the variable contains both negative and positive values; therefore, volumetric variations (ALVV) are not compared in %.

4.4.1. Validation of Water Height

The water height obtained from the developed Landsat-SRB method fits perfectly well with the *in situ* and altimetry observations for all the study sites. Lake Mead has a coefficient of determination of 0.99, which means 99% variability of the *in situ* data can be explained by variability in the Landsat-SRB and altimetry observations (Table 2). The obtained 59 cm RMSE or 0.17% NRMSE show the relative closeness of the Landsat-SRB observed water height to the ground observations. Similarly, the water height observed by altimetry for Lake Mead is also highly accurate, with marginal (6 cm) difference in RMSE from the Landsat-SRB estimates.

Unfortunately, for the Aral Sea reservoirs very few *in situ* observations are available. They are mostly collected from publications [27,38], which are given without height reference information. Therefore we cross-validated the observations due to lack of possibility of validating with respective ground observations. Altimetry (Figure 7: blue line) and Landsat-SRB (Figure 7: red dashed line) observations follow the same trend and are quite close to the limited available *in situ* points. The R^2 values for the two observations for the West Aral Sea and the East Aral Sea (January 2002–December 2007) are 0.94 and 0.82 respectively (Table 2), which shows that the two data have a very strong linear relationship for these reservoirs.

The North Aral Sea has more dispersion between the two missions' observations; nevertheless, they have good covariance of approximately 0.94. The maximum difference between the water height observed by Landsat and altimetry is less than 90 cm and RMSE is 50 cm, which is well within the error range of a typical Landsat height estimate (Figure 7). However, because of the low variation in the North Aral Sea (approximately 2 m) within the study period, the 90 cm difference has a significant impact on the statistical evaluation (Table 2). The F-distribution test is applied to evaluate variations among the methods, which shows no significant difference in the mean height of all the water bodies except for the North Aral Sea. The F-test rejected the null hypothesis for the North Aral Sea, failing the assumption that the two datasets (*i.e.*, Landsat-SRB and altimetry water heights, and eventually their volumes LBV and ABV respectively) came from normal distributions with the same variance.

4.4.2. Validation of the Estimated Water Volume (LBV, ABV and ALVV)

The Table 2 shows that absolute water volumes estimated by LBV and ABV have a very high correlation with the ground observations for Lake Mead (R^2_{LBV} = 0.98 with RMSE_{LBV} = 0.32 km^3, R^2_{ABV} = 0.97 with RMSE_{ABV} = 0.41 km^3). For an ungauged basin like Aral Sea, cross comparison of different model outputs can be considered as a validation method. The entire Aral Sea and its sub-parts showed a good LBV-ABV agreement ($R^2_{\text{entire Aral Sea}}$ = 0.91 with 4.1 km^3 RMSE). The West Aral Sea has a better agreement between the estimated volumes (0.94 R^2) relative to the East Aral Sea (0.85 R^2), similar to what we have observed for the estimated water heights. However, despite of the smaller water height RMSE for the East Aral Sea compared to the West Aral Sea, the RMSE of computed volume for the East Aral Sea increased ($\text{RMSE}_{\text{west}}$ = 1.5 km^3 and $\text{RMSE}_{\text{east2007}}$ = 2.4 km^3), which is because of its substantially greater size until 2007.

The volumetric variations estimated by ALVV showed a better agreement with the ABV than LBV for all of the reservoirs (Table 2), simply because in Equation (1) height variations are taken from altimetry and not from the Landsat-SRB. According to Birkett *et al.* (2011) [39], the accuracy of the estimate should be better than 10% of the expected seasonal amplitude and our all results are well within this range.

4.4.3. Validation of CSSME Volume

For Lake Mead, CSSME shows an extremely high agreement with LBV and ABV ($R^2_{CSSME-LBV}$ = 0.98 and $R^2_{CSSME-ABV}$ = 0.97 with a marginal difference of 0.5% in NRMSE) as well as with the ground observation (R^2 = 0.97 and RMSE = 0.35 km^3) (Table 2). The West Aral Sea CSSME fits slightly better to ABV ($R^2_{CSSME-LBV}$ = 0.97 and $R^2_{CSSME-ABV}$ = 0.99 with 1.1% difference in NRMSE). This shows a very good assimilation of the two input time series in both of the cases. The East Aral Sea CSSME has a higher tilt towards ABV ($R^2_{CSSME-LBV\_2007}$ = 0.89 and $R^2_{CSSME-ABV\_2007}$ = 0.99 with 9.3% difference in NRMSE), which implies that the ABV time series is smoother than LBV for the East Aral Sea. The North Aral Sea CSSME agrees almost equally with the LBV and the ABV ($R^2_{CSSME-LBV}$ = $R^2_{CSSME-ABV}$ = 0.83), showing their comparable contribution. The CSSME forecast (for 2012–2014) for all of the reservoirs also showed a very good agreement with the CSSME estimates (Table 2), except for the North Aral Sea, which is because of the discrepancies between the ABV and LBV observations.

4.5. Improved Bathymetry

The Aral Sea is located in an arid region with much sand, and salt deposits in the surrounding barren open land. This gives rise to the possibility of significant displacements into the lakebed of sediments by the action of wind, water, gravity, or snow. The bathymetry of the lake was last observed in the 1960s; therefore, within the last half century, the structure of the lakebed may have changed. As a by-product of our shoreline and water level time series, an updated bathymetric map is generated for the region that fell dry. Figure 12 shows the change in the structure of the lakebed of the East Aral Sea. The river mouth made its impression in the present East Aral Sea, because its shrinking led to the inflow of much sediment into the lake's interior. In addition, salt deposits along the shorelines increased the corresponding elevation, a phenomenon that is more pronounced in the reduced lakebed because of increased salinity. Note, that height estimates from satellite altimetry were only possible down to a minimum elevation of 27 m above sea level due to a lack of reliable altimetry data over the largely reduced water surface. In order to construct a complete bathymetric chart of the lakebed of the East Aral Sea heights below 27 m were obtained solely from Landsat optical images following our SRB approach. The updated bathymetry map is available as supplement to this paper at http://dx.doi.org/10.1594/PANGAEA.855779 [40].

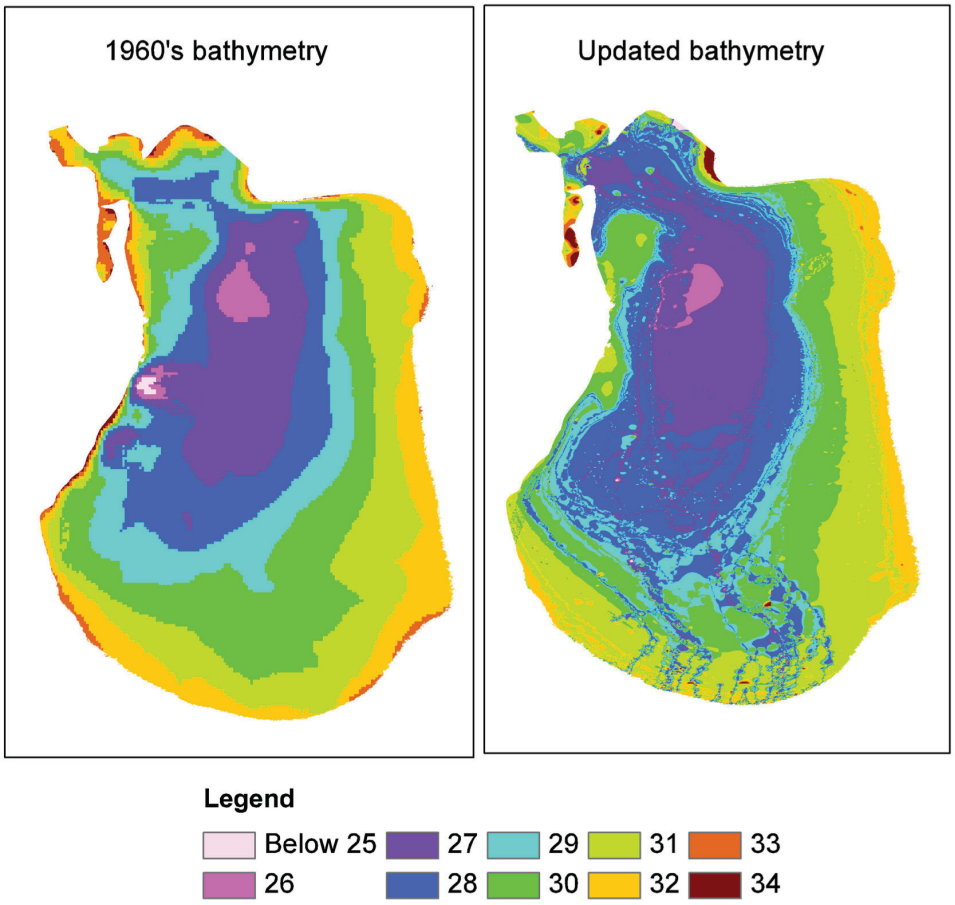

Figure 12. East Aral Sea. (**Left**) subset of the 1960s Aral Sea bathymetry; (**Right**) updated bathymetry using remote sensing data.

5. Discussion

The combination of multiple remote sensing data is a key for continuous monitoring and measurement of water resources. The size of reservoirs is the biggest limiting factor for the terrestrial application of satellite altimetry for water storage estimation, which can be compensated for by the remote sensing image based approach discussed above. Lake Mead has no altimetry observations for nearly one year (from February 2012 until March 2013), because of an intermission gap between the Jason1 extended and Saral/Altika missions. Similarly, the East Aral Sea has missing altimetry observations for nearly one year (from January 2009 until March 2010) as well as for the remaining study period from August 2011, because of its decreased size and the fact that no mission passed over the reduced Sea in this period [31]. In both cases, the water height estimated from the Landsat observations served as a good alternative. However, there are a few months in winter when neither of the two missions had observations of the Aral Sea due to snow, ice and fog, there SSM based gap filling is useful.

Our estimated water height from Landsat and altimetry have a very high agreement with the ground observations (0.99 R^2) for Lake Mead and with the ICESat-GLAS and Hydroweb database discussed in Duan *et al.* (2013) [17] and Gao *et al.* (2012) [19]. For the Aral Sea we compare the results from the two height estimation methods, because of the lack of *in situ* data for verification. The West Aral Sea has a better agreement between them, compared to the East Aral Sea (R^2_{west} = 0.94 and $R^2_{east2007}$ = 0.82) because of the inconsistencies in water mask due to classification errors of the shallow

saline East Aral Sea; therefore, the linear relationship between Landsat and altimetry observations was disturbed at some time points. However, RMSE of the West Aral Sea is 11 cm more than the East Aral Sea (January 2002–December 2007), because a few pixels of classification error will have a greater impact on the height estimation of a deeper reservoir. Depending on the accessibility of the datasets, a combination of the given methods can be used, as shown in Figure 1. If all three of the aforementioned parameters, *i.e.*, DEM, water level and areal extent, are available, their combinations can produce two independent absolute water volume time series (LBV and ABV) and one relative water volume time series (ALVV). Extrapolated digital surface models from different sources like TanDEM-X, ASTER DEM, and SRTM *etc.* can be used as an approximate bathymetry. However, they do not allow for the computation of absolute volumes. Nevertheless, the methods (LBV and ABV) can be applied on the extrapolated global DEM to obtain volumetric variations until one reaches close to the lake bed.

The estimated absolute volumes (ABV and LBV) and volumetric variations (ALVV) agree very well with each other (discussed in Section 4.4.2). Therefore, a combination of different approaches and satellites can be helpful to obtain a continuous time series of observations. Further, we assimilated the two absolute water volume time series by means of a Kalman-filter-based SSM to produce one water storage estimate (CSSME) and a six-month recursive forecast for two years for each reservoir, which also produced very good results (discussed in Section 4.4.3). The statistical parameters highlight the quality of regression of all of the volume estimation methods and the CSSME in Table 2.

The observed inconsistencies can be explained by the possibility of error in data acquisition [38,41] and its processing. In addition, for the large water bodies there is the possibility of a geoid anomaly. The presence of the Rocky Mountains could have result in a positive gravity anomaly in the Lake Mead region, and might have caused some constant offset (Figure 9) because of an uneven geoid. The observations from altimetry and Landsat-SRB are from its northern arm while *in situ* observations were collected near the Hoover dam located at the western end of the lake. The computational error for altimetry is mostly less than 5 cm with a maximum of up to 15 cm [17]. The possible range of uncertainty in Landsat observations from our algorithm for the Aral Sea is less than 1.5 m and for Lake Mead is mostly less than 4 m. Compared to altimetry, Landsat water heights have a larger error bar because the latter is highly dependent on the accuracy and spatial resolution (especially in steep terrain) of the mask and bathymetry. The spatial resolution of the mask and the bathymetry is often not the same; we therefore lose some existing information. With regard to the Aral Sea, the bathymetry had a very poor spatial resolution (though interpolated to 30 m) and may not be accurate. For example, changes in the structure of the lakebed from 1960s to the present East Aral Sea can be seen in Figure 12. Furthermore, Lake Mead and the West Aral Sea have very close contour lines, and there is a possibility of significant changes in the water height within a 30 m pixel from the Landsat mask. This is the reason why the error bar in water height extraction from the Landsat in Figure 7 is relatively high for these two water bodies. The other possible source of error is the uncertainty in the quality of the water masks derived from Landsat, which can have a few pixel registration errors or classification errors. The offset of a few pixels could induce severe problems in the height calculation, specifically for steep-sloped reservoirs.

Given the above stated many possible uncertainties, the remote sensing based estimates for reservoir height and volume from all reservoirs are promising and similar to ground observations. The results show that Lake Mead, the East Aral Sea and the West Aral Sea lost nearly 11.5, 27, 21.7 km^3, respectively, of water volume over 12 years, while in the same period the North Aral Sea gained 6–7 km^3 because of the construction of the Dike Kokaral dam in 2005. Lake Mead's downward trend was interrupted once by a flood event between May 2011 and January 2012. This was caused by heavy snowmelt in the upper Colorado and Rocky mountains, prompting the release of an extra 4.1 km^3 of water from Glen Canyon into Lake Mead, and an increase of nearly 12 m in water elevation. Continuous drought for more than a decade and increasing water and electricity demand from Las Vegas (one of the fastest-growing cities in the United States) have put Lake Mead under great strain.

The two test sites suffered significant water losses, but the effect is more pronounced on the water height observed from satellite altimetry from the hilly terrain of the Lake Mead (~28 m loss). However, the Aral Sea showed a dramatic loss in volume (~43 km^3) by shrinking a few meters in height, because of its relatively flat topography. Therefore, a three-dimensional assessment of the changes is essential and can be achieved by combining observations from different remote sensing data from different perspectives to estimate surface water hydrology at on a global scale.

6. Conclusions

The main objective of this paper was to estimate reservoir water volume from remote-sensing-based methods. We proposed a new method of absolute volume computation from Landsat and bathymetry intersection (LBV), and compared the results with absolute volume time series derived from the interaction of satellite altimetry and bathymetry (ABV) as well as with the volumetric variations from an inverted pyramid model (ALVV). Very good long-term agreement was obtained between water heights observed by satellite altimetry and the Landsat-SRB method (Figure 7) as well as between all volumetric variation estimation methods (ABV, LBV and ALVV: Figure 8) for all reservoirs. Furthermore, we demonstrated the application of a state space framework as a plausible tool to obtain one time series estimate from multiple remote sensing data products because of its attractive features of data assimilation, missing data modifications and near-future forecast. Our results are in very good agreement with the ground observations and with one another. We tested the proposed methods in both gauged and ungauged basins; the results from all are very promising.

The results show that lakes and reservoirs can be effectively monitored at a global scale using remote sensing data and even an inaccurate bathymetry. With the combined use of the proposed methods, we have a good alternative to ground-based observations, particularly for small or remotely located, ungauged or poorly gauged reservoirs. Depending on the availability of data, combinations of the given methods can be used in global hydrological models to make updated dynamic estimates of surface water storage.

Acknowledgments: The authors thank Philippe Renard from Université de Neuchâte for providing 1 m contour bathymetry of the Aral Sea. We also thank the Bureau of Reclamation for providing ground observations for Lake Mead. Alka Singh gratefully acknowledge the financial support by the Gender & Diversity Incentive Fund under the programme "Chancengleichheit für Frauen und Forschung und Lehre" of the Technische Universität München.

Author Contributions: Alka Singh conceptualized this research work, generated the remote sensing data products for reservoir water storage estimation and wrote the manuscript. Ujjwal Kumar contributed to the paper through processing of the data using the State Space Modeling algorithm and helped in the writing of SSM theory. Florian Seitz is the PI of the CLIVAR-Hydro project. He gave important guidance on the work and checked the writing.

Conflicts of Interes: The authors declare no conflict of interest.

References

1. Feng, M.; Sexton, J.O.; Channan, S.; Townshend, J.R. A global, high-resolution (30-m) inland water body dataset for 2000: First results of a topographic-spectral classification algorithm. *Int. J. Digit. Earth* **2015**. [CrossRef]
2. Verpoorter, C.; Kutser, T.; Seekell, D.A.; Tranvik, L.J. A global inventory of lakes based on high-resolution satellite imagery. *Geophys. Res. Lett.* **2014**, *41*, 6396–6402. [CrossRef]
3. Carroll, M.L.; Townshend, J.R.; DiMiceli, C.M.; Noojipady, P.; Sohlberg, R.A. A new global raster water mask at 250 m resolution. *Int. J. Digit. Earth* **2009**, *2*, 291–308. [CrossRef]
4. Cretaux, J.-F.; Letolle, R.; Bergé-Nguyen, M. History of Aral Sea level variability and current scientific debates. *Glob. Planet. Chang.* **2013**, *110*, 99–113. [CrossRef]
5. Schwatke, C.; Dettmering, D.; Bosch, W.; Seitz, F. DAHITI—An innovative approach for estimating water level time series over inland waters using multi-mission satellite altimetry. *Hydrol. Earth Syst. Sci.* **2015**, *19*, 4345–4364. [CrossRef]
6. Asadzadeh Jarihani, A.; Callow, J.N.; Johansen, K.; Gouweleeuw, B. Evaluation of multiple satellite altimetry data for studying inland water bodies and river floods. *J. Hydrol.* **2013**, *505*, 78–90. [CrossRef]

7. Forootan, E.; Rietbroek, R.; Kusche, J.; Sharifi, M.A.; Awange, J.L.; Schmidt, M.; Omondi, P.; Famiglietti, J. Separation of large scale water storage patterns over Iran using GRACE, altimetry and hydrological data. *Remote Sens. Environ.* **2014**, *140*, 580–595. [CrossRef]
8. Wulder, M.A.; White, J.C.; Masek, J.G.; Dwyer, J.; Roy, D.P. Continuity of Landsat observations: Short term considerations. *Remote Sens. Environ.* **2011**, *115*, 747–751. [CrossRef]
9. Bhagat, V.S.; Sonawane, K.R. Use of Landsat ETM+ data for delineation of water bodies in hilly zones. *J. Hydroinform.* **2011**, *13*, 661–671. [CrossRef]
10. Rokni, K.; Ahmad, A.; Selamat, A.; Hazini, S. Water feature extraction and change detection using multitemporal Landsat imagery. *Remote Sens.* **2014**, *6*, 4173–4189. [CrossRef]
11. Goward, S.N.; Williams, D.L. Landsat and earth systems science: Development of terrestrial monitoring. *Photogramm. Eng. Remote Sens.* **1997**, *63*, 887–900.
12. Cretaux, J.-F.; Kouraev, A.; Berge-Nguyen, M.; Cazenave, A.; Papa, F. Satellite altimetry for monitoring lake level changes. In *Transboundary Water Resources: Strategies for Regional Security and Ecological Stability*; Vogtmann, H., Dobretsov, N., Eds.; NATO Science Series; Springer Netherlands: Novosibirsk, Russia, 2005; pp. 141–146.
13. Medina, C.; Gomez-Enri, J.; Alonso, J.J.; Villares, P. Water volume variations in Lake Izabal (Guatemala) from *in situ* measurements and ENVISAT Radar Altimeter (RA-2) and Advanced Synthetic Aperture Radar (ASAR) data products. *J. Hydrol.* **2010**, *382*, 34–48. [CrossRef]
14. Andreoli, R.; Li, J.; Yesou, H. Flood extent prediction from lake heights and water level estimation from flood extents using river gauges, elevation models and ENVISAT data. In Proceedings of the ENVISAT Symposium 2007, Montreux, Switzerland, 23–27 April 2007.
15. Smith, L.C.; Pavelsky, T.M. Remote sensing of volumetric storage changes in lakes. *Earth Surf. Process. Landf.* **2009**, *34*, 1353–1358. [CrossRef]
16. Baup, F.; Frappart, F.; Maubant, J. Combining high-resolution satellite images and altimetry to estimate the volume of small lakes. *Hydrol. Earth Syst. Sci.* **2014**, *18*, 2007–2020. [CrossRef]
17. Duan, Z.; Bastiaanssen, W.G.M. Estimating water volume variations in lakes and reservoirs from four operational satellite altimetry databases and satellite imagery data. *Remote Sens. Environ.* **2013**, *134*, 403–416. [CrossRef]
18. Abileah, R.; Vignudelli, S.; Scozzari, A. A completely remote sensing approach to monitoring reservoirs water volume. *Int. Water Technol. J.* **2011**, *1*, 59–72.
19. Gao, H.; Birkett, C.; Lettenmaier, D.P. Global monitoring of large reservoir storage from satellite remote sensing. *Water Resour. Res.* **2012**, *48*, W09504. [CrossRef]
20. Gao, H. Satellite remote sensing of large lakes and reservoirs: From elevation and area to storage. *Wiley Interdiscip. Rev. Water* **2015**, *2*, 147–157. [CrossRef]
21. Bae, K.; Harris, D. A comparison of state space and multiple regression for monthly forecasts: U.S. Fuel consumption. *Nonrenew. Resour.* **1995**, *4*, 325–339. [CrossRef]
22. Pao, H.-T. Forecast of electricity consumption and economic growth in Taiwan by state space modeling. *Energy* **2009**, *34*, 1779–1791. [CrossRef]
23. Kumar, P. A multiple scale state-space model for characterizing subgrid scale variability of near-surface soil moisture. *IEEE Trans. Geosci. Remote Sens.* **1999**, *37*, 182–197. [CrossRef]
24. Ramos, P.; Santos, N.; Rebelo, R. Performance of state space and ARIMA models for consumer retail sales forecasting. *Robot. Comput.-Integr. Manuf.* **2015**, *34*, 151–163. [CrossRef]
25. Wallerman, J.; Vencatasawmy, C.P.; Bondesson, L. Spatial simulation of forest using Bayesian state-space models and remotely sensed data. In Proceedings of the 7th International Symposium on Spatial Accuracy Assessment in Natural Resources and Environmental Sciences, Lisbon, Portugal, 5–7 July 2006.
26. Zavialov, P.O. *Physical Oceanography of the Dying Aral Sea*; Springer Science & Business Media: Heidelberg, Germany, 2005.
27. Micklin, P. Aral sea basin water resources and the changing aral water balance. In *The Aral Sea*; Micklin, P., Aladin, N.V., Plotnikov, I., Eds.; Springer Earth System Sciences; Springer: Berlin, Germany; Heidelberg, Germany, 2014; pp. 111–135.
28. UN Documentation Centre on Water and Sanitation (UNDCWS). Available online: http://www.zaragoza.es/ciudad/medioambiente/onu/en/detallePer_Onu?id=866 (accessed on 1 October 2014).

29. Pat, S.; Esad, M.; Gyanesh, C. SLC Gap-Filled Products Phase One Methodology. Available online: http://landsat.usgs.gov 2004 (accessed on 2 October 2015).
30. Benduhn, F.; Renard, P. A dynamic model of the Aral Sea water and salt balance. *J. Mar. Syst.* **2004**, *47*, 35–50. [CrossRef]
31. Singh, A.; Seitz, F.; Schwatke, C. Application of Multi-sensor satellite data to observe water storage variations. *IEEE J. Sel. Top. Appl. Earth Obs. Remote Sens.* **2013**, *6*, 1502–1508. [CrossRef]
32. USGS. USGS Open-File Report 03-320 Mapping the Floor of Lake Mead (Nevada and Arizona): Preliminary Discussion and GIS Data Release, Metadata and Data. Available online: http://pubs.usgs.gov/of/2003/of03-320/htmldocs/datacatalog.htm#surfacesutm (accessed on 16 November 2015).
33. Hubert, M.; Vandervieren, E. An adjusted boxplot for skewed distributions. *Comput. Stat. Data Anal.* **2008**, *52*, 5186–5201. [CrossRef]
34. Kitanidis, P.K. *Introduction to Geostatistics: Applications to Hydrogeology*; Cambridge University Press: Cambridge, UK; New York, NY, USA, 1997.
35. Sawitzki, G. *Computational Statistics: An Introduction to R*; CRC Press: Boca Raton, FL, USA, 2009.
36. Durbin, J.; Koopman, S.J. *Time Series Analysis by State Space Methods*, 2nd ed.; Oxford University Press: Oxford, UK, 2012.
37. Shumway, R.H.; Stoffer, D.S. *Time Series Analysis and Its Applications: With R Examples*, 3rd ed.; Springer: New York, NY, USA, 2011.
38. Singh, A.; Seitz, F.; Schwatke, C. Inter-annual water storage changes in the Aral Sea from multi-mission satellite altimetry, optical remote sensing, and GRACE satellite gravimetry. *Remote Sens. Environ.* **2012**, *123*, 187–195. [CrossRef]
39. Birkett, C.; Reynolds, C.; Beckley, B.; Doorn, B. From research to operations: The USDA global reservoir and lake monitor. In *Coastal Altimetry*; Vignudelli, S., Kostianoy, A.G., Cipollini, P., Benveniste, J., Eds.; Springer: Berlin, Germany; Heidelberg, Germany, 2011; pp. 19–50.
40. Singh, A.; Seitz, F. *Updated Bathymetric Chart of the East Aral Sea*; Data Publisher for Earth & Environmental Science: Bremerhaven, Germany, 2015. [CrossRef]
41. Ablain, M.; Cazenave, A.; Valladeau, G.; Guinehut, S. A new assessment of the error budget of global mean sea level rate estimated by satellite altimetry over 1993-2008. *Ocean Sci.* **2009**, *5*, 193–201. [CrossRef]

Remote Sens. **2015**, *7*(12), 17113-17134; doi:10.3390/rs71215872

OPEN ACCESS

Remote Sensing

ISSN 2072-4292

http://www.mdpi.com/journal/remotesensing

Correction

Correction: Singh, A., *et al.* Remote Sensing of Storage Fluctuations of Poorly Gauged Reservoirs and State Space Model (SSM)-Based Estimation. *Remote Sensing* 2015, *Vol. 7*, pp 17113–17134

Alka Singh [1,*], Ujjwal Kumar [2] and Florian Seitz [1]

[1] Deutsches Geodätisches Forschungsinstitut, Technische Universität München, Arcisstr. 21, 80333 Munich, Germany; florian.seitz@tum.de

[2] School of Environment & Natural Resources (SENR), Doon University, 248001 Dehradun, India; ujjwalkumarin@yahoo.co.in

* Author to whom correspondence should be addressed; E-Mail: alka.singh@bv.tum.de; Tel.: +49-89-23031-1214; Fax +49-89-23031-1240.

Received: 9 October 2015 / Accepted: 7 December 2015 / Published: 18 December 2015

There are two mistakes in this article. The authors wish to make the following corrections to this paper

1. Change in Formula 1 [page 17120]. Due to typing, replace:

$$ALVV = \sum_{t=1}^{n} \frac{1}{3} \times (H_t - H_{t-1}) \times \left(A_t + A_{t+1} + \sqrt{(A_t \times A_{t+1})}\right) \quad (1)$$

With

$$ALVV = \sum_{t=1}^{n} \frac{1}{3} \times (H_t - H_{t-1}) \times \left(A_t + A_{t-1} + \sqrt{(A_t \times A_{t-1})}\right) \quad (2)$$

2. Change in Figure 10 [page 17126]. Due to mislabeling, replace:

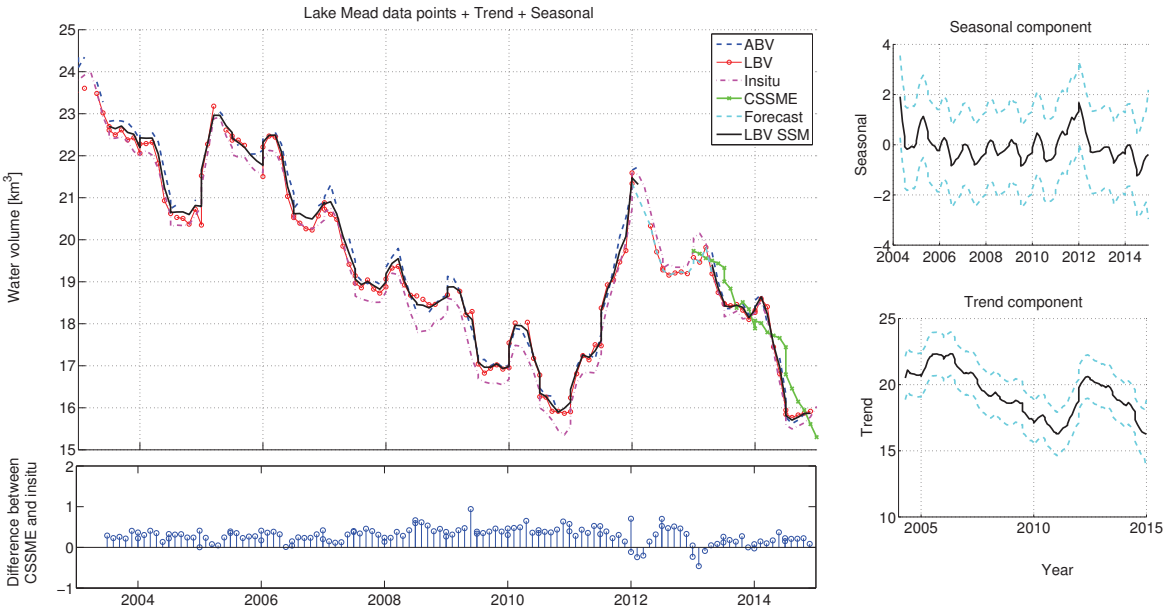

Figure 10. Lake Mead SSM analysis. (**Top left**) The combined SSM estimate (CSSME) (magenta line) and the forecast (green line) for 2013 and 2014; (**Bottom left**) difference between CSSME and in situ observations; (**Top right**) estimated seasonal component; (**Bottom right**) estimated trend component. The dashed cyan lines indicate the upper and lower 95% confidence limit.

with

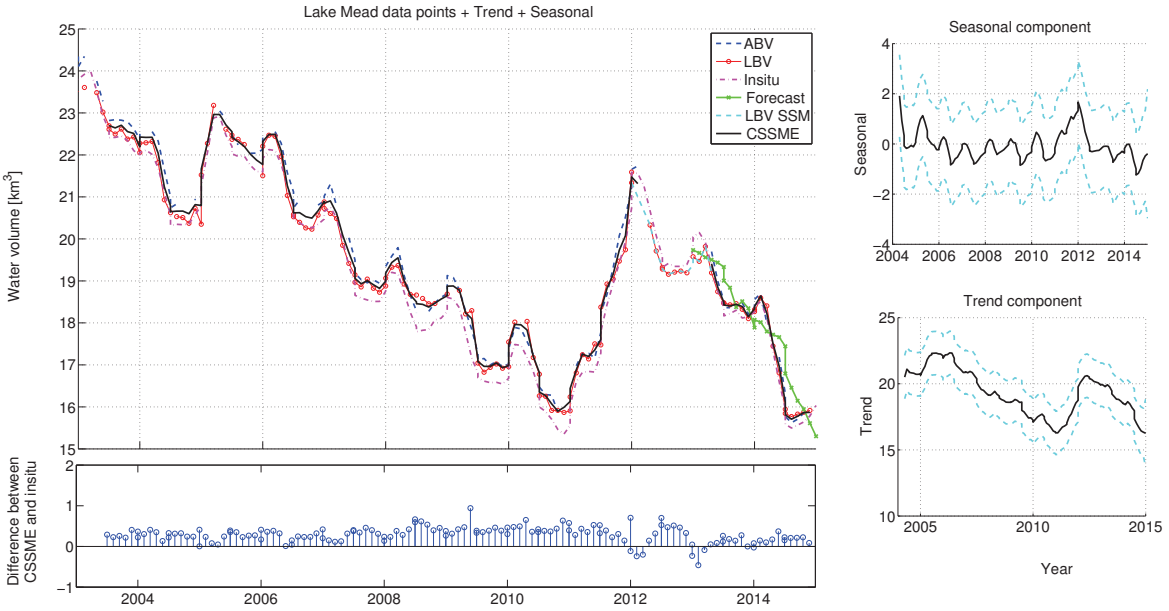

Figure 10. Lake Mead SSM analysis. (**Top left**) The combined SSM estimate (CSSME) (black line) and the forecast (green line) for 2013 and 2014; (**Bottom left**) difference between CSSME and in situ observations; (**Top right**) estimated seasonal component; (**Bottom right**) estimated trend component. The dashed cyan lines indicate the upper and lower 95% confidence limit.

These changes have no material impact on the conclusions of our paper. We apologize to our readers.

Paper-4

Singh, A.; Seitz, F.; Eicker A.; Güntner A. **Water budget analysis within the surrounding of prominent reservoirs from multi-sensor Earth observation data and hydrological models: case studies of the Aral Sea and Lake Mead;** Remote Sensing,(under review).

remote sensing

MDPI

Article,

Water budget analysis within the surrounding of prominent lakes and reservoirs from multi-sensor Earth observation data and hydrological models: case studies of the Aral Sea and Lake Mead

Alka Singh1,*, Florian Seitz1, Annette Eicker2, Andreas Güntner3,4

1 Deutsches Geodätisches Forschungsinstitut, Technische Universität München, Arcisstr. 21, 80333 Munich, Germany; florian.seitz@tum.de
2 HafenCity Universität, Überseeallee 16, 20457 Hamburg, Germany; annette.eicker@hcu-hamburg.de
3 GFZ German Research Centre for Geosciences, Telegrafenberg, 14473 Potsdam, Germany; andreas.guentner@gfz-potsdam.de
4 University of Potsdam, Institute of Earth and Environmental Science, 14476 Potsdam, Germany
* Correspondence: alka.singh@bv.tum.de; Tel.: +49-89-23031-1214; Fax: +49-89-23031-1240

Academic Editor: name
Received: 22.08.2016; Accepted: date; Published: date

Abstract The hydrological budget of a region is determined based on the horizontal and vertical water fluxes acting in both inward and outward directions. These integrated water fluxes vary, altering the total water storage and consequently the gravitational force of the region. The time-dependent gravitational field can be observed through the Gravity Recovery and Climate Experiment (GRACE) gravimetric satellite mission, provided that the mass variation is above the sensitivity of GRACE. This study evaluates mass changes in prominent reservoir regions through three independent approaches viz. fluxes, storages, and gravity, by combining remote sensing products, in-situ data and hydrological model outputs using WGHM and GLDAS. The results show that the dynamics revealed by the GRACE signal can be better explored by a hybrid method, which combines remote sensing-based reservoir volume estimates with hydrological model outputs, than by exclusive model-based storage estimates. For the given arid/semi-arid regions, GLDAS based storage estimations perform better than WGHM.

Keywords: GRACE, Water budget, Reservoir, Water fluxes, GLDAS, WGHM, Aral Sea, Lake Mead

1 Introduction

87% of Earth's open freshwater is stored in reservoirs (here, the term reservoir includes both lakes and man-made reservoirs), 2% is stored in rivers and the remaining 11% in swamps [1]. Timely and accurate knowledge of water conditions and dynamics in reservoirs and their contributing catchment areas provide a basis for efficient and sustainable management of water resources, as well as to prepare for its inevitable future variability. Water storage can be regularly quantified by applying: ground-based observations, hydrological modeling and remote sensing [2,3]. Given the decreasing number of ground-based gauging stations around the globe [4,5] and the uncertainty of hydrological models [6], the application of diverse remote sensing based technologies must be fostered. Remote sensing has provided a rich database for water-related parameters and state variables. The combination or assimilation of ground-based data and remote sensing products into models can provide extensive and more precise information about regional water resources. This study evaluates the potential of hybrid products in a reservoir-dominated region by combining model outputs, ground-based data, and remote sensing data.

Large variations in water mass change the gravity field of a region and thus map into the observations of the Gravity Recovery and Climate Experiment (GRACE) satellite mission. The study interprets the impact of reservoir dynamics on the GRACE signal. Since the resolution of GRACE is limited to large signals and regions, an appropriate window around the reservoir needs to be selected and other hydrological parameters need to be quantified. The water balance equation within a region can be recognized as a series of fluxes and storages (stocks). To observe this regional water budget variability, we have applied the following approaches:

1. Estimation of the balance of all hydrological fluxes acting vertically and horizontally. The rate of water storage change ($\Delta S/dt$) in a region is the sum of evapotranspiration (ET), precipitation (P) and net surface runoff (ΔR) (Eq. 1).

$$\Delta S/dt = P - ET + \Delta R \quad \text{Eq. 1}$$

   Based on the applied datasets, two net fluxes are derived from Equation 1. Flux-1 is obtained by combining the Global Precipitation Climatology Centre (GPCC) precipitation data with the WaterGAP Global Hydrological Model (WGHM) ET and in-situ runoff. Flux-2 is obtained by combining the Tropical Rainfall Measuring Mission (TRMM-3B43) precipitation data with the Global Land Data Assimilation System (GLDAS) ET and in-situ runoff.
2. Estimation of the water storage change (ΔS) in a region is the sum of storages in soil moisture (SM), snow water equivalent (SWE) and surface water (SW) (Eq. 2). Due to the lack of direct measurements, groundwater storage is not considered in the equation.

$$\Delta S = \Delta SM + \Delta SWE + \Delta SW \quad \text{Eq. 2}$$

   The hybrid storages combine the ΔSW from remote sensing-based reservoir volume estimates with ΔSWE and ΔSM from hydrological model outputs. The WGHM based hybrid storage is referred to as Storage-1, and the GLDAS-based hybrid storage is referred to as Storage-2.
3. Estimation of total water storage variability (ΔTWS) from time-variable gravity data observed by GRACE. The ΔTWS considers the contribution from the surface (reservoirs, river-network, snow, and ice) and subsurface (soil moisture and groundwater) storage changes. However, GRACE cannot resolve individual flux contributions to ΔTWS and the interactions among them.

The study analyzes the correlation of ΔTWS from GRACE with the sum of individual fluxes (Eq. 1) as well as with the sum of storages (Eq.2), in the reservoir-dominated region. The possible inaccuracies caused by different datasets and outputs from different global hydrological models are visualized by comparing two sets of fluxes (discussed in Section 3.1) and two sets of hybrid storages (discussed in Section 3.2). The estimate that best agrees with ΔTWS is considered as the better performer for the region.

Unlike most previous studies, which were conducted at large spatial scales (usually at the basin or global scale) and compared the GRACE signal with hydrological model outputs, this study analyzes the GRACE signal at a small scale by using more accurate storage computations based on the hybrid approach. In few of the previous studies, the GRACE signal was also compared with the combination of storages; for example [7,8] combined in-situ surface storages with other datasets, [8–10] combined multiple remote sensing data and model outputs at a larger scale but the spatial resolution of the surface water bodies was 250 m. This study investigates the impact of reservoir variability on the GRACE signal at a small scale and validates the reservoir volume variability estimated at 30 m spatial resolution from remote sensing methods [11].

2 Study area

This study estimates the hydrological budget of two reservoir regions the Aral Sea and Lake Mead during the period of January 2003- December 2014. The Aral Sea has become a major ecological disaster during the 20th century, due to large-scale irrigation abstraction for rice and cotton fields in central Asia. In comparison, Lake Mead has been declining badly for the past more than a one-and-a-half decade. However, in this case, it is predominantly because of the reoccurring drought since 2000 [12,13]. Lake Mead is the largest reservoir in the United States, formed after the creation of Hoover Dam on the Colorado River. Lake Mead has a comprehensive network of ground observations to validate the space-borne estimates, whereas the Aral Sea has limited means for evaluation. Due to constraints in the spatial resolution of GRACE, a study area larger than the size of the reservoir is selected (Figure 1) (discussed in Section 3.3).

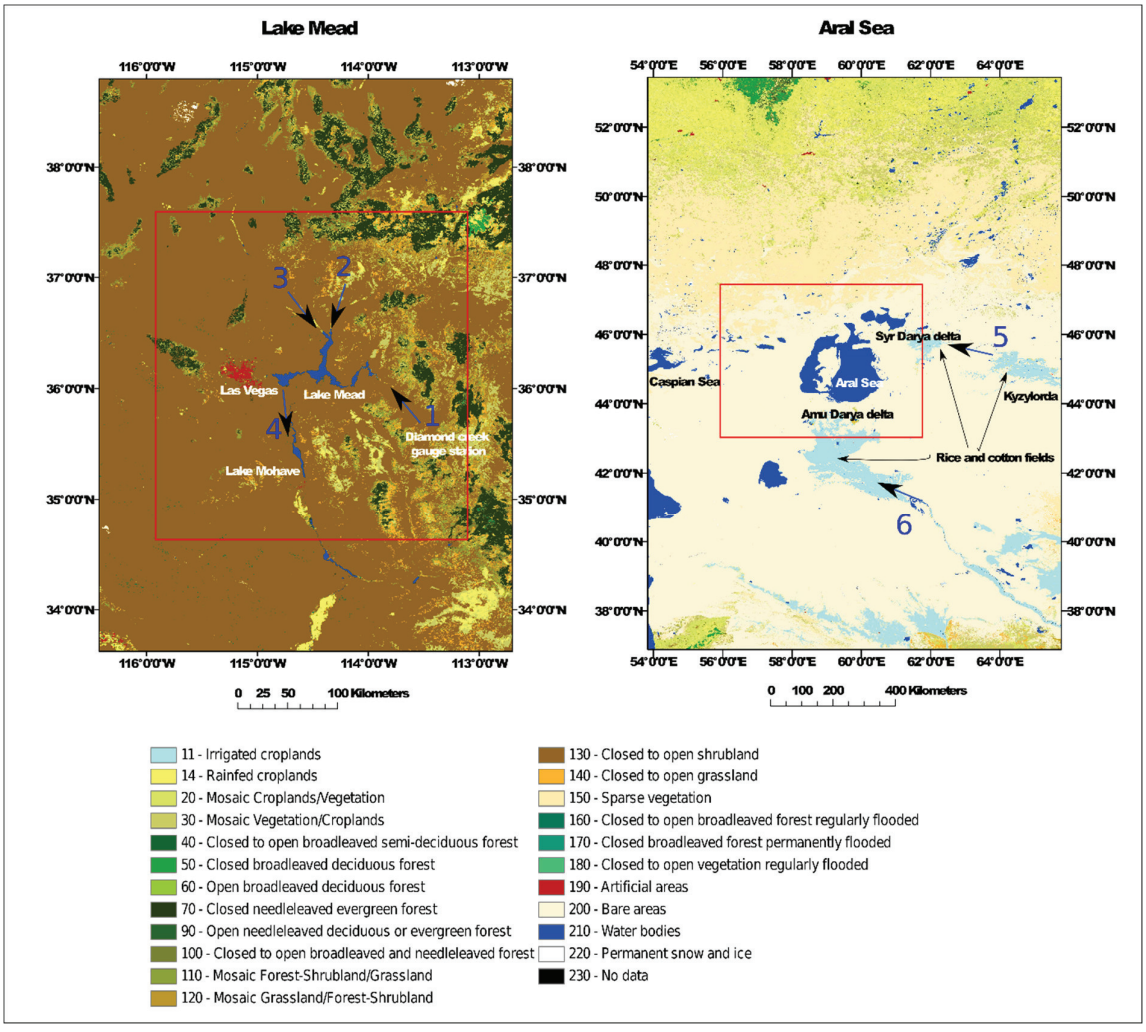

Figure 1. Study box for the Lake Mead region and the Aral Sea region. River discharge: 1 =Colorado River inflow, 2 = Virgin River, 3 =Muddy River, 4 =Colorado River outflow, 5 = Syr Darya and 6 = Amu Darya.

Figure 1 shows the geographic location of the two test sites. The study area is shown in the red rectangular box. The Aral Sea region is approx. 210,000 km^2 covering [43° to 47°N] and [56° to 62°E]. The Lake Mead region is approx. 90,000 km^2 covering [34.5° to 37.5°N] and [116° to 113°W]. The land cover map is taken from 'GlobCover2009' (http://due.esrin.esa.int/page_globcover.php) to analyze the impact of interfering GRACE signal from the surrounding features.

3 Data and Methodology

3.1 Sum of hydrological mass fluxes (ΔS/dt)

Water is continuously exchanged vertically (P and ET) and horizontally (R) between the reservoir and the surrounding land and atmosphere (Eq. 1). Flux-1 is derived by combining ET from WGHM with P from GPCC because WGHM uses GPCC as a climate forcing in the model. While Flux-2 is derived from the combination of ET from GLDAS with P from the TRMM-3B43 product because GLDAS uses a combined product of gauge data and satellite-derived precipitation (discussed in Section 3.2.1). In both of the estimates, the horizontal flux i.e. surface runoff is obtained from in-situ observations.

3.1.1 Net surface runoff (Δ R)

Reservoirs are mostly fed by rivers and normally allow water outflow to ultimately end up in an ocean (e.g. Lake Mead). The Lake Mead study region is mainly fed by the Colorado River, for which we use the Diamond Creek gauge station near Peach Springs [35.77361°N and 113.36278°W] as the inflow into the region and the Davis Dam release [35.19876°N and 114.56949°W] as the outflow from the region (Figure 2, left). These datasets are collected from the annual 'Water Accounting Reports' of the United States Bureau of Reclamation (USBR). The other two minor streams i.e. the Virgin River and the Muddy River (arrows 2 and 3 in Figure 1, left) have a negligible contribution and there are no ground observations at their locations. Therefore, they have been neglected in the calculations. On contrary, endorheic water bodies are terminal lakes with no outflow (e.g. the Aral Sea). The Aral Sea, acts as a terminal point for the two major river basins of central Asia, the Syr Darya in the north and the Amu Darya in the south. The stream inflow and precipitation may only leave out of the Aral Sea by evaporation and seepage. For this study, the Aral Sea river discharge is downloaded from http://www.cawater-info.net website. The data is limited to June 2011, and the exact locations of the gauge stations are unknown.

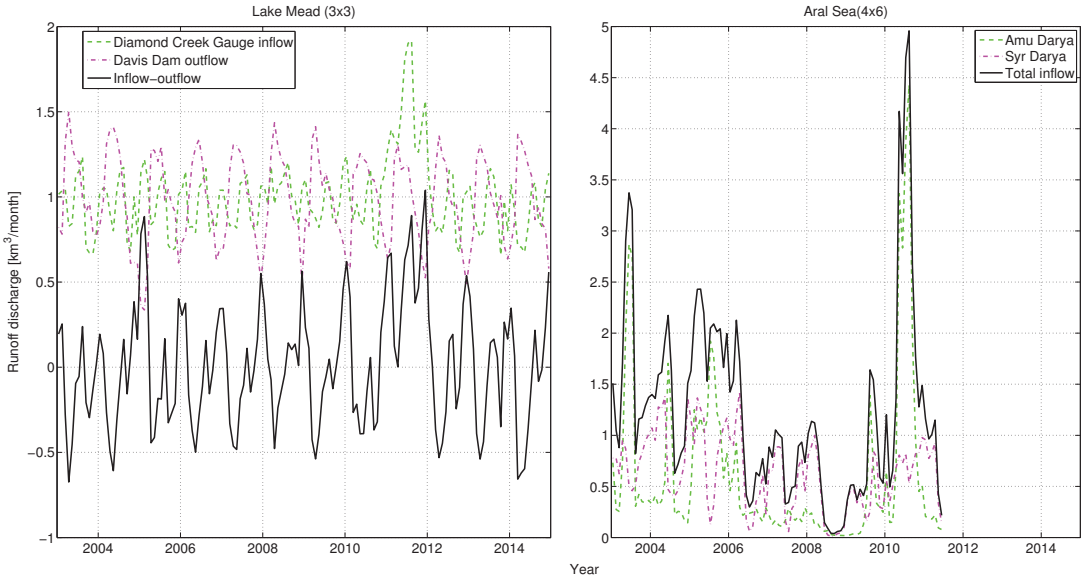

Figure 2. Runoff: (left) Lake Mead and (right) the Aral Sea

3.1.2 Precipitation (P)

Precipitation is the main input and evapotranspiration is the main output of water from the atmosphere within a catchment. The Aral Sea region has very sparse rain gauge stations; consequently, the interpolated GPCC data may be relatively less reliable. However, WGHM uses only GPCC rainfall

data as a climate forcing for its simulations. Therefore, GPCC precipitation and WGHM ET are combined to estimate the net vertical flux in Flux-1. In contrast, GLDAS uses a combination of NOAA/GDAS atmospheric analysis fields and 2.5° grid Climate Prediction Center Merged Analysis of Precipitation (CMAP), which is derived from blending of gauge data and satellite-derived precipitation and downward radiation observations [14]. Therefore, we apply a comparable TRMM 3B43 (V7) precipitation data, at 0.25° spatial resolution, with GLDAS ET for the net vertical flux estimation in Flux-2. TRMM precipitation product is also used to estimate fluxes over the Lake Mead reservoir (water body only, discussed in Section 4.1).

The dedicated precipitation satellite 'TRMM' was launched in November 1997 and turned off in April 2015. The monthly TRMM (3B43) product at 0.25° spatial resolution is obtained from http://disc.sci.gsfc.nasa.gov/SSW/. TRMM (3B43) is a combination of the four independent precipitation measurements, which include the monthly averaged TRMM Microwave Imager (TMI) estimate, the monthly averaged Special Sensor Microwave/Imager (SSM/I) estimate, the adjusted merged-infrared (IR) estimate , and the monthly accumulated GPCC rain gauge analysis[15].

We compare the rain gauge-based GPCC data with the remote sensing-based TRMM product, which combines multiple datasets (Figure 3). The GPCC data comprise monthly mean millimeter level water height and the TRMM data are the hourly precipitation rate, which is multiplied by the number of hours of the respective month to yield monthly precipitation. The monthly precipitation volume is estimated by integrating millimeter-level water height over the study area (4° × 6° for the Aral Sea region and 3° × 3° area for the Lake Mead region). The resulting TRMM and GPCC data are compared in Figure 3, which shows better agreement for the Lake Mead region than the Aral Sea region.

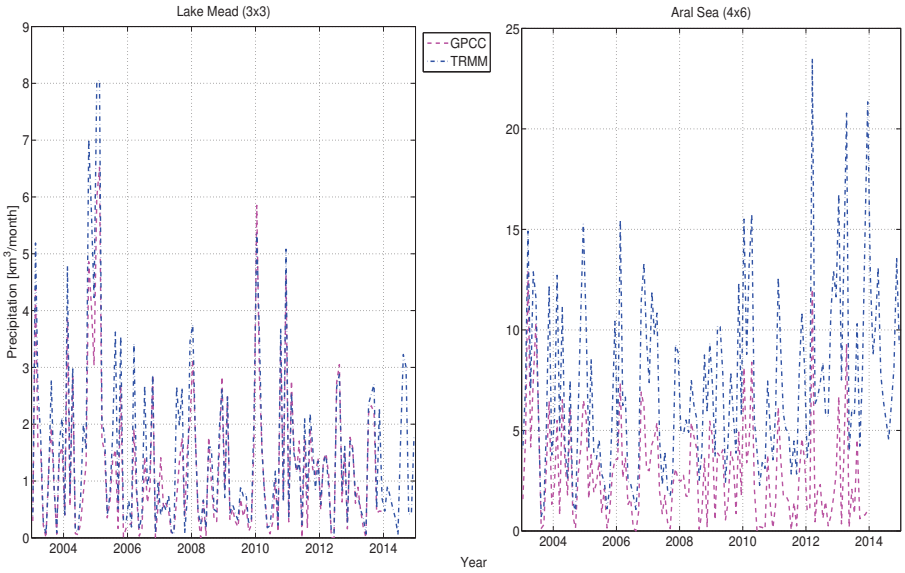

Figure 3. Precipitation: (left) the Lake Mead region and (right) the Aral Sea region.

3.1.3 Evapotranspiration (ET)

The rate of ET within a region greatly depends on the amount of water present and the available energy. ET includes evaporation of surface water and transfer of soil moisture by plants through foliage (i.e. transpiration). In arid climates, there is often plenty of available energy to drive ET, but the actual amount of ET varies with the presence of water at the surface, which varies with the change in the reservoir size and availability of upper-layer soil moisture. To derive the total ET of the study area, we use the model output from two global hydrological models: GLDAS and WGHM.

The Noah GLDAS 0.25° data product provides ET at an hourly rate per square meter [14], which is converted to volume per month by multiplying the number of hours in the respective month and the

area under study. The WGHM data are based on the Priestley and Taylor equation [16] and are provided in monthly water equivalents (i.e. mm/0.5° grid) as a mean monthly value. The GLDAS data consider the Aral Sea as an ocean and masked it out based on its 1960's size. Consequently, the ET estimation is very low compared to WGHM (Figure 4, right). However, WGHM also does not explicitly consider the variable surface area of lakes/reservoirs for ET calculation. It includes an empirical and global reduction function that reduces evaporation if the lake storage volume decreases [17]. As this function is not specifically adjusted for the Aral Sea, it may not adequately capture the huge reduction of its water surface area which may be the reason for an overestimation of ET for the region. Furthermore, according to previous studies, the evaporation over the Aral Sea is estimated around 1 m to 1.2 m/year [18–20], while WGHM estimated it much larger for the selected region. Nevertheless, the net flux for the Aral Sea region is only calculated from WGHM (as Flux-1) even with some expected overestimation, whereas outputs from both models are used and compared for the Lake Mead region.

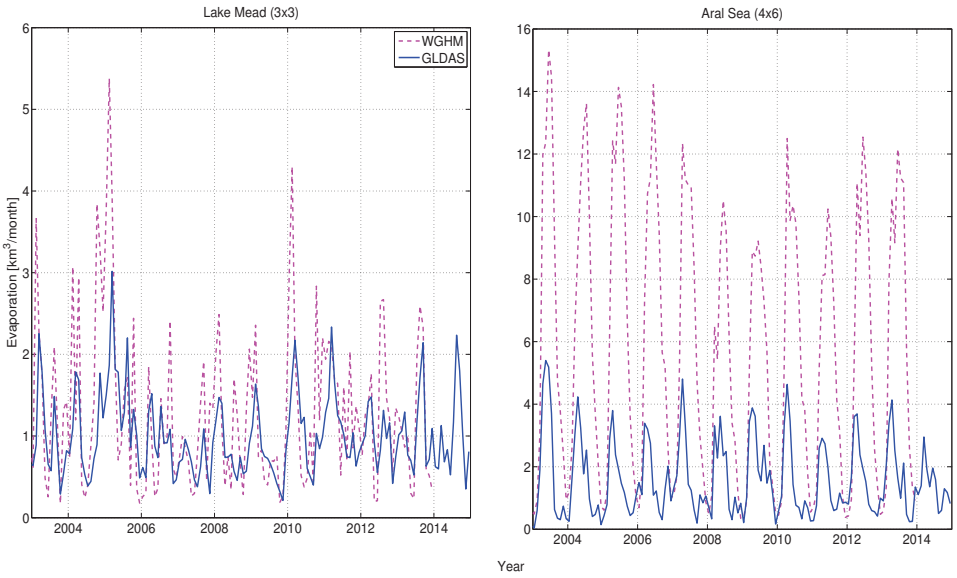

Figure 4. ET: (left) the Lake Mead region and (right) the Aral Sea region

3.2 *Sum of hydrological storage compartments (ΔS)*

Two hybrid-storage estimates are derived from the combination of outputs from hydrological models with the remote sensing based reservoir volume estimates. The study is confined to reservoir regions, therefore the respective reservoir is the main liquid surface water body. Its volume is combined with SM and SWE derived from WGHM and GLDAS to generate Storage-1, and Storage-2 respectively.

3.2.1 Liquid surface water (ΔSW)

We apply reservoir volume estimates using a combination of Landsat, satellite altimetry and bathymetry data for the Aral Sea and Lake Mead, as outlined in our previous study [11]. Figure 5 shows the mean reduced volumetric variations in the two water bodies estimated by the aforementioned remote sensing approach. In our study regions, reservoirs act as major surface water storage components. Figure 5 (left) compares the remote sensing-based reservoir volume estimate with the in-situ measurements for Lake Mead, which is diligently monitored by the United States Bureau of Reclamation (USBR). However, the Aral Sea has been poorly monitored over the last few decades. Therefore no ground-based volume estimates are available to validate our previous results [11].

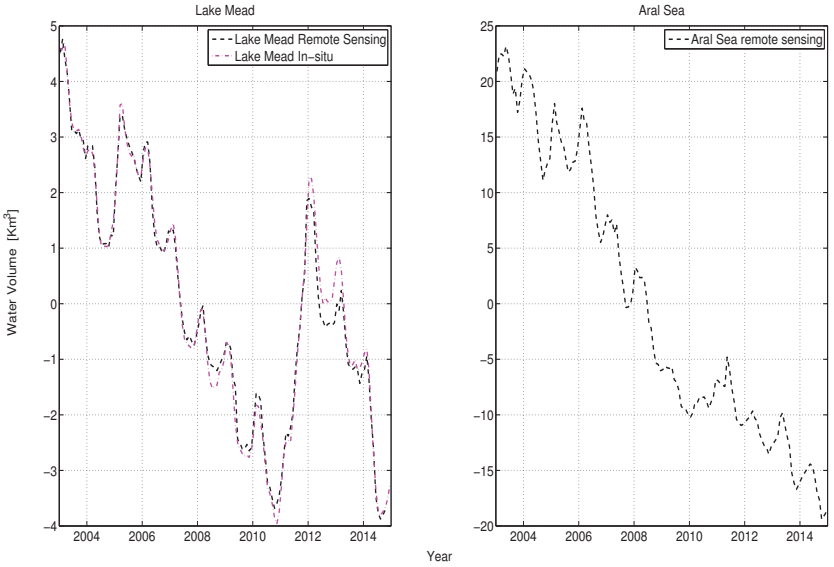

Figure 5. Mean reduced reservoir volume: (left) Lake Mead and (right) the Aral Sea.

3.2.2 Snow water equivalent (ΔSWE)

Apart from rivers and reservoirs, snow and ice are important storage units of surface water, especially for regions in higher latitudes and with large mountain ranges, and have a significant impact on the hydrology of many river systems [21][22]. However, Lake Mead is entirely free of snow and ice; nonetheless, it is fed by snow and glaciers from the Rocky Mountain. The Lake Mead study area contains some mountain ranges. Therefore, little SWE is estimated by both GLDAS and WGHM (Figure 6, left). Conversely, the Aral Sea has three to four months of snow and ice coverage, which is obtained from the two hydrological models. Again, one of the reason for the underestimation of the SWE by GLDAS for the Aral Sea region is the removal of data from the former extent of the Aral Sea water body (Figure 6, right).

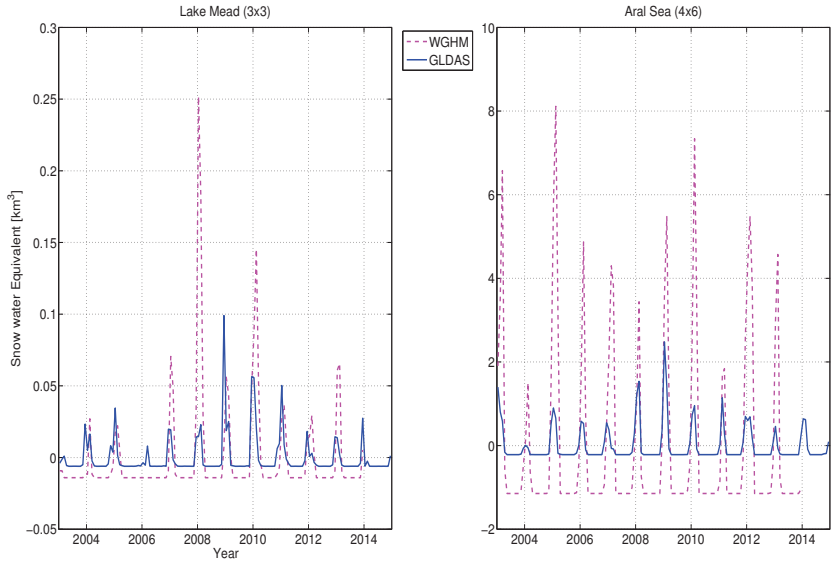

Figure 6. Mean reduced Snow Water Equivalent: (left) the Lake Mead region and (right) the Aral Sea region

3.2.3 Soil moisture (Δ SM)

Volumetric soil water content is normally expressed in percentage or volume of water in a volume of soil sample m^3/m^3. From the Noah GLDAS, we apply the sum of its four soil moisture layers (0 – 2 m depth), whereas WGHM represents SM for the complete soil profile in a single layer whose depth refers to the rooting depth of the vegetation cover. The mean reduced curves of soil moisture variability estimated by the two models are plotted in Figure 7. WGHM features lower amplitudes for both regions, even though the Aral Sea is again largely masked out in GLDAS.

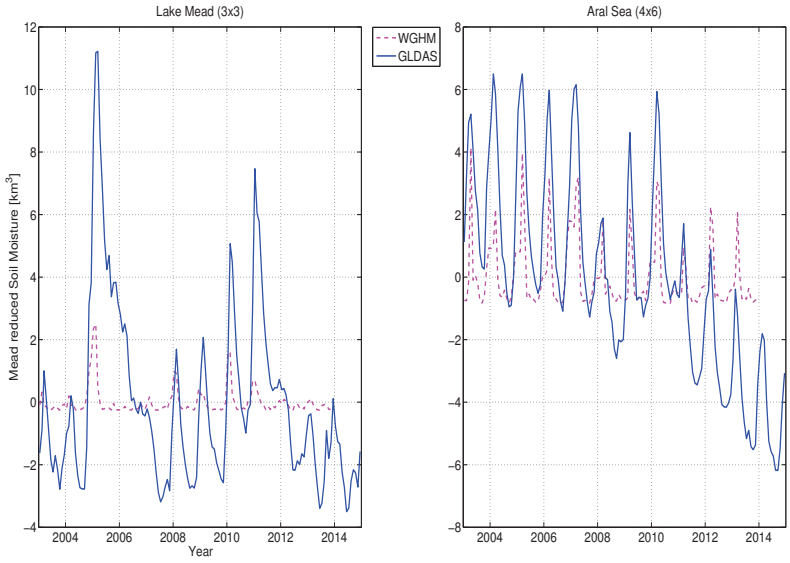

Figure 7. Mean reduced Soil Moisture: (left) the Lake Mead region and (right) the Aral Sea region

The SM estimates by GLDAS in 40 – 100 cm and 100 – 200 cm root depth have higher and smooth variations during the study period. However, after 2010 flood in the Aral Sea region, it experienced a marked decline in the GLDAS simulations for which the reasons are unknown at this point. As mentioned before, WGHM considers soil moisture for the root zone, of which the depth is determined as a function of the actual land cover. For the Aral Sea, much of the surroundings is classified as bare soil (root depth 0.1 m in the model), with smaller fractions of open shrub land (0.5 m) or grassland (1.0 m). Thus, the overall storage capacity of the soil in WGHM for this region is small which results in low storage values and low storage variations. The same applies for the Lake Mead region, which is predominantly classified as open shrub land in WGHM.

3.3 GRACE-derived ΔTWS

For over 14 years, the time-variable gravity field solutions computed from GRACE data have enabled to study the total mass change at regional and global scales [23–26]. GRACE has also been used for comparisons, validation and calibration of hydrological models [27–29]. The ΔTWS from GRACE was compared with in-situ observations [30–32], altimetry observations [31,33–35] and hydrological models [35–37].

To determine the monthly GRACE-derived water mass variability in the study area, the JPL mascon solutions [38] are evaluated. In contrast to the more common way of parameterizing the gravity field in terms of global spherical harmonic basis functions, the mascon representation is based on local

equal-area three-degree spherical cap mass concentration blocks (mascons). During the gravity field estimation process, monthly scaling coefficients are estimated for each of these mascons to represent the global mass distribution. The mascon representation allows a straightforward way to introduce both spatial and temporal constraints between individual basis functions into the GRACE data processing. These constrains allow to filter out the noise which is present in the GRACE satellite data, and which has led to a typical north-south error stripe pattern in the unconstrained monthly gravity field solutions based on spherical harmonics. While for the spherical harmonic solutions these error patterns have to be removed in a dedicated post-processing filtering step (de-striping), no post-processing filtering is necessary for the mascon solutions. However, while the constraints applied in the estimation process reduce the noise, they also result in a damping of the signal and in a coarse spatial resolution, causing a signal to be spread out over a larger area than the area which it originates from (leakage effect). This signal damping can be counteracted by applying so-called rescaling coefficients [39] to the gridded water storage changes, which are determined from a comparison of unfiltered vs. smoothed hydrological model output and which are provided on the GRACE Tellus website for download (http://grace.jpl.nasa.gov) .

We use the mascon solutions in the version which applies the Coastline Resolution Improvement (CRI) filter, for more information see [38]. The GRACE solutions were corrected for geocentric motion coefficients, according to [40] and for variations in Earth's oblateness (C20 coefficient) obtained from Satellite Laser Ranging [41]. The Glacial isostatic adjustment has been accounted for using the model by [42]. The uncertainty data is downloaded from the Tellus website at a 0.5-degree grid and represents the uncertainty of each mascon estimate. These uncertainty measures are derived from the formal covariance matrix of the mascon solutions, scaled differently over oceanic and continental areas in order to obtain more realistic error bounds that match, e.g., the errors known from a comparison between GRACE and ocean bottom pressure data.

The size of the study boxes is chosen such, that it can be resolved by GRACE and - at the same time - that hydrological mass variations in the vicinity of the reservoirs influence the GRACE measurements as little as possible. The Lake Mead study box is based on the size of the mascon (3°x3°). Lake Mead is a small reservoir (approx. 430 km^2 area and 27.5 km^3 volume in spring 2003) and resembles a point mass at the center and the study area, which is approx. 200 times larger than the reservoir area (Figure 8, left). The position of the point mass (reservoir) strongly affects the GRACE signal [43]; therefore, the study area is selected around the reservoir mass center. The Aral Sea surface area was approx. 20,000 km^2 in spring 2003 (with 92.5 km^3 volume). Hence it requires data from more than two mascons to cover the entire Aral Sea (Figure 8, right). The study area is extended towards the west of the Aral Sea in order to include the entire signal of the Aral Sea mass change from which we assume that it is smoothed over the complete western mascon. In 2003, the Aral Sea was approx. one-tenth of the size of the selected study box. In Figure 8, the twelve years (January 2003 - December 2014) mascon GRACE solution shows a negative trend in the equivalent water height (EWH in meter/year) of the selected study regions.

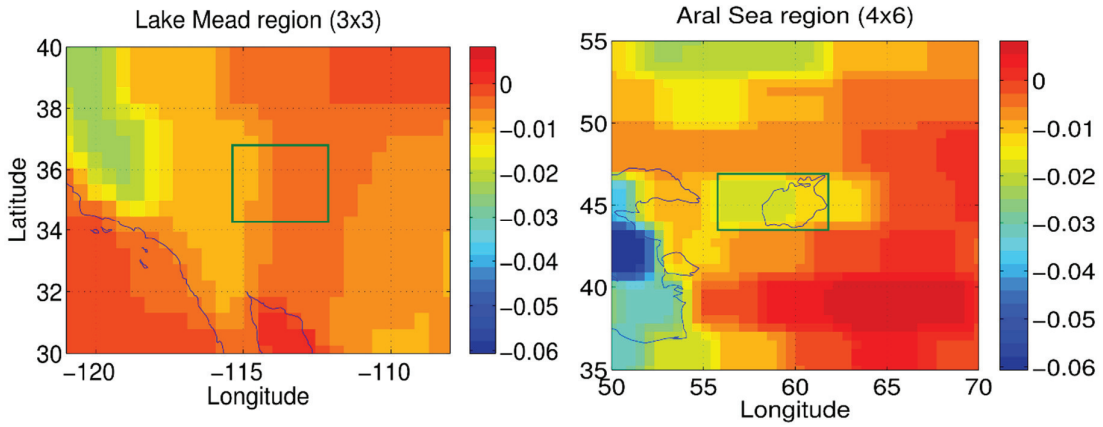

Figure 8. GRACE-derived trend of the equivalent water height (meter/year) between 2003 and 2014. The size of the study area was chosen according to the mascon grid. The Lake Mead region is 3°x3° where Lake Mead is located at the center (left). The Aral Sea region is 4°x6°covering the entire lake and two mascon grid cells.

The derived mass variations for the two regions are shown in Figure 9. The uncertainty range (red dotted line) is retrieved from GRACE Tellus on a 0.5-degree grid. It represents the uncertainty of each mascon estimate, except for November 2011. There are few data gaps in the GRACE data, especially since 2011 due to the aging batteries of the satellites. During certain orbit periods over 4-5 consecutive weeks, no ranging data are collected and hence no gravity fields can be computed approximately every 5-6 months [44].

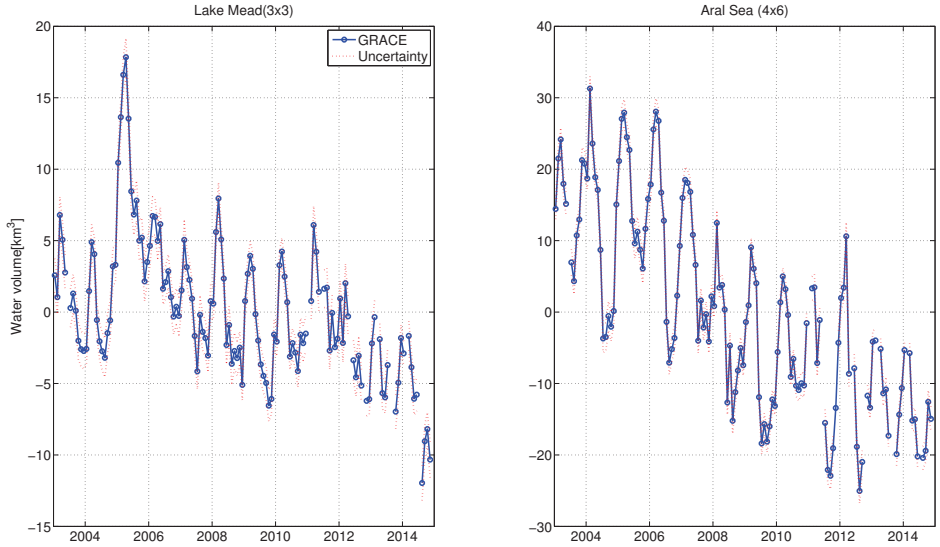

Figure 9. GRACE-derived mass variations with the uncertainty range of the measurements as provided by GRACE Tellus: (left) the Lake Mead region and (right) the Aral Sea region

4 Results

4.1 Lake Mead (reservoir) water budget

Lake Mead is mainly fed by the Colorado River and its discharge budget is summarized in Eq. 3 (Figure 1, left). The overall discharge and peak flows of the Colorado River to Lake Mead at Glen Canyon (Lake Powell) and from Lake Mead at Hoover Dam are highly regulated.

Lake Mead discharge budget = Colorado River inflow (Peach Spring gauge station) + Muddy River and Virgin River + LV Wash − Hoover Outflow − Lake Mead recreational diversions *Eq. 3*

The Hoover Dam release and Lake Mead diversions for recreational purposes are derived from the annual 'Water Accounting Reports' of the USBR (http://www.usbr.gov/lc/region/g4000/wtracct.html). Las Vegas Wash return inflow is obtained from the USGS surface water database (http://waterdata.usgs.gov/). The inflow at the north arm of Lake Mead from the Muddy River and Virgin River is not directly measured by the USBR and other agencies and therefore is not considered in the calculations. The top panel of Figure 10, shows the Lake Mead discharge budget. The bottom panel of Figure 10 compares the derivatives of the reservoir volume (computed by single differences) obtained from remote sensing and in-situ measurements (Figure 5, left) with the sum of water fluxes acting on the reservoir.

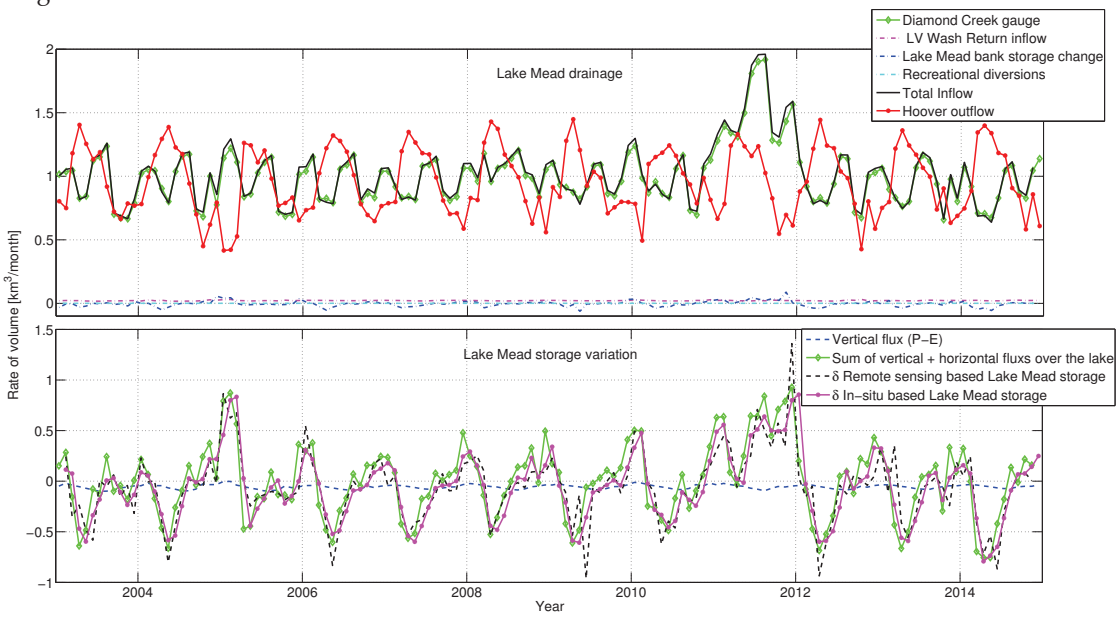

Figure 10. Lake Mead: (top) Net surface runoff of the lake: inflow–outflow and (bottom) reservoir volume variation compared with the hydrological fluxes.

The net fluxes acting on approx. 450 km² area of the reservoir is obtained by reducing the net discharge budget by the vertical flux acting over the water body and the leakage to the bank storage (Eq. 4).

ΔMead storage = Lake Mead discharge (total inflow − Hoover outflow) + Precipitation on the reservoir − Lake Mead Evaporation (in-situ) − ΔMead Bank storage

Eq. 4

Monthly time series of evaporation (only from the Lake Mead water body) are obtained from personal contacts from the Boulder Canyon Operations Office. The estimated evaporation is obtained by multiplying a monthly coefficient (derived from studies conducted by the USGS) by the average of the surface area of previous and current months. Precipitation over the reservoir is obtained from the TRMM (3B43) data. The Mead bank storage is a volumetric representation of shallow groundwater levels immediately adjacent to a reservoir. The amount of bank storage is not subject to an exact determination. However, such storage typically fills voids within nearly 5 km of the reservoir [45]. The

Mead bank storage fluctuates with changes in the reservoir storage. Therefore, the bank storage is estimated by multiplying the change in reservoir storage by a coefficient of 0.065, provided by the USBR.

Furthermore, we interpret the GRACE signal in the reservoir region. As GRACE cannot observe just the small reservoir, therefore, a 3° × 3° window around the reservoir is analyzed.

4.2 *Lake Mead region (3° × 3°) water budget*

In Figure11 (top), the sum of the fluxes (Flux-1 and Flux-2) is compared with the derivatives of the hybrid-storages (Storage-1 and Storage-2) and ΔTWS from GRACE. In the bottom panel of Figure 11, the fluxes are reduced by their seasonality (i.e. a mean value of each January, February, .. over the study period) and then integrated to obtain the inter-annual variability. Furthermore, each time series are mean reduced, to compare with each other. Similarly, the hybrid-storages and the ΔTWS GRACE are reduced by their seasonality (Figure 11, bottom). In addition, all the time series in Figure 11 are smoothed by applying a three-month moving average window to derive their gentle progression. The derivative plot (Figure 11, top) shows the variations two to three months in advance of the integral plot (Figure 11, bottom) because the prior captures changes in the trend; for example decrease in precipitation will suppress the rate of increase, however, it is still filling the storages. Furthermore, the bottom plot has only non-seasonal anomalies.

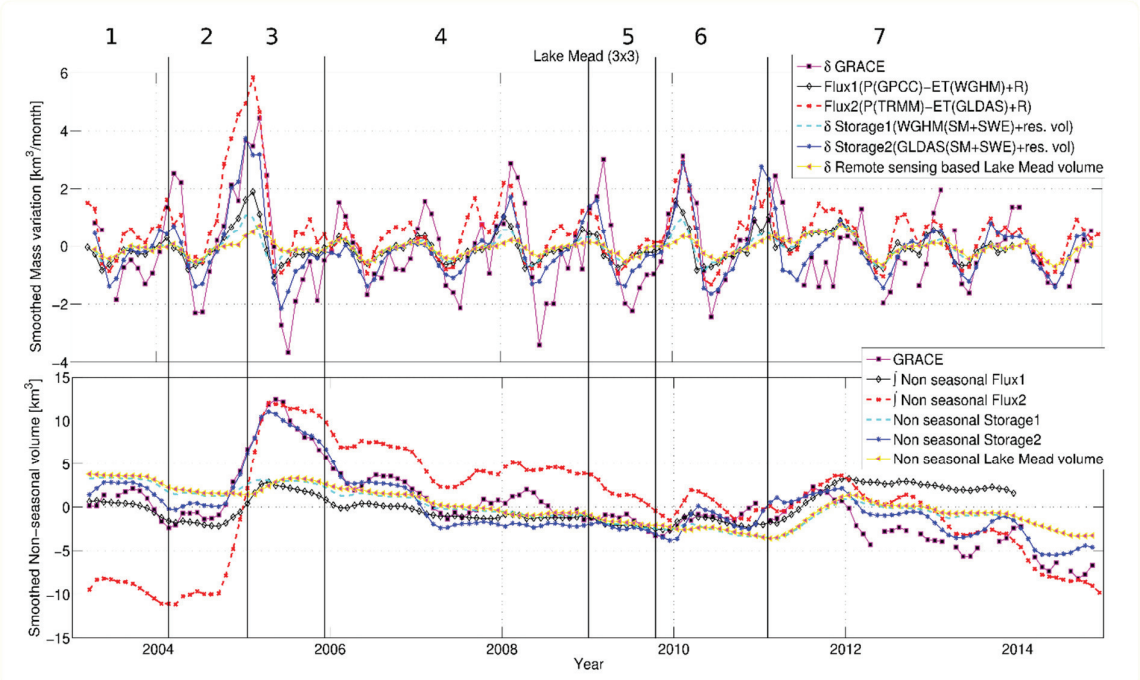

Figure 11. Lake Mead region (3° × 3°) mass variations observed by net fluxes, net storages, and GRACE: (top) monthly mass variations and (bottom) non-seasonal water storage variability. All time series in the lower panel have been reduced for their mean (i.e. mean value over the study period). The large numbers at the top of the figure are the periods of different mass evolution, discussed in Section 4.2. Here symbol δ indicates derivative and ∫ indicates integral of the signal.

This region normally receives maximum water by winter rains and spring runoff from snow and glacier melts. During the study period, the lower Colorado region underwent recurring drought [46], except between 2004 and 2005, when it experienced exceptional rain (Figure 3, left), whereas the 2011 gain in Figure 11 is mainly driven by exceptional upstream runoff.

The mass evolution and its different phases are analyzed below to understand the driving force and differences in the estimations. The periods to be discussed are shown as the large numbers at the top of Figure 11.

Period-1 (03.2003 – 09.2004): All datasets observed a slight loss (0.6 – 1.6 km^3 /year) of the water mass.

Period-2 (10.2004 – 05.2005): Heavy rain escalated the GRACE signal and Storage-2 for more than 13 km^3 within seven months (Figure 3, left). However, Storage-1 increased much less, because it is mainly driven by the reservoir trend, as soil moisture is highly underestimated by WGHM for this region (Figure 7, right). Similarly, Flux-1 increased less than 5 km^3 and Flux-2 jumped 22 km^3. The difference can mainly be attributed to the difference in ET between WGHM and GLDAS (Figure 4, right) and in precipitation from GPCC and TRMM (Figure 3, left) for this period. This shows high uncertainty in the estimation of fluxes and storages depending upon the input datasets. The reservoir itself had less gain during this period as it received regular input from upstream, but at the same time, it had relatively less outflow for a few months (Figure 2, left).

Period-3 (06.2005 – 04.2006): Due to the higher moisture availability in the soil during the previous period, the ET rate increased (Figure 4, left) in the follow-up period. GRACE and Storage-2 lost more than 10 km^3 within 10 months. Storage-1 also exhibited losses similar to the reservoir (approx. 3 km^3) due to the underestimation of SM by WGHM (Figure 7, right). This shows that possibly during the period 2 and 3, soil moisture variability might be the strongest contributor among the different storage compartments of the GRACE data.

Period-4 (05.2006 – 12.2009): GRACE observed a similar low mass loss rate as other datasets. The 2008 winter anomaly was due to added input from precipitation (Figure 3, left). The continuous runoff deficit (Figure 2, left) caused by extra withdrawal from the reservoir to cater lower basin demands and possibly a decline in the ground water table is a cause of this slow and continuous mass decline.

Period-5 (01.2010 – 12.2010): A slight gain is observed by four of the datasets, except by the reservoir and Storage-1. This may be due to above-average rainfall in January, October and December 2010 (Figure 3, left). However, reservoir volume and Storage-1 continued to decline because of no change in the runoff pattern (Figure 2, left).

Period-6 (01.2011 – 12.2011): Additional heavy input from the upper Colorado basin increased the reservoir volume during this period. All datasets exhibit an increase in volume. In contrast to the Period-2 mass gain, which is caused by precipitation in the study region, the increase during Period-6 is caused by inflow from upstream areas. This suggests that this period might be dominated by the reservoir trend (Figure 5, left).

Period-7 (01.2012 – 12.2014): Most of the increase in water from the previous period is lost again within six months, followed by continuous mass loss over the final three years of the study period at more than 1 km^3 per annum. During this persistent drought with abnormally low snow in the Rocky Mountains [46] and low rainfall in the region (Figure 3, left), GRACE exhibited greater mass loss than Storage-2, which might indicate significant ground water extraction.

Among all the applied datasets in the Lake Mead region, the GRACE signal agrees best with Storage-2 (GLDAS based estimate) (Figure 11). In Storage-1, WGHM highly underestimates the SM for these regions (as discussed in Section 3.2.3). Reservoir volume is the only major contributor to Storage-1 estimate. Therefore, in Figure 11 the Storage-1 and reservoir volume plots are overlapping. Among the fluxes, Flux-2 show a better correspondence to ΔTWS, even though, it occasionally tends to overestimate of the variability. In period-2, Flux-1 (Figure 11, top) underestimates $\Delta S/dt$ compared to ΔTWS while Flux-2 overestimates it. This can be explained by the difference between P from GPCC and TRMM (Section 3.1.2) and the ET simulation by WGHM and GLDAS (Section 3.1.3) respectively.

4.3 Aral Sea region (4° × 6° degree) water budget

In the Aral Sea region, the entire hydrological characteristics have been modified since the lake is undergoing a drastic decline. Further, unlike Lake Mead, the Aral Sea region has limited data

availability. There is almost no monthly ground observation for its volume and the applied runoff data are provided without exact coordinates and only for a limited duration. Also, the hydrological models have limited applicability in this region. GLDAS data have flagged the 1960's size Aral Sea area as an Ocean and masked it out, i.e., the model does not perform any simulations for this area. The maximum effect of not including the Aral Sea surface water in the model input becomes apparent in ET estimation. ET is mainly driven by the availability of water and temperature and neglecting such a vast water body in the model input, has a serious impact on the ET estimates (Figure 4, right). Therefore, we do not compute Flux-2. Similar to the Lake Mead region, Figure 12 (top) shows derivatives of the mass variation from GRACE, hybrid storages (Storage-1 and Storage-2) and the Aral Sea volume as well as the time series of the sum of the hydrological fluxes (Flux-1 i.e. P (GPCC) – ET (WGHM) + ΔR (in-situ)). The lower panel shows the mean reduced integrated non-seasonal variations.

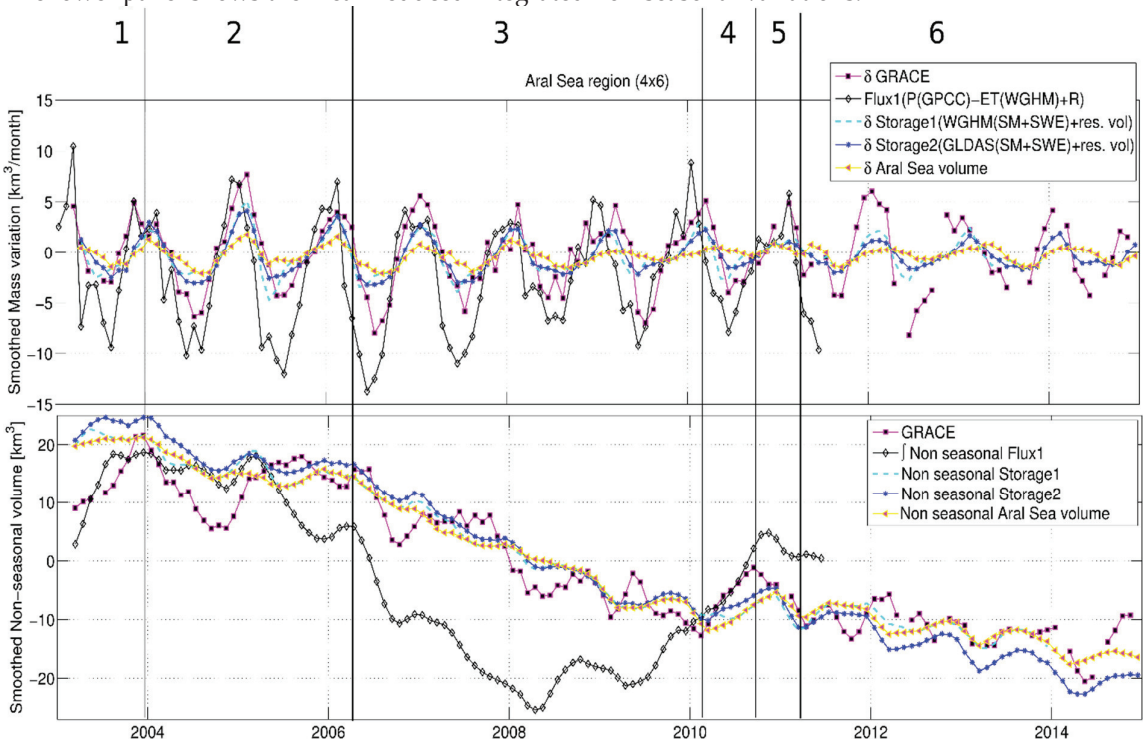

Figure 12. Aral Sea region (4° × 6°) mass variations observed by net flux, net storages, and GRACE: (top) monthly mass variations and (bottom) non-seasonal water storage variability. All time series in the lower panel have been reduced for their mean (i.e. mean value over the study period). The large numbers at the top of the figure are the periods of different mass evolution, discussed in Section 4.3. Here symbol δ indicates derivative and ∫ indicates integral of the signal.

The detail hydrological mass evolution of the Aral Sea region is given below.

Period-1 (03.2003 – 12.2003): In the first year of the study period a slight increase is observed in the lake volume resulting from some extra drainage from the Amu Darya (Figure 2, right). In contrast, GRACE and Flux-1 increased significantly because of the additional contribution from the above-average rainfall (Figure 3, right).

Period-2 (01.2003 – 04.2006): This period experienced a relatively low rate of decline (2-3 km^3/year) in the water mass. However, Flux-1 does not agree well with the results of other approaches.

Period-3 (05.2006 – 02.2010): A staggering decline was observed by GRACE and Storage-2 in this period; water mass decreased at approximately 7 km^3 per annum. The Aral Sea lake and Storage-1 also receded at a rate of 6 km^3 per annum. This period was dominated by the upstream cut off of the drainage [47], and subsequently, driven by the lake trend.

Period-4 (03.2010 – 09.2010): Within less than half a year, GRACE observed more than 9 km^3 non-seasonal gain. The region experienced above-average rainfall (Figure 3, right), followed by an increase in the lake volume (more than 4 km^3) due to heavy upstream runoff (Figure 2, right). The increase in GRACE mass signal during this period is contributed not only by the Aral Sea lake gain but possibly also by storages in the Aral Sea delta, surrounding small lakes, irrigated croplands and increase in soil moisture.

Period-5 (10.2010 – 04.2011): The region lost most of the volume that was acquired during the previous period, and the lake lost approx. 3 km^3 within six months. This decrease is possibly due to large-scale evaporation resulting from an increased water surface area in the Aral Sea and its surrounding storages, as well as moisture in the top layer of the soil.

Period-6 (05.2011 – 11.2014): Due to sporadic rain, GRACE observed relatively less decline in the last three and a half years of the study, at about 1.5 km^3/year. However, the lake shrunk to its all-time minimum in 2014 by completely losing its southeastern lobe [47,48], which indicates very limited runoff during this period.

For the Aral Sea region, Flux-1 exhibits a different inter-annual signal in the region over the entire study period (Figure 12) and features a huge mass loss between 2005 and 2010. This can be explained by the overestimation of ET by WGHM (discussed in Section 3.1.3) and the underestimation of P by GPCC (discussed in Section 3.1.2). On the contrary, both hybrid-storages show a very good agreement with the GRACE signal because of the strong contribution of the Aral Sea volume trend. The difference between hybrid storages and ΔTWS from GRACE can be predominantly explained by the underestimation of SM by the hydrological models and the role of surface water storage in the delta region. The ΔTWS also has signals from the Amu Darya and Syr Darya delta and several small lakes in the two deltas, which store a significant part of the inflow from the river.

5 Discussion

The study demonstrated that the estimated reservoir flux agrees very well with the remote sensing-based Lake Mead volumetric variation (Figure 5, left), showing 90 % correlation with the in-situ and 81% with the remote sensing-based estimates (Figure 10, bottom). Net runoff is the major contributor in the estimated total flux, as seen from Figure 10 (bottom). The vertical flux (blue line in Figure 10, bottom) is always negative, which means that evaporative loss from the reservoir is greater than precipitation, and the sum is significantly less in the total flux (green line in Figure 10, bottom). The RMSE (root mean square error) between the estimated total flux and the remote sensing-based storage variation is 0.22 km^3, which can be attributed mainly to the errors in volume estimation of the reservoir. Especially when the trend of increasing/decreasing volume changes, the prior overestimations/underestimations by the remote sensing method (Figure 5, left) become more pronounced. Furthermore, the remote sensing estimates are obtained using a combination of two data products (Landsat and altimetry). When data cannot be provided by one of the products, the combined model shifts towards the available data, which can lead to a slight drift in the variability. Furthermore, the difference between the sum of fluxes and the reservoir storage variation is also affected by limitations in the flux estimates. The net flux estimate neglects other minor inflows into Lake Mead due to data unavailability, for example, the contributions from the Virgin River and Muddy River, and the precipitation flowing into the reservoir from the surroundings. In addition, the evaporative loss from the Colorado River, covering approx. 100 km between the Gauge station and the reservoir and the ground water interactions are not considered.

This paper further analyzes the cause of mass variations in the two study regions observed by GRACE during different time periods by combining different datasets. The periods of more than average rainfall and increase in net runoff generally coincided with an increase in the GRACE signal. There were periods when GRACE and the water bodies had different signals caused by variation in the amount of precipitation in the region; for example those in periods 2, 3 and 5 of the Lake Mead region and period-1 of the Aral Sea region. During these periods, it is possible that the variability in SM dominated the mass change. Abelen et al. [49] also emphasized that the SM can strongly contribute to

the GRACE signal. Conversely, there are periods dominated entirely by the variability in the water body, e.g. period-6 of the Lake Mead region and period-3 of the Aral Sea region. This detailed analysis of water balance inconsistencies, suggests improvements in the parametrization of a particular hydrological model output should be made; for example SM and ET estimates in WGHM must be recalculated for the selected regions. It can also help to visualize some possible contribution of other geophysical parameters like ground water, canopy storage, and non-hydrological mass variations, by closing the water budget of a region. Water inflow in arid/semi-arid regions is quite unevenly distributed over time. The water gained by heavy rain/runoff was also quickly lost at both of the test sites, which can be intelligently harnessed if there is a better understanding of the different hydrological contributors in the region.

The results showed that the accuracy of the interpretation of the GRACE signal is limited by errors in the datasets and varies with different datasets/model output combinations, for example as in Period-2 of the Lake Mead region. The long-term non-seasonal flux estimates have overestimated the mass loss and gain at different time periods, due to aggregated uncertainty in the sum of vertical fluxes (P – ET) and integrated error propagation. There are substantial differences between the amount of accumulated precipitation and their intensities from different precipitation datasets [50–52] and ET is one of the most uncertain variables in the global hydrological models [28]. Overestimation of ET leads to an underestimation of potential water mass and vice versa. For example, in the Lake Mead region, most of the above average rainfall (Fig. 3, left) during period-2 (2004-2005) is directly removed by higher ET in WGHM contrary to GLDAS (Fig. 4, left). Furthermore, SM is underestimated by WGHM due to smaller root zone (discussed in Section 3.2.3). Therefore, Flux-1 and Storage-1 show lower water mass than Flux-2 (not estimated for the Aral Sea region) and Storage-2 for both study regions. This indicates a deficient model structure or parameterization of WGHM for these regions. The uncertainty of the Aral Sea flux estimate is higher because of the significant difference between TRMM and GPCC precipitation data (Figure 3, right), unavailability of gauge location of the runoff and erroneous ET estimation. Using a dynamic mask of water extent over the Aral Sea and applying the evaporation rate calculated by previous studies [18–20] might result in better ET estimates here.

Table 1. Correlation of the GRACE signal with the net fluxes [combining in-situ runoff with different vertical fluxes i.e. Flux-1 (P from GPCC and ET from GLDAS) and Flux-2 (P from TRMM and ET from WGHM)], and hybrid storages [combining remote sensing based reservoir volume estimate with the SM and SWE from global hydrological models i.e. Storage-1 (WGHM) and Storage-2 (GLDAS)]. Lag -1 means a lag of 1 month with respect to the flux.

Signals (including seasonal component)	The Lake Mead region (3x3)			The Aral Sea region (4x6)		
	Correlation		RMSE	Correlation		RMSE
	Lag 0	Lag –1	(km^3)	Lag 0	Lag –1	(km^3)
δ GRACE - Flux-1	0.58	0.80	1.3	0.76	0.8	4.2
δ GRACE - Flux-2	0.63	0.76	1.3	-	-	-
GRACE - Storage-1	0.58	-	3.7	0.87	-	6.5
GRACE - Storage-2	0.87	-	2.3	0.88	-	7
GRACE - Reservoir	0.60		4	0.82	-	7.8

Table 1 and Figure 13 compare the ΔTWS observed by GRACE with the mass variations determined by different approaches. Table-1 shows that for the Lake Mead region the fluxes correspond better with the GRACE derivatives at Lag-1, which means a time lag of 1 month. Hence, GRACE data tend to describe the water mass change a month later than the flux estimates. The reason for that is that GRACE observations need to be collected over one month before a mass change can be computed. The fluxes on the other side capture it immediately. The upper panel of Figure 11 shows that the GRACE signal almost always lagged behind the net fluxes by 1 month, except for the period-6 peak which is driven by heavy runoff inflow between late 2009 and early 2010.

The results demonstrate that among all the applied datasets Storage-2 (GLDAS and remote sensing of reservoir volume-based hybrid ΔS) worked well for these regions. However, in the Aral Sea region, both the storages have above 80% correlation with ΔTWS because the reservoir is the major contributor to the GRACE signal. However, the seasonal peaks are significantly underestimated in both hybrid storages because minor contributions also come from the Aral Sea delta and many small adjoining lakes and other hydrological compartments. The impact of hydrological outputs in the region increases with decreasing lake size (Figure 13, right). In the Aral Sea region, Storage-2 has slightly high RMSE compared to Storage-1 (Table 1) because of the masking of the 1960s lake extent in GLDAS in SM and SWE simulations. Further, in the Aral Sea region, the lake is undergoing huge water mass changes, whereas SM and SWE in the surrounding region feature almost no inter-annual signal (except GLDAS SM after 2010). This indicates anthropogenic forcing and upstream water abstraction. The contribution of SM and SWE compartments in the Lake Mead region is greater than the reservoir, that is why the reservoir trend is only 60% correlated with the GRACE signal. Further, in the Lake Mead region, SM and SW show a mostly similar inter-annual signal which indicates a uniform water storage change driven by climate forcing.

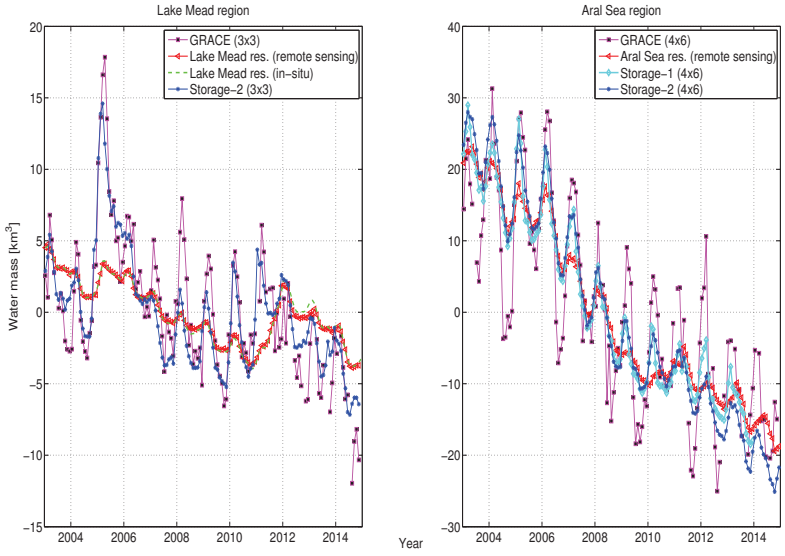

Figure 13. TWS observed by GRACE compared with the best estimates and the reservoir volume: (left) the Lake Mead region and (right) the Aral Sea region.

Due to the very small study area (90,000 km²) of the Lake Mead region compared to the GRACE resolution (200,000 km² based on satellite orbital height of ~450 km), there is a possibility that the GRACE signal dampens due to leakage to the regions outside the study box. Longuevergne et al. [43] also emphasized that when the basin area is smaller than 300,000 km² the apparent GRACE signal is underestimated for point masses. However, the signals of mass variability will remain the same, as point mass (Lake Mead) is in the center and there is no other point mass in the surrounding region. In contrast, the study area of the Aral Sea region is much larger and located close to the Caspian Sea, which can contaminate the GRACE signal. However, the mascon-based regional GRACE solution has an improved spatial resolution for this region due to the absence of a de-striping filter.

Accurately closing the water budget of any region is still an open problem. There are regions where the hydrological models fail to represent the hydrological states. For example, WGHM did not perform well in these two regions. Further, there are differences in the estimates of ΔTWS by different GRACE solutions [43]. Therefore, if the actual distribution of water is not evaluated, there can be significant error in the ΔTWS analysis of the GRACE signal. Many previous studies estimated GW storage changes

by subtracting GRACE ΔTWS by the sum of other storage compartments derived from model outputs [54–57]. However, in this study, the role of ground water storage is neglected because of the non-availability of the data. In the case of Lake Mead, GW can account for the difference in Storage-2 and ΔTWS. For example Castel et al. (2014) [58] showed declining water levels of many well stations in/around Las Vegas. However in the Aral Sea region, according to Cretaux et al. (2013) [20] the lake has an almost negligible GW contribution. Our study suggests that the combination of remote sensing-based reservoir storage with model outputs can better interpret the mass variations in GRACE, as opposed to the aforementioned entirely hydrological model-based approach. However, this method needs to be tested in more regions and for a larger area and cautious conclusions need to be drawn considering the uncertainties of the different datasets.

6 Conclusion

TWS is the integral physiographic characteristic of any territory, determined by its specific climate features, typical landscapes, and land use. The two test sites in this study are located in arid/semi-arid regions, where water is the most limiting factor for the evolution of life. Lakes/reservoirs are the major contributors of surface water volume in most of the regions. Therefore, authentic knowledge of their characteristics and dynamics is essential for short and long-term water management of a region. The main findings of the study are:

1. This study showed that the volumetric variations in a moderately sized deep reservoir, such as Lake Mead (where open water surface area is in few hundreds of kilometer square and depth is more than 100 meters) are predominately driven by the inflow – outflow runoff balance. While the vertical fluxes acting over the reservoir have negligible contributions (blue and green lines in Figure 10, bottom). Therefore, an accurate estimate of reservoir water volume variability may also help to approximate the runoff estimates at a basin level, especially in rivers connected by reservoirs, such as the Colorado River.
2. The regional variability in the hydrological state of Lake Mead is driven by the combination of runoff (Figure 2, left) and precipitation (Figure 3, left). During the study period, the region experienced mass gains twice: the first time occurred during Period-2 (2004-2005) by additional local rainfall, and the second time by the additional inflow from upstream in Period-6 (2011). This lets us conclude that GRACE is sufficiently sensitive to observe mass changes of Lake Mead if the magnitude of change is large.
3. In the study, ΔTWS observed by GRACE is compared to the estimated hydrological variations in fluxes and storages within the study area. The study showed that the long-term net flux estimation has a larger uncertainty than the total storage, due to the existing larger uncertainties in the vertical fluxes and error propagation through integration. The hybrid approach combining remote sensing-based reservoir volume estimates with hydrological model outputs provides a better possibility for the estimation of total mass change than hydrological models alone.
4. The non-seasonal mass depletion in the Aral Sea region observed by GRACE is mainly driven by the reservoir mass loss because SWE is almost stationary (Figure 6, right) and SM has a limited non-seasonal trend (Figure 7, right). This lets us conclude that the causes of mass variations in the region are not local and are driven by upstream water abstraction. On the other hand, the Lake Mead region features almost similar inter-annual variations in SM, SWE, and the reservoir, allowing us to conclude that most of the mass variations are local (except the 2012 inflow anomaly) and climatically driven.
5. Since the Aral Sea has changed dramatically in shape and size, the entire hydrological characteristics of the region have been affected. Therefore, for this region, most of the parameters are inaccurately determined by both models and no reliable in-situ data are available. Hence, for poorly monitored regions such as the Aral Sea, where reliable data is

limited, accurate reservoir storage estimates and GRACE-based mass change analysis can greatly improve the understanding of the hydrological state of the region.

Acknowledgments: This study has been supported by the German Research Foundation (DFG) through the project Clivar-Hydro of TUM's International Graduate School of Science and Engineering (IGSSE). The authors wish to express appreciation to the United States Bureau of Reclamation (USBR) and Boulder Canyon Operations Office for providing in-situ data for Lake Mead and GLDAS data providers for promptly replying to all queries. The GRACE data are available at http://grace.jpl.nasa.gov, supported by the NASA MEaSUREs Program. The Noah GLDAS data used in this study were acquired as part of the mission of NASA's Earth Science Division and archived and distributed by the Goddard Earth Sciences (GES) Data and Information Services Center (DISC). The authors are thankful to J. F. Cretaux and four anonymous reviewers for their constructive comments to improve the quality of the manuscript.

Author Contributions: A. Singh conceptualized the idea of the computation of an overall water budget of the lake dominated regions through different approaches. A. Eicker provided the EWH from mascon GRACE solution matrices and wrote a paragraph on mascon theory. A. Güntner provided the WGHM output matrices and discussed the results. F. Seitz being P.I. of the project provided the necessary guidelines. The creation of figures and the writing of the first manuscript has been done by A. Singh. All the co-authors helped in the improvement of the manuscript through constructive comments.

Conflicts of Interest: The authors declare no conflict of interest. The funding sponsors had no role in the design of the study; in the collection, analyses, or interpretation of data; in the writing of the manuscript, and in the decision to publish the results.

Reference

1. *Water in crisis: a guide to the world's fresh water resources*; Gleick, P. H.; Pacific Institute for Studies in Development, Environment, and Security; Stockholm Environment Institute, Eds.; Oxford University Press: New York, 1993.
2. Hall, A. C.; Schumann, G. J.-P.; Bamber, J. L.; Bates, P. D. Tracking water level changes of the Amazon Basin with space-borne remote sensing and integration with large scale hydrodynamic modelling: A review. *Phys. Chem. Earth Parts ABC* **2011**, *36*, 223–231.
3. Duan, Z.; Bastiaanssen, W. G. M. Estimating water volume variations in lakes and reservoirs from four operational satellite altimetry databases and satellite imagery data. *Remote Sens. Environ.* **2013**, *134*, 403–416.
4. Zhang, J.; Xu, K.; Yang, Y.; Qi, L.; Hayashi, S.; Watanabe, M. Measuring Water Storage Fluctuations in Lake Dongting, China, by Topex/Poseidon Satellite Altimetry. *Environ. Monit. Assess.* **2006**, *115*, 23–37.
5. Shiklomanov, A. I.; Lammers, R. B.; Vörösmarty, C. J. Widespread decline in hydrological monitoring threatens Pan-Arctic Research. *Eos Trans. Am. Geophys. Union* **2002**, *83*, 13.
6. Rodell, M.; Chen, J.; Kato, H.; Famiglietti, J. S.; Nigro, J.; Wilson, C. R. Estimating groundwater storage changes in the Mississippi River basin (USA) using GRACE. *Hydrogeol. J.* **2006**, *15*, 159–166.
7. Famiglietti, J. S.; Lo, M.; Ho, S. L.; Bethune, J.; Anderson, K. J.; Syed, T. H.; Swenson, S. C.; de Linage, C. R.; Rodell, M. Satellites measure recent rates of groundwater depletion in California's Central Valley. *Geophys. Res. Lett.* **2011**, *38*, L03403.
8. de Paiva, R. C. D.; Buarque, D. C.; Collischonn, W.; Bonnet, M.-P.; Frappart, F.; Calmant, S.; Bulhões Mendes, C. A. Large-scale hydrologic and hydrodynamic modeling of the Amazon River basin: HYDROLOGIC AND HYDRODYNAMIC MODELING OF THE AMAZON RIVER BASIN. *Water Resour. Res.* **2013**, *49*, 1226–1243.
9. Frappart, F.; Papa, F.; Güntner, A.; Werth, S.; Santos da Silva, J.; Tomasella, J.; Seyler, F.; Prigent, C.; Rossow, W. B.; Calmant, S.; Bonnet, M.-P. Satellite-based estimates of groundwater storage variations in large drainage basins with extensive floodplains. *Remote Sens. Environ.* **2011**, *115*, 1588–1594.
10. Papa, F.; Frappart, F.; Malbeteau, Y.; Shamsudduha, M.; Vuruputur, V.; Sekhar, M.; Ramillien, G.; Prigent, C.; Aires, F.; Pandey, R. K.; Bala, S.; Calmant, S. Satellite-derived surface and sub-surface water storage in the Ganges–Brahmaputra River Basin. *J. Hydrol. Reg. Stud.* **2015**, *4*, *Part A*, 15–35.
11. Singh, A.; Kumar, U.; Seitz, F. Remote Sensing of Storage Fluctuations of Poorly Gauged Reservoirs and State Space Model (SSM)-Based Estimation. *Remote Sens.* **2015**, *7*, 17113–17134.
12. Rosenberg, E. A.; Clark, E. A.; Steinemann, A. C.; Lettenmaier, D. P. On the contribution of groundwater storage to interannual streamflow anomalies in the Colorado River basin. *Hydrol Earth Syst Sci* **2013**, *17*, 1475–1491.
13. Barsugli, J. J.; Nowak, K.; Rajagopalan, B.; Prairie, J. R.; Harding, B. Comment on "When will Lake Mead go dry?" by T. P. Barnett and D. W. Pierce. *Water Resour. Res.* **2009**, *45*, W09601.

14. Rodell, M.; Houser, P. R.; Jambor, U.; Gottschalck, J.; Mitchell, K.; Meng, C.-J.; Arsenault, K.; Cosgrove, B.; Radakovich, J.; Bosilovich, M.; Entin*, J. K.; Walker, J. P.; Lohmann, D.; Toll, D. The Global Land Data Assimilation System. *Bull. Am. Meteorol. Soc.* **2004**, *85*, 381–394.
15. Huffman, G. J.; Bolvin, D. T.; Nelkin, E. J.; Wolff, D. B.; Adler, R. F.; Gu, G.; Hong, Y.; Bowman, K. P.; Stocker, E. F. The TRMM Multisatellite Precipitation Analysis (TMPA): Quasi-Global, Multiyear, Combined-Sensor Precipitation Estimates at Fine Scales. *J. Hydrometeorol.* **2007**, *8*, 38–55.
16. Döll, P.; Kaspar, F.; Lehner, B. A global hydrological model for deriving water availability indicators: model tuning and validation. *J. Hydrol.* **2003**, *270*, 105–134.
17. Müller Schmied, H.; Eisner, S.; Franz, D.; Wattenbach, M.; Portmann, F. T.; Flörke, M.; Döll, P. Sensitivity of simulated global-scale freshwater fluxes and storages to input data, hydrological model structure, human water use and calibration. *Hydrol Earth Syst Sci* **2014**, *18*, 3511–3538.
18. Small, E. E.; Sloan, L. C.; Hostetler, S.; Giorgi, F. Simulating the water balance of the Aral Sea with a coupled regional climate-lake model. *J. Geophys. Res. Atmospheres* **1999**, *104*, 6583–6602.
19. Small, E. E.; Giorgi, F.; Sloan, L. C.; Hostetler, S. The Effects of Desiccation and Climatic Change on the Hydrology of the Aral Sea. *J. Clim.* **2001**, *14*, 300–322.
20. Cretaux, J.-F.; Letolle, R.; Bergé-Nguyen, M. History of Aral Sea level variability and current scientific debates. *Glob. Planet. Change* **2013**, *110*, *Part A*, 99–113.
21. Hou, A. Y.; Kakar, R. K.; Neeck, S.; Azarbarzin, A. A.; Kummerow, C. D.; Kojima, M.; Oki, R.; Nakamura, K.; Iguchi, T. The global precipitation measurement mission. *Bull. Am. Meteorol. Soc.* **2014**, *95*, 701–722.
22. Dery, S. J.; Brown, R. D. Recent Northern Hemisphere snow cover extent trends and implications for the snow-albedo feedback. *Geophys. Res. Lett.* **2007**, *34*, L22504.
23. Papa, F.; Prigent, C.; Rossow, W. B.; Legresy, B.; Remy, F. Inundated wetland dynamics over boreal regions from remote sensing: the use of Topex-Poseidon dual-frequency radar altimeter observations. *Int. J. Remote Sens.* **2006**, *27*, 4847–4866.
24. Seitz, F.; Schmidt, M.; Shum, C. K. Signals of extreme weather conditions in Central Europe in GRACE 4-D hydrological mass variations. *Earth Planet. Sci. Lett.* **2008**, *268*, 165–170.
25. Forootan, E.; Didova, O.; Kusche, J.; Löcher, A. Comparisons of atmospheric data and reduction methods for the analysis of satellite gravimetry observations. *J. Geophys. Res. Solid Earth* **2013**, *118*, 2382–2396.
26. Jiang, H.; Feng, M.; Zhu, Y.; Lu, N.; Huang, J.; Xiao, T. An Automated Method for Extracting Rivers and Lakes from Landsat Imagery. *Remote Sens.* **2014**, *6*, 5067–5089.
27. Eicker, A.; Schumacher, M.; Kusche, J.; Döll, P.; Schmied, H. M. Calibration/Data Assimilation Approach for Integrating GRACE Data into the WaterGAP Global Hydrology Model (WGHM) Using an Ensemble Kalman Filter: First Results. *Surv. Geophys.* **2014**, *35*, 1285–1309.
28. Schumacher, M.; Eicker, A.; Kusche, J.; Schmied, H. M.; Döll, P. Covariance Analysis and Sensitivity Studies for GRACE Assimilation into WGHM. In; International Association of Geodesy Symposia; Springer Berlin Heidelberg, 2015; pp. 1–7.
29. Tangdamrongsub, N.; Steele-Dunne, S. C.; Gunter, B. C.; Ditmar, P. G.; Weerts, A. H. Data assimilation of GRACE terrestrial water storage estimates into a regional hydrological model of the Rhine River basin. *Hydrol Earth Syst Sci* **2015**, *19*, 2079–2100.
30. Swenson, S.; Yeh, P. J.-F.; Wahr, J.; Famiglietti, J. A comparison of terrestrial water storage variations from GRACE with in situ measurements from Illinois. *Geophys. Res. Lett.* **2006**, *33*.
31. Swenson, S.; Wahr, J. Monitoring the water balance of Lake Victoria, East Africa, from space. *J. Hydrol.* **2009**, *370*, 163–176.
32. Strassberg, G.; Scanlon, B. R.; Rodell, M. Comparison of seasonal terrestrial water storage variations from GRACE with groundwater-level measurements from the High Plains Aquifer (USA). *Geophys. Res. Lett.* **2007**, *34*.
33. Becker, M.; LLovel, W.; Cazenave, A.; Güntner, A.; Crétaux, J.-F. Recent hydrological behavior of the East African great lakes region inferred from GRACE, satellite altimetry and rainfall observations. *Comptes Rendus Geosci.* **2010**, *342*, 223–233.
34. Singh, A.; Seitz, F.; Schwatke, C. Application of Multi-Sensor Satellite Data to Observe Water Storage Variations. *IEEE J. Sel. Top. Appl. Earth Obs. Remote Sens.* **2013**, *6*, 1502–1508.
35. Forootan, E.; Rietbroek, R.; Kusche, J.; Sharifi, M. A.; Awange, J. L.; Schmidt, M.; Omondi, P.; Famiglietti, J. Separation of large scale water storage patterns over Iran using GRACE, altimetry and hydrological data. *Remote Sens. Environ.* **2014**, *140*, 580–595.
36. Aus der Beek, T.; Voß, F.; Flörke, M. Modelling the impact of Global Change on the hydrological system of the Aral Sea basin. *Phys. Chem. Earth Parts ABC* **2011**, *36*, 684–695.

37. Long, D.; Longuevergne, L.; Scanlon, B. R. Global analysis of approaches for deriving total water storage changes from GRACE satellites. *Water Resour. Res.* **2015**, *51*, 2574–2594.
38. Watkins, M. M.; Wiese, D. N.; Yuan, D.-N.; Boening, C.; Landerer, F. W. Improved methods for observing Earth's time variable mass distribution with GRACE using spherical cap mascons: Improved Gravity Observations from GRACE. *J. Geophys. Res. Solid Earth* **2015**, *120*, 2648–2671.
39. Wiese, D. N. GRACE MONTHLY LAND WATER MASS GRIDS NETCDF RELEASE 5.0 | PO.DAAC https://podaac.jpl.nasa.gov/dataset/TELLUS_LAND_NC_RL05 (accessed Mar 31, 2016).
40. Swenson, S.; Chambers, D.; Wahr, J. Estimating geocenter variations from a combination of GRACE and ocean model output. *J. Geophys. Res. Solid Earth* **2008**, *113*, B08410.
41. Cheng, M.; Tapley, B. D.; Ries, J. C. Deceleration in the Earth's oblateness. *J. Geophys. Res. Solid Earth* **2013**, *118*, 740–747.
42. A, G.; Wahr, J.; Zhong, S. Computations of the viscoelastic response of a 3-D compressible Earth to surface loading: an application to Glacial Isostatic Adjustment in Antarctica and Canada. *Geophys. J. Int.* **2013**, *192*, 557–572.
43. Longuevergne, L.; Wilson, C. R.; Scanlon, B. R.; Crétaux, J. F. GRACE water storage estimates for the Middle East and other regions with significant reservoir and lake storage. *Hydrol Earth Syst Sci* **2013**, *17*, 4817–4830.
44. Overview - Monthly Mass Grids http://grace.jpl.nasa.gov/data/monthly-mass-grids (accessed Oct 10, 2016).
45. Rechard, P. A. Determining Bank Storage of Lake Mead. *J. Irrig. Drain. Div.* **1965**, *91*, 141–158.
46. Lindsey, R. World of Change: Water Level in Lake Powell : Feature Articles http://earthobservatory.nasa.gov/Features/WorldOfChange/lake_powell.php (accessed Jul 19, 2016).
47. Lindsey, R. World of Change: Shrinking Aral Sea : Feature Articles http://earthobservatory.nasa.gov/Features/WorldOfChange/aral_sea.php (accessed Jul 19, 2016).
48. Aladin, N.; Plotnikov, I.; Micklin, P.; Ballatore, T. Aral Sea: Water level, salinity and long-term changes in biological communities of an endangered ecosystem-past, present and future. *Nat. Resour. Environ. Issues* **2009**, *15*.
49. Abelen, S.; Seitz, F. Relating satellite gravimetry data to global soil moisture products via data harmonization and correlation analysis. *Remote Sens. Environ.* **2013**, *136*, 89–98.
50. Yin, X.; Gruber, A.; Arkin, P. Comparison of the GPCP and CMAP Merged Gauge–Satellite Monthly Precipitation Products for the Period 1979–2001. *J. Hydrometeorol.* **2004**, *5*, 1207–1222.
51. Negrón Juárez, R. I.; Li, W.; Fu, R.; Fernandes, K.; de Oliveira Cardoso, A. Comparison of Precipitation Datasets over the Tropical South American and African Continents. *J. Hydrometeorol.* **2009**, *10*, 289–299.
52. Shin, D.-B.; Kim, J.-H.; Park, H.-J. Agreement between monthly precipitation estimates from TRMM satellite, NCEP reanalysis, and merged gauge-satellite analysis. *J. Geophys. Res. Atmospheres* **2011**, *116*, D16105.
53. Gaybullaev, B.; Chen, S.-C.; Kuo, Y.-M. Large-scale desiccation of the Aral Sea due to over-exploitation after 1960. *J. Mt. Sci.* **2012**, *9*, 538–546.
54. Brena, A.; Kendall, A. D.; Hyndman, D. W. Improved methods for GRACE-derived groundwater storage change estimation in large-scale agroecosystems. *AGU Fall Meet. Abstr.* **2013**, *24*.
55. Chen, J.; Li, J.; Zhang, Z.; Ni, S. Long-term groundwater variations in Northwest India from satellite gravity measurements. *Glob. Planet. Change* **2014**, *116*, 130–138.
56. Richey, A. S.; Thomas, B. F.; Lo, M.-H.; Reager, J. T.; Famiglietti, J. S.; Voss, K.; Swenson, S.; Rodell, M. Quantifying renewable groundwater stress with GRACE. *Water Resour. Res.* **2015**, *51*, 5217–5238.
57. Chen, J.; Famigliett, J. S.; Scanlon, B. R.; Rodell, M. Groundwater Storage Changes: Present Status from GRACE Observations. *Surv. Geophys.* **2015**, *37*, 397–417.
58. Castle, S. L.; Thomas, B. F.; Reager, J. T.; Rodell, M.; Swenson, S. C.; Famiglietti, J. S. Groundwater depletion during drought threatens future water security of the Colorado River Basin. *Geophys. Res. Lett.* **2014**, *41*, 2014GL061055.